JOURNAL OF APPLIED PHYSICS

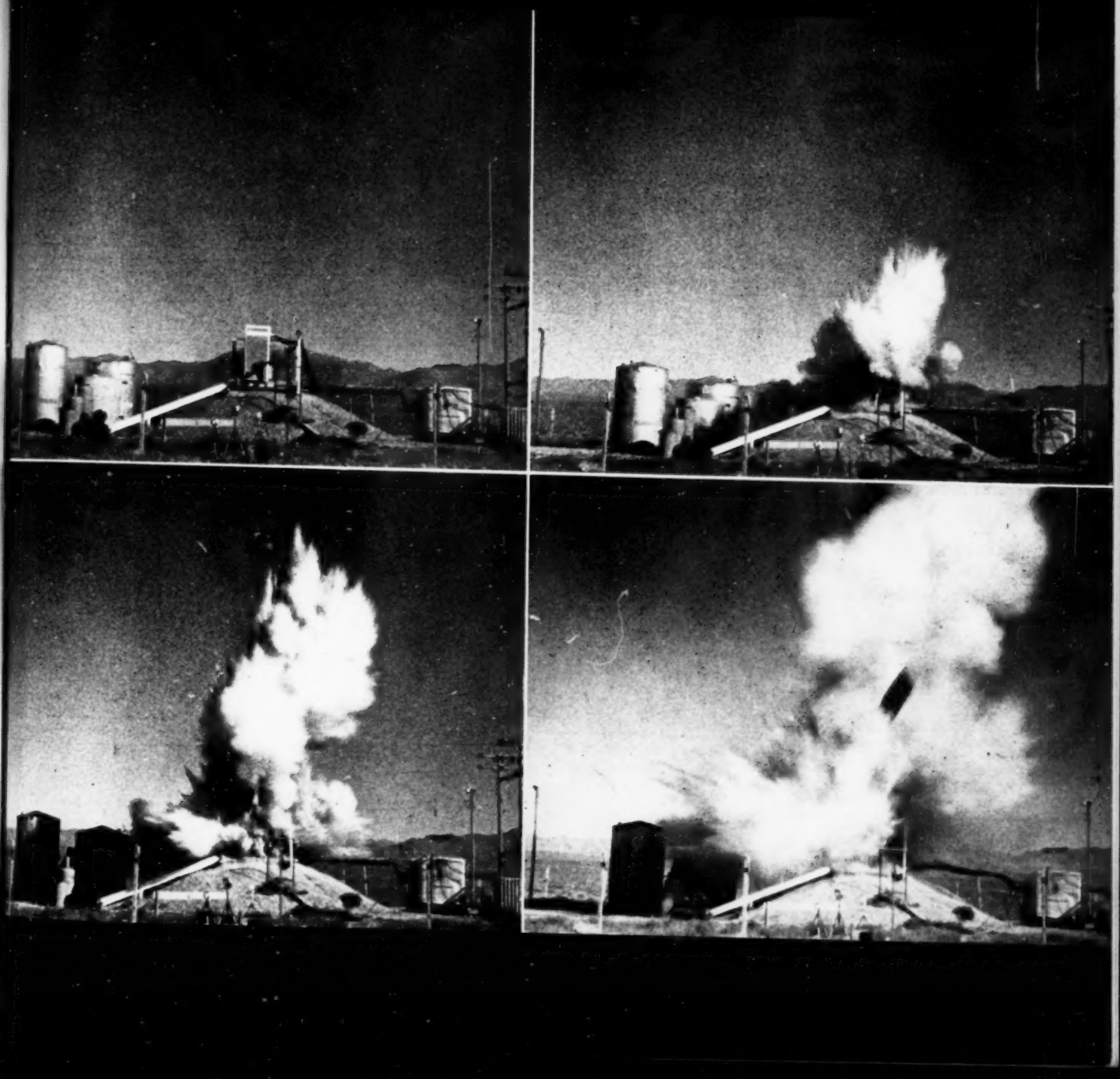

FAST WORK BY

NEWTON RINGS

capturing pressure transients

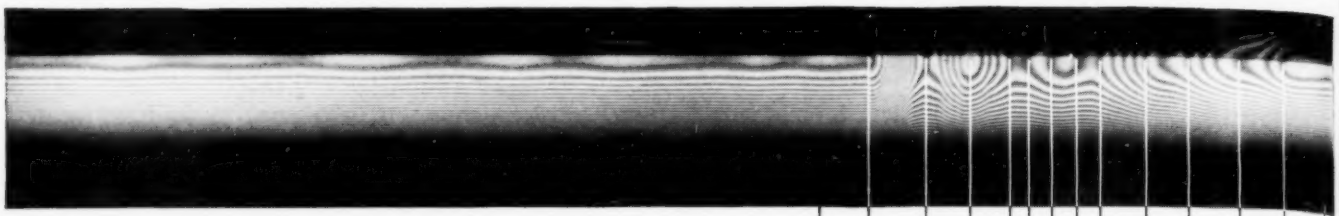

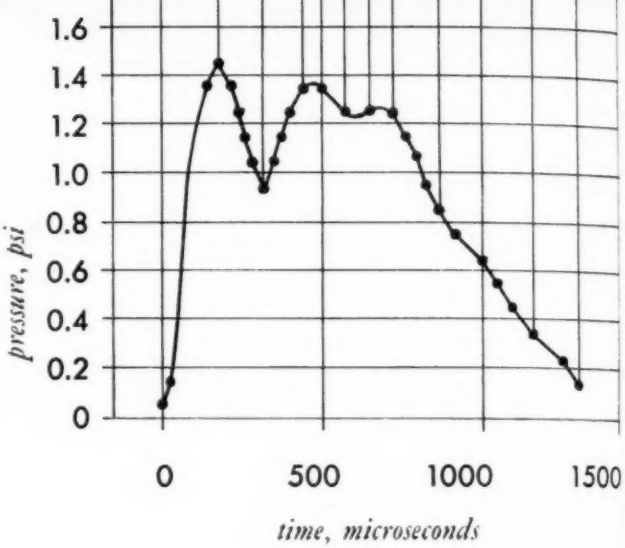

Light, the ideal yardstick for measuring rapid events, creates a pressure-transient measuring system of unusual capability in the Beckman & Whitley Model 216 Pressure Recorder. Having stable linear calibration, the unit can cover pressure ranges from 3 to 50,000 psi, with a 1 per cent full-scale accuracy in both pressure and time, and exhibits a frequency response from 10,000 to 50,000 cps.

To cover the widest possible variety of application requirements, the recorder is engineered so it can be used in three ways: (1) exposed to free air manifestations, (2) attached directly to a pressure vessel, or (3) fed by a hydraulic line from the pressure source.

The instrument is organized into two units, shown below. Transducer, optical system, and camera with timing-pip system are in the unit at left. The control unit, right, permits records to be made remotely.

Rapid response, accurate measurement of small displacements, high sensitivity, and stable zero reference points are all achieved by recording on moving film the motion of small arcs of optical-interference rings responding to the influence of the pressure fluctuations under measurement. Such fringe changes can be seen in the typical record above, while underneath, the simple procedure of translating the pattern into a plot of pressure-versus-time is outlined.

SEND FOR FURTHER DETAILS.

Beckman & Whitley INC.

instruments for physical research

SAN CARLOS 8, CALIFORNIA

JOURNAL OF APPLIED PHYSICS

Vol. 26, No. 10 OCTOBER, 1955

In This Issue

Methods for the Correction of X-Ray Intensities for Primary and Secondary Extinction in Crystal Structure Analysis . . . . . Vladimir Vand 1191

On Zone Refining . . . . . Joseph L. Birman 1195

Streaming Birefringence as a Hydrodynamic Research Tool—Applied to Rotating Cylinder Apparatus above the Transition Velocity . . . . . Harold Wayland 1197

Study of the Initial Stages of Sintering Solids by Viscous Flow, Evaporation-Condensation, and Self-Diffusion . . . . . W. D. Kingery and M. Berg 1205

Theory of Steady-State Creep Based on Dislocation Climb . . . . . J. Weertman 1213

Shape and Crystal Anisotropy of Alnico 5 . . . . . E. A. Nesbitt and H. J. Williams 1217

Precise Investigation of the Theory of Damping by Transverse Thermal Currents . . . . . B. S. Berry 1221

Hysteresis Effect in Multiplier Phototube Noise . . . . . C. A. Ziegler and H. H. Seliger 1225

On Electron Mirror Microscopy . . . . . Ludwig Mayer 1228

On Representation of Electromagnetic Fields in Cavities in Terms of Natural Modes of Oscillation . . . . . S. A. Schelkunoff 1231

Spatial Distribution of Thermal Neutrons from a Polonium-Beryllium Source in Water-Zirconium Mixtures . . . . . William Baer 1235

Outgassing of Glass . . . . . B. Johnson Todd 1238

Prebreakdown Current and Noise in Insulators . . . . . D. A. Powers and T. Suita 1244

Surface Friction in Ballistic Penetration . . . . . Joseph M. Krafft 1248

Preferred Orientation of Platelets in X-Ray Diffractometer Powder Samples . . . . James E. Manson 1254

Conduction and Breakdown in Hexane . . . . . W. B. Green 1257

Effect of Water Vapor on Grown Germanium and Silicon *np* Junction Units . J. T. Law and P. S. Meigs 1265

Permanent-Magnet Properties of Elongated Single-Domain Iron Particles . . . . . L. I. Mendelsohn, F. E. Luborsky, and T. O. Paine 1274

Letters to the Editor:

Magnetically Controlled Microwave Directional Coupler . . . . . R. W. Damon 1281

New Type Ferrite Microwave Switch . . . . . R. F. Sullivan and R. C. LeCraw 1282

Failure of the Ionic Centrifuge Prior to the Ionic Expander . . . . . Joseph Slepian 1283

Erratum: Rocket Measurements of Upper Atmosphere Ambient Temperature and Pressure in the 30-to-75 Kilometer Region . . . H. S. Sicinski, N. W. Spencer, and W. G. Dow 1284

Erratum: Nucleation of Lead with Preferred Orientation. H. A. Atwater and B. Chalmers 1284

Research Reports 1284

Books Reviewed 1284

Books Received 1285

Cover Photograph 1286

Index to Advertisers xxxii

JOURNAL OF APPLIED PHYSICS

A journal of applications of physics to other sciences and to industry

Published by the

American Institute of Physics

GOVERNING BOARD

Allen V. Astin
Robert F. Bacher
H. A. Bethe
J. W. Buchta
S. A. Goudsmit
Deane B. Judd
Hugh S. Knowles
W. H. Markwood, Jr.
William F. Meggers
Philip M. Morse
Brian O'Brien
Harry F. Olson
R. F. Paton
Eric Rodgers
Ralph A. Sawyer
Frederick Seitz
William Shockley
H. D. Smyth
J. H. Van Vleck
Mark W. Zemansky

OFFICERS AND STAFF

Frederick Seitz
Chairman, Governing Board

Henry A. Barton
Director

George B. Pegram
Treasurer

Wallace Waterfall
Executive Secretary

Theodore Vorburger
Advertising Manager

Ruth F. Bryans
Publication Manager

Edith I. Neftel
Circulation Manager

Kathryn Setze
Assistant Treasurer

Melvin Loos
Consultant on Printing

Editor
Robert L. Sproull

Editorial Board

Maurice A. Biot
Walker Bleakney
Wallace J. Eckert
Elmer Hutchisson
D. O. North
Louis A. Pipes
W. R. Smythe
Arthur V. Tobolsky
A. M. Weinberg

THE JOURNAL OF APPLIED PHYSICS is devoted to the application of physics to other sciences, to engineering, and to industry. Previous to 1937, this journal was called PHYSICS.

The JOURNAL OF APPLIED PHYSICS welcomes articles of two distinct kinds: (1) Descriptions of new results in experimental or theoretical physics which are of general interest to applied physicists. The author should explain his contribution in such a way that a physicist or engineer in another field of specialization can appreciate its objectives and essential features. (2) Critical reviews of particular areas of applied physics. Authors contemplating writing such reviews should correspond with the Editor before they begin writing.

The JOURNAL OF APPLIED PHYSICS welcomes letters to the editor which describe in a few words the content of laboratory reports and theses and which tell readers how they may obtain copies of such reports.

Manuscripts should be submitted to the Editor, Rockefeller Hall, Cornell University, Ithaca, New York. Authors should read the "Information for Contributors," facing page 1 of the January issue, before writing articles or letters. The *Style Manual* of the American Institute of Physics is also helpful to writers preparing manuscripts for journals published by the American Institute of Physics. It can be obtained for $1.00 from the American Institute of Physics, 57 East 55th Street, New York 22, New York.

Corrected proofs and all correspondence concerning papers in the process of publication should be addressed to the Publication Manager, American Institute of Physics, 57 East 55 Street, New York 22, New York.

Subscriptions, renewals, and orders for back numbers should be addressed to the American Institute of Physics, 57 East 55 Street, New York 22, New York.

Subscription Price	U.S. and Canada	Elsewhere
To members of the American Institute of Physics and Affiliated Societies	$10.00	$11.00
To all others	12.00	14.00

Back Number Prices

Yearly back number rate when complete year is available: $15.00.
Single copies: $1.50 each.

Changes of address should be sent to the American Institute of Physics.

Advertising rates supplied on request. Orders, advertising copy, and cuts should be sent to the American Institute of Physics.

Entered as second class matter January 22, 1937, at the Post Office at Lancaster, Pennsylvania, under the Act of March 3, 1879. Accepted for mailing at the special rate of postage provided for in paragraph (d-2), section 34.40, P. L. & R. of 1948, authorized May 2, 1932.

Journal
of
Applied Physics

Volume 26, Number 10 October, 1955

Methods for the Correction of X-Ray Intensities for Primary and Secondary Extinction in Crystal Structure Analysis*

VLADIMIR VAND
X-Ray and Crystal Analysis Laboratory, Department of Physics, Pennsylvania State University, University Park, Pennsylvania
(Received January 19, 1955)

The theory of x-ray extinction in diffraction studies is reviewed, and application to small crystals completely bathed in the incident beam is considered. Using a suitable approximation to a sum of Bessel functions, a correction formula is obtained, valid in the region of small Bragg angle θ where the extinction is likely to be greatest. The formula is discussed; and it is shown that when the crystal structure is essentially known, as in later stages of refinement, it is possible to separate the effects of primary from secondary extinction and to correct the experimental data accordingly.

I. INTRODUCTION

A number of experimental and theoretical developments have permitted a significant increase in the accuracy of x-ray structure determination in the last few years. It is well known that even when all refinements are applied, there often remain large discrepancies in the observed and calculated intensities of the strongest low-order diffracted beams. These are caused by extinction effects. The best contemporary practice for dealing with these effects is to ignore the discrepancies by excluding the affected reflections from the refinement cycle. This is a legitimate procedure when atomic coordinates and temperature oscillation parameters are sought. The discrepancies appear to represent the largest obstruction to completely satisfactory comparison of *all* the measured and calculated intensities; and they are particularly disturbing in studies of accurate bonding-electron distributions. For such studies, the observations have to be corrected for the extinction effects.

The presence of extinction can often be detected in the usual plot of log $(F_0/F_c^{(\text{cold})})$ against $\sin^2\theta$, where $F_c^{(\text{cold})}$ are calculated using good atomic scattering curves (see McWeeny[1]). Here F_0 are observed structure factors, and $F_c^{(\text{cold})}$ are calculated factors for atoms without temperature vibration. The graph should give a straight line, from which the over-all temperature factor for the structure should be obtainable. It is often found that all the points (obtained by grouping reflections in small ranges of $\sin^2\theta$) lie on a satisfactory straight line, with the exception of a few points of lowest $\sin^2\theta$—which usually contain strong low-order reflections. Due to extinction, this part of the graph is, as a rule, curved towards small values of F_0.

No entirely satisfactory methods of correction for primary and secondary extinction have yet been proposed in the literature, although a considerable volume of theoretical work is available. The mosaic model of the crystal structure was first proposed by Darwin[2,3] as early as 1914, and the dynamical theory of x-ray diffraction was thoroughly worked out by Ewald[4–7] in a series of papers. Good treatments of this theory can also be found in Zachariasen's treatise[8] and in a paper by Lonsdale[9] and another, slightly more geometrical description, appears in R. W. James' volume.[10] Formulas are also given in the second volume

* Research supported by Contract No. N6onr-26916, T. O. 16 with the Office of Naval Research, and by Grant A-228 from the National Institute of Health.

[1] R. McWeeny, Acta. Cryst. **4**, 513 (1951).

[2] C. G. Darwin, Phil. Mag. **27**, 325, 675 (1914).
[3] C. G. Darwin, Phil. Mag. **43**, 800 (1922).
[4] P. P. Ewald, Ann. Physik **54**, 519, 577 (1917).
[5] P. P. Ewald, Z. Physik **2**, 232 (1920).
[6] P. P. Ewald, Z. Physik **30**, 1 (1924).
[7] P. P. Ewald, Physik. Z. **26**, 29 (1925).
[8] W. H. Zachariasen, *Theory of X-Ray Diffraction in Crystals* (John Wiley and Sons, Inc., New York, 1945).
[9] K. Lonsdale, Mineralog. Mag. **28**, 14 (1947).
[10] R. W. James, *Optical Principles of the Diffraction of X-Rays* (G. Bell and Sons, London, 1948).

of the *Internationale Tabellen*,[11] p. 563. The theory of extinction has been treated by Miyake[12] (in Japanese) more fully than in the above texts. Extinction in powders is discussed by Lang[13] and in the case of neutron diffraction by Bacon and Lowde.[14]

II. CAUSE OF EXTINCTION EFFECTS

If the diffracted beam is of appreciable intensity, it drains energy from the primary beam; and the effect is the greater, the stronger the diffracted beam. Since energy must be conserved, this means that the primary beam is attenuated more rapidly than it would be if reflection of x-rays were not present and attenuation had been caused by true absorption only. However, in the formula for the diffracted beam intensity by a small crystal it is assumed that the intensity of the primary beam is the same throughout the crystal; and when this is not fulfilled, the formula gives a calculated intensity higher than the true intensity. This manifests itself ultimately when the F_0 and F_c structure factors of a solved structure are compared. The strongest reflections may show appreciably lower values of F_0 as compared with F_c.

The conditions for the primary (coherent) extinction are large size of perfect blocks, but high angular dispersion of orientations of individual blocks from block to block. For secondary (incoherent) extinction small-sized perfect blocks are required, with small angular dispersion of orientations of individual blocks, so that many are operative at a time.

Two cases are to be distinguished in the theoretical treatment of extinction. In the "Bragg case," x-rays are reflected from a face of a large thick crystal, such as was used in an early type of spectrometer. The primary and the diffracted beams are then situated on the same side of the crystal face. In the "Laue case" a relatively thin crystal plate is involved; the incoming beam strikes one face of the plate, and the scattered beam emerges from the opposite face.

In present-day x-ray analyses the crystal under study is usually small and completely bathed in the primary x-ray beam. The extinction effects are greatest for the strongest diffracted beams, and those in turn occur in the region of small Bragg angles θ, because of the general decrease of F with θ due to atomic scattering curves and temperature factors. As a consequence, the case which occurs in practice is the Laue, and not the Bragg, case. Since the Bragg case has been treated in the original papers and textbooks more fully than the Laue case, some investigators have attempted to use a wrong formula for correction of their intensities, where the latter have been obtained using small crystals in the transmission arrangement.

[11] *Internationale Tabellen zur Bestimmung von Kristallstrukturen* (Borntraeger, Berlin, 1935).
[12] S. Miyake, *Diffraction of X-Rays* (in Japanese) (Asakura, Tokyo, 1950).
[13] A. R. Lang, Proc. Phys. Soc. (London) **B66**, 1003 (1953).
[14] G. E. Bacon and R. D. Lowde, Acta Cryst. **1**, 303 (1948).

III. MATHEMATICAL TREATMENT

The integrated intensity I_H of coherent scattering for a small crystal of volume δV with negligible absorption, and completely bathed in the x-ray beam of intensity I_0, is given by

$$I_H = I_0 R = E\omega = I_0 Q \delta V. \tag{1}$$

Here $R = I_H/I_0$ is the ratio of intensities in the secondary and primary beams, and E is the total energy reflected by a crystal rotating with velocity ω; and, for the rotating crystal method,

$$Q = \left(\frac{e^2}{mc^2 V}\right)^2 \cdot L.p. \cdot |F_H|^2 \cdot \frac{\lambda^3}{2} \tag{2}$$

[see Zachariasen,[8] Eq. (3.78)], where e, m, c, λ have the usual meanings of electronic charge, electronic mass, velocity of light, and wavelength of x-rays, V is the volume of one unit cell, F_H is the structure factor, and $L.p.$ is the Lorentz and polarization factor which, for equatorial reflections only and a cylindrical camera, is

$$L.p. = \frac{1+\cos^2 2\theta}{\sin 2\theta}, \tag{3}$$

where θ is the Bragg angle.

If the absorption of x-rays in the crystal is taken into account, then, for a crystal plate of thickness T and the symmetrical Laue case, instead of Eq. (1) we have

$$R = \frac{Q}{\cos\theta} e^{-\mu T/\cos\theta} \delta V \tag{4}$$

[see, e.g., Zachariasen,[8] Eq. (4.41)]. Here μ is the linear absorption coefficient and θ the glancing angle.

From the theory of diffraction of x-rays by mosaic and perfect crystals it follows that the effect of primary extinction can be included in formula (4) by the simple procedure of replacing Q by the more general expression $Q' = f \cdot Q$ (see Zachariasen,[8] p. 170). Similarly, the effect of secondary extinction can be included by replacing μ by $(\mu_0 + gQ')$ [Zachariasen,[8] Eq. (4.43b)], where μ_0 is the linear absorption coefficient without the extinction effect.

In these equations, f is a function of intensity depending on the size of the perfect regions; and g, although usually varying with the crystallographic direction, is usually assumed to be a constant coefficient for a given crystal, depending only on the nature and angular spread of its mosaic structure. For a statistical Gaussian distribution of tilts of perfect blocks,

$$g = \frac{1}{2\sqrt{\pi\eta}}, \tag{5}$$

where η is the mean angular dispersion of blocks (Zachariasen,[8] p. 168). As an example, if the dispersion is 4′ of arc, $\eta = 1.1 \cdot 10^{-3}$ and $g = 260$.

We have thus for the most general case with linear absorption, primary and secondary extinction all present,

$$R=\frac{Q'\delta V}{\cos\theta}e^{-(\mu_0+gQ')T/\cos\theta}, \tag{6}$$

where $Q'=fQ$ and T is the thickness of the crystal plate. If the crystal is irregular, so that the conditions of the symmetrical Laue case are only approximately fulfilled, T can be replaced by T_e, the effective thickness of the crystal, to a first approximation (see Zachariasen,[8] p. 135).

If the absence of the absorption and extinctions is assumed, R would have the value

$$R_0=\frac{QdV}{\cos\theta}; \tag{7}$$

so that the true value of R can be obtained from R_0, calculated under the assumption of absence of extinction effects:

$$R=R_0fe^{-(\mu_0+gQ')T_e/\cos\theta}, \tag{8}$$

which is the correction formula for absorption and extinction effects.

For a perfect crystal and the Laue case,

$$f(A)=\frac{\sum_{n=0}^{\infty}J_{2n+1}(2A)+\cos2\theta\sum_{n=0}^{\infty}J_{2n+1}(2A\cos2\theta)}{A(1+\cos^2 2\theta)} \tag{9}$$

[see Zachariasen,[8] Eq. (4.46b)]. Here

$$A=\frac{e^2\lambda|F|T_e}{mc^2V} \tag{10}$$

where T_e is the average path through or the effective linear dimension of the crystal, V is the volume of one unit cell, and e, λ, m, and c have their usual meaning [see Zachariasen,[8] Eq. (3.169)].

Equation (9) for $f(A)$ is rather unwieldy, because it involves sums of Bessel functions J_{2n+1}. The individual terms converge to zero rather rapidly with increasing n. For small x the following series expansion can be used:

$$\sum_{n=0}^{\infty}J_{2n+1}(2x)=x-\frac{x^3}{3}+\frac{x^5}{20}-\cdots\pm\frac{x^{2n+1}}{(2n+1)(n!)^2}\mp\cdots. \tag{11}$$

However, this expansion converges rather slowly for $x>1$.

For small values of x, the sum can also be approximated by

$$\tanh x=x-\frac{x^3}{3}+\frac{2x^5}{15}-\cdots,$$

which is a function involved in the Bragg case. For large x, $\sum J_{2n+1}(2x)$ approaches $\frac{1}{2}$, whereas $\tanh x$ approaches 1; so that, for large A, $f(A)$ for the Bragg case is twice the value of $f(A)$ for the Laue case.

After some search, a satisfactory approximation has been found:

$$\sum J_{2n+1}(2x)\cong x\exp(-\tfrac{1}{3}x^2). \tag{12}$$

This can be seen from the series development:

$$x\exp(-\tfrac{1}{3}x^2)=x-\frac{x^3}{3}+\frac{x^5}{18}-\cdots. \tag{13}$$

This approximation holds quite accurately over a range of $0<x<2$, which is usually several times greater than the range encountered in crystals used for modern structure determination.

For more accurate work, or for $x>2$, the values of the sum of Bessel functions should be directly used in the computations; but for values of $x\leqq 2$, the replacement by $x\exp(-\frac{1}{3}x^2)$ is fully justified for all practical purposes.

We can thus write:

$$\begin{aligned}f(A)&=\frac{\exp(-\frac{1}{3}A^2)+\cos2\theta\exp(-\frac{1}{3}A^2\cos^2 2\theta)}{1+\cos^2 2\theta}\\&=\frac{\exp(-\frac{1}{3}A^2)[1+\cos2\theta\exp(\frac{1}{3}A^2\sin^2 2\theta)]}{2-\sin^2 2\theta}\\&=\exp(-\tfrac{1}{3}A^2)[1+(\tfrac{1}{4}+\tfrac{1}{6}A^2)\sin^2 2\theta+\cdots].\end{aligned} \tag{14}$$

If the crystal is truly a thin extended plate, this variation with $\sin^2 2\theta$ should be taken into account for larger values of θ; the correction, however, amounts only to about 7% for $\theta=15°$. For a crystal of a more compact shape, the geometry of the Laue case fails to be satisfied for larger angles of θ, since the rays will begin to emerge from the sides of the crystal, and the application of the $\sin^2 2\theta$ term becomes questionable. In fact, for large θ the expression for $f(A)$ will finally change from the Laue to the Bragg case. It appears thus that since we at present lack the correct formula for a compact (spherical or cylindrical) crystal, and the extinction effects are confined to small values of θ, we can omit the variation with θ and write for this low-angle region,

$$f(A)=\exp(-\tfrac{1}{3}A^2). \tag{15}$$

For small θ, we are equally justified to omit $\cos\theta$ in Eq. (8). After substituting (15) in (8), substituting for Q' and taking a logarithm, the final formula for small angles θ is then:

$$\ln\frac{R}{R_0}=-\tfrac{1}{3}A^2-\mu_0T_e-gT_eQ\exp(-\tfrac{1}{3}A^2); \tag{16}$$

or, after development of the exponential in a series,

$$\ln\frac{R}{R_0}=-\mu_0 T_e-\tfrac{1}{3}A^2-gT_eQ+\tfrac{1}{3}gT_eQA^2+\cdots. \quad (17)$$

We shall now make the following abbreviations:

(1) for the ordinary absorption effect,

$$\mu_0 T_e=a; \quad (18)$$

(if the absorption has been taken into account in R_0, a may still be retained as an absolute scale factor adjustment);

(2) for the primary extinction effect,

$$\tfrac{1}{3}A^2=bF_c^2; \quad (19)$$

(3) for the secondary extinction effect,

$$gT_eQ=cL.p.F_c^2. \quad (20)$$

We have then

$$-\ln\left(\frac{R}{R_0}\right)=a+bF_c^2+cL.p.F_c^2-bcL.p.F_c^4+\cdots. \quad (21)$$

Neglecting higher terms than F_c^2 (i.e., the cross influence of primary and secondary extinction),

$$-\ln\left(\frac{R}{R_0}\right)=-\ln\left(\frac{F_0}{F_c}\right)^2=-2\ln\frac{F_0}{F_c}$$
$$=a+bF_c^2+cL.p.F_c^2. \quad (22)$$

In this equation, the coefficients a, b, c, can easily be determined if the values of F_0 and F_c are known with sufficient accuracy. For example, a system of linear equations for the unknowns, a, b, c, can be formed; and these can be solved by the method of least squares. However, in this method, care must be taken to weigh the equations, since the terms having small values of F, require proportionally smaller weights. The smaller these are, the greater is the probable error of the fraction. For this reason, graphical methods are often preferable to "blind" mathematical treatment, since they may reveal unsuspected sources of error not otherwise taken into account in the least squares treatment.

One possibility for separating the primary and secondary extinction effects reveals itself. If we take in turn the limiting cases of $b=0$ (no primary extinction) and of $c=0$ (no secondary extinction), we have in the first case

$$-\ln\frac{R}{R_0}=a+cL.p.F_c^2, \quad (23)$$

and in the second case

$$-\ln\frac{R}{R_0}=a+bF_c^2. \quad (24)$$

If $-\ln(R/R_0)$ is plotted graphically against $L.p.F_c^2$ or against F_c^2, a straight line should result in the appropriate case: i.e., if $b=0$ or $c=0$ is fulfilled. If both graphs are prepared and compared, then that graph which looks "better" would suggest whether the secondary or the primary extinction is predominant. If both types are present, then both graphs or the better of the two graphs may at least yield the value of the constant a, which may also contain the absolute scale correlation.

Once a is known, we can go a step further and write:

$$\frac{-\ln\dfrac{R}{R_0}-a}{F_c^2}=b+cL.p. \quad (25)$$

This relation suggests plotting the left side of the equation against the values of $L.p$. A straight line should result, with the intercept b and slope c. These values should give us the proportions of primary and secondary extinction present in the crystal.

This method, however, is practicable only at the later stages of crystal structure refinement when comparatively accurate values of both F_0 and F_c are already available. The points on the graph should be given their appropriate weights proportional to F; otherwise the graph becomes obscured by dispersed points of small accuracy originating from weak reflections.

The method has been successfully applied to a number of organic and inorganic structures.

IV. ACKNOWLEDGMENTS

The author is greatly indebted to Professor Ray Pepinsky for advice, encouragement, and correction of the manuscript, and also to Dr. Yoshiharu Okaya for valuable discussions. He is also grateful to the Office of Naval Research and the National Institute of Health, for support of the programs under which this study was undertaken.

JOURNAL OF APPLIED PHYSICS VOLUME 26, NUMBER 10 OCTOBER, 1955

On Zone Refining

JOSEPH L. BIRMAN
Sylvania Electric Products Inc., Bayside, New York
(Received March 12, 1955)

A matrix method is used to solve the difference equations which describe the zone refining of a bar. The matrix method is designed for direct numerical calculation of the solute distribution, after any number of passes, with any initial solute distribution. The method is illustrated with a simple example.

IN this note we will present a matrix method for determining the concentration of solute along a bar which has been subjected to any number of zone passes. The matrix method of solution differs in a number of respects from the other methods previously discussed.[1] The boundary conditions which are often troublesome (particularly at the end where "normal freezing" occurs) are contained within the basic matrix; also, we do not need to assume a uniform initial solute distribution.

Consider the bar divided into N equal segments, designated as $S(n)$, $n=1,\cdots N$. At the start of a pass, $S(1)$ to $S(M)$ $(M<N)$ inclusive are melted and mixed completely, then $S(1)$ freezes in equilibrium with $S(2)\cdots S(M)$. The zone then advances by melting $S(M+1)$ and complete mixing of $S(2)\cdots S(M+1)$, then $S(2)$ freezes, and the process continues. Finally when $S(N-M+2)\cdots S(N)$ remain liquid, normal freezing occurs by progressive freezing of segments to the end, with each solid segment freezing in equilibrium with the remaining liquid.

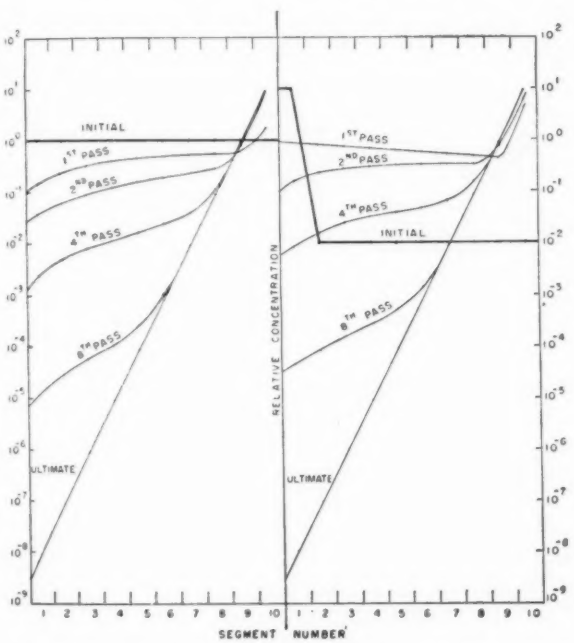

FIG. 1. Zone refining of a bar with uniform and nonuniform initial solute concentrations. The bar is divided into 10 segments, zone width is 2 segments, $k=0.1$. Note the "leveling" which occurs after the first pass, if the initial concentration is nonuniform (right side of the figure).

Let $S_p(n)$ be the concentration of solute in the nth segment after the pth pass. The initial concentrations, which may be arbitrary, are assumed known, and designated $S_0(n)$. The problem is to find the $S_p(n)$ in terms of the $S_0(n)$ and the distribution coefficient k (ratio of the concentration of solute in the frozen segment to that in the liquid in equilibrium with it). For $p\geq 1$ the following difference equations hold (see Appendix A)

$$\left[1+\frac{M-1}{k}\right]S_p(1)=\sum_{n=1}^{M}S_{p-1}(n), \tag{1}$$

$$-\frac{(M-1)}{k}S_p(n-1)+\left[1+\frac{M-1}{k}\right]S_p(n)$$
$$=S_{p-1}(n+M-1), \quad n=2\cdots(N-M+1), \tag{2}$$

$$-\left[\frac{M-(1+m)}{k}\right]S_p(N-M+(1+m))$$
$$+\left[1+\frac{M-(2+m)}{k}\right]S_p(N-M+(2+m))=0,$$
$$m=0,\cdots(M-2). \tag{3}$$

For any p

$$\sum_n S_p(n)=\sum_n S_0(n)=\text{constant}. \tag{4}$$

Equations (1) to (3) can be written in matrix form[2]

$$\mathcal{K}\mathcal{S}_p=\mathcal{L}\mathcal{S}_{p-1} \tag{5}$$

where $\mathcal{K}$ and $\mathcal{L}$ are known $N\times N$ matrices of the coefficients, and $\mathcal{S}_p$ and $\mathcal{S}_{p-1}$ are $N\times 1$ column matrices formed from the $S_p(n)$ and $S_{p-1}(n)$, respectively. Now $\mathcal{K}$ is not singular, and it is simple to find $\mathcal{K}^{-1}$ by inspection (see Appendix B) so

$$\mathcal{S}_p=(\mathcal{K}^{-1}\mathcal{L})\mathcal{S}_{p-1}$$

and

$$\mathcal{S}_p=(\mathcal{K}^{-1}\mathcal{L})^p\mathcal{S}_0. \tag{6}$$

[1] W. G. Pfann, Trans. Am. Inst. Mining Met. Engrs. **194**, 747 (1952); N. W. Lord, Am. Inst. Mining Met. Engrs. **195**, 1531 (1953); Burris, Stockmann, and Dillon, "Contribution to the mathematics of zone melting," Argonne National Laboratory Report 5294, July, 1954; H. Reiss, J. Metals **6**, 1053 (1954).

[2] For a review of the necessary matrix algebra see H. Margenau and G. M. Murphy, *The Mathematics of Physics and Chemistry* (D. Van Nostrand Company, Inc., New York, 1943), Chap. 10.

From (6) we can determine $S_p(n)$ from the initial concentrations $S_0(n)$, the distribution coefficient k, the width of the zone M, and the number of the pass p, by taking powers of the basic matrix $\mathcal{K}^{-1}\mathcal{L}$.

As a simple illustration of the use of this method we can explicitly work out the case with $N=10$, $M=2$, $k=0.1$. For this case we have for the elements of $\mathcal{K}^{-1}\mathcal{L}$,

$$\begin{aligned}(\mathcal{K}^{-1}\mathcal{L})_{\lambda\mu} &= k(1+k)^{\mu-\lambda-2}, \qquad 1\leqslant\lambda\leqslant 9;\ 2\leqslant\mu\leqslant\lambda+1\\ &= 0, \quad \mu>\lambda+1\\ (\mathcal{K}^{-1}\mathcal{L})_{\lambda 1} &= (\mathcal{K}^{-1}\mathcal{L})_{\lambda 2},\\ (\mathcal{K}^{-1}\mathcal{L})_{10\mu} &= (1/k)(\mathcal{K}^{-1}\mathcal{L})_{9\mu}. \end{aligned} \tag{7}$$

The results are shown in Fig. 1 for uniform and non-uniform initial solute distributions. The ultimate concentrations $S_\infty(n)$ are obtained from the conditions $S_p(n)=S_{p-1}(n)$ for $p\to\infty$, and (4).

Although another choice of N and M would yield more quantitatively accurate results, the case chosen for calculation illustrates the matrix method, and the results of zone refining, without extensive, although straightforward, calculations which would be required for a more accurate answer. The main advantage of using the matrix method is that for given conditions (N and M) the matrix $\mathcal{K}^{-1}\mathcal{L}$ needs to be evaluated only once for each k since it does not depend on the initial distribution.

ACKNOWLEDGMENTS

The writer wishes to thank Dr. D. Wahl who suggested a number of improvements in the original manuscript. He also wishes to thank Mrs. Joan Birman, Dr. E. M. Loebl, Dr. S. Mayburg, and Dr. H. Vasileff for a number of discussions.

APPENDIX A: DISCUSSION OF EQS. (1) TO (3)

These equations follow from the conservation of solute, and the definition of k. If a weight of solute A_s contained in a volume V_s of solid solvent freezes in equilibrium with a weight of solute A_l in a volume V_l of liquid solvent then

$$k\equiv(A_s/V_s)/(A_l/V_l). \tag{A.1}$$

It will not affect the generality of the results to assume now that each segment is of unit cross section and length, that $V_s=1$, and that V_l is given as the number of liquid segments.

At the start of the pth pass, the total weight of solute melted is $\sum_{n=1}^{M}S_{p-1}(n)$. The weight of solute in the first segment which freezes is $S_p(1)$, and in the remaining $(M-1)$ liquid segments is $(M-1)S_p(1)/k$. Equating, we get (1). When $S(M+1)$ melts, it adds a weight of solute $S_{p-1}(M+1)$ to $(M-1)S_p(1)/k$. The weight of solute in the solid which next freezes is $S_p(2)$, and in the remaining liquid is $(M-1)S_p(2)/k$. Equating, we get (2) which holds until $S(N)$ is melted (i.e., the zone reaches the end of the bar). When $S(N-M+2)$ freezes it does so in equilibrium with the remaining $(M-2)$ segments, and so on until $S(N-1)$ freezes in equilibrium with $S(N)$. This is normal freezing, described by (3).

A little care is required to pass from the difference equations (1) to (3) for $S_p(n)$ to the more common differential equations for $S_p(x)$, where x is a continuous variable measured from the end of the bar where refining starts. The basic definition is still (A.1), only now let $V_s=\epsilon$, $V_l=l-\epsilon$, where l is the zone width, and ϵ will go to zero. The length of the bar is L.

Instead of (1) we write

$$\left[\epsilon+\frac{l-\epsilon}{k}\right]S_p(\epsilon)=\int_\epsilon^l S_{p-1}(x)dx. \tag{A.2}$$

Instead of (2) we write

$$\left[\frac{l-\epsilon}{k}\right]\frac{S_p(x)-S_p(x-\epsilon)}{\epsilon}+S_p(x)=S_{p-1}(x+l-\epsilon)$$

$$0<x\leqslant L-l. \tag{A.3}$$

Instead of (3) we write

$$\left[\frac{L-x}{k}\right]\frac{S_p(x)-S_p(x-\epsilon)}{\epsilon}=S_p(x)\left[\frac{1-k}{k}\right]$$

$$L-l\leqslant x<L. \tag{A.4}$$

When $\epsilon\to 0$ these become the familiar differential equations. See, for example, Eqs. (12), (10), (15), (16) in Reiss.[1]

APPENDIX B: DISCUSSION OF $\mathcal{K}$, $\mathcal{K}^{-1}$, $\mathcal{L}$

From Eqs. (1) to (3) we see that the only nonzero elements $(\mathcal{K})_{\lambda\mu}$ are for $\mu=\lambda-1$ and $\mu=\lambda$, so that for the determinant of $\mathcal{K}$ we have

$$|\mathcal{K}|=\prod_{\alpha=1}^{N}(\mathcal{K})_{\alpha\alpha}.$$

Now[2] $(\mathcal{K}^{-1})_{\lambda\mu}=(\mathcal{K})^{\mu\lambda}/|\mathcal{K}|$ where $(\mathcal{K})^{\mu\lambda}$ is the cofactor of the element $(\mathcal{K})_{\mu\lambda}$. When $\mu>\lambda$, $(\mathcal{K})^{\mu\lambda}=0$. When $\mu<\lambda$

$$(\mathcal{K})^{\mu\lambda}=\prod_{\alpha=1}^{\mu-1}\prod_{\beta=\mu+1}^{\lambda}\prod_{\gamma=\lambda+1}^{N}(\mathcal{K})_{\alpha\alpha}(\mathcal{K})_{\beta,\beta-1}(\mathcal{K})_{\gamma\gamma}(-1)^{\lambda+\mu}.$$

When $\mu=\lambda$

$$(\mathcal{K})^{\lambda\lambda}=\prod_{\alpha=1}^{\lambda-1}\prod_{\beta=\lambda+1}^{N}(\mathcal{K})_{\alpha\alpha}(\mathcal{K})_{\beta\beta}.$$

So

$$(\mathcal{K}^{-1})_{\lambda\mu}=0 \quad \mu>\lambda,$$

$$(\mathcal{K}^{-1})_{\lambda\mu}=(-1)^{\lambda+\mu}\prod_{\beta=\mu+1}^{\lambda}(\mathcal{K})_{\beta,\beta-1}\Big/\prod_{\alpha=\mu}^{\lambda}(\mathcal{K})_{\alpha\alpha} \quad \mu<\lambda$$

and

$$(\mathcal{K}^{-1})_{\lambda\lambda}=1/(\mathcal{K})_{\lambda\lambda}. \tag{B.1}$$

Since the elements of $\mathcal{L}$ are

$$(\mathcal{L})_{1\mu}=\begin{cases}1 & \mu=1,\cdots,M\\ 0 & \mu>M\end{cases}$$

$$(\mathcal{L})_{\lambda\mu}=\delta_{\lambda,\lambda+M-1} \qquad \lambda=2,\cdots N-M,$$

$$(\mathcal{L})_{\lambda\mu}=0, \quad \lambda>N-M \text{ for all } \mu,$$

it is a straightforward matter of matrix multiplication to obtain $\mathcal{K}^{-1}\mathcal{L}$.

For the illustrative example $(\mathcal{K})_{\mu\mu}=(1+k)/k$, $\mu=1,\cdots 9$; $(\mathcal{K})_{10,10}=1$; $(\mathcal{K})_{\lambda,\lambda-1}=-(1/k)$, $\lambda=1,\cdots 10$, and with a little algebra (7) follows.

JOURNAL OF APPLIED PHYSICS VOLUME 26, NUMBER 10 OCTOBER, 1955

Streaming Birefringence as a Hydrodynamic Research Tool—Applied to a Rotating Cylinder Apparatus above the Transition Velocity*

HAROLD WAYLAND
Division of Engineering, California Institute of Technology, Pasadena, California

(Received March 7, 1955)

Streaming birefringence was studied in the annular space between a fixed outer and a rotating inner cylinder at velocities on both sides of transition to Taylor vortex flow. With a well-collimated light beam, quantitative measurements were possible as close as 0.1 mm from a wall. For an aqueous colloidal solution of bentonite, shear stress could be evaluated from birefringence measurements only when, for a given birefringence, the angle of extinction was the same in the unknown flow as in a known laminar flow. In turbulent shear flow this is not generally the case. For a pure liquid, ethyl cinnamate, the angle of extinction remained at 45° to the streamlines, within experimental error, under all flow conditions obtainable; thus even in turbulent shear flow the birefringence appears to arise primarily from the principal stresses. Assuming birefringence proportional to mean shear stress permits construction of a velocity profile across the gap, yielding the correct value of velocity of the moving wall within limits of experimental error. Thus in this type of two-dimensional shear flow the mean shear stress can be measured by means of the streaming birefringence of a pure liquid.

I. INTRODUCTION

SINCE the pioneering work of Sadron and Alcock[1] numerous attempts have been made to study hydrodynamic phenomena by making use of the fact that certain liquids and solutions become doubly refracting when subjected to shear flow. The method has been effectively applied to design problems[2] in which a qualitative knowledge of the flow is all that is necessary, and it has been effectively applied to the study of the onset of turbulence in pipe flow by Binnie, Binnie and Fowler, and Lindgren.[3] To date the possibility of a quantitative determination of a complex flow field by means of streaming birefringence (SBR)† measurements has not been established. Rosenberg[4] has pointed out a fundamental difficulty in the use of the SBR of colloidal solutions for fluid flow measurements due to lack of an adequate theory of orientation when the flow field has velocity gradients along the streamline. Rosenberg in his Model Basin Report gives a fairly extensive bibliography of the subject. An even more extensive bibliography, with considerable analysis of the contents of the articles, is given by Peebles, Prados, and Honeycutt.[5]

The vast bulk of quantitative work on SBR has been done by physical chemists interested in the properties of macromolecules and colloids. For this work it has

*This work was carried out at the Centre de Recherche sur les Macromolecules (C.R.M.), Strasbourg, France, with the assistance of a grant from the John Simon Guggenheim Memorial Foundation.

[1] C. Sadron, Compt. rend. acad. sci. **197**, 1293 (1933); Alcock and C. Sadron, Physics **6**, 92 (1935).

[2] W. Leaf, Mech. Eng. **67**, 586 (1945).

[3] A. M. Binnie, Proc. Phys. Soc. (London) **57**, 390 (1945); A. M. Binnie and J. S. Fowler, Proc. Roy. Soc. (London) **A192**, 32 (1947); E. Rune Lindgren, Arkiv Fysik **7**, 293 (1953); E. Rune Lindgren, Appl. Sci. Research **A4**, 313 (1953).

† SBR = streaming birefringence = double refraction associated with shear flow.

[4] B. Rosenberg, U. S. Navy Department, David Taylor Model Basin, Report No. 617, (1951); B. Rosenberg, Proc. First U. S. Natl. Congr. Appl. Mech. (June, 1951), (Edwards Brothers, Inc., Ann Arbor, Michigan 1952), p. 807.

[5] Peebles, Prados, and Honeycutt, Jr., "A study of laminar flow phenomenon utilizing a doubly refracting liquid," Progress Report 1, Engr. Expt. Sta. and Dept. of Chem. Engr., University of Tennessee, Knoxville, Tennessee (July, 1954).

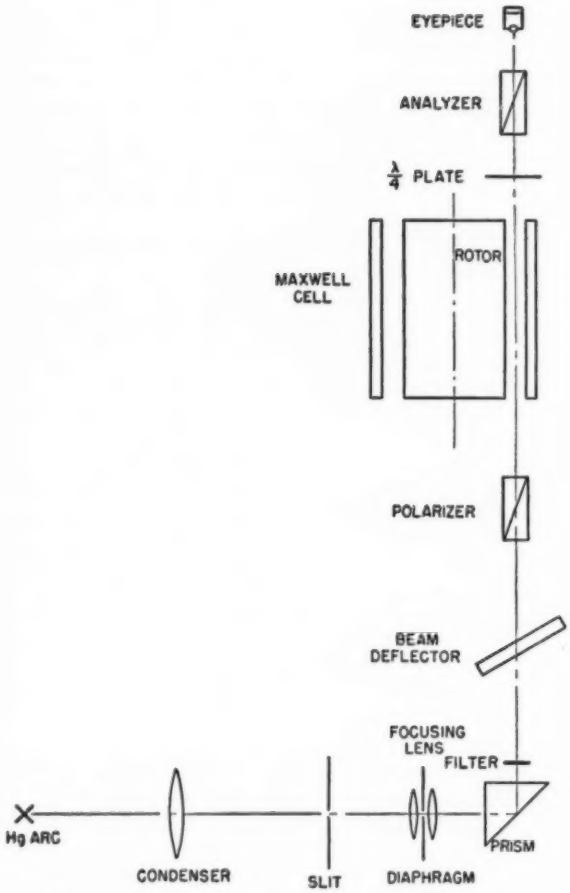

FIG. 1. Schematic drawing of optical arrangement.

been common practice to study streaming birefringence in the annular gap between concentric circular cylinders, one of which is held stationary and the other rotated. In 1923 G. I. Taylor[6] showed both theoretically and experimentally that, for rotating inner cylinder, there was a critical angular velocity for a given apparatus and a given fluid above which the fluid motion was no longer a simple two-dimensional laminar shear flow, but became three-dimensional. The new type of flow was characterized by a stable vortex pattern with vortices whose axes were tangential to the cylinder and perpendicular to its axis. The diameters of the first group of stable vortices were approximately equal to the width of the annular gap. For higher velocities other stable vortex configurations were observed, but for velocities sufficiently high, the vortex motion degenerates into true turbulent motion.

In his 1923 paper Taylor indicated that if the inner cylinder were fixed and the outer cylinder were rotated there would be no stable vortex motion of the type demonstrated for inner cylinder rotating. This has frequently been misinterpreted as meaning that turbulence would not arise for any velocity with the internal cylinder fixed and the external cylinder rotating. Taylor himself showed experimentally[7] that turbulence does arise above a certain velocity for external cylinder rotating.

For streaming birefringence work, an adequate theory exists only for two-dimensional laminar flow in which the velocity gradient is constant perpendicular to the streamlines and is zero along the streamlines. Signer and Gross[8] were the first to point out the necessity of keeping the velocity of the rotor of a rotating cylinder apparatus below Taylor's critical value for SBR measurements. Some of the effects of nonlaminar flow on birefringence were observed as early as 1881 by Kundt,[9] although he was unable to interpret the results. Sadron,[10] Signer and Gross,[8] and Cerf[11] have all made birefringence measurements above the critical velocity with results which appear to be contradictory, since Signer and Gross found a decrease in birefringence above transition, Cerf found an increase, and Sadron could get either. Jerrard[12] has made a critical review of the literature on streaming birefringence in systems in which the flow was nonlaminar, and has qualitatively pointed out the effects to be expected. Some experimental results for colloidal solutions in nonlaminar flow have been reported elsewhere by the author of this paper.[13] It is the purpose of the present paper to describe in greater detail quantitative experiments made with a collodial solution and to report on measurements in a pure liquid in the nonlaminar regime in a rotating cylinder apparatus with inner cylinder rotating. These results confirm Jerrard's qualitative predictions as well as clarifying some of the problems of using SBR as a quantitative hydrodynamic research tool.

II. EXPERIMENTAL ARRANGEMENT

A conventional Maxwell cell with internal cylinder rotating was used. The fixed cylinder had an internal diameter of 5.00 cm, and the system had an optical path of 7.00 cm in the liquid. Rotating cylinders of different diameters were available, permitting a choice of widths of annular gap of 0.50 mm, 1.00 mm, and 2.00 mm. All metallic surfaces in contact with the fluid being studied were of stainless steel. It was desired to "section" the flow optically so that the birefringence and angle of extinction could be measured as a function of position across the gap.

A sketch of the optical setup is shown in Fig. 1. A condensing lens focused a high pressure mercury arc on an adjustable slit. This was usually set at about 0.040 mm in width, and its image was focused by means of a camera lens to give an image somewhere near the middle of the Maxwell cell. The diaphragm on the lens

[6] G. I. Taylor, Trans. Roy. Soc. (London) **A223**, 289 (1923).

[7] G. I. Taylor, Proc. Roy. Soc. (London) **A157**, 565 (1936).
[8] R. Signer and H. Gross, Z. Physik. Chem. **165A**, 161 (1933).
[9] A. Kundt, Wied. Ann. **13**, 110 (1881).
[10] C. Sadron, J. phys. radium **7**, 263 (1936); Schweiz. Z. Angew Wiss. Tech. **3**, 8 (1937).
[11] R. Cerf, J. chim. phys. **48**, 85 (1951).
[12] H. G. Jerrard, J. Appl. Phys. **21**, 1007 (1950).
[13] H. Wayland, J. phys. radium **16**, 275 (1955).

was stopped down so that the maximum distance between the two first minima of the diffraction pattern was never greater than 0.2 mm anywhere along the 7 cm path within the cell. Although two or three fringes were visible when the polarizer and analyzer were parallel, the fringes disappeared completely when near extinction so their presence did not effectively increase the width of the pencil of light. The system was carefully adjusted so that the beam was accurately parallel to the walls of the cell. Translation of the beam across the gap was effected by a plate of glass with plane parallel sides which could be rotated about an axis perpendicular to the light path. This permitted very precise positioning of the light beam across the gap without loss of the adjustment for parallelism.

Glan-Thompson prisms were used as polarizer and analyzer. The mounting was such that they could be clamped at extinction and rotated together for determining the position of the extinction angle. The full emission of the mercury arc was used for the extinction angle measurements. For birefringence measurements a Wratten green filter was used, placed between the prism and the polarizer. Birefringence measurements were made by setting the polarizer at 45° to the angle of extinction, which gave equal intensities to the components of the light polarized along the two optic axes lying in a plane perpendicular to the cylinder axis. The emerging light was then elliptically polarized by the birefringent medium in the cell. A properly oriented quarter-wave plate converted this into plane-polarized light, and the rotation of the plane of polarization gave a measure of the amount of retardation of the one component relative to the other. For analyzer rotations of greater than 15° the angle was obtained by setting on the position of minimum intensity. For smaller rotations a half shadow compensator, employing a half-wave plate of mica in half the field, was used to locate the direction of polarization by an intensity-comparison method.

III. EXPERIMENTAL RESULTS ON BENTONITE

Measurements were first made with a colloidal solution of white hector bentonite, stablized with $Na_4P_2O_7$. The results are for a solution of approximately 8 mg per 100 cc of solution. Bentonite was chosen as the colloidal solution to be studied primarily because it is the substance most commonly used in studies of fluid flow by means of streaming birefringence. The hector bentonites

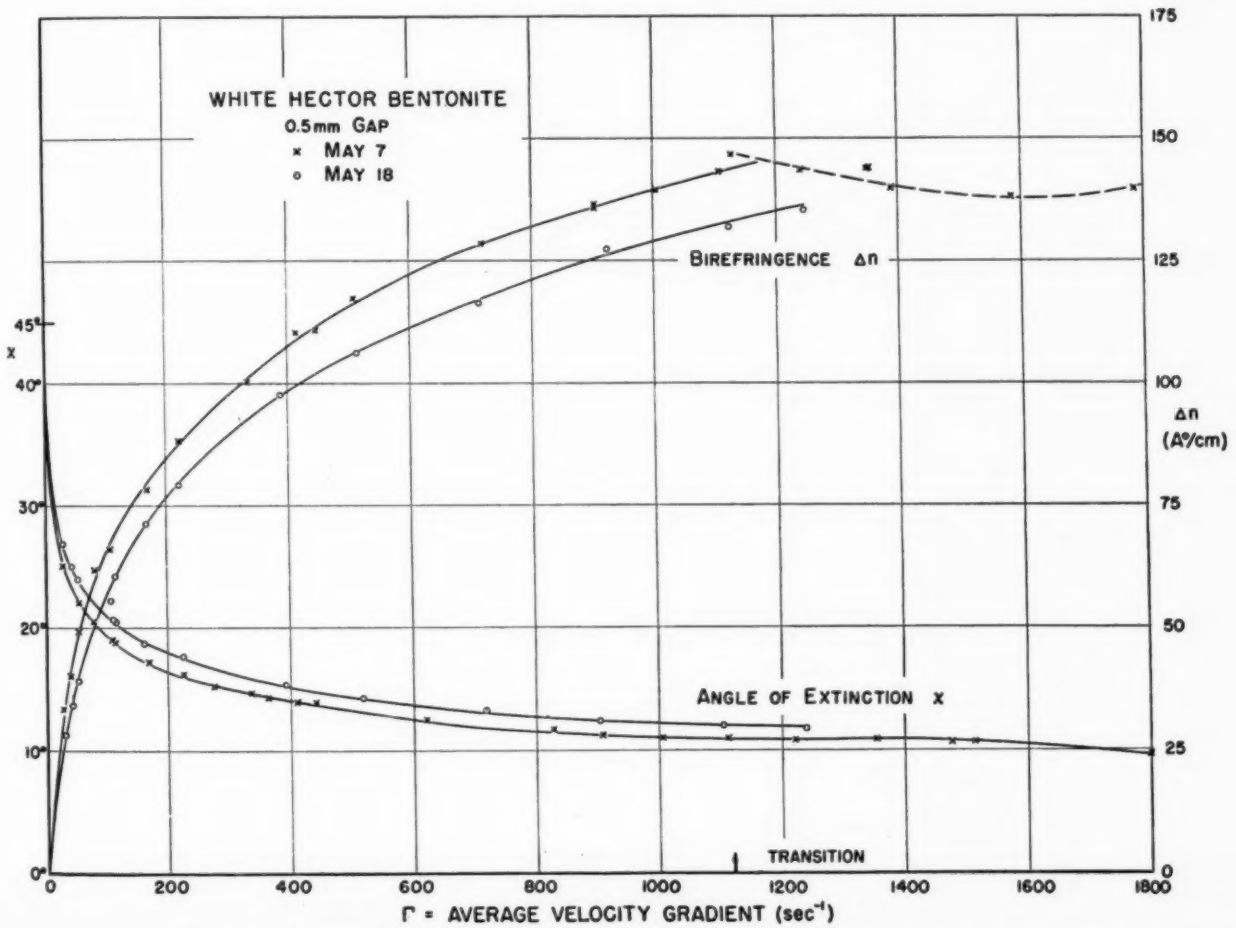

FIG. 2. Birefringence and angle of extinction for a bentonite solution showing effects of aging.

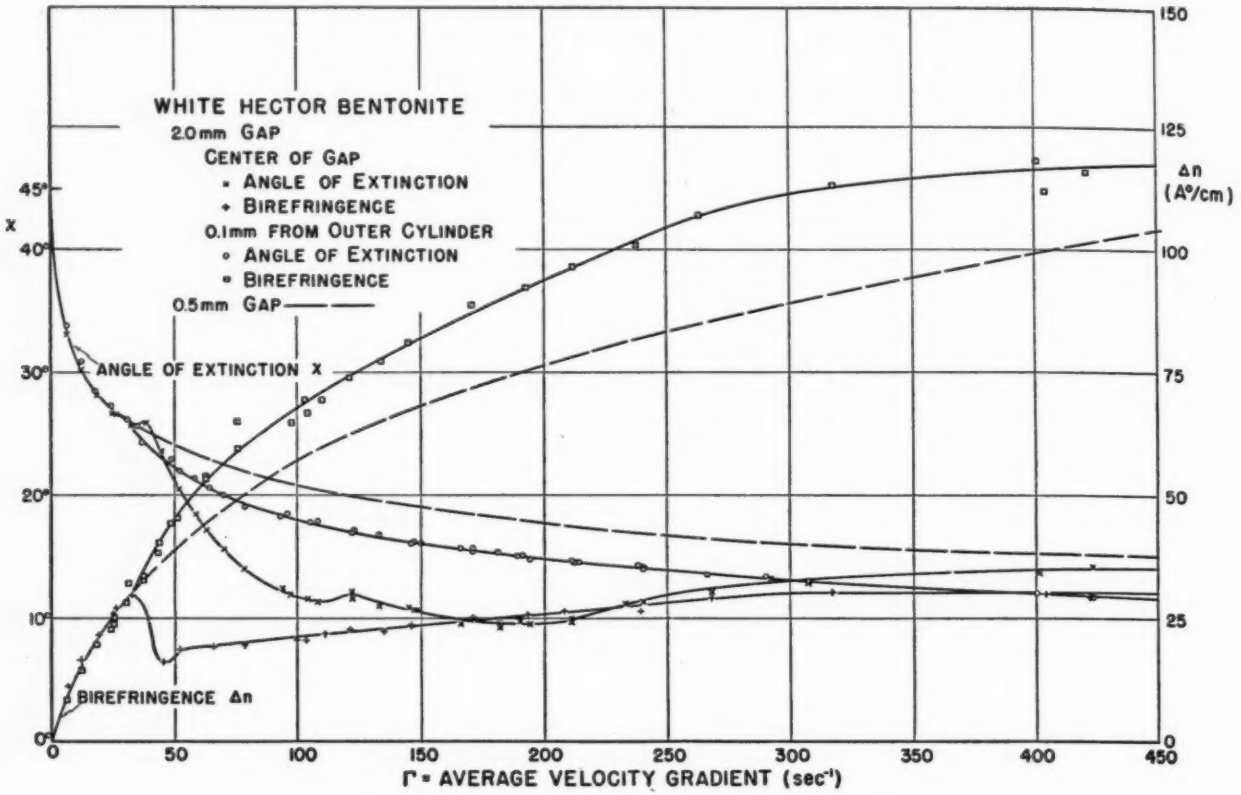

FIG. 3. Effect of turbulence on birefringence of bentonite.

are somewhat more asymmetric than those from other natural sources, and hence show a stronger streaming birefringence.

Figure 2 shows the angle of extinction and the birefringence of this bentonite solution taken with the 0.5 mm gap. The measurements were taken with the beam carefully centered in the gap. Two sets of curves are shown, taken eleven days apart, showing the aging effect in the solution. Later measurements showed that the solution was quite stable and it was possible to complete the next series of measurements without a serious change in the birefringent properties of the systems. These curves show the typical behavior of a colloidal solution both in the fact that the birefringence is not linear with velocity gradient and both the birefringence and angle of extinction appear to be approaching saturation values for high gradients. There is a definite change in the behavior of the birefringence curve above the velocity at which transition to Taylor vortex motion occurs, with a tendency for the birefringence to drop below the expected curve for the laminar flow case. At 17.2°C the solution had a viscosity relative to water of 1.0100 ± 0.0001 and showed no thixotropy down to gradients as low as $\frac{1}{4}$ sec^{-1}.‡ Assuming that the temperature dependence of viscosity is the same as that for water, the transition to Taylor vortex motion would be at $\Gamma=1120$ for the solution at 22.5°C, the temperature at which the measurements plotted in Fig. 2 were taken. The agreement with the break in the curve is within the experimental error.

Figure 3 compares the measurements made in the 0.50-mm gap (dashed curves) with those made at the center and near the fixed wall for a 2.00-mm gap. The abscissa is the velocity gradient at the center of the gap which would obtain if the flow remained laminar. This gives the correct abscissa for the 0.50-mm gap but above transition does not represent the correct velocity gradient for the 2 mm gap but is always proportional to the speed of the rotor. Near the wall the birefringence curve shows a rise, while in the center of the gap it shows a drop with increasing wall velocity. This is consistent with the results of Signer and Gross.[8] The rise in the value of streaming birefringence above transition as observed by Cerf is probably due to the fact that he illuminated the entire gap, and his observations were biased toward the region of highest birefringence—i.e., the effect near the walls. One might qualitatively explain these results by observing that above transition one expects the velocity gradient near the walls to rise more rapidly than linearly with wall velocity and the velocity gradient at the center of the gap to be correspondingly lower. The lack of experimental data on the actual velocity distribution in this regime makes a quantitative comparison impossible but the very large

‡ The author is grateful to Mr. J. Pouyet of the C.R.M. for making these viscosity measurements.

drop in the streaming birefringence value makes it seem improbable that it is due merely to the decrease in mean velocity gradient.

The behavior of the angle of extinction curve tends to confirm this latter point. Near the wall the more rapid descent of the angle of extinction curve toward zero is quite consistent with the more rapid increase of velocity gradient near the wall. The very marked drop in the angle of extinction curve at the center of the gap is, however, inconsistent with a mere decrease in the mean velocity gradient: the presence of the vortices and/or turbulence is having a profound influence on the birefringence pattern.

Figure 4 shows the results of making birefringence measurements across the annulus for the 2 mm gap for three different velocities, all well above the critical. The birefringence curves are very similar through the center of the gap, but near the walls a marked increase in birefringence with velocity is shown. The qualitative

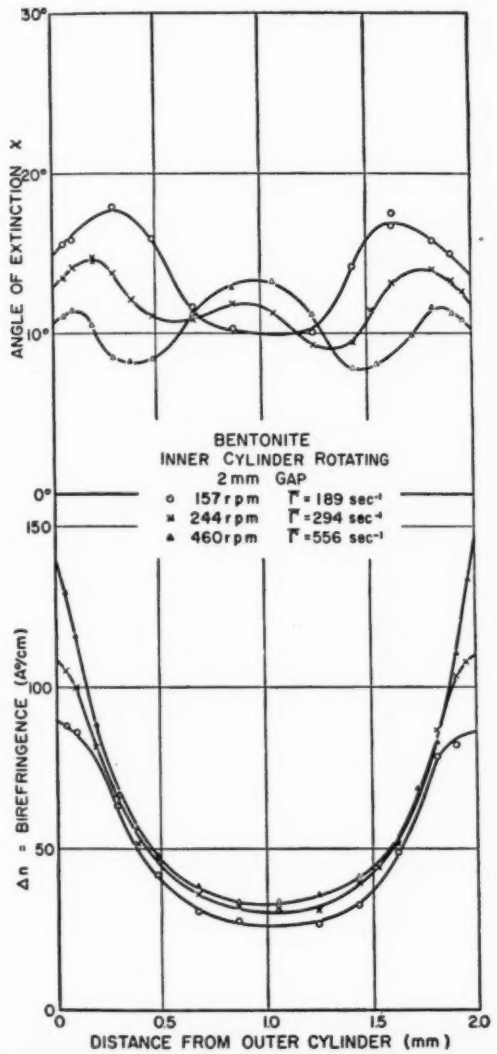

FIG. 4. Birefringence of bentonite as a function of position across the gap for velocities above transition.

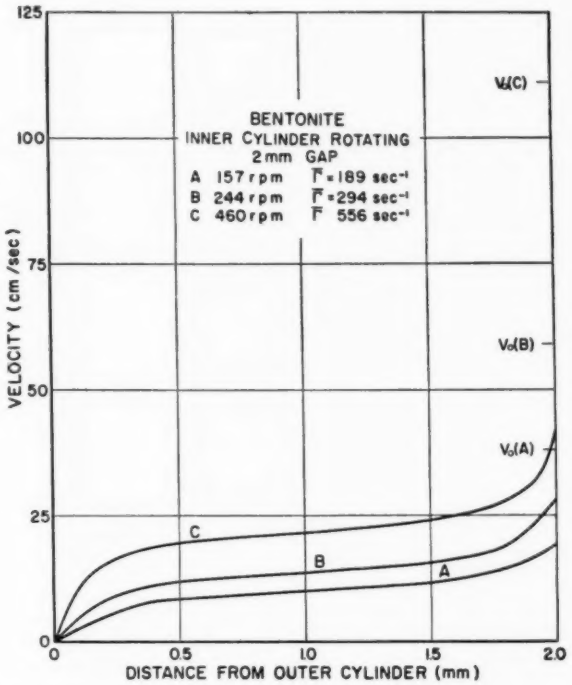

FIG. 5. Velocity profile constructed from birefringence measurements in bentonite for velocities above transition.

behavior can be interpreted from the angle of extinction curves. If we assume that the vortex and/or turbulent motion does not penetrate completely to the wall, then we should expect an increase in extinction angle to be associated with a decrease in birefringence as we go away from the wall. We should also expect this "boundary layer" to become thinner at higher velocities of rotation. This is borne out in Fig. 4. If we consider the curve for $\Gamma = 189$ sec^{-1} we find that, as we go away from the wall, after an initial increase, the angle of extinction drops rapidly as we approach the center of the cell, coupled with a continued monotonic decrease in the birefringence. The drop in birefringence as we approach the center is coupled both with a decrease in mean velocity gradient and the changed character of the flow. In the case of the angle of extinction the effect of the changed character of the flow is over-riding the effect of the reduced mean velocity gradient, as was observed in the discussion of Fig. 3. For the case in which $\Gamma = 556$ sec^{-1} the angle of extinction curve rises only for a short distance from the wall, and then follows through the characteristic pattern of the rapid drop toward zero as the flow character changes, followed by a rise. This would tend to indicate that the rapid drop in the value of χ is associated with the character of the flow rather than the mean velocity gradient, since the velocity gradient should decrease monotonically from the wall to the center of the gap.

The monotonic character of the birefringence curves leads one to investigate the hypothesis that the mean velocity gradient is the determining factor for the bire-

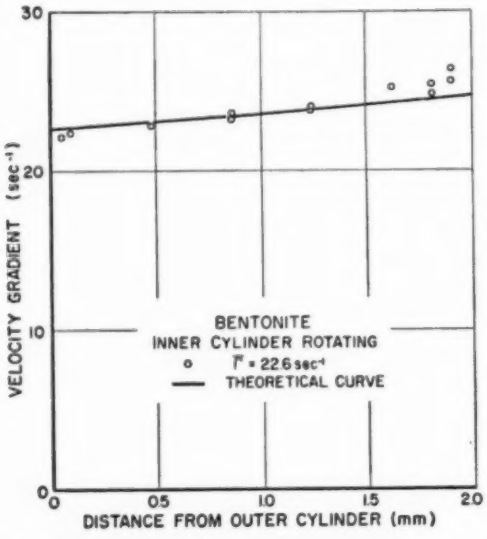

FIG. 6. Velocity gradient profile from birefringence measurements on bentonite solution in the laminar region.

fringence, regardless of the direction of χ. Measurements for the velocity distribution in such rotating cylinder systems exist only for cases so different from those at hand that extrapolation is impossible. If, however, the velocity gradient is known across the gap, the velocity difference between the fixed and moving walls can be calculated by means of a numerical or graphical integration. By assuming that the measured birefringence corresponds to the velocity gradient yielding that same birefringence in laminar flow, the curves of Fig. 5 were obtained. The wide discrepancy with the measured wall velocities indicates the nonvalidity of the assumptions.

In the laminar region the agreement between measured value of velocity gradient using streaming birefringence and the theoretical value is shown in Fig. 6. The only significant check comes from a comparison of the slopes of the curves, as the absolute value is adjusted from experimental calibration. The agreement is well within experimental error except very close to the rotor. It is impossible to distinguish between errors caused by reflections from the rotor and errors caused by strain in the glass windows.

In the present state of theoretical knowledge concerning the streaming birefringence of colloidal solutions it is not possible to make a quantitative determination of an arbitrary fluid flow pattern by birefringence measurements. It is believed, however, that the following working hypothesis can be enunciated: In a colloidal solution one can determine the mean local velocity gradient by birefringence measurements for those cases in which, for a given birefringence value, the position of the angle of extinction is the same in the unknown flow as in a known laminar flow.

IV. EXPERIMENTAL RESULTS ON A PURE LIQUID

For those pure liquids showing streaming birefringence, the direction of the angle of extinction remains at 45° to the streamlines in all flow situations yet studied in a rotating cylinder apparatus. This would

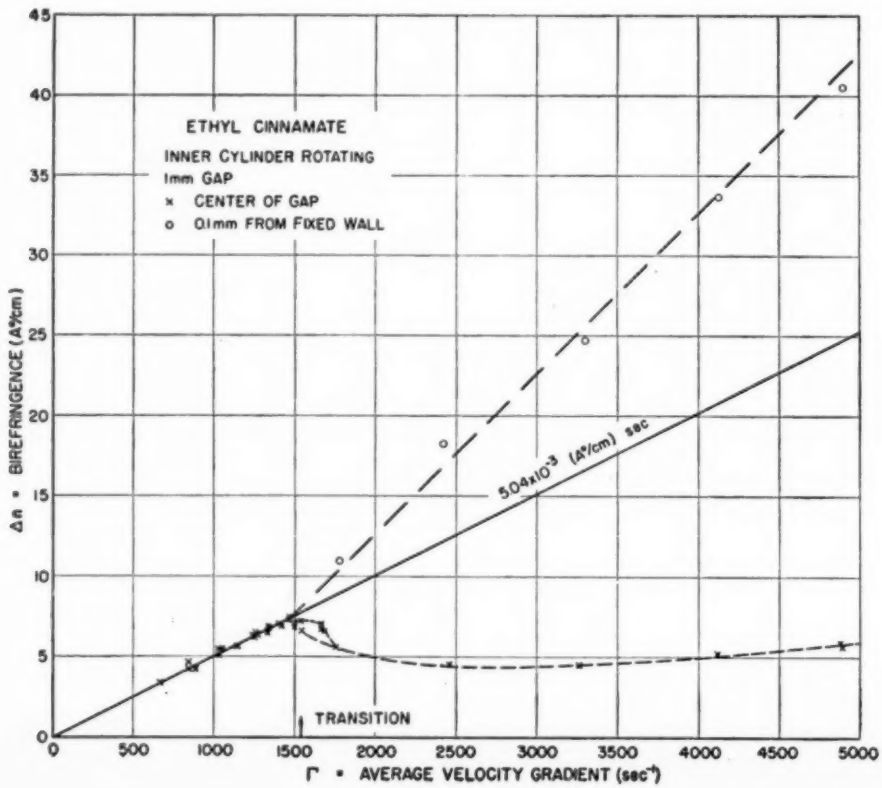

FIG. 7. Birefringence of ethyl cinnamate as a function of velocity gradient in different parts of the gap.

indicate that the birefringence effects arise primarily from the principal stresses rather than being influenced by the velocity differences along the length of the molecule. Even if one accepts the hypothesis of Peterlin and Stuart[14] that the effects are qualitatively the same in colloidal solutions and pure liquids, the small size of the molecules for the pure liquids would account for the negligible effects of velocity gradients.

Measurements similar to those made in bentonite were made in ethyl cinnamate. Because of the feeble birefringence the sectioning was done in a 1.00 mm gap. For all velocities obtainable (up to average velocity gradient of 5000 sec^{-1}) the position of the angle of extinction was found to be $45°\pm2°$ in all parts of the gap. No systematic variation could be found, and the fluctuations were within the experimental error. χ was then assumed to be precisely 45° and measurements of birefringence were made.

The birefringence values at the center and 0.1 mm from the fixed wall for a 1.00 mm gap are plotted in Fig. 7. From the measured viscosity of the ethyl cinnamate at the ambient temperature at the time the measurements were made, transition should occur at 1540 sec^{-1}. This is slightly higher than the point at which the curves change character, but the temperature of the liquid would be higher than the ambient due to the mechanical work being done on it, and an increased temperature would decrease the viscosity and drop the transition point, so the break measures the onset of the Taylor vortex motion. Up to this break the birefringence is linearly proportional to the velocity gradient, and the constant of proportionality agrees within experimental error with that measured for the same sample in a different apparatus[15] to considerably higher velocity gradients, which assures the validity of the linear extrapolation of the curve for laminar flow. Measurements made at the center of the 1.00 mm gap and 0.1 mm from the wall are qualitatively similar to the results found in bentonite solutions. The linear rise of birefringence near the wall with rotor velocity is almost certainly fortuitous. The scatter of points taken at the center of the gap just above $\Gamma=1500$ cm^{-1} is probably due to the existence of different modes of Taylor vortex flow which were instigated under slightly different starting conditions, apparatus vibration and velocity of rotor.

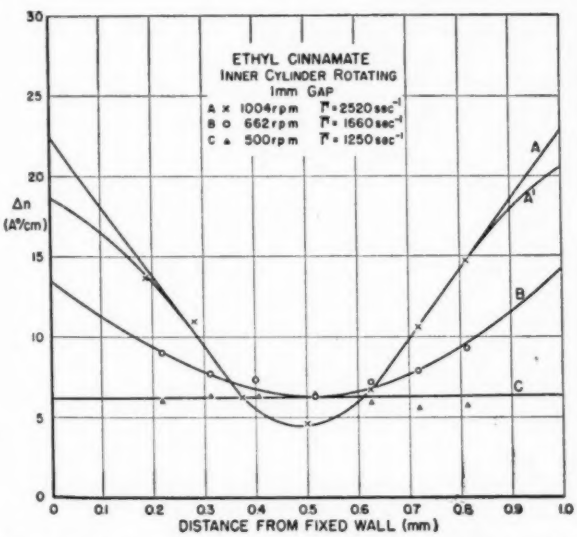

FIG. 8. Birefringence of ethyl cinnamate as a function of position across the gap for laminar and turbulent flow.

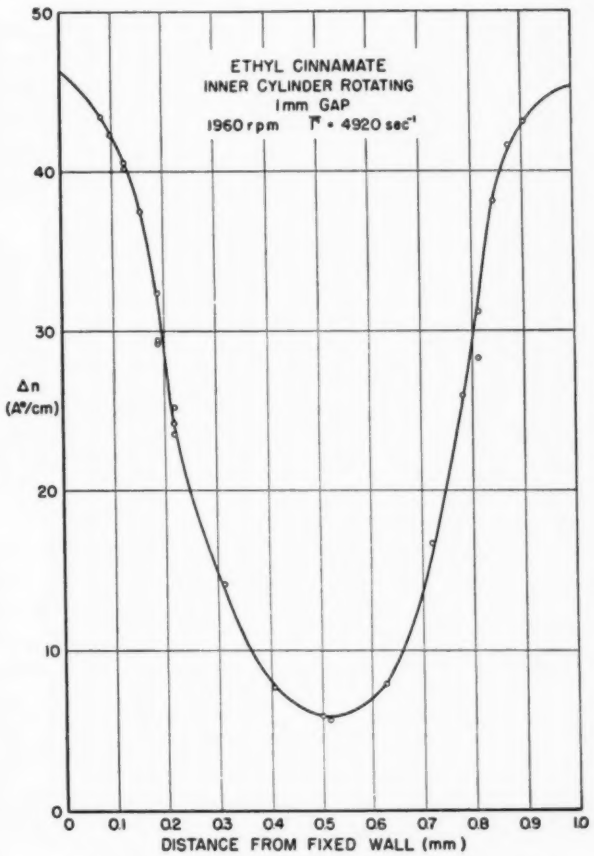

FIG. 9. Birefringence of ethyl cinnamate as a function of position across gap for $\Gamma=4920$ sec^{-1}.

The flow was sectioned for various angular velocities ranging from laminar flow (Fig. 8, curve *C*) to various velocities above the critical value (Fig. 8, curves *A*, *B*; Fig. 9). Curve *C* in Fig. 8 compares experimental measurements made in the laminar region with the birefringence values calculated from the theoretical values of the gradient and the birefringence constant obtained from Fig. 7. The discrepancies of the points to the right of the center are outside the limits of error of the individual measurements but are due to birefringence of the windows of the apparatus. The windows show a small residual birefringence which differs from point to point across the gap. For these measurements

[14] A. Peterlin and H. A. Stuart, Hand-u. Jahrb. Chem. Phys. 8, (A) IB.

[15] J. Leray, C.R.M., Strasbourg, France (private communication).

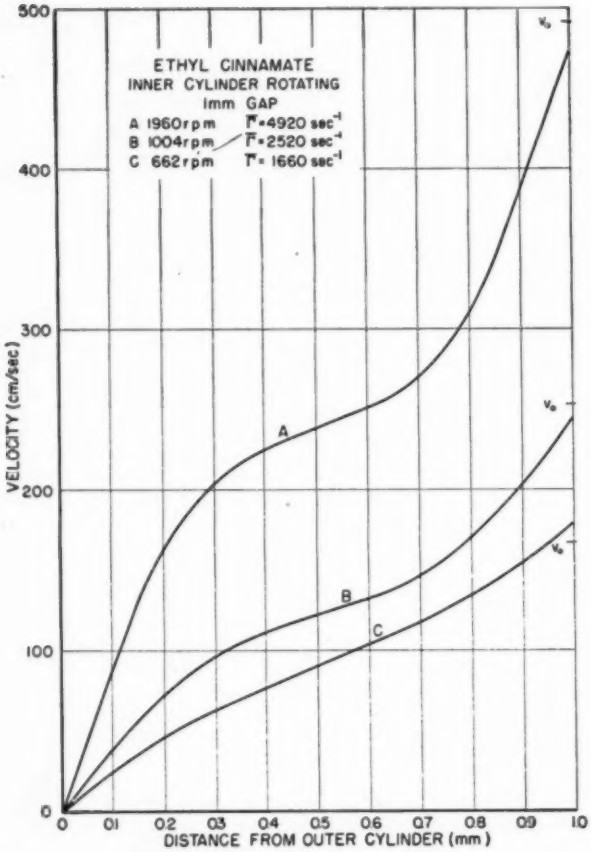

FIG. 10. Velocity profile as interpreted from birefringence measurements in ethyl cinnamate for velocities above transition.

the extreme variation of the background gives 0.28° rotation of the analyzer, while the birefringence of the liquid gives a rotation of 1.46°. It is impossible to correct for this error without knowing how it is divided between the windows, as successive birefringent bodies must be treated as matrix operators and their effects are not commutative. It was not possible to measure the effects of the windows separately as the process of removing and replacing a window always changed the state of strain. Furthermore, the pressures generated in the cell by rotation will also change the state of strain in the windows, mitigating any attempt to make corrections from measurements in the zero velocity condition.

If one assumes that for ethyl cinnamate the birefringence gives a measure of the mean velocity gradient regardless of the type of flow, one can associate a velocity gradient with each point of the curves in Figs. 8 and 9. In fact, the curves will have precisely the same shape as the birefringence curves, thanks to the linearity of birefringence with shear in laminar flow. Numerical integration gives the velocity-position curves shown in Fig. 10, with the measured velocity of the rotor marked for each curve. These results are well within the experimental error. In the case of the results for $\Gamma = 2520\ \text{sec}^{-1}$, two different curves are found in Fig. 8. The values of the wall velocity from these are 244 cm/sec for A and 234 cm/sec for A'. The most significant results are those for $\Gamma = 4920\ \text{sec}^{-1}$. Here the data for three different runs, taken on different days, are plotted on the same graph. For these runs the optical system was aligned with extreme care, and measurements were taken as close to the walls as possible. For closest approach the light beam was actually vignetted by the wall. Because of the extremely narrow beam, and hence the very small divergence of the beam, the angle of incidence of any light falling on the wall was very small. For grazing incidence reflected light will suffer a 180° phase shift, which will merely reduce the intensity of the beam through destructive interference without contributing to the ellipticity of the emergent light, so that the errors of measurement due to wall reflections are small. Unfortunately time did not permit making such measurements for other velocities.

The data of Fig. 10 are replotted with the dimensionless ordinate v/v_0 in Fig. 11, showing the change of velocity distribution with mean shear stress for various velocities above transition compared with the theoretical curve for laminar flow. It is seen that the flow pattern changes gradually with increasing velocity in a manner similar to that observed by Taylor for external cylinder rotating. The extreme behavior indicated by Jerrard in which the double refraction is confined to a region very close to the walls can be expected to obtain only much further from transition than any of the measurements made here, or, for that matter, in any measurements likely to be made with the narrow gaps common in streaming birefringence work.

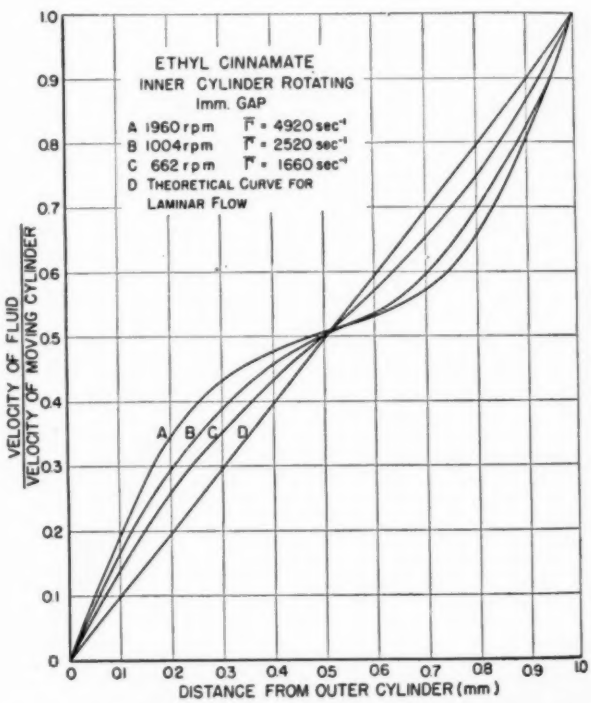
ETHYL CINNAMATE
INNER CYLINDER ROTATING
Imm. GAP
A 1960rpm Γ = 4920 sec⁻¹
B 1004rpm Γ = 2520 sec⁻¹
C 662rpm Γ = 1660 sec⁻¹
D THEORETICAL CURVE FOR LAMINAR FLOW
VELOCITY OF FLUID / VELOCITY OF MOVING CYLINDER
DISTANCE FROM OUTER CYLINDER (mm)

FIG. 11. Variation of velocity distribution with velocity of rotor as deduced from birefringence measurements on ethyl cinnamate.

V. CONCLUSION

1. It is possible to make quantitative measurements of streaming birefringence within 0.1 mm of a wall provided the light beam is sufficiently narrow and sufficiently well collimated.

2. In a colloidal solution one can evaluate quantitatively the mean velocity gradient by streaming birefringence measurements only in the case in which, for a given birefringence, the angle of extinction is the same in the unknown flow as in a known laminar two-dimensional flow. Quantitative interpretation in other cases will require the establishment of a more comprehensive theory for the streaming birefringence of colloidal solutions.

3. In a pure liquid streaming birefringence appears to depend on the mean shear stress even though the flow be turbulent. This has been experimentally verified only for the case in which the velocity gradient is normal to the streamlines. In order to confirm completely the validity of the streaming birefringence of a pure liquid as a tool for quantitative hydrodynamic measurements it will be necessary to establish the validity of this result in converging and diverging flows.

VI. ACKNOWLEDGMENTS

The author wishes to express his thanks to the members of the entire staff of the Centre de Recherche sur les Macromolecules at Strasbourg, France, for their helpful cooperation during the course of this research. In particular, he wishes to thank Professor Charles Sadron, Director of the C.R.M., for many stimulating discussions and Mr. Joseph Leray for the assistance which he gave in the development of the experimental techinques. He also wishes to thank the John Simon Guggenheim Memorial Foundation for the financial aid which made this work possible.

JOURNAL OF APPLIED PHYSICS VOLUME 26, NUMBER 10 OCTOBER, 1955

Study of the Initial Stages of Sintering Solids by Viscous Flow, Evaporation-Condensation, and Self-Diffusion*

W. D. KINGERY AND M. BERG
Ceramics Division, Department of Metallurgy, Massachusetts Institute of Technology, Cambridge, Massachusetts
(Received May 4, 1955)

The mechanism of material transport in sintering can be elucidated in some cases by direct observation of the rate of interface growth and approach of centers between spherical particles. Measurements with glass, sodium chloride, and copper indicate that with these materials viscous flow, evaporation-condensation, and self-diffusion are the rate-determining mechanisms. Values of viscosity, vapor pressure, and diffusion constants have been determined, but calculations of diffusion constants from these data are subject to uncertainties of interpretation. A model is presented for the behavior of copper during the initial stages of sintering, which is in agreement with available experimental data, and which requires vacancy elimination at dislocations or grain boundaries. Data for refractory oxides indicate the importance of purity and fabrication pressure, but the sintering mechanism for these materials is not determined by the present data.

1. INTRODUCTION

THE sintering process whereby solid particles in contact adhere and grow together into a solid body is complex. Changes of bulk density, electrical conductivity, and other compact properties with time are difficult to interpret unambiguously. A method of isolating the initial stage of the process is to employ small spheres or other simple shapes in contact and observe the rate of increase of the contact area. This rate depends on the mechanism of material transport.[1] Similarly, the effect of changing size scale on this rate depends on the mechanism of material transport.[2] Several measurements of this kind have been reported[1,3–8]; none have included sufficient data for a critical analysis of results and a determination of the validity of the method. In this paper, we shall compare the results obtained for glass, sodium chloride, and copper with predicted behavior.

2. CALCULATION OF RATES AND DETERMINATION OF SINTERING MECHANISM FROM MODELS

Various types of material transport including viscous flow, plastic flow, evaporation-condensation, surface diffusion, and volume diffusion may occur during

* With funds from the U. S. Atomic Energy Commission under Contract No. AT(30-1)-1192.

[1] G. C. Kuczynski, Trans. Am. Inst. Mining Met. Engrs. **185**, 169 (1949).

[2] C. Herring, J. Appl. Phys. **21**, 301 (1950).

[3] G. C. Kuczynski, J. Appl. Phys. **21**, 632 (1950).

[4] G. Cohen and G. C. Kuczynski, J. Appl. Phys. **21**, 1339 (1950).

[5] J. H. Dedrick and A. Gerds, J. Appl. Phys. **20**, 1042 (1949).

[6] A. J. Shaler, Trans. Am. Inst. Mining Met. Engrs. **185**, 796 (1949).

[7] G. C. Kuczynski, J. Appl. Phys. **20**, 1160 (1949).

[8] Alexander, Kuczynski, and Dawson, "Relations between Diffusion and Viscous Flow in Metals," p. 202, *The Physics of Powder Metallurgy*, W. E. Kingston, editor (McGraw-Hill Book Company, Inc., New York, 1951).

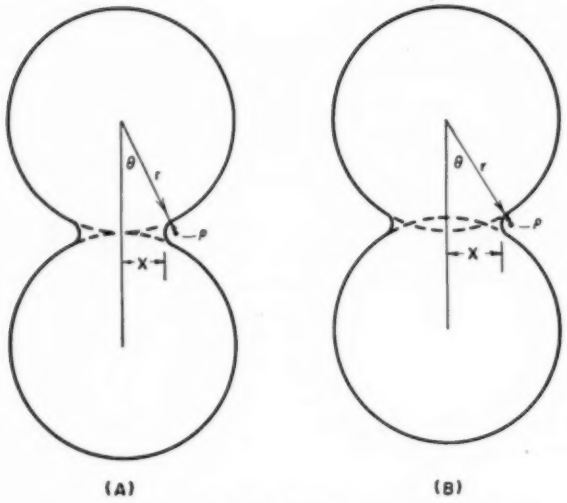

FIG. 1. Two models for initial stages of sintering of small spheres.

sintering. We shall consider only viscous flow, evaporation-condensation, and diffusion processes for the sintering of two spheres in contact, as shown in Fig. 1. Sintering may occur by material filling in between the spheres [Fig. 1(A)] or by the centers of the spheres approaching [Fig. 1(B)]. If, as in Fig. 1(A), the spheres have an initial radius r, assumed unchanged during the sintering process, and the interface grows to a radius x, the radius of curvature of the contact point can be taken as equal to $x^2/2r$ to a good approximation for $x/r<0.3$. The volume of material filling in between the spheres is approximately equal to $\pi x^4/2r$ and its area is π^2x^3/r. In the case corresponding to Fig. 1(B), the radius of curvature is not uniquely defined but is approximately $x^2/4r$. The volume change is $\pi x^4/2r$, and the area is given by $\pi^2x^3/2r$. By equating the rate of material transfer and the volume change, the rate of interface growth can be estimated.

A. Viscous Flow

The case of viscous flow was considered by Frenkel.[9] The growth of the interface with time is given by:

$$\frac{x^2}{r}=\frac{3\gamma t}{2\eta} \tag{1}$$

where γ is the surface energy, η the viscosity, and t the sintering time. By plotting x^2/r *vs* t, a straight line is obtained with the slope $(3\gamma/2\eta)$.

B. Evaporation-Condensation

The vapor pressure over a small negative radius of curvature (P_1) such as in Fig. 1 is decreased due to the surface energy in accordance with the Kelvin equation:

$$RT\ln\frac{P_1}{P_0}=\frac{M\gamma}{d}\left(\frac{1}{\rho}+\frac{1}{x}\right) \tag{2}$$

[9] J. Frenkel, J. Phys. (U.S.S.R.) **9**, (5), 385 (1945).

where P_0 is the equilibrium vapor pressure over a flat surface, M is the molecular weight, and d is the density. Since $x\gg\rho$ and $P_0-P_1=\Delta P$ is small, $\ln P_1/P_0=\Delta P/P_0$, and we can write:

$$\Delta P=\frac{M\gamma P_0}{d\rho RT}. \tag{3}$$

Taking the Langmuir equation as an approximation to the rate of material transfer m,

$$m=\alpha\Delta P\left(\frac{M}{2\pi RT}\right)^{\frac{1}{2}}\text{g/cm}^2\text{/sec}. \tag{4}$$

Then the rate of condensation is equal to the volume increase, and taking the accomodation coefficient α as unity:

$$\left(\frac{m}{d}\right)A=\frac{dV}{dt},$$

and

$$\frac{x^3}{r}=\frac{3\pi M\gamma(M/2\pi RT)^{\frac{1}{2}}P_0t}{d^2RT}. \tag{5}$$

By plotting x^3/r *vs* t, a straight line should be obtained, and the vapor pressure determined by the slope:

$$P_0=\left(\frac{x^3/r}{t}\right)\left[\frac{d^2RT}{3\pi M\gamma(M/2\pi RT)^{\frac{1}{2}}}\right]. \tag{6}$$

C. Diffusion

The calculation of sintering rates due to diffusion is complicated by considerable uncertainties in fixing the actual diffusion path. In any case, since the free energy at the small radius of curvature is less than at a plane surface, there will be a greater concentration of vacancies at ρ and a diffusion flow toward this point.

Cabrera,[10] Schmed,[11] and Kuczynski[1] have considered the case of surface diffusion with somewhat divergent results as to the rate of sintering. For samples of different size scale, it has been shown by Herring[2] that if $r_1=\lambda r^2$, the relative times for configurational changes are given by $\Delta t_1=\lambda^4\Delta t_2$.

Material transport into the neck may also occur by volume diffusion from the flat surface area to the neck area of lower free energy. The excess concentration of vacancies ΔN over the concentration at a plane surface $N(\infty)$ is given by:

$$\frac{\Delta N}{N(\infty)}=\frac{\gamma a^3}{kT}\left(\frac{1}{\rho}+\frac{1}{x}\right)\cong\frac{\gamma a^3}{kT\rho} \tag{7}$$

where a is the atomic radius and k is the Boltzmann constant. If it is assumed (Cabrera) that the vacancies diffuse uniformly with cylindrical symmetry from the

[10] N. Cabrera, Trans. Am. Inst. Mining Met. Engrs. **188**, 667 (1950).

[11] P. Schmed, Trans. Am. Inst. Mining Met. Engrs. **191**, 245 (1951).

radius ρ to a radius of approximately r with a concentration difference ΔN and a vacancy diffusion constant D', the number of vacant sites diffusing from the neck area/sec/cm of length is given by:

$$J=\frac{\pi D'\Delta N}{\ln(r/\rho)} \tag{8}$$

and since, corresponding to Fig. 1(A), $\rho=x^2/2r$, $V=\pi x^4/2r$, $dV/dt=2\pi x a^3 J$, and $D_V=a^3D'N(\infty)$, where D_V is the self-diffusion coefficient:

$$\frac{x^5}{r^2}=\frac{10\pi\gamma a^3 D_V t}{\ln(r/\rho)kT}. \tag{9}$$

For regions of measurement $\ln r/\rho\sim 4$, so that:

$$\frac{x^5}{r^2}\cong\frac{2.5\pi\gamma a^3 D_V t}{kT}. \tag{10}$$

By plotting x^5/r^2 *vs* t, a straight line is obtained with the slope giving D_V as:

$$D_V=\left(\frac{x^5/r^2}{t}\right)\left[\frac{kT}{2.5\pi\gamma a^3}\right]. \tag{11}$$

Kuczynski[1] has essentially taken $r/\rho\cong 2$ in (9), so that his analysis results in:

$$\frac{x^5}{r^2}\cong\frac{10\pi\gamma a^3 D_V t}{kT}. \tag{12}$$

Another analysis of the diffusion path can be made by assuming that the vacancy concentration remains constant at the source in the neck and at the sink taken as the surface of the large spheres. Analytical solution is difficult, but a graphical solution after the method of Wedmore[12] leads to the following result for the number of vacant lattice points diffusing away from the neck area per second per cm of length:

$$J=4D'\Delta N \tag{13}$$

with diffusion paths as shown in Fig. 2(A). This leads to

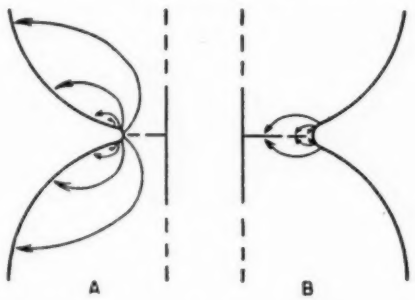

FIG. 2. Diffusion paths from neck to particle surface (A) and grain boundary (B).

[12] E. B. Wedmore, J. Inst. Elec. Engrs. (London) **61**, App. IV (1923); **68**, App. I (1930).

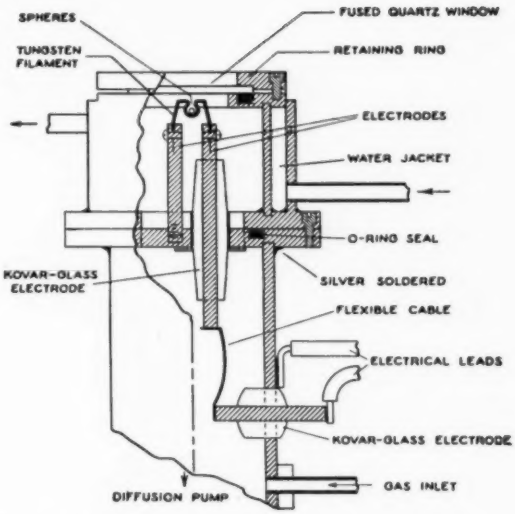

FIG. 3. Cross section of microscope heating unit.

the result:

$$\frac{x^5}{r^2}\cong\frac{40\gamma a^3 D_V t}{kT}. \tag{14}$$

If the model corresponding to Fig. 1(B) is assumed, it is obvious that the surface cannot act as sink for the vacancies diffusing from the neck. Instead it must be assumed that the grain boundary between the particles acts as a sink for vacancies along paths as indicated in Fig. 2(B). It may also be possible that vacancies diffuse away from the neck and are eliminated at dislocations. Assuming the grain boundary acts as a sink, Eq. (13) will very nearly apply. In this case, corresponding to Fig. 1(B), $\rho=x^2/4r$, $V=\pi x^4/2r$, and $dV/dt=2\pi x a^3 J$, and:

$$\frac{x^5}{r^2}\cong\frac{80\gamma a^3 D_V t}{kT} \tag{15}$$

$$D_V=\left[\frac{x^5/r^2}{t}\right]\left[\frac{kT}{80\gamma a^3}\right]. \tag{16}$$

If samples of different size scales are observed, it has been shown by Herring[2] that if $r_1=\lambda r_2$, the relative time for configurational changes by volume diffusion are given by $\Delta t_1=\lambda^3\Delta t_2$.

D. Experimental Determination of Sintering Mechanism

The unambiguous determination of sintering mechanism is complicated by the possible effects of combined mechanisms and in the case of diffusion, by the similarity of the time dependence of surface and volume diffusion. In addition, in cases where creep or plastic flow may be important, the experimental stress-strain relationship may lead to power functions of the sintering rate which cannot be anticipated by any simple analysis.

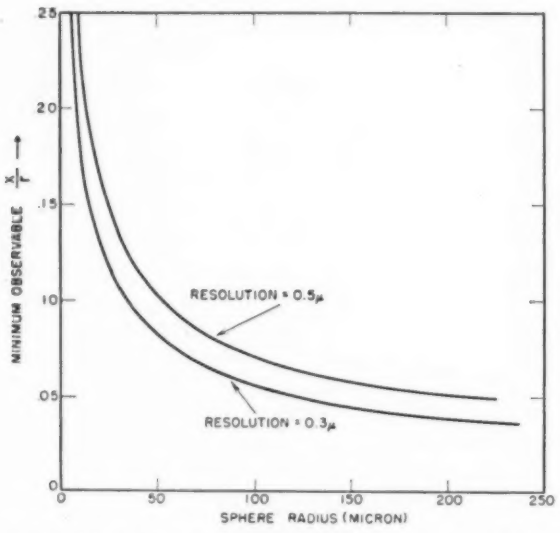

FIG. 4. Effect of resolution and sphere radius on the minimum value of x/r which can be reliably observed.

Only data which are in agreement with the absolute values of calculated rates (i.e., quantitative agreement of viscosity, vapor pressure, and diffusion constant), with the scaling laws of Herring, and showing the correct temperature dependence for the proposed mechanism can be accepted with much confidence.

Another method of separating the mechanisms of surface diffusion or evaporation-condensation from viscous flow, creep, or volume diffusion is by observing the decrease in center-center distance of the spheres in Fig. 1. If evaporation-condensation or surface diffusion occurs, there can be no change in the distance between centers (and correspondingly, no shrinkage in a compact).[6,13,14]

Considering the rate of approach of the spheres, we may calculate the volume filling in the "neck" area, and assume that the particles remain spherical decreasing in volume by an equal amount [corresponding to Fig. 1(A)] for the case of viscous flow or volume diffusion. In this case, $V=\pi x^4/2r$, and for viscous flow, from Eq. (1):

$$V_{\text{neck}}=\frac{9\pi r\gamma^2 t^2}{4\eta} \tag{17}$$

so that the volume decrease in the sphere at each contact will be given by:

$$\frac{dV}{V_0 dt}=\frac{-27\gamma^2 t}{8r^2\eta^2}. \tag{18}$$

If n is the number of contacts per sphere, then for a compact of spheres:

$$\frac{dV}{V_0 dt}=\frac{-27n\gamma^2 t}{8r^2\eta^2} \tag{19}$$

$$\frac{\Delta V}{V_0}=\frac{-27n\gamma^2 t^2}{16r^2\eta^2}. \tag{20}$$

Similarly, for volume diffusion, as in Fig. 1(A), from Eq. (14):

$$V_{\text{neck}}=\frac{\pi r^{3/5}}{2}\left(\frac{40\gamma a^3 D_V}{kT}\right)^{4/5} t^{4/5} \tag{21}$$

so that the volume decrease in a sphere having n contacts is given by:

$$\frac{dV}{V_0 dt}=\frac{-3n}{10}\left[\frac{40\gamma a^3 D_V}{r^3 kT}\right]^{4/5} t^{-1/5} \tag{22}$$

$$\frac{\Delta V}{V_0}=\frac{-3n}{8}\left[\frac{40\gamma a^3 D_V}{r^3 kT}\right]^{4/5} t^{4/5}. \tag{23}$$

These expressions can only be expected to hold to a volume shrinkage of about 2% with reasonable precision, and should fail completely at shrinkage much greater than 6%. For small shrinkages, $3\Delta L/L_0\cong\Delta V/V_0$, so for diffusion, equivalent to Eq. (23):

$$\frac{\Delta L}{L_0}=\frac{-n}{8}\left[\frac{40\gamma a^3 D_V}{r^3 kT}\right]^{4/5} t^{4/5}. \tag{24}$$

For the model assumed in Fig. 1(B), the rate of approach will be considerably greater and is given by:

$$\frac{d(1-\cos\theta)}{dt}=\frac{d(x^2/2r)}{dt}. \tag{25}$$

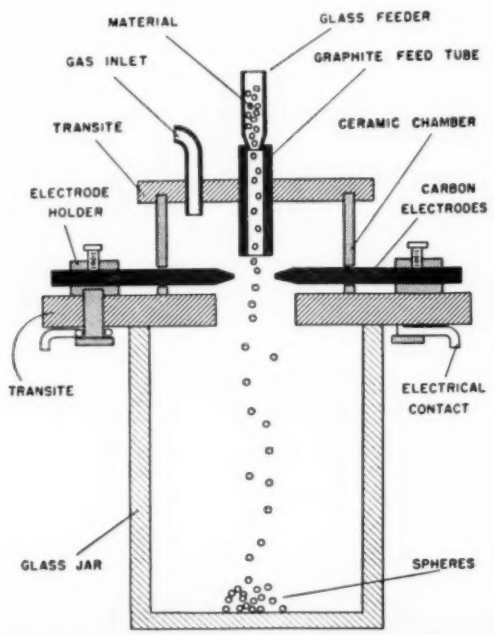

FIG. 5. Cross section of apparatus for preparing spheres.

[13] B. Y. Pines, J. Tech. Phys., U.S.S.R. **16**, 737 (1946).
[14] V. A. Ivensen, J. Tech. Phys., U.S.S.R. **17**, 1301 (1947).

This relationship, in combination with Eq. (16), leads to the result:

$$\frac{\Delta L}{L_0}=\left[\frac{20\gamma a^3 D_V}{\sqrt{2}r^3 kT}\right]^{2/5} t^{2/5}. \tag{26}$$

The volume shrinkage is given from Eq. (16) as:

$$\frac{\Delta V}{V_0}=\frac{-3n}{8}\left[\frac{80\gamma a^3 D_V}{r^3 kT}\right]^{4/5} t^{4/5}. \tag{27}$$

E. EXPERIMENTAL

In order to observe the growth of contact area between spheres such as shown in Fig. 1, a high-temperature microstage furnace for use with an ordinary petrographic microscope was constructed. The furnace consists of an electrical heating filament supported by two slotted contacts (Fig. 3). One contact is grounded and the other is connected with a Kovar seal. Power is supplied from a constant voltage regulator, variac, and transformer. The furnace is connected to a vacuum diffusion pump, and can be used *in vacuo* or with a purified helium or hydrogen atmosphere to 2200°C with a tungsten filament. A platinum filament can be used for oxidizing conditions up to about 1400°C. Temperature is measured with an optical pyrometer calibrated against known melting point materials on the filament.

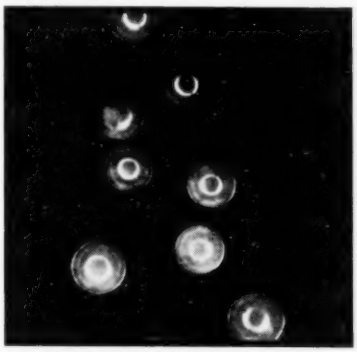

FIG. 6. Photomicrograph of spheres formed by arc-melting process.

A microscope is mounted to focus on the heating ribbon and is used in conjunction with a camera for micrographs or a filar micrometer eyepiece for direct measurements. The magnification employed varied between 100× and 366×. Resolution was checked by observing one micron latex Dow spheres and estimated to be <0.5 micron. The value of resolution obtained determines the minimum size spheres and ratio of (x/r), which can be reliably observed as indicated in Fig. 4.

Nearly perfect spheres of a variety of materials have been prepared by arc fusion. Powder samples of NaCl, Cu, Al_2O_3, ZrO_2, and other materials are sized with standard Tyler screens. The material of desired particle size is fed into the center of a three-phase carbon arc through a graphite tube extending through the cover of a chamber surrounding the arc (Fig. 5). A closed chamber around the arc is essential to decrease convection currents around the arc. For materials requiring a neutral or reducing atmosphere, a slow stream of hydrogen or helium can be passed through the melting chamber. The material is collected after passing through the arc and rolled down an incline or around a glass cylinder to separate the perfect spheres.

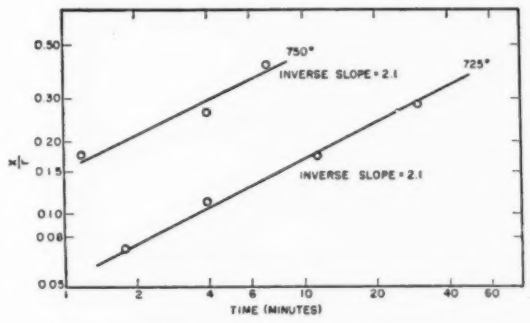

FIG. 7. Rate of interface growth between glass spheres ($r=49$ microns).

These spheres, such as shown in Fig. 6, are placed in contact on the microscope furnace heater and rapidly heated. Due to the low heat capacity of the furnace, only a few seconds are required to reach the sintering temperature.

Materials which have been investigated in the present study include a soda-lime-silica glass (Minnesota Mining & Manufacturing Company, "Sta-brite" beads), sodium chloride (Mallinckrodt A.R.), cp copper, Norton Company 38X alumina (0.04 Na_2O, 0.05 SiO_2, 0.04 Fe_2O_3, 0.002 TiO_2), Norton Company stabilized zirconia (4 CaO, 4 HfO_2, 1 Al_2O_3), cp ZrO_2, and calcined $Al(OH)_3$ (Baker's A.R.).

4. RESULTS AND DISCUSSION

A. Glass

Cursory measurements of glass sintering were carried out to test the apparatus and technique with the results shown in Fig. 7, where $\log(x/r)$ is plotted *vs* $\log t$. The inverse slope of approximately 2 is in agreement with

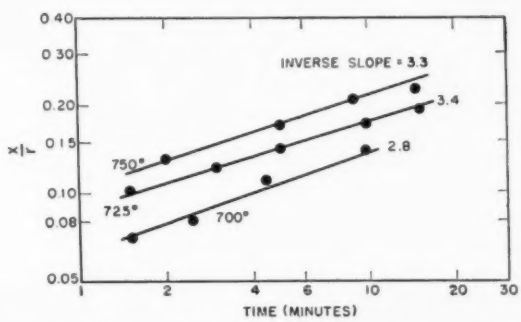

FIG. 8. Rate of interface growth between sodium chloride spheres ($r=60$–70 microns).

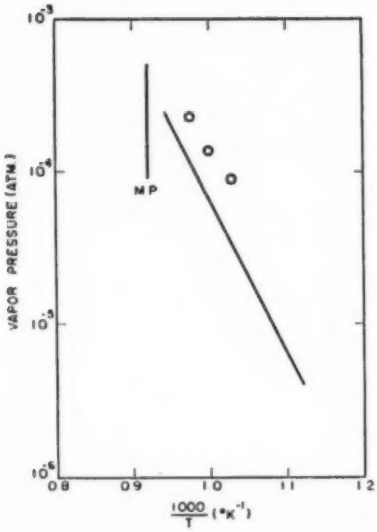

FIG. 9. Vapor pressure of NaCl determined by sintering experiments. (Solid line is mean value of direct measurements.)

previous work with glass, and indicates viscous flow is occurring as indicated in Eq. (1). The viscosities calculated from these data (taking $\gamma=313$ dyne cm^{-1}) and Eq. (1) are 7.2×10^8 poise at 725°C and 8.8×10^7 poise at 750°C, in agreement with the order of magnitude expected.

B. Sodium Chloride

Measurements of the rate of sintering of sodium chloride spheres 61.5–70 microns in diameter were made at 700–750°C with the results shown in Fig. 8. The inverse slope of 2.8–3.4 observed corresponds to an evaporation-condensation mechanism. The vapor pressures calculated from Eq. (6) are shown in Fig. 9 compared with the mean curve of direct vapor pressure measurements.[15] The absolute value calculated is high by a factor of two, while the temperature dependence is in good agreement with other data. This agreement is probably better than can be expected from the crude analysis of the rate problem. The center-to-center distance of the sodium chloride spheres did not measurably change during the experiment, but the individual spheres became elliptical, as shown in Fig. 10.

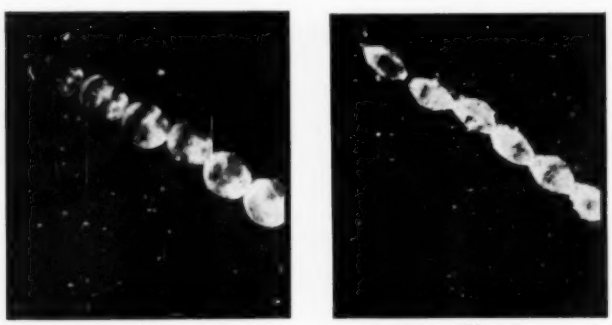

FIG. 10. Photomicrographs of sintering of sodium chloride at 750°C. (a) one minute, (b) ninety minutes.

[15] O. Kubashewski and E. L. Evans, *Metallurgical Thermochemistry* (Butterworth-Springer Ltd., London, 1951).

All of these observations are consistent with an evaporation-condensation process, and the observation of no shrinkage is direct experimental evidence that this process cannot lead to densification of a compact. As a check on this observation, loose compacts of NaCl were prepared with various particle sizes and sintered at 750°C with no decrease in density, although the strength increased appreciably. These results are in agreement with electron microscopic observations[16] and previously reported sintering behavior.[17,18]

C. Copper

Measurements of the sintering behavior of copper spheres about 100 microns in diameter were made at 950–1050°C with the results shown in Fig. 11. The inverse slope of 5.0–5.5 observed corresponds to a diffusion process. A decrease in the center-center distance of spheres was observed, indicating that volume diffusion must be taking place. The model of sintering assumed [Fig. 1(A) and Fig. 1(B)] can be tested by measuring the rate of approach of the centers of the spheres. These data for the copper spheres are shown in Fig. 12. The relationship observed corresponds to Fig. 1(B) ($\Delta L/L_0\sim t^{2/5}$); neither the time dependence nor the magnitude of the linear shrinkage can be explained on the basis of a model such as Fig. 1(A).

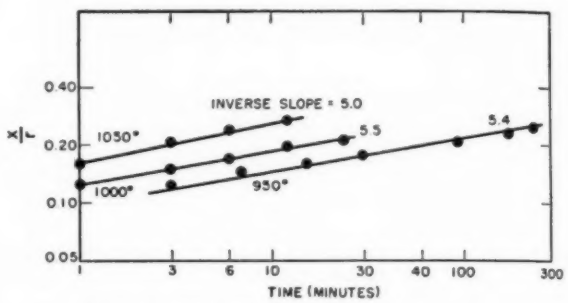

FIG. 11. Rate of interface growth between copper spheres ($r=50$–57 microns).

The self-diffusion coefficient has been calculated from Eq. (16), which corresponds to the observed rate of shrinkage. These results, together with results calculated from other observations of sintering†,[1,4–6,1]

[16] K. Endel and M. V. Ardenne, Z. Kolloid. **104**, 223 (1943).
[17] H. V. Mueller, Z. Physik. **96**, 279, 307, 321 (1935).
[18] A. G. Smekal, "Mechanism of Crystal Growth," in *The Physics of Powder Metallurgy*, W. A. Kingston, editor. (McGraw-Hill Book Company, Inc., New York, 1951), Chap. 2.

† Recalculated from the equivalent of Eq. (16) for the following cases. Spheres on plate:

$$D_V=\left(\frac{x^5/r^2}{t}\right)\left(\frac{kT}{320\gamma a^3}\right);$$

wire on plate:

$$D_V=\left(\frac{x^5/r^2}{t}\right)\left(\frac{kT}{640\gamma a^3}\right).$$

These values are different from those calculated by the original

(taking $\gamma=1670$ dyne cm^{-1}) and radioactive tracer measurements[19–22] are shown in Fig. 13. The mean value of the diffusion coefficient from the tracer measurements is $D=2.7\ \exp(-53\,000/RT)$ and sintering measurements give about the same result. This substantial agreement in absolute value and temperature dependence of the diffusion constant calculated from various experimenters' sintering data and measured directly with radioactive tracers is strong evidence for a volume diffusion mechanism. In addition, all the comparable sintering results are in agreement with Herrings's scaling law for volume diffusion ($\Delta t_1=\lambda^3\Delta t_2$).

The diffusion constant can also be calculated from the rate of approach of the spheres' centers (Fig. 12) and Eq. (26). Results of this calculation are shown in Fig. 13 and are in good agreement with results calculated from the rate of growth of the interface between spheres.

The rate of volume shrinkage of a compact of spherical particles should be given by Eq. (27) for the

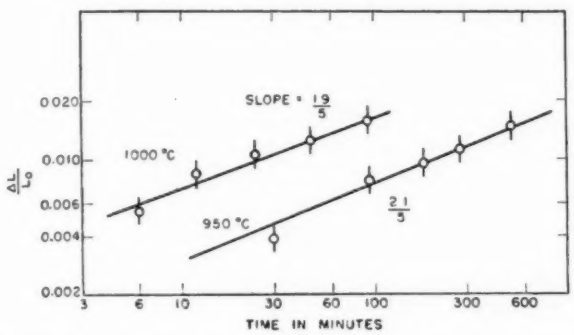

FIG. 12. Rate of approach of centers of copper spheres in contact.

proposed model, i.e.:

$$\frac{\Delta V}{V_0}=\frac{-3n}{8}\left[\frac{80\gamma a^3 D_V}{r^3 kT}\right]^{4/5} t^{4/5}.$$

Data reported by Clark, Cannon, and White[23] for the volume shrinkage of compacts of spherical copper particles ($r=37.5$ microns) are shown in Fig. 14. The time dependence of the observed initial shrinkage is well represented by Eq. (27). Diffusion coefficients calculated from the volume shrinkage by Eq. (27) are included in Fig. 13, and are in good agreement with other data.

The agreement found for the absolute value of the self-diffusion constant, and temperature dependence

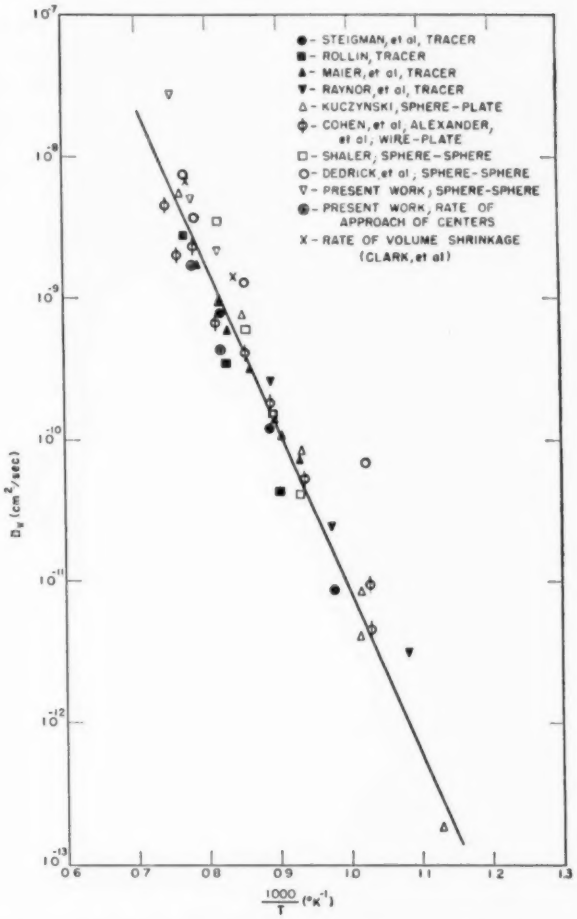
● - STEIGMAN, et al, TRACER
■ - ROLLIN, TRACER
▲ - MAIER, et al, TRACER
▼ - RAYNOR, et al, TRACER
△ - KUCZYNSKI, SPHERE-PLATE
◈ - COHEN, et al, ALEXANDER, et al, WIRE-PLATE
□ - SHALER, SPHERE-SPHERE
○ - DEDRICK, et al, SPHERE-SPHERE
▽ - PRESENT WORK, SPHERE-SPHERE
◉ - PRESENT WORK, RATE OF APPROACH OF CENTERS
X - RATE OF VOLUME SHRINKAGE (CLARK, et al)
D_V (cm^2/sec)
$\frac{1000}{T}$ (°K^{-1})

FIG. 13. Self-diffusion constant of copper calculated from sintering data and measured with radioactive tracer techniques.

of the self-diffusion constant determined from rate of interface growth, rate of approach of centers, and rate of compact volume shrinkage shows that all the available data for the initial stages of sintering are in agreement with a rate controlling self-diffusion process in the model shown in Fig. 1(B). This model requires that the source of material for volume diffusion is not on the surface of the spheres, as has been previously assumed. Vacancies may be eliminated either at dislocations or

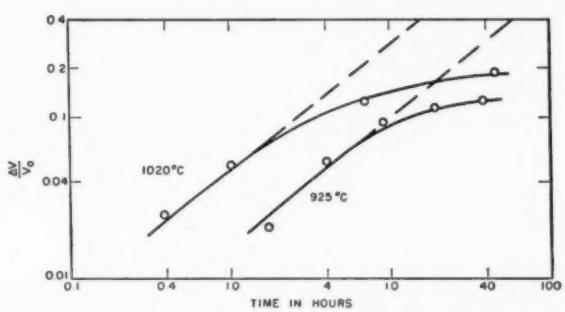

FIG. 14. Volume shrinkage of compacts of spherical copper particles ($r=37.5$ microns). Dashed lines are for relation: $\Delta V/V_0 \sim t^{4/5}$. (Data from Clark *et al.*)

authors—by several orders of magnitude in the case of Dedrick and Gerds.[5]

[19] Raynor, Thomassen, and Rouse, Trans. Am. Inst. Mining Met. Engrs. **30**, 313 (1942).

[20] M. S. Maier and H. R. Nelson, Trans. Am. Inst. Mining Met. Engrs. **147**, 39 (1942).

[21] D. V. Rollin, Phys. Rev. **55**, 231 (1939).

[22] Steigman, Shackley, and Nix, Phys. Rev. **56**, 13 (1939).

[23] Clark, Cannon, and White, Trans. Brit. Ceram. Soc. **52**, 1 (1953).

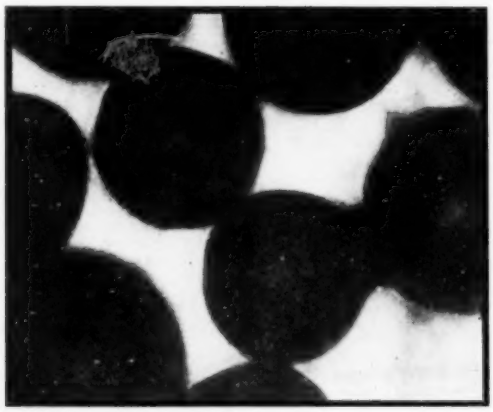

FIG. 15. Sintering at 1750°C of stabilized zirconia spheres prepared from material as received (366×). Note the nonuniform behavior of contact points.

at the grain boundary between the spheres. The existence of the Kirkendall effect makes vacancy elimination at dislocations seem probable. However, the requirement that grain boundaries be present for appreciable flow of copper wires under small stresses at elevated temperatures[24] and the observation that shrinkage of pores is very markedly accelerated by the presence of grain boundaries[25] makes it seem more probable that vacancies are mainly eliminated at the grain boundary. The complex boundary conditions for diffusion make it impossible to place much confidence in the quantitative diffusion constants calculated from sintering data. However, the order of magnitude observed and the temperature dependence (activation energy) should be reliable.

D. Al_2O_3 and ZrO_2

Rate of interface growth measurements were carried out for 50–150 micron spheres of Al_2O_3 and ZrO_2 at temperatures in the range from 1500°C to 2200°C. Adherence of spheres was observed to occur at 1300°C. Initial measurements made with commercial fused alumina and fused stabilized zirconia showed a rapid interface increase to about $x/r=0.2$ and then a slow increase, but results varied widely. A group of spheres sintered together showed wide differences in behavior as indicated in Fig. 15. Samples prepared from cp Al_2O_3 and ZrO_2 gave an interface of $x/r\sim0.12$ after very short times at temperatures, and this remained unchanged within experimental error at times up to 100 minutes and at temperatures up to 2020°C for Al_2O_3 and 2200°C for ZrO_2. In addition to these measurements, samples of alumina were prepared as loose compacts and as pressed compacts (41 000 psi.). These were simultaneously fired to 1800°C. While no measurable density changes took place in the loose compact, the pressed compact showed 22.7% linear shrinkage. These results indicate that the surface energy is insufficient to cause appreciable sintering in the particle sizes observed here (50–100 micron diameter), but that pressing introduces sufficient strain energy (no particle fracture was observed but this may have occurred at the contact points) to increase the sintering rate.

[24] A. P. Greenough, R. A. E. Tech. Note No. MET 151 (October, 1951).

[25] B. H. Alexander and R. Balluffi, J. Metals **188**, 1219 (1950).

5. SUMMARY

Sintering of glass spheres in agreement with a viscous flow process was observed.

Sintering of sodium chloride spheres occurs by an evaporation-condensation process. Calculation of the vapor pressure and its temperature dependence are in reasonable agreement with direct measurements. No shrinkage or densification occurs by this process.

Sintering data for copper spheres are in agreement with a model where volume diffusion occurs with grain boundaries or possible dislocations acting as vacancy sinks. This model is in good agreement with the time and temperature dependence of interface growth, linear shrinkage, volume shrinkage, and the effect of particle size.

Sintering data for spherical particles of Al_2O_3 and ZrO_2, 50–150 microns in diameter, indicate that little sintering occurs with this particle size material at temperatures near the melting point. Small amounts of impurities were observed to have a significant effect on the sintering process.

JOURNAL OF APPLIED PHYSICS VOLUME 26, NUMBER 10 OCTOBER, 1955

Theory of Steady-State Creep Based on Dislocation Climb

J. WEERTMAN
Metallurgy Division, Naval Research Laboratory, Washington, D. C.
(Received April 21, 1955; revised manuscript received July 8, 1955)

A theory of steady-state creep is developed using Mott's mechanism of dislocation climb. It is assumed in the analysis that the rate-controlling process is the diffusion of vacancies between dislocations which are creating vacancies and those which are destroying them. The concentration of vacancies along a dislocation line is determined by setting the change in the free energy caused by a decrease or increase in the number of vacancies equal to the change in the elastic energy occuring during dislocation climb. The creep equation that results from the analysis is

$$\text{creep rate} = \text{const}\ (\sigma^{\alpha}/kT)\exp(-Q/kT)$$

where α is a constant ($\alpha \sim 3$ to 4), Q is the activation energy of self-diffusion, kT has its usual meaning, and σ is the stress. This equation is valid in the stress range from the critical shear stress to a stress about equal to 10^8 to 10^9 dynes/cm^2. At larger stresses the creep rate increases much more rapidly with stress.

INTRODUCTION

RECENTLY Sherby, Orr, and Dorn[1] and Dorn[2] have reviewed much of the experimental work on high temperature creep of pure metals. The experimental data considered by them seem to show that the activation energy of steady-state creep is about equal to that of self-diffusion. In addition Dorn[2] has suggested that the stress dependence of steady-state creep at low stresses is given by the equation

$$\text{creep rate} = C\sigma^{\alpha}\exp(-Q/kT) \qquad (1)$$

where C and α are constants, Q is the activation energy (equal to self-diffusion) of creep, σ is the stress, and kT has its usual meaning. (In Table I are listed values of α from the work of many investigators.) To our knowledge no theoretical treatment of creep exists which leads to a creep rate given by Eq. (1). We wish to develop in this paper a creep theory which leads in a natural way to Eq. (1).

THEORY

We shall consider creep only in pure metals or simple alloys. In addition we shall consider only metals in which slip can occur on more than one slip system. Thus we exclude the hexagonal metals.* The dislocation model that will be used in this paper is briefly the following: dislocations are pictured to be held up by obstacles; they circumvent the obstacles by climbing over them through creation or destruction of vacancies or interstitials.[3] We shall assume that the obstacles are immobile dislocations. Lomer[4] has shown how dislocations on intersecting slip systems may combine to form an immobile dislocation. Mott[3] has suggested that when dislocations are piled up in groups their stress field induces dislocations on a second slip system to move to the group and form Lomer dislocations. Thus we might picture (see Fig. 1) the process leading up to the creation of a Lomer dislocation blocking a Frank-Read source as follows. After an external stress is applied, many loops are produced from a Frank-Read source. These move until they are stopped by some natural obstacle such as a grain boundary. The stresses produced by the piled-up group induce other Frank-Read sources on different slip systems to produce dislocations. These combine with those of the piled-up group, creating Lomer dislocations. The obstacle blocking the movement of the original Frank-Read source is now the closest Lomer dislocation. Dislocations between the closest Lomer dislocation and the natural obstacle disperse through climb. Dislocations between the Frank-Read source and the closest Lomer dislocation escape through climb but are continually replaced by newly created dislocations. We shall as-

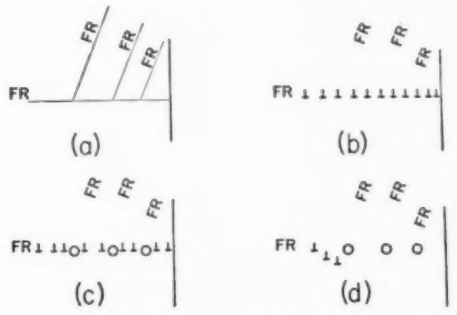

FIG. 1. Process leading up to a Frank-Read source being blocked by a Lomer dislocation. (a) Before application of a shear stress. The horizontal line represents the slip plane of the Frank-Read source on the left. The oblique lines represent the slip planes of the sources on the right. The plane of the paper is perpendicular to the intercept of the planes of the two slip systems. (b) Just after application of a stress activating the far left source. The dislocations are represented by the symbol of a pure edge dislocation although they are not in general pure edge dislocations. (c) After creation of immobile dislocations (represented by circles). (d) Dislocations lying between the Lomer dislocations have moved away by climb.

[1] Sherby, Orr, and Dorn, J. Metals **6**, 71 (1954).
[2] J. E. Dorn, J. Mech. Phys. Solids **3**, 85 (1954).
* This exclusion may, however, be necessary only for single crystals of the hexagonal metals. Slip on other than the basal plane has been observed in polycrystalline samples of the hexagonal metals when tested in creep.
[3] N. F. Mott, Proc. Phys. Soc. (London) **B64**, 729 (1951); Phil. Mag. **43**, 1151 (1952); **44**, 741 (1953); Proc. Roy. Soc. (London) **A220**, 1 (1953).
[4] W. M. Lomer, Phil. Mag. **42**, 1327 (1951); A. H. Cottrell, Phil. Mag. **43**, 645 (1952).

sume that there is a uniform distribution of blocked Frank-Read sources such as is shown in Fig. 1(d). This model would produce a rather uniform creep strain throughout a crystal. McLean[5] has shown that the major portion (in aluminum) of the total creep deformation does occur in a rather uniform fashion throughout a specimen.

In order to calculate the creep rate from this model it is necessary to know the rate of escape of dislocations past the Lomer dislocation. To calculate this rate it is necessary to know the height a dislocation must climb in order to escape and the rate of climb. This height is easily calculable from the results of dislocation theory.[6]† If one takes into account the fact that if there are n dislocations piled up, the stress on the leading dislocation is increased by a factor of n ($n=2\sigma\mathfrak{L}/\mu b$ where σ is the stress, $\mathfrak{L}$ the width of the piled-up group, b the length of the Burgers vector, and μ the shear modulus,[7,8] breakaway can occur at a height h given by

$$h=2\tau/n\sigma b=\tau\mu/\sigma^2\mathfrak{L} \qquad (2)$$

where τ is equal to $\mu b^2/12\pi(1-\nu)$ and ν is Poisson's ratio.

Consider next the rate of climb. If the concentration of vacancies (we assume interstitials are unimportant; the following analysis can be repeated assuming that they are important) at each climbing dislocation is known, the rate of climb can be calculated from the gradient of the vacancy concentration. The concentration of vacancies in the neighborhood of a dislocation can be easily calculated if the dislocation lines are able to create or destroy vacancies with sufficient ease so as to always maintain the "equilibrium concentration" in their immediate neighborhood. The "equilibrium concentration" is the concentration which a dislocation line would seek to maintain if it were the only one in a small crystal coated with some anticatalyst that prevents vacancy creation or destruction at the crystal surface. If σb is the force acting normal to the slip plane on an edge dislocation (and this is the approximate normal force when a mobile dislocation is pushed against a Lomer dislocation, see reference †), the energy lost or gained when an atomic length of dislocation line climbs one atom distance is σb^3. The equilibrium concentration is found by equating this energy to the chemical potential of the vacancies. The chemical potential of the vacancies is equal to $kT\log N/N_0$ where N is the actual number of vacancies per unit volume and N_0 is the equilibrium concentration in a dislocation free crystal. (See Bardeen and Herring[9] for a discussion of vacancy concentration and forces on dislocations.) The concentration, N_e, of vacancies in equilibrium with the lead dislocation in a piled-up group of n dislocations is thus

$$N_e=N_0\exp(\pm n\sigma b^3/kT)=N_0\exp(\pm 2\mathfrak{L}\sigma^2b^2/\mu kT). \qquad (3)$$

Since about half of the lead dislocations in a crystal will be maintaining the concentration given by Eq. (3) with the plus sign and half with the minus sign, vacancy flow will occur between the different piled-up groups. The concentration of vacancies midway between the piled-up groups will be equal to N_0. Under steady-state conditions (i.e. $d/dr(rdN/dr)=0$ where r is the perpendicular distance from a lead dislocation) the concentration of vacancies is approximately

$$N_0+(N_e-N_0)\log(r_1/r)/\log(r_1/r_0)$$

where r_1 is half the average distance between piled-up groups and r_0 is the distance in which the concentration is maintained at the level given by Eq. (3). The rate of flow of vacancies from a unit length of dislocation line is equal to $2\pi rD(dN/dr)$ which is approximately $N_0Dn\sigma b^3/kT$, where D is the diffusion coefficient of the vacancies, when $n\sigma b^3/kT$ is less than one. This rate of flow gives a rate of climb given by

$$\text{rate of climb}=N_0Dn\sigma b^5/kT=2N_0D\sigma^2\mathfrak{L}b^4/\mu kT \qquad (4)$$

when $n\sigma b^3/kT$ is less than one.

CREEP RATE

Once the rate of climb and the height of climb are known, the creep rate may be calculated. Let M be the number of active Frank-Read sources per unit volume, L the distance the edge portion of a dislocation loop moves after breakaway from the barrier, L' the distance the screw portion moves, then the creep rate, K, is equal to

$$K=n^2\sigma^2b^7N_0DLL'M/2\tau kT \approx 30\sigma^4b^3N_0DLL'M\mathfrak{L}^2/\mu^3kT \qquad (5)$$

when $n\sigma b^3/kT<1$. For $n\sigma b^3>1$ the above analysis can be generalized and one obtains

$$K=15\sigma^2bN_0DLL'M\mu^{-2}\mathfrak{L}\exp(2\sigma^2\mathfrak{L}b^2/\mu kT). \qquad (6)$$

Consider the stress dependence of the terms M, L, L', and $\mathfrak{L}$ in the above equations. In a single crystal of small cross section the terms L and L' are probably equal to the crystal cross section. For this case they would not depend on stress. In a polycrystalline sample L is probably equal to the average dimension of the subcells. The distance L' is probably equal to the grain dimension since it would be difficult to form obstacles

[5] D. McLean, J. Inst. Metals **80**, 507 (1951–52); **81**, 287, 293 (1952–1953).

[6] M. Peach and J. S. Koehler, Phys. Rev. **80**, 436 (1950).

† For example a positive $b/\sqrt{2}[0\bar{1}1]$, $(11\bar{1})$ mobile dislocation pushed against a $b/\sqrt{2}[\bar{1}10]$, $(00\bar{1})$ Lomer dislocation will be repelled by the force $\tau r^{-1}(\cos\theta'\cos2\theta'+4\sqrt{2}\sin\theta'\cos^2\theta')$ in the slip plane and $\tau r^{-1}(2\sqrt{2}\cos\theta'\cos2\theta'-\sin\theta'(1+2\sin^2\theta'))$ normal to the slip plane where $\theta'=\theta-\cos^{-1}/\sqrt{3}$. The origin is at the Lomer dislocation, r and θ are the usual polar coordinates with θ measured from the slip plane of the mobile dislocation, and τ is the constant given above.

[7] G. Leibfried, Z. angew. Phy. **6**, 251 (1954).

[8] Eshelby, Frank, and Nabarro, Phil. Mag. **42**, 351 (1952).

[9] J. Bardeen and C. Herring, *Imperfections in Nearly Perfect Crystals* (John Wiley and Sons, Inc., New York, 1952), p. 261.

to pure screw dislocations. The data of Servi, Norton, and Grant[10] indicate that the dimensions of the subcells (in aluminum) are proportional to (stress)$^{-1}$ and seem to be independent of temperature.

Koehler[11] finds that M is almost a constant for stresses greater than the critical shear stress if no interaction hardening takes place.‡ The term M, therefore, is independent of stress.

The stress dependence of the term $\mathfrak{L}$ can be estimated as follows: The shear stress due to the piled-up loops falls off[6,7] approximately as $4\sigma\mathfrak{L}^2/R^2$ where R is the distance from the center of a loop. Let $\bar{\sigma}$ be the activation stress of a Frank-Read source. Then any Frank-Read source in a second slip system in a cylinder of height $2\mathfrak{L}$ and radius $4\mathfrak{L}(\sigma/\bar{\sigma})^{\frac{1}{2}}$ could be activated. If any were activated a Lomer dislocation would be produced at a closer distance to the Frank-Read source and the value of $\mathfrak{L}$ would be reduced. The condition determining the value of $\mathfrak{L}$ is thus that the density of sources, M, times the volume in which the shear stress is greater than $\bar{\sigma}$ be less than one. This condition gives for $\mathfrak{L}$ the equation

$$\mathfrak{L}\sim\tfrac{1}{2}(\bar{\sigma}/\sigma)^{2/9}M^{-\frac{1}{3}}. \tag{7}$$

We conclude, therefore, that the product $\sigma^4LL'M\mathfrak{L}^2$ appearing in Eq. (5) should contain about a fourth-power stress dependence for single crystals and about a third-power dependence for polycrystalline samples.

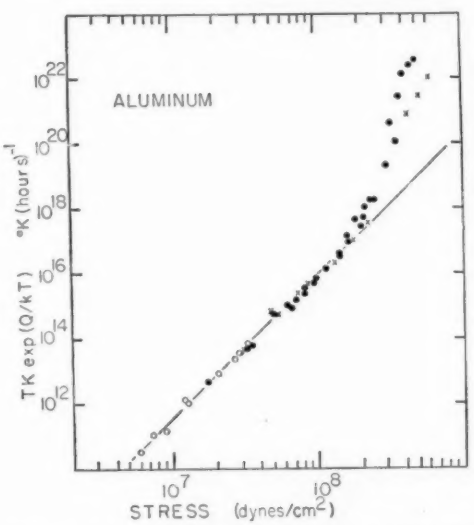

FIG. 2. Creep data of Servi and Grant[13] on polycrystalline aluminum. $TK\exp(Q/kT)$ is plotted as a function of applied stress. (o 593° and 482°C, coarse grain. ● 482°, 371°, 260°, and 193°, coarse grain. × 371°, 260°, 193°C fine grain.) The activation energy is equal to 36 000 cal/mole.

[10] Servi, Norton, and Grant, J. Metals 4, 965 (1952).
[11] J. S. Koehler, Phys. Rev. 86, 52 (1952).
‡ For our model the extent of interaction hardening can be estimated. At large distances from a piled-up group of dislocation loops the shear stress due to the group will be[6,7] approximately $4\sigma\mathfrak{L}^2/R^2$ times a function of angle, where R is the distance from the center of the piled-up loops. If this stress is larger than σ, the applied stress, interaction hardening can take place. We see that hardening can take place only when R is less than $\mathfrak{L}$. But $\mathfrak{L}$ is the approximate distance between sources. Thus interaction hardening should not be very important.

TABLE I. Creep data in the low stress range.

Material	Temperature °C	Stress range dynes/cm^2	α
Al[a]	371 to 593	6×10^6 to 2×10^8	4.4
Al(0.94%Mg)[b]	260 to 482	2×10^7 to 2×10^8	3.0
Al(1.9%Mg)[b]	260 to 482	2×10^7 to 2×10^8	3.0
Al(5.1%Mg)[b]	260 to 482	2×10^7 to 2×10^8	3.0
Al[c]	480	3×10^6 to 3×10^7	3.9
Al(1.1%Mg)[c]	480	4×10^7 to 7×10^7	3.6
Al(2.1%Mg)[c]	480	2×10^7 to 7×10^7	3.4
Al(3.1%Mg)[c]	258 to 580	3×10^6 to 4×10^8	3.2
Al[d]*	300	4.5×10^7 to 7×10^7	4.5
Al(2%Mg)[d]	250 to 380	5×10^7 to 3×10^8	4.0
Sn[e]	21	5×10^7 to 10^8	4.6
Pb[f]	43	3.5×10^6 to 10^7	2 to 4
Pb[g]	30 to 100	7×10^6 to 2×10^7	5.5
Pb[h]	100	3×10^7 to 9×10^7	4.3
Pt[d]	1118 to 1285	10^8 to 2.5×10^8	5.0
AgBr[i]†	310 to 407	6×10^5 to 1.5×10^7	4.0
Ice[j]	−12 to 0	9×10^5 to 9×10^6	3.2

* Grains extended across specimen cross section.
† Single crystals.
[a] I.S. Servi and N. J. Grant, reference 13.
[b] A. W. Mullendore and N. J. Grant, J. Metals **6**, 973 (1954).
[c] Laks, Wiseman, Sherby, and Dorn, Inst. of Engineering Research, Univ. of Calif., Berkeley, Series No. 22, Issue No. 37 (September 1954).
[d] Dushman, Dunbar, and Huthsteiner, J. Appl. Phys. **15**, 108 (1944).
[e] J. E. Breen, Master's thesis, University of Maryland (June, 1954).
[f] Moore, Betty, and Dollins, Univ. of Illinois Bulletin **35**, No. 102 (1938).
[g] A. A. Smith, Trans. Am. Inst. Mining Met. Engrs. **143**, 165 (1941).
[h] E. N. da C. Andrade, Proc. Roy. Soc. (London) **90**, 329 (1914).
[i] R. W. Christy, Acta Metallurgica **2**, 284 (1954).
[j] J. W. Glen, Proc. Roy. Soc. (London) **A228**, 519 (1955).

The temperature dependence of Eq. (5) resides almost entirely in the term N_0D. This product is[12] about equal to $b^{-1}\nu\exp(S/k)\exp(-Q/kT)$ where Q is the activation energy of self-diffusion, S the entropy of activation of self-diffusion, and ν the frequency of vibration of a vacancy. The activation energy of creep is thus equal to that of self-diffusion. This is true provided self-diffusion is taking place principally through vacancy (or interstitial) movement and provided that the dislocations can always maintain in their immediate neighborhood the equilibrium concentration.

Equations (5) and (6) can be simplified and written as

$$K=C(\sigma^\alpha/kT)\exp(-Q/kT) \quad \text{for} \quad n\sigma b^3/kT<1 \tag{8}$$

$$K=C'\sigma^\gamma\exp(A\sigma^\beta/kT)\exp(-Q/kT) \quad \text{for} \quad n\sigma b^3/kT>1 \tag{9}$$

where $\alpha\sim3$ to 4, $\beta\sim2$, $\gamma\sim1$ to 2, and A, C, and C' are constants.

For $\bar{\sigma}\sim10^6-10^7$ dynes/cm^2, $M\sim10^9-10^{12}$ sources/cm^3, Eq. (8) is valid up to a stress of 10^8-10^9 dynes/cm^2 for typical values of μ and T. Equation (9) is no longer valid when the stress becomes great enough that the height of climb becomes comparable to b. For reasonable values of M, $\bar{\sigma}$, μ, and T Eq. (9) is invalid for a stress greater than about 10^9 dynes/cm^2. Since the critical shear stress is of the order of 3×10^6 dynes/cm^2 and the theoretical yield stress is of the order of

[12] C. Zener, *Imperfections in Nearly Perfect Crystals* (John Wiley and Sons, Inc., New York, 1952), p. 289.

TABLE II.

Applied stress dynes/cm²	$KT\exp(Q/kT)$ (degrees absolute sec⁻¹) Theory	Mullendore and Grant[a] Al(1.9%Mg)	Servi and Grant[b] Al	Dushman *et al.*[c] Al(2%Mg)
7×10^6	6×10^7		2×10^7	
2×10^7	10^9	2×10^8	2×10^9	
7×10^7	4×10^{10}	8×10^9	5×10^{11}	2×10^9
2×10^8	10^{12}	2×10^{11}	5×10^{13}	1.5×10^{11}
Grain size	1 mm	0.9 mm	0.05 and 1 to 3 mm	0.2 mm

[a] A. W. Mullendore and N. J. Grant, J. Metals **6**, 973 (1954).
[b] See reference 13.
[c] Dushman, Dunbar, and Huthsteiner, J. Appl. Phys. **15**, 108 (1944).

3×10^{10} dynes/cm² for reasonable values of μ, the present theory would explain steady state creep over about three orders of magnitude of the stress out of a possible four orders of magnitude. The creep at very high stresses is left unexplained.

In Fig. 2 creep data on pure aluminum are plotted to show that a power law stress dependence has been observed. In Table I are listed values of α calculated from the data of a number of investigators. The range of stress in much of this work is too limited to prove that a power law dependence is actually obeyed. But where the stress range is over a factor of ten there can be no doubt that a power law is obeyed. These data show that α is about equal to 4. In Table II are listed experimental and theoretical values of $KT\exp(Q/kT)$ for aluminum and aluminum-magnesium alloys. The theoretical values were calculated using the experimental value of Q and the following values for the quantities entering into Eq. (8): $b=2.5\times10^{-8}$ cm, $\mu=2.5\times10^{11}$ dynes/cm², $\nu=3\times10^{12}$ sec⁻¹, $M^1=10^3$ cm⁻¹, $\bar{\sigma}=3\times10^6$ dynes/cm², and $L=(0.02\text{ cm})(\bar{\sigma}/\sigma)^{\frac{1}{2}}$ (experimental result of Servi, Norton, and Grant). The entropy of activation was estimated using the relationship developed by Zener.[12] It was assumed that the resolved shear stress on the slip plane is one-half the applied stress.

The data of Servi and Grant[13] (Fig. 2) show most clearly that the creep data can be separated into a low stress and a high stress region. (It should be pointed out that their data for the two highest temperatures may be in doubt because grain growth occurred during the tests. However, the grain growth does not seem to have altered the results since there is no discontinuity in the curve at these tests.) The stress separating the two regions agrees well with that predicted by the present theory. They suggest, however, that two regions occur because of a difference in the deformation at the grain boundaries. That is, in the high stress region there is little grain boundary movement while in the low stress region there is boundary sliding. One way to decide whether this is truly the reason for having the two regions would be to make tests on single crystals.§

[13] I. S. Servi and N. J. Grant, J. Metals **3**, 909 (1951).

§ Grain boundary sliding can be explained using dislocation climb. If the slip plane of a dislocation is at an angle to the grain boundary, climb by a dislocation parallel to the boundary will result in shear parallel to the boundary. The amount of shear at a boundary will be equal to the product of the total length of dislocation line reaching the boundary, the distance climbed parallel to the boundary, and the Burgers vector, divided by the area of the grain boundary. In the present model if $\bar{M}$ is the total number of loops which have been created per unit volume and if the average distance a dislocation climbs along a grain is equal to the subgrain size, L, the mean grain boundary displacement is of the order of $\bar{M}L^2L'b$. The total strain due to grain boundary displacement is of the order $\bar{M}L^2b$. The model developed in this paper gives the strain within the grains to be of the order $\bar{M}LL'b$. The ratio of these last quantities is L/L'. (Or deformation at grain boundaries/deformation within grains = subgrain size/grain size.) This relationship has been experimentally observed by McLean.[5] Since the subgrain size increases as the stress is lowered, we expect that the amount of grain boundary sliding will also increase as the stress is lowered.

DISCUSSION

The analysis just given has shown how a creep rate with a power law stress dependence and an activation energy equal to that of self-diffusion can arise. These results are contingent on the ability of a dislocation line to create or destroy vacancies with sufficient ease so as to always maintain in its immediate vicinity the concentration given by Eq. (3). For some metals the dislocation line may not have this ability. For example, in f.c.c. metals a dislocation line may split up into half dislocations with a stacking fault between them. Dislocation climb is now more difficult because the stacking fault must also climb.[14] In the noble metals this stacking fault is rather wide (~20 atoms). Our analysis may not apply for these metals. In aluminum on the other hand the stacking fault is rather narrow (~2 atoms). Dislocations in aluminum probably are able to create or destroy vacancies with the required ease.

It had been thought that the occurrence of porosity in Kirkendall effect experiments might mean that large deviations can occur from the equilibrium concentration of vacancies.[15] This would imply that dislocations cannot maintain very easily the equilibrium concentration of vacancies. Recently, however, Brinkman[16] has given a more subtle consideration to this question and concluded that pores may be able to form at equilibrium concentrations. Also Barnes[17] has interpreted certain surface features (rippled surface in the diffusion zone) in a Kirkendall experiment as arising from extensive dislocation climb.

The answer to the question of whether or not dislocations can easily maintain an equilibrium concentration will probably be given by theoretical studies of jog formation energies such as have been carried out by Seeger[18] and by Stroh.[19]

In the case where dislocations have difficulty in creating or destroying vacancies, Eqs. (8) and (9) may

[14] R. S. Barnes, Acta Metallurgica **2**, 380 (1954).
[15] F. Seitz, Acta Metallurgica **1**, 355 (1953).
[16] J. A. Brinkman, Acta Metallurgica **3**, 140 (1955).
[17] R. S. Barnes, *Defects in Crystalline Solids* (Physical Society, London, 1954), p. 359.
[18] A. Seeger, *Defects in Crystalline Solids* (Physical Society, London, 1954), p. 391.
[19] A. N. Stroh, Proc. Phys. Soc. (London) **B67**, 427 (1954).

possibly still apply but with an activation energy not equal to that of self-diffusion. For this case the rate of flow of vacancies can probably be calculated from the usual rate of reaction theory which shows that the effect of the application of a stress is to increase the rate of creation of vacancies along a unit length of dislocation line to $V\exp(n\sigma b^3/kT)$ and decrease the rate of destruction to $V\exp(-n\sigma b^3/kT)$ or vice versa. Here V is the rate of creation or destruction of vacancies when the applied stress is zero. Equations (8) and (9) would follow but the activation energy, Q, would be that contained in V.

JOURNAL OF APPLIED PHYSICS VOLUME 26, NUMBER 10 OCTOBER, 1955

Shape and Crystal Anisotropy of Alnico 5

E. A. NESBITT AND H. J. WILLIAMS
Bell Telephone Laboratories, Incorporated, Murray Hill, New Jersey
(Received May 7, 1955)

It is concluded from torque measurements on single crystals of Alnico 5 that the high coercive force of these crystals depends upon the shape anisotropy of the fine precipitated plates and that the crystal anisotropy of the plates is negligible. The present physical picture of the alloy is that it consists of plates of precipitate of high magnetic saturation separated by a matrix of comparatively low magnetic saturation. The plates are made up of rods of precipitate (approximately 75 A in diameter ×400 long) but they act magnetically like single domain plates. The magnetization vector turns in the plane of the plates, and it is the length-to-width dimension ratio of the plates which determines the effective shape anisotropy and the resulting coercive force of the alloy.

IN 1952, Heidenreich and Nesbitt[1,2] demonstrated that Alnico 5 is composed of fine particles having dimensions of the order of 10^{-6} cm. Electron micrographs of crystals heat treated in a magnetic field along the [001] direction showed that the precipitate grew in the direction of the field applied during heat treatment, but not at right angles to it. For optimum permanent magnet properties the spacing between the plates of the precipitated phase was found to be about 200 A and the plates themselves were made up of rows of rods. The rods of precipitate were approximately 75–100 A in diameter, and 400 A long. These dimensions of the fine particles for optimum conditions were obtained by extrapolation. Later, Kronenberg,[3] and also Fahlenbrach,[4] confirmed the thickness of these precipitated particles.

Recently it was demonstrated that the orientation of fine precipitated particles could be detected by measuring the magnetic torque on single crystals at various field strengths.[5] In addition, it was also shown that the separate effects of shape and crystal anisotropy on the coercive force could be determined. This work was done on Fe_2NiAl and led to a better understanding of the alloy. It is the purpose of this paper to report similar experiments on Alnico 5 using this new technique. Figure 1 shows an electron micrograph of a (100) surface on a single crystal of Alnico 5 after it had been heated at 800°C for one hour. This crystal was heat treated in a magnetic field, and it is clearly evident

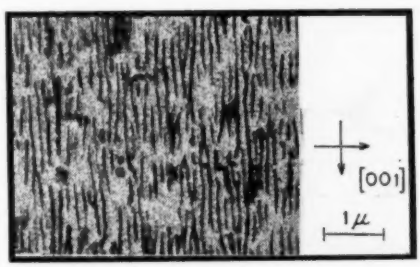

FIG. 1. Electron micrograph of single crystal of Alnico 5 (100) heat treated in a magnetic field in [001] direction showing permanent magnet precipitate growing in direction of applied field.

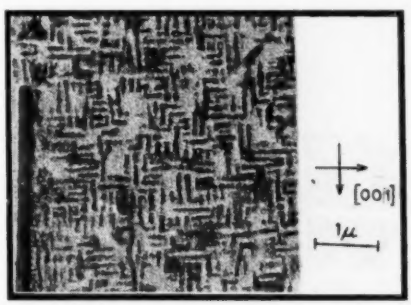

FIG. 2. Electron micrograph of single crystal of Alnico 5 (100) not heat treated in field showing permanent magnet precipitate growing in [010] and [001] directions.

[1] R. D. Heidenreich and E. A. Nesbitt, J. Appl. Phys. **23**, 352 (1952).
[2] E. A. Nesbitt and R. D. Heidenreich, J. Appl. Phys. **23**, 366 (1952).
[3] K. J. Kroneberg, Z. Metallkunde **45**, No. 7, 440 (1954).
[4] H. Fahlenbrach, Tech. Mitt. Krupp **12**, No. 7, 177 (1954).
[5] Nesbitt, Williams, and Bozorth, J. Appl. Phys. **25**, 1014 (1954).

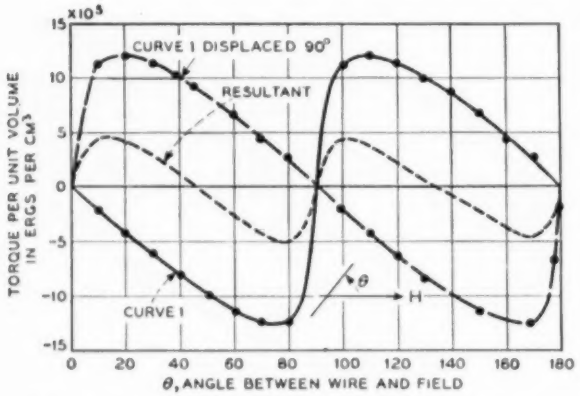

FIG. 3. Torque curve for a single Mo permalloy wire at $H=4000$ oersteds.

that the black precipitate grows in the direction of the applied field [001]. The reason the precipitate grows in the field direction is that only nuclei parallel to the field are formed, because in this direction they have a low demagnetizing factor, while the nuclei at right angles to the field have a high demagnetizing factor and are suppressed.[6] Figure 2 shows an electron micrograph of a single crystal of Alnico 5 (100) after heating at 800°C for one hour without a magnetic field. The black precipitate is clearly evident, in both the [001] and [010] directions.

Models simulating these precipitated structures were made, and the experimental torque curves obtained on them agreed with the analytical curves in a previous article.[5] The torque curves on these models are reproduced here so that they may be compared with those obtained on single crystals of Alnico 5. Figure 3 shows torque curves obtained on a model which consists of a single wire of annealed molybdenum permalloy having a length to diameter ratio of approximately 9, imbedded in Lucite. This model corresponds to an Alnico 5 structure heat treated in a magnetic field. Curve 1 shows the torque obtained on this single wire at a field strength, H, of 4000 oersteds. The curve

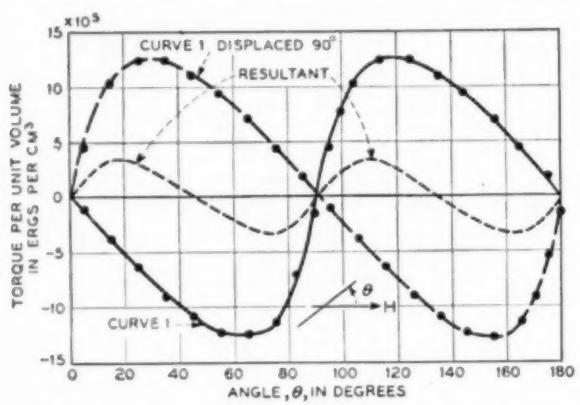

FIG. 4. Torque curve for a single Mo permalloy wire at $H=7000$ oersteds.

[6] Kittel, Nesbitt, and Shockley, Phys. Rev. **77**, 839 (1950).

is skewed because at low values of field strength the magnetization vector tends to align itself along the axis of easy magnetization of the wire even when the latter is at a considerable angle to the applied field. The crystal anisotriopy of the wire is negligible and therefore does not effect the observed behavior. Curve 1 is displaced 90° and added to the original curve; the resultant of these curves is a curve of twice the original frequency. This resultant torque is what is observed in the case of two wires crossed at 90° and it also corresponds to the case of an Alnico 5 crystal (100) not heat treated in a field.

Figure 4 shows the torque curve obtained on a single wire at $H=7000$ oersteds. Note that the curve is skewed less at this higher field strength and that the resultant curve is consequently of lower amplitude. If H is increased further, the torque on a single wire tends to become symmetrical in the 90° interval and

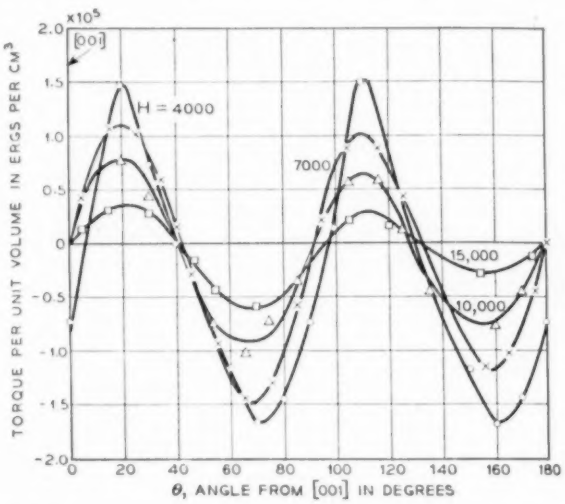

FIG. 5. Torque curves for Alnico 5 single crystal disk (100) not heat treated in a field. Coercive force of disk is 540 oersteds.

the resultant of the two curves which are displaced 90° from each other approaches zero. From this it is apparent that the torques on two single wires displaced 90° from each other tend to become equal in magnitude and since they are of opposite sign, the resultant torque approaches zero. As can be observed from the experiments on the wires of moderate length to diameter ratios, it takes an extremely high field to reduce the torque to zero.

RESULTS ON SINGLE CRYSTALS NOT HEAT TREATED IN A FIELD

Figure 5 shows the torque curves obtained with a (100) single crystal disk of Alnico 5 not heat treated in a field. The curves have a fourfold symmetry which is characteristic of cubic crystals in this plane. The torque diminishes with increasing H in much the same manner as the torque did for the molybdenum permalloy wires crossed at 90°. This indicates that the torque is

due to the shape anisotropy of the precipitate and not to the crystal anisotropy. If one plots the peak values of these torques *versus* $1/H$ a linear curve is obtained which when extrapolated shows that the torque is practically zero for infinite field. This means that the crystal anisotropy is negligible in comparison with the shape anisotropy and therefore it is not important in determining the torque on the crystal. The directions of easy magnetization in this plane for all values of H are the ⟨011⟩ directions. These easy directions result from the precipitate lying in the [001] and [010] directions.

Figure 6 shows the torque curves obtained for a (110) disk of Alnico 5 not heat treated in a field. The curves have a twofold symmetry which is characteristic of cubic crystals in this plane. The torque in this plane also diminishes with increasing H and this again indicates that the torque is due to the shape anisotropy

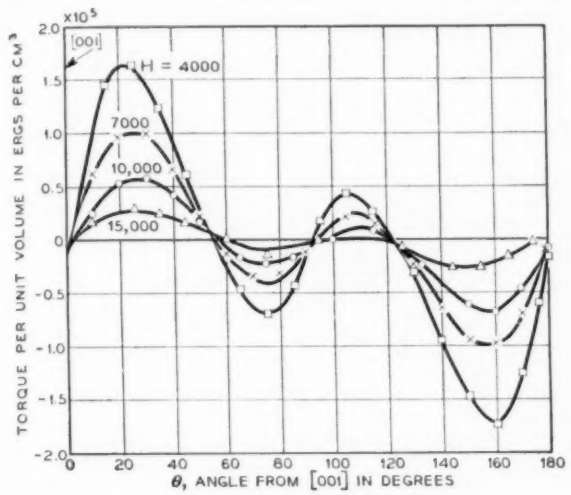

FIG. 6. Torque curves for Alnico 5 single crystal disk (110) not heat treated in a field. Coercive force of disk is 512 oersteds.

of the precipitate and not the crystal anisotropy. The directions of easy magnetization in this plane are the ⟨111⟩ directions because the precipitate lies in the three ⟨001⟩ directions.

RESULTS ON SINGLE CRYSTALS HEAT TREATED IN A FIELD

Figure 7 shows the torque curves obtained on a (100) single crystal disk heat treated in a field perpendicular to its face. The torque curves again have a fourfold symmetry because we have two sets of plates at right angles to each other. The torque diminishes with increasing field strength which again indicates that it is due to the shape anisotropy of the precipitate and not to the crystal anisotropy. These curves also show that the precipitate acts magnetically like plates, since all the rods of precipitate lie perpendicular to the measuring field. In this case, it is the ratio of the width to the thickness of the plates which determines the shape

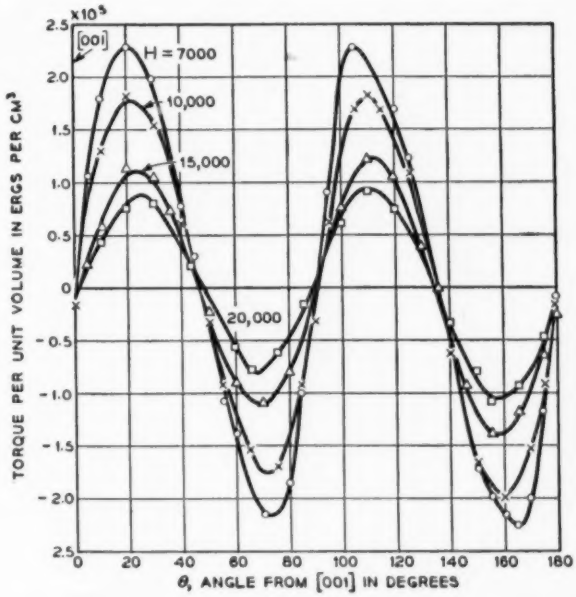

FIG. 7. Torque curves for Alnico 5 single crystal disk (100) heat treated in a field perpendicular to its face. Coercive force of disk is 160 oersteds.

anisotropy. Furthermore, if we again plot the peak value of the torque curves *versus* $1/H$, the linear curve obtained intersects the point of zero torque indicating practically zero crystalline anisotropy for optimum permanent magnet conditions (Fig. 8).

Figure 9 shows the torque curves obtained on a (110) plane single crystal disk heat treated in a field in a [001] direction. With this type of treatment there is no cross precipitation and therefore the torque curves should not decrease with increasing H or show any tendency toward fourfold symmetry. This is borne out by the experimental curves which show twofold symmetry. At an H of 20 000 the torque is slightly higher than at an H of 4000 and the curve has become less skewed. This value of torque is 1.08×10^6 ergs per cm³, and according to fine particle theory, the calculated coercive force is

$$H_c=\frac{2K_{sh}}{I_s}=\frac{2\times1.08\times10^6}{1100}=1960 \text{ oersteds}$$

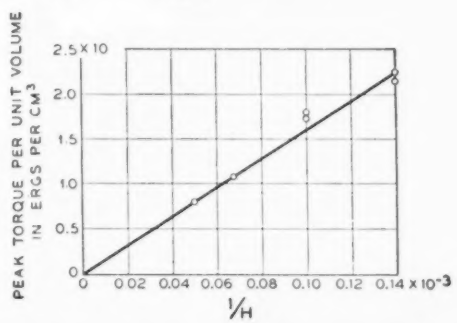

FIG. 8. Peak torque *vs* $1/H$ for Alnico 5 crystal (100) heat treated in a field perpendicular to its face. Maximum value of ordinate scale is 2.5×10^6.

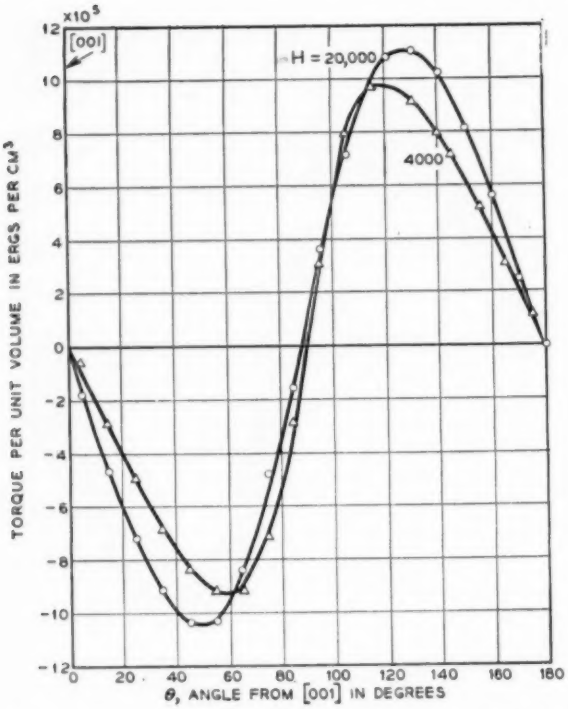

FIG. 9. Torque curves for Alnico 5 single crystal (110) heat treated in a field in the [001] direction. Coercive force of disk is 715 oersteds.

where K_{sh} is the anisotropy due to shape, equal to the maximum torque resulting from a parallel alignment of rods. The measured value of coercive force on this disk is 715 oersteds. This difference between the calculated and measured values of coercive force is due to the fact that when the torque is measured the magnetization vector rotates in a different plane from that in which the coercive force is measured. When the torque is measured the magnetization is pulled out of the plane of the plates, which gives a high value of the anisotropy, and when the coercive force is measured the magnetization vector rotates in the plane of the plates, a process involving less anisotropy.

When the magnetization vector is pulled out of the plates, as occurs in the torque measurement, the effective shape anisotropy is determined by the ratio of the length of the plate to its thickness or approximately 400 A/100 A or 4. When the magnetization vector is rotated in the plane of the plate, as occurs in a coercive force measurement, the effective shape anisotropy is determined by the ratio of the length of the plate to its width or approximately 400 A/200 A or 2. Hence, one would expect the calculated value of the coercive force to be much higher than the measured value as is the case.

Figure 10 shows the torque curves obtained on a (110) plane single crystal disk heat treated in a field perpendicular to its face. This treatment suppresses the growth of nuclei in the [001] direction and consequently there is practically no cross precipitation. The torque curves indicate this since the torque does not diminish with increasing field and the curves show twofold symmetry. There is evidence, however, of some cross precipitation when a crystal cut in the (100) plane is heat treated in a field in the [011] direction. Actually the precipitation in this case lies in the same plane as the previous case but the torque is measured in a different plane. At low values of field $H=5000$ (Fig. 11) the curve is somewhat irregular but it still shows twofold symmetry. The curve becomes regular when the field is increased to $H=22{,}000$. In this case, if the coercive force is calculated, we obtain

$$H_c=\frac{2K_{sh}}{I_s}=\frac{2\times 400\,000}{1100}=730 \text{ oersteds.}$$

This value compares favorably with the measured value of coercive force of 540 oersteds.

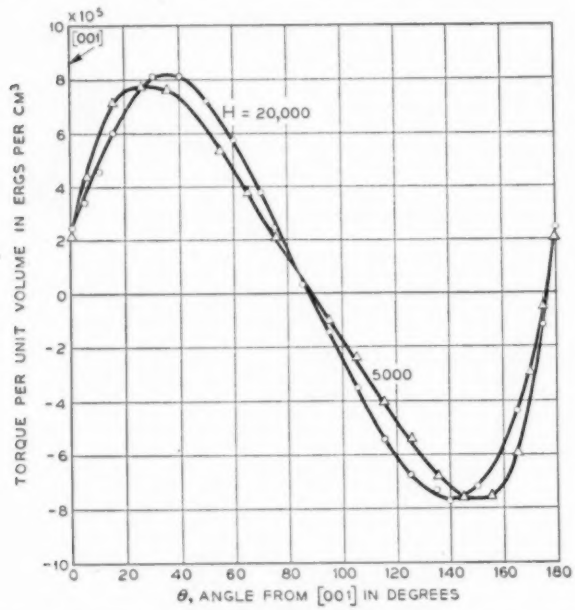

FIG. 10. Torque curves for Alnico 5 single crystal disk (110) heat treated in a field perpendicular to its face.

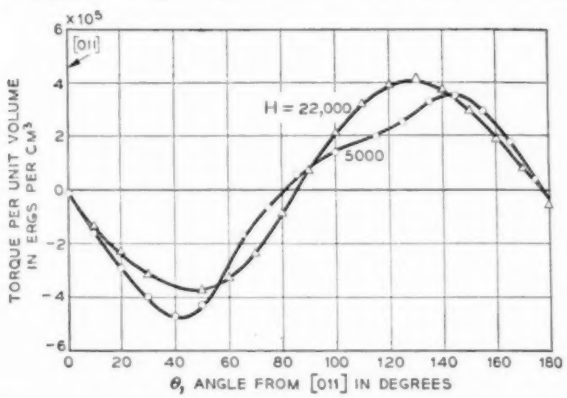

FIG. 11. Torque curves for Alnico 5 single crystal disk (100) heat treated in a field in the [011] direction. Coercive force of disk is 540 oersteds.

These torque curves indicate that when a (100) crystal is heat treated with the field in the [011] direction, the plates of precipitate are parallel to the (100) plane and have their longest dimension parallel to the [011] direction. Since the amount of cross precipitation is small, the magnetization vector rotates mainly in the plane of the plates of precipitate both when measuring the torque and the coercive force, and there is reasonable agreement between the measured (540) and calculated (730) values of coercive force.

CONCLUSIONS

The coercive force of Alnico 5 has been shown to be due primarily to the shape anisotropy of the plates of precipitate and not the crystalline anisotropy which was found to be negligible. A series of torque curves taken on a single crystal not heat treated in a magnetic field has peak values of torque that decrease with increasing field. This unusual behavior is shown to be due to the shape anisotropy of the plates of precipitate. Furthermore, the peak values of the torque curves extrapolate to zero for infinite field, indicating that the alloy has zero crystalline anisotropy. In a previous investigation of Fe_2NiAl the torque curves were found to decrease, pass through zero and then change sign as the field was increased. Extrapolation of the peak values of torque curves of Fe_2NiAl gave a crystal anisotropy constant of 130 000 ergs/cm^3 as compared with a negligible crystal anisotropy for Alnico 5.

ACKNOWLEDGMENTS

The authors are greatly indebted to R. M. Bozorth for valuable discussions during the work, to R. D. Heidenreich for the electron micrographs, to D. H. Wenny for supplying the alloys, and to A. J. Williams for growing and orienting the single crystals.

JOURNAL OF APPLIED PHYSICS VOLUME 26, NUMBER 10 OCTOBER, 1955

Precise Investigation of the Theory of Damping by Transverse Thermal Currents

B. S. Berry*
Department of Metallurgy, University of Manchester, Manchester, England
(Received June 6, 1955)

The frequency-dependence of internal friction of four α brass (62.5% Cu) reeds was measured at room temperature under conditions where contributions to the internal friction other than that arising from transverse thermal currents were small and assessable. Measurements were made by the free-decay method, at maximum strain amplitudes of 5×10^{-6}. By using specimens of two different thicknesses, frequencies differing from the frequency of peak damping by nearly a factor of 20 were obtained by measurements in the range 7–370 cy/sec. The results, in conjunction with measurements of Young's modulus (1.06×10^{12} dynes/cm$^2\pm0.5\%$), coefficient of linear expansion (18.7×10^{-6}/°C$\pm0.5\%$), density (8.42 g/cc$\pm0.2\%$), specific heat (0.088 cal/g/°C$\pm2\%$), and thermal diffusivity (0.34 cm^2/sec$\pm5\%$), indicate that Zener's theory of damping by transverse thermal currents is probably valid exactly. From the position of the peak, the thermal diffusivity is found more precisely as 0.346 cm^2/sec$\pm1.5\%$.

I. INTRODUCTION

QUANTITATIVE knowledge of established relaxations becomes increasingly important as new phenomena are discovered and as attempts are made to separate observed internal friction into its various contributions. Transverse vibration is used frequently for internal friction investigations, and at room temperature the major contribution often may be ascribed to damping by transverse thermal currents. The theory of this relaxation has been given by Zener.[1] The strength and position of the peak are predicted completely in terms of the thickness of the specimen† and a number of its physical properties. Hitherto, the most satisfactory experimental results in support of the theory appear to be those obtained on German silver by Bennewitz and Rötger.[2] Even here there exists a discrepancy between theory and experiment which approaches a factor of two at frequencies differing from the frequency of the peak by more than a factor of ten. Although arguments can be advanced to explain this discrepancy, for example in terms of apparatus losses, further direct experimental support seemed necessary before the theory could be relied upon to predict the internal friction in close detail.

II. THEORY

It will suffice here to give only the results of Zener's analysis. The complete internal friction behavior can be regarded as the superposition of an infinite number of simple relaxations, thus:

$$\frac{\delta}{\pi}=\Delta_E\sum_{j=0}^{\infty}F_j\cdot\frac{\omega\tau_j}{1+(\omega\tau_j)^2}, \qquad (1)$$

* Now at the Hammond Metallurgical Laboratory, Yale University, New Haven, Connecticut.

[1] C. Zener, Phys. Rev. **53**, 90 (1938).

† The transverse dimension that controls the frequency of vibration.

[2] K. Bennewitz and H. Rötger, Z. tech. Phys. **XIX**, 521 (1938).

TABLE I. Details of the internal friction specimens.

Specimen number	Length cm	Thickness cm	Frequency of peak damping f_0 cy/sec	Frequency range f cy/sec	Range of $\log_{10} f/f_0$
Material: annealed α brass, 62.5% Cu					
1	12.02	0.06352	135 (observed)	21.9 →161	−0.789 → 0.0760
2	29.97	0.06480	130 (calculated)	7.00→ 26.7	−1.267→−0.686
3	12.63	0.1601	21.25 (calculated)	78.4 →367	0.567 → 1.273
4	27.55	0.1614	20.87 (calculated)	24.2 → 78.1	0.0635→ 0.502

Width of all specimens: $\frac{3}{8}$-in.
Mean grain size of each specimen: 0.05 mm

where δ = the logarithmic decrement. F_j = a numerical factor giving the relative strength of the jth relaxation, and defined so that

$$\sum_{j=0}^{\infty} F_j = 1.$$

τ_j = the relaxation time of the jth relaxation, and ω = the circular frequency of vibration.

The relaxation strength Δ_E may be shown by other considerations to be

$$\Delta_E = \frac{\alpha^2 E T}{\rho S} \tag{2}$$

where α = the coefficient of linear expansion. E = Young's modulus. T = the absolute temperature. ρ = the density. S = the specific heat.

For a reed of thickness d, the characteristic relaxation times are given by

$$\tau_j^{-1} = (2j+1)^2 \pi^2 D/d^2 \tag{3}$$

where D is the thermal diffusivity of the material.

Using the result

$$F_j = 96/\pi^4 (2j+1)^4 \tag{4}$$

it is seen that the summation given in Eq. (1) converges very rapidly, and for comparison with experiment the precision of measurement does not warrant consideration of terms beyond the second. Hence, using Eqs. (1)–(4), the predicted internal friction arising from transverse thermal currents may be written as

$$\frac{\delta}{\pi} = \frac{E\alpha^2 T}{\rho S}\left\{0.986\frac{ff_0}{f_0^2+f^2} + 0.108\frac{ff_0}{81f_0^2+f^2}\right\} \tag{5}$$

where

$$f_0 = \pi D/2d^2. \tag{6}$$

The frequency f_0 is the predicted frequency of peak damping, and f is the frequency of vibration.

III. EXPERIMENTAL PROCEDURE

A. Apparatus and Specimens

Conditions of measurement were chosen so that other contributions to the internal friction were as small as possible. New apparatus was developed to secure a small and assessable external loss.[3] Specimens were suspended vertically from a specially designed piezoelectric pickup which served in turn to excite and detect transverse free-free vibrations, and internal friction measurements were made by the free-decay method. The method of frequency variation consisted of loading the specimens with weights.[3]

Due to the large range of f/f_0 values required in this investigation, four different specimens were employed (Table I). An α brass was used because the background damping at room temperature is known to be very small ($\delta \sim 5.10^{-6}$), and because the intercrystalline thermal current loss has been determined for this material.[4,5] The grain size of the specimens (0.05 mm) places the intercrystalline thermal current peak at 66 kc/sec, and the maximum contribution to the internal friction from this cause at the frequencies used here is less than 5.10^{-6}, which is trivial compared with the lowest internal friction reported here.

The brass used was free from lead and analyzed 62.5% Cu. Specimens were prepared from strip cut from sheet nominally 0.064 in. thick and of good surface finish. After a homogenizing anneal of 30 hr at 550°C, some of the strip was set aside for specimens 3 and 4, and the rest was cold rolled to the thickness of specimens 1 and 2. Specimens of $\frac{3}{8}$-in. width, uniform to approximately 0.001 in., were produced by clamping the strips between a pair of precision ground steel flats of $\frac{3}{8}$-in. thickness and then filing away the projecting edges of the strip. After being cut to length the specimens were given a final anneal of $2\frac{1}{2}$ hr at 550°C, and prior to use were polished to a bright surface finish.

B. Internal Friction Measurements

At pressures of 10^{-4} mm Hg, the only significant external energy loss was caused by the piezoelectric pickup. The correction to the internal friction for this loss was found experimentally under a wide variety of conditions, and these results were used to estimate the correction in cases where this was not determined experimentally. The corrections were greater for the thinner specimens (Nos. 1 and 2), and naturally were larger for lower internal friction. For example, the

[3] Rev. Sci. Instr., to be published.
[4] K. M. Entwistle, J. Inst. Metals **75**, 97 (1948).
[5] Randall, Rose, and Zener, Phys. Rev. **56**, 343 (1939).

correction was less than 3% for specimens 1 and 2 when the decrement was greater than 2×10^{-3}. The largest correction encountered (specimen 2 at 7 cy/sec and $\delta=0.67_5\times10^{-3}$) was 11% of the measured internal friction.

The error in the measurement of internal friction caused by the uncertainty in the correction for external loss was estimated to range from sensibly zero (in many cases) to a maximum of $\pm2\%$. Because absolute values of internal friction are required for the present investigation, this error must be added to the error of measurement, which is $\pm2\%$.

The logarithmic decrement was used as the measure of internal friction. This was determined from the frequency of vibration of the specimen and the time required for the amplitude of free vibration to fall to one half of a selected value. Measurements were made in the amplitude-independent range at a starting strain amplitude of 5.10^{-6}. The limits of room temperature during the course of the investigation were 19 and 24°C, but most measurements were made at 22±1°C. No difference was observed in the internal friction of a specimen when the polished surface became tarnished.

C. Measurement of Physical Properties

The modulus, expansion coefficient, and density were determined from the reeds used for the internal friction measurements. Other specimens were used for the specific heat and thermal diffusivity measurements, but these were made from the same sheet of material and given the same anneal as the internal friction specimens. Apart from the thermal diffusivity, which is given for a mean temperature of 70°C, the values of all the properties refer to 20–25°C.

Young's Modulus, E

Using the density given below, the modulus was found from resonant frequency measurements to be 1.06×10^{12} dynes/cm² ±0.5%. In calculating this result, account was taken of the small frequency correction arising from the constraint imposed on the specimen by the pickup from which it was suspended.

The Coefficient of Linear Expansion, α

The most rigid of the internal friction specimens (No. 3) was selected for this measurement. The specimen was held vertically by a number of horizontal cantilever supports attached to a main upright of silica. The lower end of the specimen rested on a silica bracket fused to the main upright, and a silica push-rod, held with other cantilever supports, rested on the top end of the specimen. A tilt-table carrying a plane galvanometer mirror straddled the upper ends of the main upright and push-rod, and this was used in conjunction with a scale and telescope for measuring the relative expansion of the specimen. The over-all magnification obtained was 1000. The mounted specimen was immersed in a water bath and measurements made in the range 0–45°C. Over this range a linear expansion behaviour was observed, and after correction for the expansion of the silica, the result

$$\alpha=18.7\times10^{-6}/°C\pm0.5\%$$

was obtained.

The Density, ρ

The density was obtained by the method of weighing in air and water, using the usual corrections. The result was

$$\rho=8.42\text{g/cc}\pm0.2\%.$$

The Specific Heat, S

The specimen used for this measurement was submerged in distilled water in a calorimeter containing a thermometer and heating coil. With the exception of the contribution from the specimen, the thermal capacity of the system was known. The thermal capacity (and hence the specific heat) of the specimen was determined from the temperature rise produced by the liberation of a known quantity of electrical energy in the calorimeter. The specimen itself was used as a stirrer, and for this purpose was constructed as a form of paddle wheel from a number of disks and strips cut from the 0.064-in. thick brass sheet used throughout this investigation. The specimen contained a central hole to receive the bulb of a 5°C Beckmann thermometer, and was suspended by glass rods from the stationary cover of the calorimeter. Stirring was obtained by revolving the calorimeter itself on a turntable. The heating coil was wrapped round the specimen in the manner to give the greatest dispersion of heat, and measurements were made over a range of a few degrees centered on the current room temperature. The resistance of the coil and the heating current were measured potentiometrically. The Beckmann thermometer was calibrated for the immersion depth used against a platinum resistance thermometer. The mean value obtained for the specific heat was

$$S=0.088\text{cal/g/}°C\pm2\%.$$

The Thermal Diffusivity, D

This property may be calculated from the relation

$$D=\frac{K}{\rho S}, \tag{7}$$

where K is the thermal conductivity, However, the difficulty of obtaining an accurate value for K prompted the direct determination of D by Angström's method.[6,7] A servomechanism was built for the production of sinusoidal temperature oscillations at one end of a strip 1.3 cm wide and 76 cm long. The period of oscillation

[6] A. J. Angström, Phil. Mag. **25**, 130 (1863).
[7] P. H. Sidles and G. E. Danielson, J. Appl. Phys. **25**, 58 (1954).

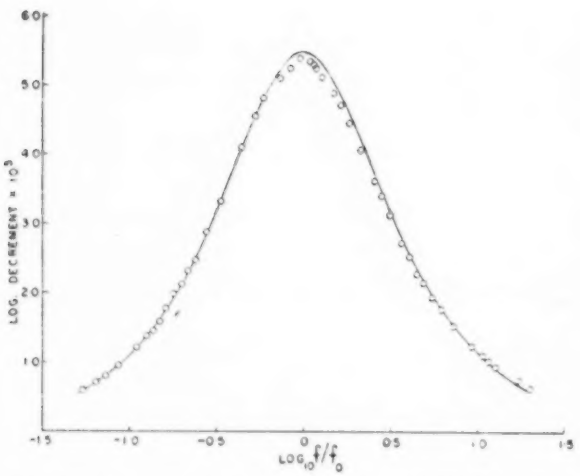

FIG. 1. Frequency-dependence of internal friction of four annealed α brass reeds. Actual frequencies f are divided by the frequency of peak damping f_0. The curve is given by theory with no arbitrary parameters.

was adjustable in the range 14–26 min. The specimen was suspended in still air and, after a stationary state had been established, the temperature oscillations at two points A and B a known distance l apart were observed by means of small thermocouples brazed to the specimen. The diffusivity was calculated from the equation[7]

$$D=l^2/2t \ln\theta_A/\theta_B$$

where t=the time lag for the appearance of a temperature maximum at B after one at A. θ_A, θ_B=the amplitudes of the temperature oscillations at A and B. (Note: $\theta_A>\theta_B$.) The mean result of three runs, $D=0.34$ cm²/sec ±5%, applies to a mean temperature of 70°C. Correction of this result to room temperature was considered unnecessary.

IV. RESULTS AND DISCUSSION

To combine the results obtained from specimens 1–4, internal friction is shown plotted in Fig. 1 as a function of $\log_{10}f/f_0$ where f is the frequency of vibration and f_0 the predicted frequency of peak damping. Because a peak was observed in specimen 1 only, it was assumed with Zener that f_0 varies inversely as the square of the specimen thickness, and this relationship, which does not involve the proportionality constant $\pi D/2$ of Eq. (6), was used in the calculation of f_0 for each of the other three specimens. The validity of the inverse square relationship is seen from the fact that the overlapping results from all four specimens fall on a smooth curve. Thus, a complete verification of Eq. (6) was obtained by comparison of the experimentally determined diffusivity (0.34 cm²/sec ±5%) with that calculated from the position of the peak, namely 0.346 cm²/sec ±1.5%.

Using the experimentally determined values of the physical properties, the relaxation strength given by Eq. (2) follows as 0.00355±2.3% probable error, and the theoretical frequency dependence of damping, calculated from Eq. (5), is shown by the full line in Fig. 1. The experimental points in Fig. 1 have been corrected for external energy loss. It will be seen, especially round the peak where differences are most noticeable, that the experimental points fall about 2% below the theoretical curve. As the probable error in the measurement of internal friction is ±2% (most often) and in the relaxation strength is ±2.3%, this difference is within experimental error and it was concluded that Zener's theory of damping by transverse thermal currents is probably valid exactly.

It may be noted that nonuniformity of specimen thickness would cause a decrease in the height and a broadening of the peak. However, variations in the thicknesses of the specimens used were so small that this effect was expected to be negligible. The uniqueness of the relaxation times obtained from a specimen of uniform thickness, together with the fact that the strength and position of the peak are calculable completely, would seem to make this source of internal friction the most nearly perfect example of anelasticity yet reported.

That some internal friction peaks obtained as a function of temperature can be used to obtain useful information about rates of atomic movements is well known. The counterpart of this information which is given by the transverse thermal current peak is the thermal diffusion constant D. Two advantages arise from the measurement of D by this method. First, the measurement is made at a virtually constant temperature, and secondly the accuracy of measurement is high. Finally, if the specific heat and density of the material are known also, Eq. (7) may be used to calculate the thermal conductivity K. In the present case the calculated value of K is 0.256 cal/cm²/sec/°C/cm, within a probable error of ±2.5%.

ACKNOWLEDGMENTS

Thanks are expressed to Professor F. C. Thompson and Dr. K. M. Entwistle for their help and encouragement, and to Mr. Peter Roberts and Mr. A. G. Todd for undertaking the measurement of thermal diffusivity.

Hysteresis Effect in Multiplier Phototube Noise

C. A. ZIEGLER AND H. H. SELIGER
National Bureau of Standards, Washington, D. C.
(Received April 18, 1955)

A hysteresis effect in multiplier phototube noise as a function of tube gain has been found for both RCA 5819 and DuMont 6292 tubes. The effect is a function of both temperature and the length of time that a tube has "rested." The hysteresis is seen to be a noise buildup with time but not a change in dynode multiplication. The reasons for this effect are not clear. Several possible mechanisms are discussed. Conditions are determined for obtaining reproducible noise counts for liquid scintillation counting of low-energy beta emitters.

INTRODUCTION

A HYSTERESIS effect in multiplier phototube noise as a function of tube gain has been found for both RCA 5819 and DuMont 6292 tubes. The effect is readily observable under conditions of high phototube gain and high external amplifier gain (20 000) necessary for liquid scintillation counting of low-energy beta emitters such as C^{14} and H^3. The effect is sometimes masked at room temperature by excessive noise due possibly to cesium vapor molecules.[1] However at 0°C, the temperature at which most of the present measurements have been made, the vapor pressure of the cesium molecules is apparently negligible and the total noise is greatly reduced.

MEASUREMENTS

The multiplier phototube voltage-noise hysteresis effect is shown in Fig. 1. Measurements were made as follows. At point *A* the negative high voltage was applied to the phototube and readings of noise count rate *versus* phototube voltage were taken to point *B*, the entire process requiring 5–10 minutes. At point *B* the voltage was held fixed for a period of 1–2 hours, during which the counting rate increased to a maximum at *C*. Then readings of noise count rate *versus* decreasing phototube voltage were taken to point *D*, the initial voltage. The phototube voltage was then reduced to zero and the tube permitted to "rest" for several hours. Upon reapplication of phototube voltage the curve *ABCD* was able to be reproduced. The length of the portion *BC* depended upon the time required to proceed from *A* to *B*. However, point *A* and the portion *CD* were quantitatively precise for any given tube. If now instead of reducing the phototube voltage to zero from point *D* the voltage is permitted to remain constant at 1000 v for several hours, it is possible to obtain the closed loop *DEF*. The portion *DE* corresponds to *AB*, *EF* corresponds to *BC* and, of course, *FD* is just part of the larger reproducible curve *CD*. Thus it is not necessary to reduce the voltage to zero in order to obtain the hysteresis loop. This effect was found to be independent of the voltage on external shields surrounding the phototube. In all cases the phototube voltage was monitored to 5 significant figures and the temperature inside of the refrigerator which contained the phototube and its cathode follower preamplifier was constant to ±1°C.

In Fig. 2 the noise counting rate is plotted as a function of time for several phototube voltages applied after the phototube had "rested" for one hour. In each case a plateau region is reached after approximately one hour. The initial and the final counting rates are very reproducible. However, there was a variation in the initial rise of the plateau curves at any particular voltage, depending upon the length of time that the tube had "rested." The variations in the buildup of noise with "resting time" are shown in Fig. 3 where the "resting time," Δt, had been varied from 5 minutes to 99 hours. The data were taken at 0°C with a constant phototube voltage of −1100 volts. Both 5819 and 6292 tubes exhibited the same qualitative features.

In addition to the variation of these approximately exponential rises in phototube noise with Δt there is a dependence upon the phototube temperature, as shown in Fig. 4. The data again were taken with constant phototube voltage. The tremendous increase in tube noise at +10°C is again probably due to ionized cesium molecules.

In order to determine whether this effect was a change in tube gain in the ordinary sense of increased

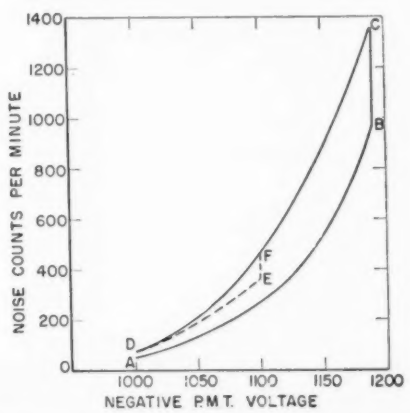

FIG. 1. Noise as a function of negative PMT voltage at constant external amplifier gain for a representative 6292 PMT.

[1] D. J. Rosenthal and H. O. Anger, Rev. Sci. Instr. **25**, 670 (1954). (Both 5819 and 6292 PMT's have Cs–Sb photocathodes.)

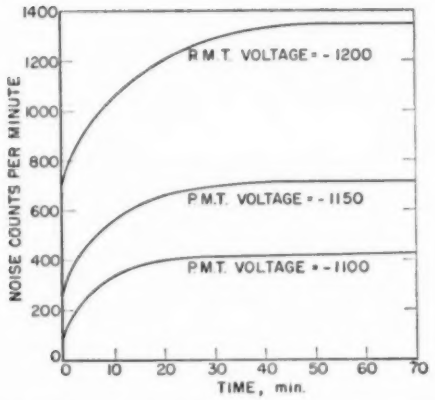

FIG. 2. PMT noise as a function of time at constant PMT voltage and external amplifier gain.

dynode multiplication the measurements were repeated with an anthracene crystal atop the phototube and an external $Cs^{137}-Ba^{137}$ γ-ray source. The phototube voltage was held at the same values as before while the external amplifier gain was reduced until the integral discrimination curve due to light pulses from the anthracene crystal had the same shape as the original noise discrimination curve. The integral discriminator was then set on the far steep side of the discrimination curve. Since the pulses coming from the amplifier were unsaturated, this position was most sensitive to changes in tube gain due to changes in dynode multiplication. No changes in observed counting rate with time were found. The counting rate was constant and reproducible. Next the measurements were repeated with a lower intensity source of γ rays and at the same phototube voltage and high amplifier gain settings as in the noise measurements. No increase in observed counting rate with time over that due to noise buildup was found. As a final check, a very tiny light leak was made in the refrigerator so that the counting-rate at high phototube voltage and high external amplifier gain was increased by a factor of approximately 10. Still no increase in observed counting rate with time over that due to the original noise buildup was found. It was found that when the phototube itself is placed in a γ-ray field the observed counting rate is increased. However, the data become erratic and for some reason no longer follow a Poisson distribution. Therefore, for all other experiments with a γ-ray source, the phototube was shielded by lead from the direct γ radiation.

DISCUSSION

Of a total of 6 DuMont 6292 and 3 RCA 5819 tubes tested only 1 of each type did not exhibit the noise buildup with time. These however were excessively noisy and were not considered as good counting tubes under any conditions. The fact that the time buildup is present only for tube noise and is completely absent for pulses due to light leads to the conclusion that the effect is associated with the very low-energy thermal or field-emission electrons emitted by the photocathode or with positive ion feedback. The additional fact that the effect is present only with high external amplifier gain further strengthens this view. The distribution of pulse heights due to noise in a multiplier phototube measured by Morton and Mitchell[2] indicates that noise pulses are due mainly to the emission of 1–3 electrons from the photocathode so that a high amplifier gain is necessary in order that these be detected.

The buildup of the tube noise with time is approximately exponential. When the data of Fig. 3 are fitted to an expression of the form

$$y=B+A(1-e^{-t/\tau}) \quad (1)$$

the time constant τ appears to be a slowly varying function of the "resting-time," Δt. This dependence is shown in Fig. 5 where τ is plotted as a function of Δt. The empirical relation in this range appears to be

$$\tau=4.7\Delta t^{0.21} \text{ min.} \quad (2)$$

Although B, A, and τ vary with the temperature as shown in Fig. 4, it was not possible to determine the functional temperature dependence. Above 0°C the noise was complicated by the cesium vapor molecules and below −15°C the noise was so low that the counting statistics became very poor and the effect became very small. However, it can be seen that while B and A decrease with decreasing temperature, τ appears to increase.

Several possible explanations for this effect have occurred to us. Some can be wholly discounted on the basis of the experimental results, while parts of others have some degree of plausibility. The effect is not due to ionization of residual gases in the multiplier phototube. The possibility that the effect is caused by a heating of the photocathode by the power dissipation in the phototube bleeder chain can be discounted.

Another line of reasoning was that the noise electrons, being thermal in energy and having an isotropic angular distribution might therefore show preferred directions for collection because of slight changes in the focusing

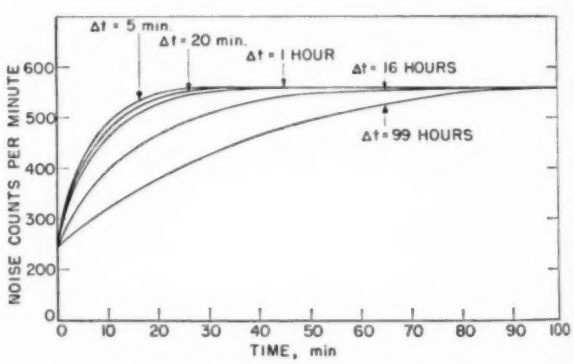

FIG. 3. PMT noise as a function of time for various "resting-times" at constant PMT voltage andex ternal amplifier gain.

[2] G. A. Morton and J. A. Mitchell, Nucleonics 4, No. 1, 16 (1949).

field with time. The angular distribution of the photoelectrons as conditioned by the experimental arrangement might have been such that the effect was absent for the photoelectrons. To test this, light pulses from the anthracene were collimated and caused to impinge on the photocathode at various angles with the plane of the photocathode from normal to approximately 80° from normal. The fact that the photoelectrons have approximately 1 ev of energy as compared with the thermal energies of the noise electrons is not too important since the photocathode-first dynode potential difference is approximately 150 volts. No increase in observed counting rate with time as in the case of the noise buildup was observed at any angle of incidence.

Dr. L. Marton pointed out to us that these effects have the same general form as the Malter effect[3] of delayed field emission and the self-sustained field emission observed by Dobischek, Jacobs, and Freely.[4] The interpretation given by Malter was that because of the high resistivity of the oxide layer a positive charge was built up which set up sufficiently intense field gradients to cause field emission. The secondary emission was found to vary with the primary bombarding current and to decrease with increasing temperature. Malter found that the effect was unstable and not reproducible. Our time-buildup effect, however, does not appear to be dependent upon the phototube counting rate; it decreases markedly with *decreasing* temperature and apparently is quite consistent and reproducible.

The time constants of the self-sustained field emission observed by Dobischek, Jacobs, and Greely for MgO films are of the same order of magnitude as the τ's observed in the present noise buildup measurements. They postulated that the origin of the electrons which initiate the self-sustained emission is a photoelectric effect from the quanta emitted as a result of the recombination of positive ions and electrons in the film. However, if this mechanism were valid to explain our own results, we should again have observed a buildup proportional to the counting rate, since positive ions are produced in the photocathode as the result of the photoelectric process.

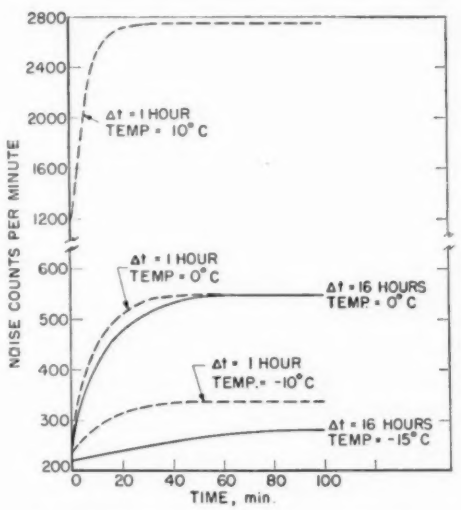

FIG. 4. PMT noise as a function of time for various operating temperatures and "resting-times." The PMT voltage and the external amplifier gain were constant.

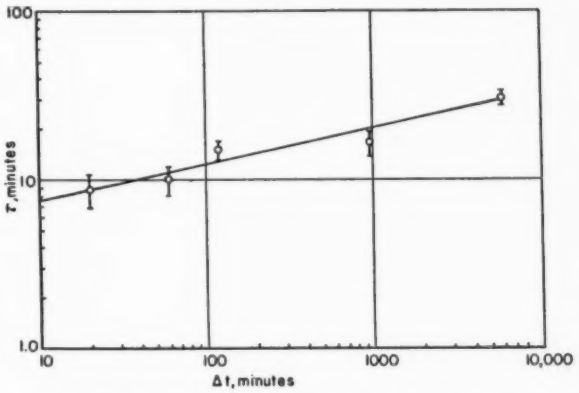

FIG. 5. Data showing dependence of the buildup time-constant, τ, on the "resting-time," Δt.

Finally, the long time-constants observed are compatible with the time-constants in the buildup of space charge effects in colored alkali-halide crystals.[5] It is possible for impurity centers or for cesium or antimony ions in the photocathode to exhibit a slow "flow" upon application of a field between the photocathode and first dynode. This change in charge distribution could alter the depths of surface energy levels in such a way as to make thermal escape more probable. Alternatively the accumulation of charges at thin layers could produce field gradients intense enough to cause field emission. A rapid recombination of positive ions and electrons upon removal of the external field is to be expected and could explain the rapid recovery of the phototube even after short Δt's.

Of practical significance in the counting of low-energy beta emitters by liquid scintillation counting, and especially in those cases where the multiplier phototube noise is an appreciable fraction of the "true" counting rate, the conditions under which noise can be accurately reproduced have been determined. The time required for buildup of noise varies with the voltage, the previous "resting time" and the temperature at which the tube is operated. However, for any particular tube, these factors are seen to have a reproducible effect and provision can be made for obtaining precise noise counting rates.

ACKNOWLEDGMENTS

The authors thank Dr. R. G. Breckenridge and Dr. L. Marton for their helpful comments as to the nature of these effects.

[3] L. Malter, Phys. Rev. **50**, 48 (1936).
[4] Dobischek, Jacobs, and Freely, Phys. Rev. **91**, 804 (1953).
[5] Von Hippel, Gross, Jelatis, and Geller, MIT Technical Report 59, 1953.

On Electron Mirror Microscopy

LUDWIG MAYER
*Electronic Components Laboratory, Wright Air Development Center, Wright-Patterson Air Force Base, Ohio**
(Received May 27, 1955)

This paper deals with a new kind of electron microscopy in which the specimen constitutes an electron mirror. The low velocity of the electrons in front of this mirror-specimen enables pictorial representations of potential distributions on surfaces. A resolving power comparable to that of the light microscope has been obtained. Sample micrographs depicting surface reliefs, potential distributions on surfaces, and the distribution of electrical conductivity are shown. The peculiar kind of image formation is briefly discussed and reference is made to the potentialities of such a research tool for surface physics and metallurgy.

A METHOD for obtaining pictorial representation of an electron beam by its own space charge has previously been reported by the author.[1] This electron optical image of an electron beam was actually a by-product of a more general investigation directed toward electron micrographs of potential distributions on surfaces. It is felt that a brief interim report on this work might be in order pointing out the potentialities of this kind of microscopy. Application of the underlying principle[2–4] has led to a new kind of electron microscopy with a resolving power already comparable to that of the light microscope and capable of depicting the distribution of such purely electrical properties as contact potential, surface charge, conductivity and, of course, also of any geometrical profile on the surface.[5]

The essential feature of this kind of microscopy is the use of slow electrons, achieved by utilizing the microscopic specimen as an electron mirror. The axial velocity of the electrons is slowed down to zero in front of the mirror-specimen. Any irregularity of the potential surfaces in front of the mirror acts like an inhomogeneity in the refractive index, which influence rapidly decreases with increasing distance from the mirror. The returning electron beam therefore carries a kind of electron optical schlieren-picture of the potential distribution in front of the mirror-specimen.

The electron mirror microscope used and the schematic of it is shown in Fig. 1. Originating from a modified Steigerwald electron gun *G*,[6] the illuminating electron beam is shot through a small neck *N* in the center of the viewing luminescent screen *S*. After traversing the electron optical system *EO*, the electron beam is reflected on the potential surfaces in front of the specimen *M*, which is generally a few tenths of a volt negative with respect to the cathode and acts therefore as an electron optical mirror. Every irregularity of the potential surfaces in front of the mirror (be it caused by differences in contact potential, by differences in surface charge, by differences in conductivity, or simply by the geometrical relief on the mirror) influences the low velocity electron beam and the electrons returning through the electron optics *EO* project a magnified pictorial representation of the potential distribution in front of the specimen *M* onto the viewing screen *S*.

The voltages used for this experimental model ranged from 7 kv to 35 kv. The electrostatic lens *EO* was a combination of a cathode lens with an einzel-lens similar to one described by A. Septier[7] for an emission type electron microscope. The specimen holder *MH* was constructed to permit movement in direction of the axis and also in the plane perpendicular to it. Tilting of the specimen could also be accomplished by the same mechanism.

Figures 2 to 5 are a few samples of micrographs one obtains with this kind of microscope. (The dark shadow extending from the center of the pictures to the right is the electron gun protruding from the center of the viewing screen.) Figure 2 is the electron mirror micrograph of a polished stellite disk onto which gold has been evaporated through a 200-mesh-per-inch net to a thickness of less than 200 A. The white rimmed squares are the gold spots. The fact that these spots are distinguishable from their surrounding is due to actual potential differences on the surface. Their geometrical elevation is too small to be resolved in this case; this has been proven by evaporating gold spots of the same thickness on gold. The cause of the potential differences will not be discussed here; their interpretation is often difficult. Not only an effective difference in contact potential, but also differences in surface conductivities can result in potential differences because electrons from the tail end of the Maxwell distribution as well as ions impinge on the surface of the specimen. In addition to the gold squares the crystalline structure of the alloy is also made visible by this method. Figure

* Now with Mechanical Division of General Mills, Inc., Minneapolis, Minnesota.

[1] Ludwig J. Mayer, J. Appl. Phys. **24**, 105 (1953).

[2] G. Hottenroth, Ann. Physik **30**, 689 (1937).

[3] Fiat Review of German Science, Electronics, 100 (1948).

[4] R. Orthuber, Z. angew. Phys. **1**, 79 (1948).

[5] The referee of this paper has informed the author that a paper is presently in print under the title of "Ein auflichtelektronenmikroskop" by G. Bartz, G. Weissenberg, and D. Wiskott reporting substantially the same results. This paper will appear as a part of the Proceedings of the International Conference on Electron Microscopy in London. The referee also stated that V. S. Vavilov deals with a related subject in the J. Tech. Phys. (U.S.S.R.) **22**, 10, 1644 (1952).

[6] H. H. Steigerwald, Optik **5**, 469 (1949).

[7] A. Septier, Ann. radioélec. compagne. franç. assoc. T.S.F. **9**, 1 (1954).

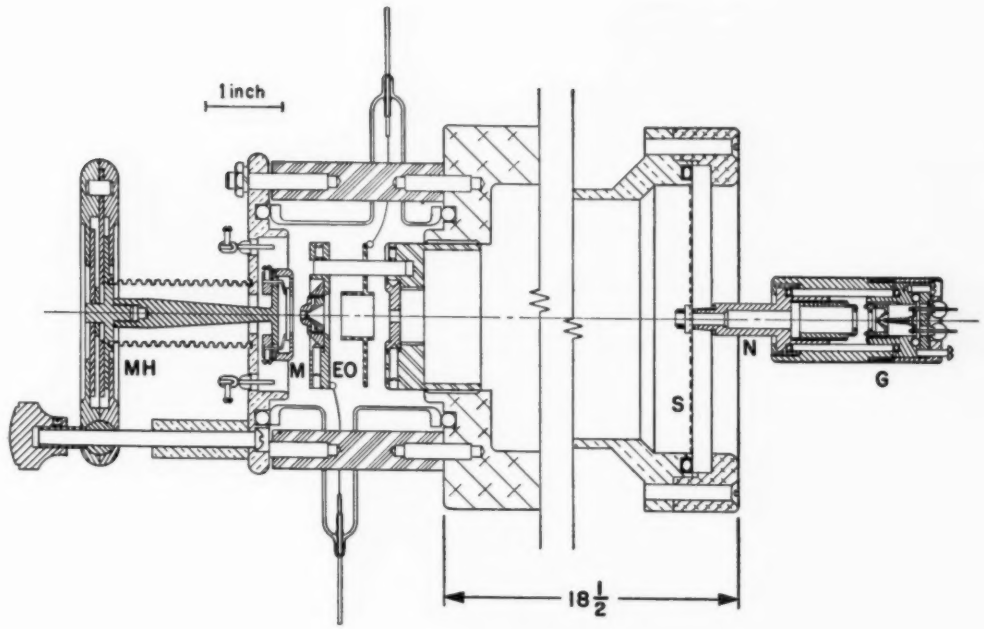

FIG. 1. Cross section of the electron mirror microscope.

3 is included in order to show the resolving power obtained at present. It is a micrograph of a polished chromium surface onto which gold has been evaporated, this time through a 300-mesh-per-inch net. Besides the white rimmed dark spots, separated by 1/300 of an inch and representing the gold spots, fine lines caused by polishing scratches are also visible. Their profile is, of course, also represented in the potential relief in front of the specimen and they are therefore, although not electrical in origin, depicted on the screen. They permit a rough estimate of the resolving power obtained at present. From Fig. 4, which is a sixfold photographic enlargement of the encircled part of Fig. 3, one can estimate that two points separated 0.3μ can be resolved. This is a resolving power comparable to that of the light microscope. Experimentally there are strong indications that this will not be the limit. In fact, nothing has been done with the particular aim to increase the resolving power. The ratio of obtainable magnification to granulation of the luminescent screen is for the time being the limiting factor. No effort has as yet been devoted to align the electron optical system very accurately, to minimize aberration, nor was the center electrode of the einzel-lens grounded or the voltage source stabilized.

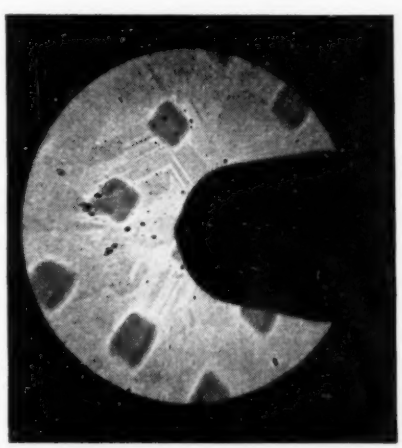

FIG. 2. Electron mirror micrograph of gold on stellite. Electron optical magnification approximately 200. Photographic reduction, 2.

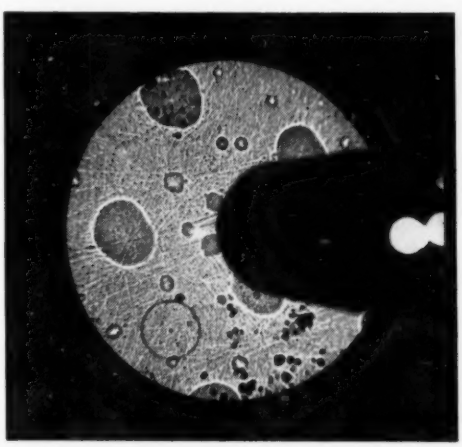

FIG. 3. Electron mirror micrograph of gold on chromium. Electron optical magnification approximately 470. Photographic reduction, 2.

What the theoretical limit of the resolving power for this kind of image formation will be is not yet quite clear, but there is no apparent reason why it should be less than that attributed to the emission type electron microscope. (See e.g., A. Septier.[8])

Figure 5 is included to demonstrate the possibility of obtaining micrographs of the distribution of con-

[8] A. Septier, J. phys. radium **15**, 573 (1954).

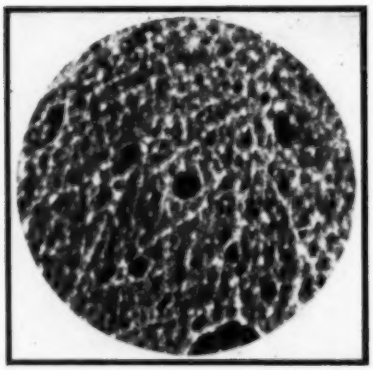

FIG. 4. Encircled part of Fig. 3. Photographic magnification 6. (Electron optical magnification times photographic magnification approximately 1400.) Points separated by a distance of 1/2 mm are approximately 0.35μ apart.

ductivity in thin films. The specimen used was a sample with an artificially created periodic distribution of conductivity. The sample was prepared by evaporating gold through a 200-mesh-per-inch net onto a polished glass disk. Then a germanium film was evaporated onto the entire disk until an average surface conductivity of about 0.5 μmho was reached. In a normal electron mirror micrograph of this specimen the gold squares beneath the germanium are not visible. However, if an electric current is passed through the specimen the gold squares show up because of the lower area conductivity at their location. They appear elevated against their surroundings and as if illuminated from the side where the negative voltage is applied (Fig. 5). If the direction of the current is reversed, the apparent illumination of the hills is of course also reversed. In addition, there is an electron optical tilting of the specimen plane caused by the average voltage drop across the specimen, which results in a shift of the viewing area in the direction opposite to the current flow.

Because of the peculiar kind of image formation, care must be taken in the interpretation of electron mirror micrographs. The potential relief in front of the mirror is the actual image forming medium. Optically speaking it represents a medium of changing refractive index with inhomogeneities in front of an irregular electron reflecting surface. This irregular reflecting surface in connection with the inhomogeneous refracting medium forms the image. The image is in fact the electron density distribution of the caustic of these two inhomogeneities in the plane of the luminescent screen. The amount of the small negative bias of the mirror against the cathode determines how far the electrons penetrate into the potential relief in front of the mirror specimen and which potential surface will become the reflecting one. This potential relief rapidly loses its detail and its refracting influence on the electron beam with increasing distance from the mirror. The closer the electrons are permitted to penetrate toward the mirror-specimen the more detailed the image formed by the potential relief will be. One is, of course, inclined to bias the mirror for obtaining the most detailed image, i.e. in such a way that the focal points of those focusing irregularities which represent the fine details fall into the plane of the luminescent screen. Hence, focusing is at present accomplished by applying proper bias to the mirror rather than by adjusting the voltages of the electron lenses. At present, therefore, these lenses provide mainly the desired magnification and are not properly used as focusing elements in the meaning of the Gaussian dioptrics. This requires, of course, that the electrical as well as geometrical roughness of the specimen be rather uniform within the viewing area. This is a disadvantage in this kind of electron microscopy. The rather high field strength in front of the specimen is another disadvantage. However, as has been shown here very briefly, the potentialities of this kind of mirror microscopy are great and one can visualize many applications. Taking into account that what has been reported here is just an early beginning, it appears justified to expect that electron mirror microscopy may become a useful research tool in surface physics in general, and in metallurgy in particular.

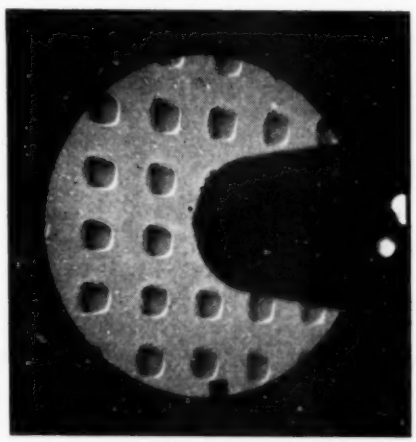

FIG. 5. Electron mirror micrograph of artificial periodic distribution of conductivity. Electron optical magnification approximately 130. Photographic reduction, 2.

ACKNOWLEDGMENTS

The author would like to express his sincere thanks to Mr. Werner Jehn for the construction of the microscope and his very helpful suggestions in the design of it.

JOURNAL OF APPLIED PHYSICS VOLUME 26, NUMBER 10 OCTOBER, 1955

On Representation of Electromagnetic Fields in Cavities in Terms of Natural Modes of Oscillation

S. A. SCHELKUNOFF
Bell Telephone Laboratories, Inc., Murray Hill, New Jersey
(Received April 28, 1955)

In this paper we illustrate by a simple example that when we wish to express the admittance of a cavity excited through a hole in terms of natural frequencies of oscillations which can exist when the cavity is short-circuited, it is important to remember that the short-circuit must conform to the impressed field. When this is done, one need not fear that the "obvious" set of natural modes may be incomplete.

IN a fairly recent paper[1] Teichmann and Wigner stated: "It seems to have been generally assumed that the short-circuit modes of the junction, regarded as a closed cavity, form a complete set with respect to an arbitrary admissible electromagnetic field (excited by the wave-guide fields through the openings). While these modes can indeed be made basic to any such expansion, they are not complete. Instead, it is necessary to add an irrotational magnetic field; similarly, in the case of open-circuit modes (i.e., modes satisfying the boundary condition $n\times H=0$ on S) it is necessary to add an irrotational electric field in order to permit expansion of the relevant fields. Since these facts do not appear to be widely known, this paper is intended to elucidate them and to estimate the effect of the additional filed on the admittance matrix." The contribution of the allegedly missing term to the input admittance is proportional to ω^{-1}, where ω is the angular frequency.

While it appears to be true that in references cited in the above-mentioned paper the term proportional to ω^{-1} is missing, there are other references in which this term is included.[2] One objective of this paper is to call attention to this fact and give a clean bill of health to some previously published formulas for the admittance of cavities.

But the major objective is to correct a widely held assumption that when a cavity is "short-circuited," one mode is automatically suppressed so that the remaining modes are insufficient for representing the field which had existed before the short-circuiting took place. As we shall see, this assumption is due apparently to a misunderstanding of what is meant by "short-circuit." It was during a discussion of our paper on "Generalized Telegraphist's Equations"[3] in which we expressed the fields in dissipative wave guides and horns in terms of modes appropriate to wave guides of uniform cross section and with perfectly conducting boundaries, that the question was raised about the completeness of this set of modes under altered boundary conditions. At that time Dr. W. K. Saunders called our attention to the above-mentioned paper since the situations appeared to be similar.

We also wish to point out that the use of the adjective "irrotational" in connection with the "dc mode," that is the mode proportional to ω^{-1}, may be misleading since it seems to set it apart from other modes. While Teichmann and Wigner derive this mode from a gradient of a scalar function, thus implying magnetic charges over the aperture, we can also obtain it from electric currents which can flow in the aperture when the aperture is short-circuited. As a matter of fact, there is no way in which one could distinguish between "rotational" and "irrotational" static fields in *limited source-free regions*.

In some instances the appearance of natural modes proportional to ω^{-1} is easy to understand. Thus in a dipole with open terminals there is a static electric mode due to the equal and opposite charges on the two arms of the dipole. The contribution of this mode to the impedance of the dipole is $1/j\omega C$, where C is the capacitance of the dipole. In the case of electric networks the presence of such a mode was long recognized.[4] And after all shielded networks are cavities with one set of natural frequencies relatively close to zero and another set very far away. Similarly the admittance of a pair of parallel wires short-circuited at the far end CD, Fig. 1, as seen across AB in terms of the short-circuit modes, will involve a term corresponding to a static mode in which steady current flows in the loop $ACDBA$. The magnetic field associated with this current is obviously rotational. However, in the case of closed cavities with holes, considered by Teichmann and Wigner, it may seem that no such mode exists when the holes are short-circuited.

So let us now consider a cavity with a hole. The

FIG. 1. A section of a two-wire transmission line.

[1] T. Teichmann and E. P. Wigner, J. Appl. Phys. **24**, 262–267 (1953).

[2] S. A. Schelkunoff, *Electromagnetic Waves* (D. Van Nostrand Company, Inc., New York, 1943), p. 123; also Proc. Inst. Radio Engrs. **32**, 83–90 (1944).

[3] S. A. Schelkunoff, "Solution of field problems with the aid of distributed circuit parameter concepts," presented at a joint meeting of the International Scientific Radio Union, the Institute of Radio Engineers, and American Geophysical Union, May 4, 1954, Washington, D. C.

[4] R. M. Foster, Bell System Tech. J. (1924).

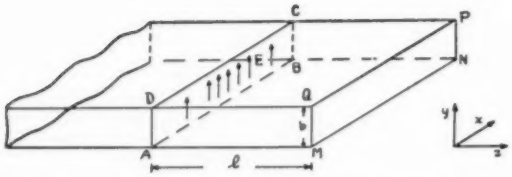

FIG. 2. A rectangular wave guide supporting a TE_{10} wave.

following simple example from Slater's book[5] was suggested to us by Dr. E. T. Jaynes. This example was used by him to demonstrate that some formulas for the admittance are inadequate. We shall find, however, that our formula (see reference 2) is adequate. Thus let us consider a TE_{10} mode in a rectangular wave guide shorted at one end, Fig. 2. Our first problem is to express the admittance looking to the right from the plane $ABCD$ in terms of natural frequencies of the cavity $ABCDMNPQ$, shorted at both ends. The same problem arises when we wish to find a similar

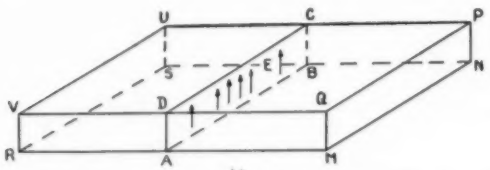

FIG. 3. A cavity excited in the middle plane by a field conforming to the TE_{10} mode.

expression for the admittance looking from the central plane of a closed cavity either to the right or to the left, when excited by a sinusoidally distributed electric field conforming to the pattern of the TE_{10} mode, Fig. 3.

One expression for the required admittance is[2]

$$Y(j\omega)=\sum\frac{j\omega}{2\mathcal{E}_n(\omega_n^2-\omega^2)}, \tag{1}$$

where $\mathcal{E}_n$ is the energy stored in the cavity at the nth natural frequency when the input terminals are short-circuited and when the current amplitude at these terminals is unity. When applying this formula to the present problem we have do decide what is meant by "short-circuiting the terminals." Do we mean replacing the plane $ABCD$ by an *isotropic* perfect conductor? The answer is certainly, no. This kind of short-circuit would be too drastic. In fact, it would not permit us to distinguish between fields conforming to the TE_{10} mode, Fig. 3, and fields conforming to the TE_{01}, Fig. 4. The short-circuit must be only vertical. The current distribution in the surface $ABCD$ covering the input hole must be constrained to conform to the field of the TE_{10} mode. Then it becomes obvious that we have a dc mode with steady loop current similar to that in a section of a transmission line, Fig. 1, or in a cavity in which the input terminals are shorted by a rod AB, Fig. 5. If this mode is not included, then one must compensate for the omission, as was done by Teichmann and Wigner, by inserting a term corresponding to a certain irrotational field due to magnetic charge distributions over the holes.

Let us now exhibit the solution. First, we have the well-known set of modes corresponding to the non-vanishing natural frequencies

$$E_y=A_n\sin(\pi x/a)\sin(n\pi z/l),$$

$$H_x=\frac{n\pi A_n}{j\omega_n\mu l}\sin(\pi x/a)\cos(n\pi z/l),$$

$$H_z=-\frac{\pi A_n}{j\omega_n\mu_a}\cos(\pi x/a)\cos(n\pi z/l), \tag{2}$$

$$\omega_n(\mu\epsilon)^{\frac{1}{2}}=\left(\frac{\pi^2}{a^2}+\frac{n^2\pi^2}{l^2}\right)^{\frac{1}{2}},$$

where $n=1, 2, 3,\cdots$. These modes are the same for *isotropic* perfectly conducting boundary $ABCD$ and for the boundary which is perfectly conducting only in the vertical direction. To obtain the dc natural mode in the latter case we have to solve

$$\frac{\partial H_x}{\partial z}-\frac{\partial H_z}{\partial x}=0,\quad \frac{\partial H_x}{\partial x}+\frac{\partial H_z}{\partial z}=0,\quad H_z(x,l)=0, \tag{3}$$

subject to the condition $H_x\propto\sin(\pi x/a)$. The solution

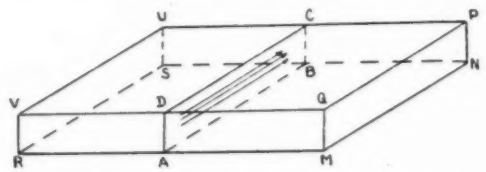

FIG. 4. A cavity excited in the middle plane by a field conforming to the TE_{01} mode.

is

$$H_x=A_0\sin\frac{\pi x}{a}\cosh\frac{\pi(l-z)}{a},$$

$$H_z=A_0\cos\frac{\pi x}{a}\sinh\frac{\pi(l-z)}{a}. \tag{4}$$

If we desire the admittance with reference to power and the longitudinal current entering the cavity across AB,[6]

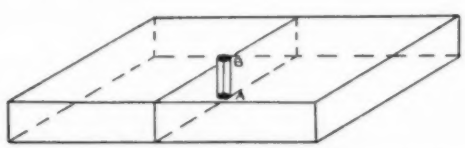

FIG. 5. A cavity with input terminals A, B shorted by a wire.

[5] J. C. Slater, *Microwave Electronics* (D. Van Nostrand Company, Inc., New York), p. 82.

[6] See reference 2, p. 319.

then

$$\mathcal{E}_0=\tfrac{1}{16}\mu\pi b\tanh(\pi l/a),\quad \mathcal{E}_n=\frac{\mu^2\epsilon\omega_n{}^2bl^3}{32n^2a},\tag{5}$$

and Eq. (1) yields

$$Y(j\omega)=\frac{8}{j\omega\mu\pi b}\coth(\pi l/a)+\sum_{n=1}^{\infty}\frac{j\omega 16n^2a}{\omega_n{}^2\mu^2\epsilon bl^3(\omega_n{}^2-\omega^2)}.\tag{6}$$

On the other hand, solving the problem of forced oscillations directly, we find

$$Y(j\omega)=\frac{8\Gamma_a}{j\omega\mu\pi^2b}\coth\Gamma l,\quad \Gamma=\left(\frac{\pi^2}{a^2}-\frac{4\pi^2}{\lambda^2}\right)^{\frac{1}{2}}.\tag{7}$$

Expanding this function of ω in the Mittag-Leffler series of partial fractions with the aid of residues, we verify Eq. (6).

From Eqs. (2), (4), and (6) we can obtain the expressions for the field in the cavity. First we note the following relation between the wave admittance Y_1, defined as the ratio of transverse field components, and the admittance Y, defined on the power current basis,[6]

$$Y_1(j\omega)\equiv-\frac{H_x(x,0)}{E_y(x,0)}=\frac{\pi^2b}{8a}Y(j\omega).\tag{8}$$

Hence, if $E_y(x,0)=E_0\sin(\pi x/a)$, then

$$H_x(x,0)=-E_0\sin\frac{\pi x}{a}\left[\frac{\pi}{j\omega\mu a}\cot\frac{\pi l}{a}+\sum_{n=1}^{\infty}\frac{j\omega 2n^2\pi^2}{\omega_n{}^2\mu^2\epsilon l^3(\omega_n{}^2-\omega^2)}\right].\tag{9}$$

Since the individual terms correspond to the natural modes, we have the following continuation of $H_x(x,0)$ into the cavity

$$H_x(x,z)=-E_0\sin\frac{\pi x}{a}\left[\frac{\pi\cosh[\pi(l-z)/a]}{j\omega\mu a\sinh(\pi l/a)}+\sum_{n=1}^{\infty}\frac{j\omega 2n^2\pi^2\cos(n\pi z/l)}{\omega_n{}^2\mu^2\epsilon l^3(\omega_n{}^2-\omega^2)}\right].\tag{10}$$

In order to obtain E_y we should either expand the first term of the above expression in the cosine series and then use Eqs. (2) for converting H_x into E_y, or use one of the following relations between H_x and E_y,

$$\frac{\partial E_y}{\partial z}=j\omega\mu H_x,\quad \frac{\partial H_x}{\partial z}=\left(j\omega\epsilon+\frac{\pi^2}{j\omega\mu a^2}\right)E_y.\tag{11}$$

These equations are obtained from Maxwell's equations by eliminating H_z and taking into account the particular dependence on x in the present case. Substituting from (10) into the first equation of the set (11) and integrating from $z=l$ to $z=z$, we find

$$E_y(x,z)=E_0\sin\frac{\pi x}{a}\left[\frac{\sinh[\pi(l-z)/a]}{\sinh(\pi l/a)}+\sum_{n=1}^{\infty}\frac{\omega^2 2n\pi\sin(n\pi z/l)}{\omega_n{}^2\mu\epsilon l^2(\omega_n{}^2-\omega^2)}\right].\tag{12}$$

It must be conceded that the above approach to our problem is rather unconventional. Just for comparison let us consider another approach in which we must indeed include a term which makes sense mathematically but is quite odd from the physical point of view. We are going to solve Eqs. (11) subject to the following boundary conditions

$$E_y(x,0)=E_0\sin(\pi x/a),\quad E_y(x,l)=0.\tag{13}$$

We shall seek that particular form of the solution which forms to the field distributions appropriate to natural oscillations with both ends of the cavity shorted, so that $E_y(x,0)=E_y(x,l)=0$. This time we shall not include the dc mode. Hence, we shall represent E_y by a sine series and H_y by a cosine series,

$$E_y=\sin(\pi x/a)\sum A_n\sin(n\pi z/l),\quad 0<z\leq l,\quad n=1,2,3,\cdots;$$
$$H_x=\sin(\pi x/a)\sum B_n\cos(n\pi z/l),\quad 0\leq z\leq l,\quad n=0,1,2,\cdots.\tag{14}$$

It is to be noted that due to the nature of sine functions it is impossible to express E_y by such a series when $z=0$. But the representation is possible in the open interval indicated above. It is also clear that we must include in the cosine series for H_x a term independent of z since the average value of H_x along a typical line $x=$const does not, in general, vanish. But we can hardly interpret the corresponding term as a "natural mode." The corresponding field is: $E_y=0$, $H_z=0$, $H_x=B_0e^{j\omega t}\times\sin(\pi x/a)$. It can be generated only by a continuous distribution of magnetic charge in the cavity. Separately from the rest of the series, these expressions do not satisfy Eqs. (11). From the theory of Fourier series we know, however, that expansions (14) exist, and, in the present case, we can actually obtain the coefficients A_n, B_n from the usual solution of (11) for forced oscillations. But here we shall find these coefficients directly from Eqs. (11). The above series for E_y represents a function discontinuous at $z=0$. Hence, as n increases indefinitely, A_n will vary asymptotically as $1/n$. The series, therefore, cannot be differentiated and we cannot substitute it in the first equation of the set (11) in order to relate A_n's to B_n's. This substitution is not necessary, however. Let us substitute only the series for H_x and then integrate from $z=0$ to $z=l$. Thus we shall find

$$-E_0=j\omega\mu lB_0,\quad B_0=-E_0/j\omega\mu l.\tag{15}$$

Next let us multiply both sides of the first equation in (11) by $\cos(n\pi z/l)$ and integrate from $z=0$ to $z=l$,

$$\int_0^l \frac{\partial E_y}{\partial z} \cos\frac{n\pi z}{l} dz = j\omega\mu \int_0^l H_x \cos\frac{n\pi z}{l} dz. \quad (16)$$

Integrating the left side by parts, we have

$$E_y \cos\frac{n\pi z}{l}\Big|_0^l + \int_0^l \frac{n\pi}{l} E_y \sin\frac{n\pi z}{l} dz = j\omega\mu \int_0^l H_x \cos\frac{n\pi z}{l} dz. \quad (17)$$

Now we shall substitute from (14), integrate, and obtain

$$-E_0 + \frac{n\pi}{2} A_n = \tfrac{1}{2} j\omega\mu l B_n. \quad (18)$$

It should be noted that the series for E_y does not converge uniformly at $z=0$ since it represents a function which is discontinuous there. It is known that uniformly convergent series may be integrated term by term. However, the uniform convergence is only a sufficient condition for integrability and not a necessary one. In the present case we may integrate from $z=\delta$ to $z=l$ where the series is uniformly convergent and then let δ approach zero.

Similarly we find

$$-\frac{n\pi}{l} B_n = \left(j\omega\epsilon + \frac{\pi^2}{j\omega\mu a^2}\right) A_n. \quad (19)$$

Solving (18) and (19), we have

$$A_n = \frac{2n\pi E_0}{l^2(\omega_n^2 - \omega^2)\mu\epsilon}, \quad B_n = \frac{2[\omega^2\mu\epsilon - (\pi/a)^2]E_0}{j\omega\mu l(\omega_n^2 - \omega^2)\mu\epsilon}. \quad (20)$$

Substituting B_n's in (14) and noting that $E_y(x,0)=E_0$, we find the following expression for the wave admittance,

$$Y_1 = -\frac{H_x(x,0)}{E_y(x,0)} = \frac{1}{j\omega\mu l} + \sum_{n=1}^{\infty} \frac{2[(\pi/a)^2 - \omega^2\mu\epsilon]}{j\omega\mu l(\omega_n^2 - \omega^2)\mu\epsilon}. \quad (21)$$

To compare it with the corresponding formula given by (8) and (6), we separate B_n into two partial fractions

$$B_n = -\frac{2\pi^2 E_0}{j\omega\mu l\omega_n^2\mu\epsilon a^2} - \frac{j\omega 2n^2\pi^2 E_0}{\omega_n^2\mu^2\epsilon l^3(\omega_n^2 - \omega^2)}. \quad (22)$$

The sum of the series formed by the first components of B_n's and the first term in (21) happens to be expressible in terms of the hyperbolic cotangent. Thus (21) becomes

$$Y_1 = \frac{\pi}{j\omega\mu a} \coth\frac{\pi l}{a} + \sum_{n=1}^{\infty} \frac{j\omega 2n^2\pi^2}{\omega_n^2\mu^2\epsilon l^3(\omega_n^2 - \omega^2)}. \quad (23)$$

Similarly we can transform (14) into (10) and (12) and vice versa. Series (10) and (12) converge more rapidly than (14).

Coming back to the Teichmann-Wigner conclusion about the fields in cavities with holes, we feel that it is too strong and needs some qualifications even though the mathematical formulas are undoubtedly correct. In a special but representative case we have actually obtained the admittance (6) and the magnetic field (10) by considering the natural modes satisfying the condition $E\times n=0$. We concede, however, that the dc mode may be easily overlooked because one may inadvertently substitute isotropic short-circuiting of the holes for the required nonisotropic short-circuiting. While the condition $E\times n=0$ is satisfied by the natural modes for the appropriate natural frequencies, the expression (12) for the forced oscillations does not satisfy it. And, of course, it is known *ab initio* that in the case of forced oscillations the tangential component in the input aperture does not vanish, in general. Nevertheless, this does not mean that the electric field *in the interior* of a cavity cannot be expressed in terms of only those modes which satisfy the condition $E\times n=0$ everywhere. Equation (14) is an example.

The situation remains essentially the same in the case of cavities with one or more small holes. There will exist expansions similar to (10) and (12) in which there will be terms corresponding to the first terms in (10) and (12) and representing the principal coupling between holes at very low frequencies. This coupling is similar to that between two loosely coupled coils.

JOURNAL OF APPLIED PHYSICS VOLUME 26, NUMBER 10 OCTOBER, 1955

Spatial Distribution of Thermal Neutrons from a Polonium-Beryllium Source in Water-Zirconium Mixtures*

WILLIAM BAER
Westinghouse Electric Corporation, Bettis Field, Pittsburgh 30, Pennsylvania
(Received December 31, 1954; revised manuscript received June 13, 1955)

The spatial distribution of neutrons emitted by a Po–Be source and moderated by water-zirconium mixtures has been measured for four water-zirconium volume ratios. From these data, migration areas of source neutrons to energies below the cadmium cutoff have been determined with an uncertainty of ±2%. The experimental values of the migration area M^2 are:

Zr/H_2O ratio	$M^2(cm^2)$
0.00	69.6
0.25	81.3
0.50	89.7
1.00	112.8

INTRODUCTION

ZIRCONIUM has been used extensively as a structural material in water moderated nuclear reactors, and it is therefore of interest to measure spatial distributions of thermal neutrons in H_2O–Zr mixtures. Such an experiment has been performed using Po–Be source neutrons. Few reliable theoretical estimates of neutron slowing down in metal-water mixtures are available, because only a small number of measurements of inelastic scattering cross sections and angular distributions in elastic scattering of neutrons have been made.

EXPERIMENTAL PROCEDURE

The neutron source was placed in an aluminum tank 50 cm wide×100 cm long×50 cm deep. The tank was made of $\frac{1}{16}$-inch thick aluminum and shielded with a 0.020-inch thick cadmium sheet on the outside. The water level in the tank was kept at 40 cm throughout the course of the experiment. The source was suspended on a polystyrene rod 25 cm from one end of the tank, so that its center was 20 cm from the surface of the water and 25 cm from the sides of the tank. The Po–Be source used was a standard source obtained from the U. S. Atomic Energy Commission, and is a right circular nickel cylinder 0.70 inch in diameter and 0.70 inch high. The source emitted 5.1×10^7 neutrons/sec and contained 21.90 curies of polonium at the start of the experiment.

Data were taken along the center line of the tank parallel to the 100 cm dimension at the midplane of the water. Spatial distributions were measured in water and zirconium/water mixtures with volume ratios of 1:4, 1:2, and 1:1. The zirconium used in the experiment was crystal bar in its rough shape with rod diameters varying from $\frac{1}{2}$ inch to $\frac{3}{4}$ inch. The rods were positioned vertically with axes normal to the 100 cm face of the tank. A typical spectroscopic analysis of the crystal bar showed 0.04 weight percent hafnium, and total impurities amounting to 0.09 weight percent.

Metal-to-water ratios higher than 1:1 were not obtainable due to the irregularities of the crystal bar, and the resultant impossibility of closer rod packing. All metal-to-water volume ratios were determined by measuring the volume of the water displaced by the zirconium rods which were placed in the tank.

The neutron detector used was a small BF_3 proportional counter $\frac{1}{4}$ inch in diameter and 1 inch long, filled to one atmosphere of BF_3 enriched to 96% in the B^{10} isotope. Pulses from the counter were amplified by an Atomic Instrument Company 206-A cathode follower and 204-C amplifier. With this amplifying system, the detector had a plateau of approximately 100 volts and operated at 1875 volts. Operation in the water tank was achieved by sealing the counter in a thin aluminum cylinder. The counter was shielded electrically from the cylinder by a polyethylene jacket, and a coaxial signal and high voltage cable ran through the aluminum tube inside the polyethylene shield.

EXPERIMENTAL RESULTS

The mean square slowing down length for neutrons of energy E in a given medium may be written as

$$\langle r^2\rangle=\frac{\int_v \varphi(E)r^2dV}{\int_v \varphi(E)dV} \tag{1}$$

where $\varphi(E)$ is the flux of neutrons of energy E. Hence, if the spatial distribution of neutrons of energy E is measured, it is possible to calculate $\langle r^2\rangle$. Since the counting rate, C, of the detector is proportional to neutron flux (assuming a response to neutrons of energy E only), then changing to spherical co-ordinates,

$$\langle r^2\rangle=\frac{4\pi\int_0^\infty Cr^4dr}{4\pi\int_0^\infty Cr^2dr}. \tag{2}$$

*This investigation was conducted under Contract AT-11-1-GEN-14 with the U. S. Atomic Energy Commission.

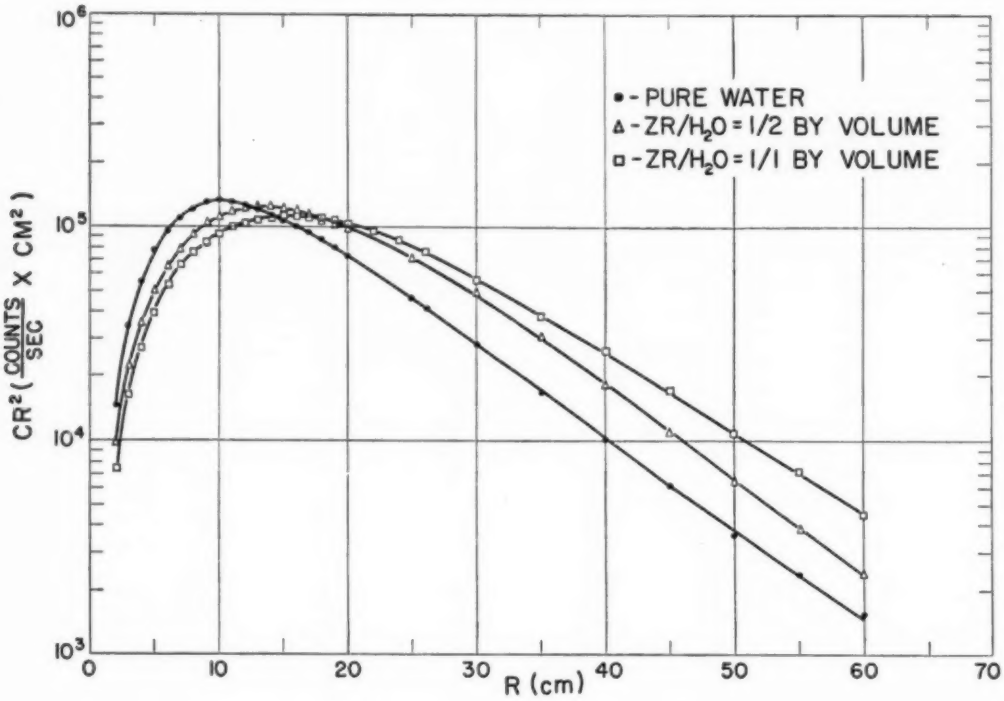

FIG. 1. Spatial distribution of thermal neutrons in water and zirconium-water mixtures.

A quantity called the migration area, M^2, can be defined as

$$M^2=\frac{\langle r^2\rangle}{6} \tag{3}$$

where $\langle r^2\rangle$ is the mean square distance a neutron travels from birth to capture in the thermal energy range.[1]

In this experiment, data were taken with the counter bare or cadmium shielded, and the difference between these two counting rates used to determine the net counting rate C in (2). A 0.020-inch thick cadmium shield was used, and cadmium ratios of the order of 40/1 were observed. No significant differences in the distributions with and without the cadmium cover were observed. B^{10} is a $1/v$ absorber, and the $\langle r^2\rangle$ determined is therefore not representative of slowing down to a single neutron energy, but rather it represents the slowing down to and subsequent diffusion in a broad energy band below the cadmium cutoff.

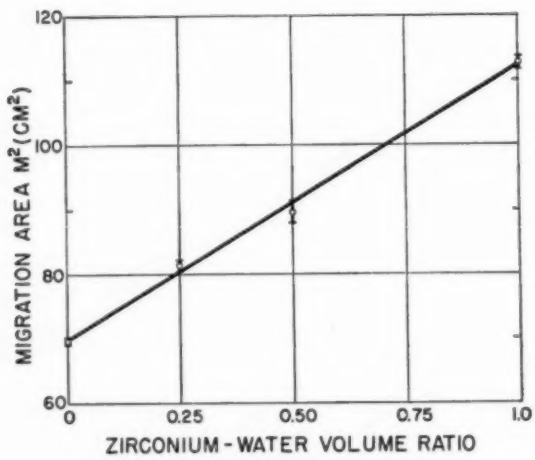

FIG. 2. Migration area as a function of zirconium-water volume ratio.

In interpreting the M^2 measured it is assumed that the neutron source is effectively a point source emitting neutrons isotropically, and that the walls of the tank are effectively at infinity. No source anisotropy was detected which was not within the most probable counting rate deviation of $\pm 2\%$. The effect of wall scattering was investigated by moving the tank from the middle of a large room to a position against the walls of the room. No change in the shape of the slowing down distribution was found. Because of the large and varied size of the zirconium rods, and the random spacing between rods, it might be expected that the neutron distribution would be affected by the disorder in the array. An attempt was made to observe such an effect by rearranging the zirconium rods surrounding a fixed position of the counter in a 1:2 volume ratio of zirconium/water. Again, no change in counting rate was observed that was not within the most probable counting rate deviation of $\pm 2\%$.

In Fig. 1 are shown typical spatial distributions, Cr^2 *vs* r, for pure water, and zirconium/water volume ratios of 1:2 and 1:1. These data have been normalized to account for source decay during the course of the experiment.

[1] S. Glasstone and M. C. Edlund, *The Elements of Nuclear Reactor Theory*, (D. Van Nostrand Company, Inc., New York, 1952), Chap. vii.

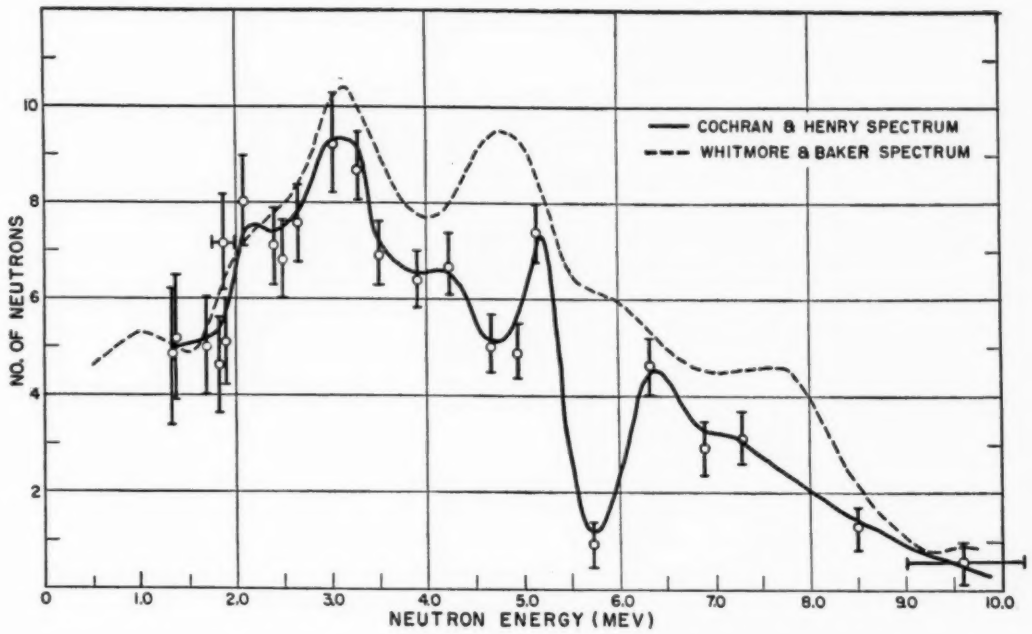

FIG. 3. Po–Be neutron source spectrum.

Values of the migration area, M^2, calculated by numerical integration of the spatial distributions, are shown in Fig. 2, where M^2 is plotted as a function of the zirconium/water volume ratio. The uncertainties indicated are due to counting statistics and the finite distance over which data were taken. Numerical integration of the area under the curves was made to 60 cm. Beyond that point, an exponential falling off of the curve to infinity was assumed, and the remainder of the area was determined analytically. Values of the extrapolation constant λ are given in Table I. The extrapolation added from 0.6% (for pure water) to 1.7% (for 1:1 Zr/H_2O) to the areas under the Cr^2 *vs* r curves, and they contribute an uncertainty in the values of M^2 of from 1.0% to 1.8%.

DISCUSSION OF RESULTS

Comparison of experimental values of M^2 with results of other investigators is possible only for the pure water case. Spinks and Graham[2] report $M^2=58.5$ cm², but recently R. H. Graham and co-workers[3] have found $M^2=64.7$ cm². In addition, R. H. Graham has re-evaluated Spinks' data and obtained a value of $M^2=66.0$ cm².

Theoretical comparisons with these results are made more difficult since the experimental technique measures a quantity which includes both the mean square slowing down length and the thermal diffusion area. If the neutron source spectrum and scattering cross sections are known, then it is possible to calculate the mean square slowing down length rigorously in all cases. However, calculation of the thermal diffusion area for metal-water mixtures is not amenable to such treatment at this time.

The experimental value of M^2 obtained for pure water has been compared with a theoretical value by calculation of the second moment of the slowing down distribution, assuming a value of 8.1 cm² for the thermal diffusion area.[4] This calculation was made using the Marshak formula,[5] by treating the oxygen scattering as both isotropic and elastic in the laboratory system. If the neutron spectrum of the Po–Be source reported by Whitmore and Baker[6] is used in this calculation, a value of $M^2=67.6$ cm² is obtained. The spectrum of the source used in this experiment has been measured by Cochran and Henry[7] and is shown in Fig. 3. The distribution reported by Whitmore and Baker is given for comparison. Using the spectrum determined by Cochran and Henry in the calculation, the migration area is found to be 60.9 cm². Since differences in energy spectra of Po–Be sources of the same construction have been observed,[7] the disagreement between the two neutron energy distributions of Fig. 3 is not surprising. The low theoretical value of M^2 is presumed to be

TABLE I. Extrapolation constants.

Zr/H_2O ratio	Extrapolation constant λ (cm^{-1})
0	0.097±0.007
0.25	0.092±0.007
0.5	0.103±0.010
1.0	0.089±0.006

[2] V. W. T. Spinks and G. A. R. Graham, Can. J. Research **28A**, 60 (1950).
[3] R. H. Graham, private communication.
[4] D. J. Hughes, *Pile Neutron Research* (Addison-Wesley Press, Inc., Cambridge, 1953), p. 223.
[5] R. E. Marshak, Revs. Modern Phys. **19**, 209 (1947).
[6] B. G. Whitmore and W. B. Baker, Phys. Rev. **78**, 799 (1950).
[7] R. G. Cochran and K. M. Henry, unpublished report ORNL-1479.

largely due to the anisotropy in the forward direction[8] of neutron scattering from oxygen, which would tend to raise the calculated value of M^2. However, the neutron energy degradation accompanying oxygen scattering tends very largely to compensate this effect.

CONCLUSIONS

The migration areas of neutrons emitted by a Po–Be neutron source moderated by water-zirconium mixtures have been measured experimentally, with an uncertainty of $\pm 2\%$. Comparison of these results with work by other investigators is difficult, since the neutron source spectrum is unique for each experiment.

[8] Baldinger, Huber, and Proctor, Helv. Phys. Acta **25**, 142 (1952).

ACKNOWLEDGMENTS

The author is indebted to Mr. A. G. McElroy, who designed and built the BF_3 counter used in the experiment, and obtained the data reported above. The assistance of Mr. John J. Taylor, who suggested the problem to the author, made the theoretical calculations of the migration area, and contributed many helpful discussions throughout this work, is gratefully acknowledged. Dr. R. L. Hellens contributed valuable advice and criticism in the preparation of the manuscript. Thanks are also due to Dr. R. G. Cochran and Dr. K. M. Henry of the Oak Ridge National Laboratory, who determined the neutron spectrum of the source used in the experiment.

JOURNAL OF APPLIED PHYSICS VOLUME 26, NUMBER 10 OCTOBER, 1955

Outgassing of Glass

B. JOHNSON TODD
Corning Glass Works, Corning, New York
(Received May 17, 1955)

The gas evolved from glass at temperatures below the softening point, which is of interest in bake-out problems, is primarily water. The water evolved from unit surface at constant temperature above 300°C is linear with respect to the square root of the time of bake-out. The intercept of the linear plot, which can be altered by different surface treatments, is a measure of the easily removed water residing at the surface. The slope is a measure of the rate of evolution of water that has diffused to the surface from the interior.

Values of the diffusion constant for water and concentration gradients after bake-out have been calculated for a soda-lime glass. The diffusion constant is an exponential function of the reciprocal of the absolute bake-out temperature. Values of the activation energy for the diffusion process are given for eight glasses.

A method of calculating the amount of water that will diffuse from glass for any time-temperature conditions following any bake-out is presented.

I. INTRODUCTION

THE work of other investigators[1,2] has established that when glass is heated in a vacuum a rapid evolution of gas (primarily water) occurs upon first heating, followed by an evolution which becomes increasingly persistent as the bake-out temperature approaches the softening point of the glass. The major part of the initial evolution has been attributed to gases held on the surface; the persistent evolution at higher temperatures has been attributed to diffusion from the interior. These earlier data afford no adequate means of separation of these two outgassing processes. Also, it is impossible to predict from the data, except in a very general way, the outgassing characteristics of a glass after some arbitrary bake-out.

The present results confirm the above mechanism of outgassing, and they permit differentiation between the water residing at the surface and that which diffuses from the glass interior. The differentiation is based on the observation that the persistent evolution at the higher temperatures is proportional to the square root of the bake-out time. Since the surface gases are rapidly and completely removed at these temperatures, the water diffusion process is of primary importance with regard to the pressure rise in a baked-out glass envelope. The temperature dependence of the water diffusion rate from several glasses has been determined. From these results one can calculate the amount of water that will be evolved from glass for any time-temperature conditions following any bake-out in which the surface gases have been removed.

[1] R. G. Sherwood, Phys. Rev. **12**, 448 (1918).
[2] J. E. Harris and E. E. Schumacher, Bell System Tech. J. **2**, 122 (1923).

II. APPARATUS AND METHOD

A schematic diagram of the apparatus used in this work is shown in Fig. 1. The gas volumes are determined by measuring the pressure in a known volume. The volumes between cut-off points in the system, indicated by dashed lines, are calibrated by using the McLeod gauge as a gas buret. Water vapor pressures are measured with the Pirani gauge. Pressures of other gases are measured with the McLeod gauge. The Pirani gauge is

calibrated for water using the McLeod gauge with a steam heated jacket. The PV unit used throughout is micron (Hg)-liters at 25°C.

In general, the following procedure is used for measuring the outgassing rate. A sample whose surface area can be calculated from its shape is placed in the fused quartz container. These samples are usually in the shape of tubing or cane, but some work has been done with granular samples prepared according to the method of Berger, Geffcken, and v. Stoffert.[3] They present equations which allow the surface area of a granular sample to be calculated provided certain precautions in crushing and sieving the sample are observed.

The system is evacuated, both oil and mercury diffusion pumps running, and the system (except the container) is torched until the outgassing from the sample at room temperature is slight. At this point the mercury cutoff $C3$ is closed, liquid nitrogen is placed around trap $T2$, and a preheated furnace is placed around the sample. Blank measurements have shown that outgassing from the container alone is negligible. Condensable gases evolved from the glass are trapped in $T2$, while the permanent gases are pumped by the mercury pump into the volume bounded by the jet of the pump and $C3$. At the end of the first time interval, mercury cutoff $C1$ is closed, and liquid nitrogen is placed around trap $T1$. The outgassing for the second time interval proceeds while measurements on the gases evolved in the first interval are made. Since 95% or more of the gases are condensable, the pressure in the sample container remains low.

The permanent gas pressure is read on the McLeod gauge, and these gases, primarily CO and NO, are then pumped out. The liquid nitrogen bath around $T2$ is replaced with a dry ice-alcohol slush, and the gases which evaporate, primarily CO_2, are pumped over by the mercury pump and their pressure read on the McLeod gauge. The transfer of these gases is carried out in about one minute so as not to remove an appreciable amount of the water, which has a vapor pressure of 0.6 micron at −78.5°C. After discarding the CO_2 fraction, the mercury pump is turned off and cooled. The system is then ready for measurement of the water fraction. The dry ice-alcohol slush is removed from $T2$ and is replaced with a warm water bath. This quickly evaporates the water, but the water is rapidly adsorbed on the dry walls of the system. For this reason readings of the Pirani gauge are taken as a function of time, and the value obtained by extrapolating to the time of evaporation is taken as the water vapor pressure. After the water measurement the system is torched-out, and the gases which have accumulated in $T1$ are transferred for similar measurement.

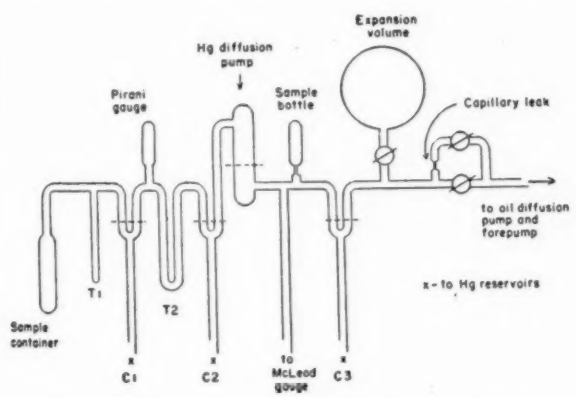

FIG. 1. Schematic diagram of the apparatus used for measuring the outgassing rate of glass.

[3] Berger, Geffcken, and v. Stoffert, Glastechn. Ber. **13**, 301 (1935).

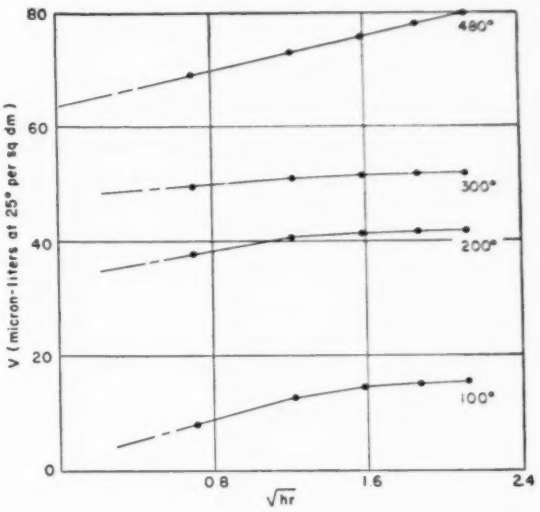

FIG. 2. No. 0080 glass. (V *vs* square root of bake-out time.)

Sample bottles located as shown in Fig. 1 are used to take samples of the three gas fractions for mass spectrometer analysis. The bottles are sealed to the system with a constriction in order that they can be tipped off. The tops are constructed in such a way that they can be broken open in vacuum on the mass spectrometer sample system.

The two liter expansion volume is useful in keeping large water volumes within the range of the Pirani gauge. The capillary leak is used as a flowmeter[1] for water volumes which are too large even when the expansion volume is used.

III. OUTGASSING OF NO. 0080 GLASS[4]

In all of the experiments reported here the bake-out temperatures are low enough so that the apparent surface area of the glass is not changed. Thus the amount of gas evolved depends on the extent of the sample surface, and the volumes, V, are given in micron (Hg)-liters at 25° per square decimeter of glass surface. Three micron (Hg)-liters per sq dm are comparable to the

[4] No. 0080 is the Corning Glass Works code number for one of its soda-lime glasses. Other glasses discussed are also referred to by the Corning code number, and a correlation of code numbers and glass types is given in Table I.

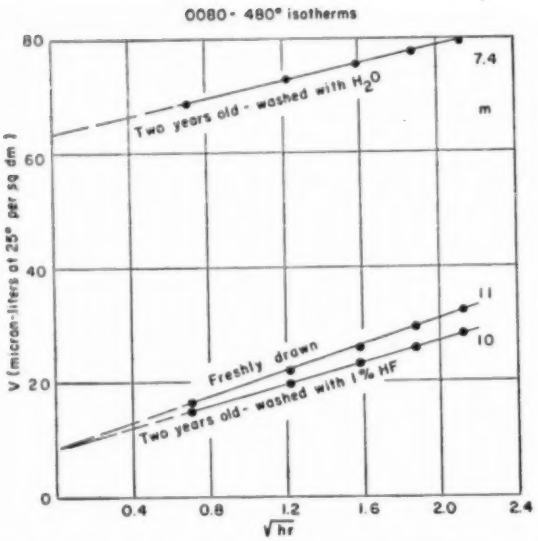

FIG. 3. Comparison of old and new No. 0080 glass and old No. 0080 glass washed with 1% HF at a bake-out temperature of 480°C. (V *vs* square root of bake-out time.)

water contained in a unimolecular adsorbed water layer.

The four isotherms of Fig. 2 show the water evolved from No. 0080[4] glass tubing as a function of the square root of the bake-out time. A separate sample was used for each of the bake-out temperatures. The samples were lengths of 8 mm. o.d. tubing, about two years old, and were cleaned by washing with water, acetone, and drying in air. In 4.5 hours at 100°, 200°, 300°, and 480°C, water was, respectively, 100%, 99.7%, 98.6%, and 98.2% of the total gas evolved. In general, water represents such a major part of the evolved gas that only the water volumes are reported in this paper.

In Fig. 3 the 480° isotherm of the water washed sample is compared with the 480° isotherms for the same two year old glass washed with 1% HF for 3 minutes and for No. 0080 glass installed in the sample container one-half hour after the tubing was drawn.

The water evolution at 480° can be expressed by the equation,

$$V = mt^{\frac{1}{2}} + s, \tag{1}$$

where V is the water evolved per unit surface, t is the time of bake-out, and m and s are constants. The solution of Fick's law for diffusion into a vacuum from a semi-infinite body of a solute with initial uniform concentration C_0 and diffusion constant D is given by

$$V = 2C_0(Dt)^{\frac{1}{2}}/\pi^{\frac{1}{2}}, \tag{2}$$

where V is the volume lost per unit surface, and t is the time the diffusion has been proceeding. The similarity between the above two equations suggests that the water evolution at 480°, after a rapid initial burst of gas of volume equal to the intercept s, is a diffusion process. The slope m of the isotherm then is given by

$$m = 2C_0D^{\frac{1}{2}}/\pi^{\frac{1}{2}} = 1.13C_0D^{\frac{1}{2}}. \tag{3}$$

The evolution at the lower temperatures does not follow the square root law, so some mechanism other than diffusion is predominant at these temperatures. The facts that the amount of water evolved at these temperatures increases with ageing of the glass, and that the gas sources can be largely removed by a 1% HF wash which mildly attacks the glass surface indicate that these gases reside at the surface, probably in the form of a layer of hydrates. The 100°, 200°, and 300° isotherms of Fig. 2 appear to be approaching different limiting values. This indicates that the hydrate layer must be complex in structure, since if only a single molecular species were involved, these isotherms would approach the same limit at different rates.

These considerations lead to the conclusion that the intercept s of Eq. (1) is a measure of the gases released from the surface hydrate layer. The HF wash of the older glass decreased s to a value comparable to that for the freshly drawn glass, leaving m relatively unchanged. Other reagents such as HCl, H_2SO_4, NH_4OH, NaOH, all 2.5 molar solutions, and the usual chromic acid cleaning solution were used to clean the glass. None of these showed any effect on s or m. The value of s can be greatly increased, leaving m unchanged, by storing the glass in contact with an atmosphere of 100% relative humidity at 90°C.

The dependence of m on temperature for this glass was determined by obtaining m's for HF washed samples at five temperatures. The isotherms are given in Fig. 4, where the s values are clustered together. When m is plotted on a logarithmic scale against the reciprocal of the absolute temperature (see Fig. 5) a straight line is obtained. Since m is proportional to the square root of the diffusion constant, the activation energy ΔH_a for the diffusion process is obtained from this plot using the expression,

$$\Delta H_a = 2 \times 2.303 \times RA, \tag{4}$$

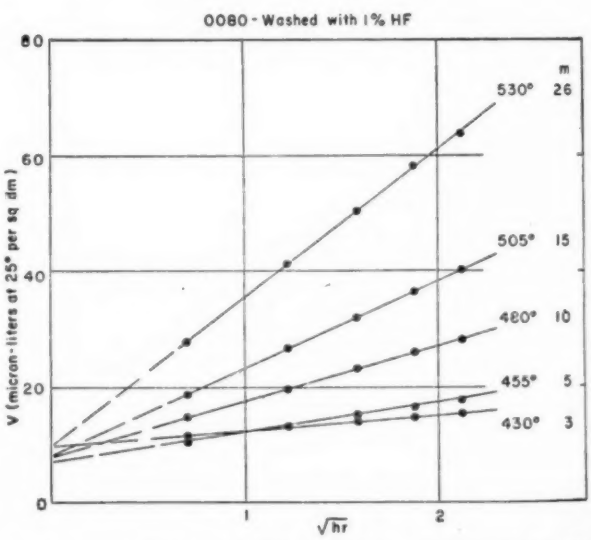

FIG. 4. Determination of m at different temperatures for No. 0080 glass. (V *vs* square root of bake-out time.)

where A is the absolute value of the slope of the line, and R is the gas constant. ΔH_a for No. 0080 glass is 50 kcal/mole.

IV. RESULTS WITH OTHER GLASSES

The temperature dependence of m for some other Corning Glass Works glasses is shown in Fig. 6. The glass code numbers and corresponding glass types are listed in Table I.

The Nos. 0080, 7740, 7910, and 7911 samples were in the form of tubing, while the others were granular samples. The granular samples give results consistent with those using tubing or cane except in the case of the Vycor brand 96% silica glasses, Nos. 7910 and 7911. The process[5] for the 96% silica glasses produces a glass with a water concentration gradient along a cross section, a situation not obtained with conventionally melted glasses. Because of the low water concentration near the surface with a higher concentration in the

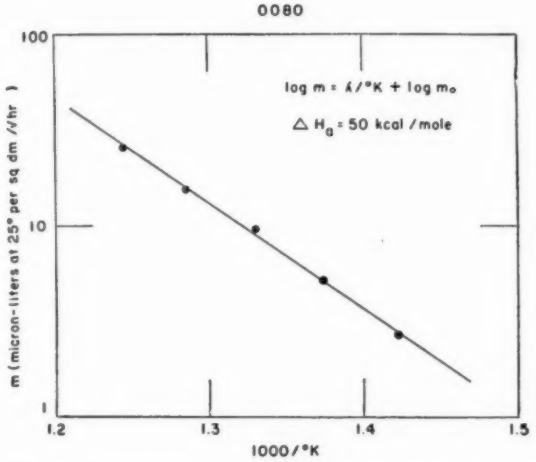

FIG. 5. Temperature dependence of m for No. 0080 glass. (m *vs* reciprocal temperature.)

middle of a cross section, the 96% silica glass tubing samples give a lower m than the granular samples prepared by crushing the glass. Glass No. 7911 is a vacuum-fired product, and it is unique in that the permanent gas evolution is comparable to the very low water evolution.

In general, the plots of V against $\sqrt{t}$ from which the m values were computed are quite linear over the five hour observation period with the exception of the 96% silica glasses and No. 9014. In the case of the 96% silica glasses the plots tend to be slightly concave towards the V axis. This could be the result of the concentration gradient existing in the glass when the outgassing measurements are started. Another possible explanation is that a layer near the surface exists with a diffusion constant which is lower than the diffusion constant for glass further in the interior.

[5] M. E. Nordberg, J. Am. Ceram. Soc. **27**, 299 (1944).

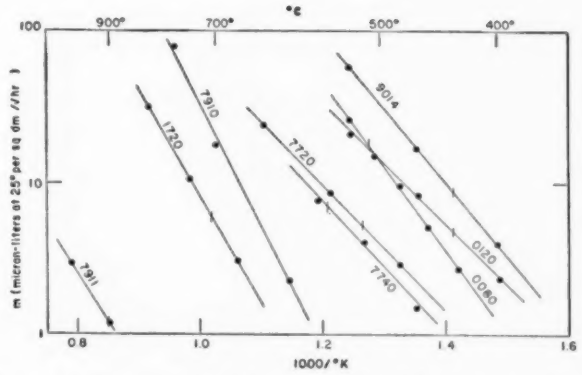

FIG. 6. Temperature dependence of m for eight glasses produced by Corning Glass Works. (m *vs* reciprocal temperature.)

With No. 9014 at 530° a plot of V against $\sqrt{t}$ has two linear portions, giving a higher m at the beginning of the bake-out than at later times. Apparently the diffusion constant is changing with time at this temperature. The m used in Fig. 6 is the earlier one.

The curves of Fig. 6 can be expressed by the equation,

$$\log m = (-A/T) + B, \tag{5}$$

where T is the absolute temperature, and A and B are constants. Values of A, B, and ΔH_a are given in Table I. The dash on each curve of Fig. 6 indicates the annealing temperature of the glass.

V. DIFFUSION CONSTANT FOR WATER IN NO. 0080 GLASS

From Eq. (3) for diffusion from a semi-infinite body one can obtain an estimate of D, the diffusion coefficient, provided the value of C_0, the initial uniform concentration of water, is known. A probable value of C_0 for No. 0080 glass is 495 mm (Hg)-cc at 25° per cc of glass. This value of C_0 was obtained by measuring the amount of water evolved when this glass was remelted in vacuum at 1300° for ½ hour. The collecting system of Fig. 1 was used in this measurement, but the container and furnace were of the type described by Dalton.[6] In using this value for C_0 the assumption is made that all the water evolved at 1300° in ½ hour would be evolved

TABLE I. Constants for the calculation of m [micron (Hg)-liters at 25° per sq dm/√hr] at an arbitrary temperature from the equation, $\log m = (-A/T) + B$.

Glass code no.	Glass type	A (°K)	B	ΔH_a (kcal/mole)
7911	Vycor brand 96% silica	6230	5.397	57
7910	Vycor brand 96% silica	8240	9.772	75
1720	Lime-aluminum	7000	7.952	64
7740	Borosilicate	4510	6.310	41
7720	Lead-borosilicate	4150	5.983	38
0080	Soda-lime	5420	8.153	50
0120	Potash-soda-lead	3910	6.208	36
9014	Potash-soda-barium	4840	7.799	44

[6] R. H. Dalton, J. Am. Chem. Soc. **57**, 2150 (1935).

TABLE II. Values of the diffusion constant for water in No. 0080 glass at various temperatures.

Temperature (°C)	Diffusion constant (cm^2/sec)
430°	6.1×10^{-13}
455°	2.3×10^{-12}
480°	8.4×10^{-12}
505°	2.0×10^{-11}
530°	6.1×10^{-11}

at any lower temperature in a sufficiently long time. Values of D calculated in this way are given in Table II.

The variation in relative concentration C/C_0 in the semi-infinite body after some time t with distance from the surface exposed to the vacuum χ can be calculated from the following expression:

$$\frac{C(\chi,t)}{C_0}=\frac{2}{\sqrt{\pi}}\int_0^{\chi/2\sqrt{Dt}}\exp(-y^2)dy. \tag{6}$$

A plot of C/C_0 against χ after two bake-outs is given in Fig. 7. Figure 7 shows that only a thin layer of glass is involved in the diffusion process at bake-out temperatures and times. This has been checked experimentally by baking-out a sample, then polishing off about 3 mils from the surface, and observing that the original value of m was obtained when the sample was baked-out again.

The relative concentration at a point depends upon the value of $\sqrt{Dt}$, as does the volume evolved per unit surface. Thus the concentration gradient is determined by the volume of water removed from the glass. The same gradient is obtained if the same volume is removed in a short bake-out at high temperature as in a long bake-out at low temperature.

The diffusion from three simple shapes, a slab of thickness $2a$, an infinite circular cylinder of diameter $2a$, and a sphere of diameter $2a$, has been treated using solutions for the analogous heat flow problems presented in Carslaw and Jaeger.[7] The curves of Fig. 8

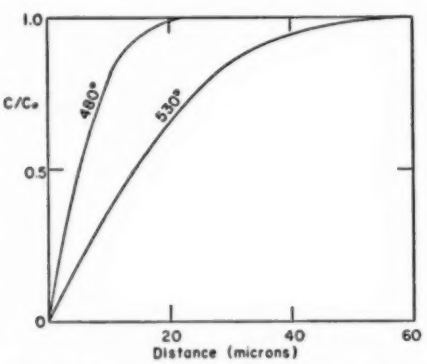

FIG. 7. Relative water concentration in No. 0080 glass as a function of distance from surface exposed to vacuum after a 10 hour bake-out at 480° and after a 10 hour bake-out at 530°C.

[7] H. S. Carslaw and J. C. Jaeger, *Conduction of Heat in Solids* (Oxford University Press, New York, 1947), first edition, p. 84.

which show, for a body of volume ω and surface σ, the ratio of the amount of gas lost by diffusion V_L to the initial amount of diffusing material V_0 plotted against $[(Dt)^{\frac{1}{2}}/a]$ have been calculated from their data. In the linear portion of the curves of Fig. 8 the expression,

$$V_L/V_0=V\sigma/C_0\omega=\lambda(Dt)^{\frac{1}{2}}/a, \tag{7}$$

holds. For the slab, cylinder, and sphere λ is, respectively, 1.13, 1.96, and 2.81. Also, m is given by the expression,

$$m=V/t^{\frac{1}{2}}=(\omega\lambda/\sigma a)C_0D^{\frac{1}{2}}. \tag{8}$$

For the slab, cylinder, and sphere the factor $(\omega\lambda/\sigma a)$ is, respectively, 1.13, 0.98, and 0.94. The ratio of outside diameter to inside diameter for the No. 0080 tubing samples was 1.3. The evolution from such a hollow cylinder more nearly resembles evolution from a slab than a cylinder, so the use of Eq. (3), which is

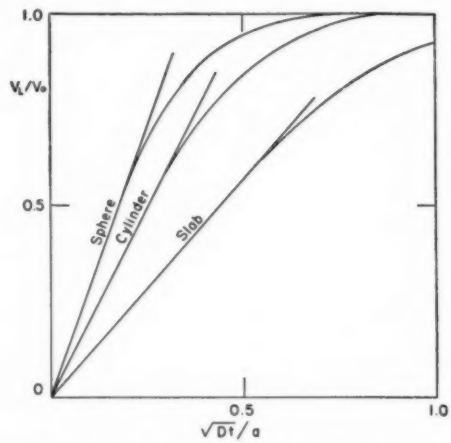

FIG. 8. Ratio of the amount lost by diffusion to the initial amount of diffusing material plotted against $(Dt)^{\frac{1}{2}}/a$ for a slab of thickness $2a$, an infinite circular cylinder of diameter $2a$, and a sphere of diameter $2a$.

identical to Eq. (8) for the slab, in calculating D does not introduce a serious error.

Figure 8 also allows one to compute the time at which departure of the V *vs* $\sqrt{t}$ plot from linearity can be expected. For instance, for a slab one mm thick departure from linearity will not occur until $(Dt)^{\frac{1}{2}}/a$ is approximately 0.53. Using the values of D from Table II, 37, 2.6, and 0.4 years would be required for the plots for No. 0080 glass to depart from linearity at 430°, 480°, and 530°, respectively.

VI. APPLICATION TO BAKE-OUT PROBLEMS

If m is known as a function of temperature for a glass with initial uniform water concentration, it is possible to calculate the amount of water that will diffuse out with time at any temperature after some arbitrary bake-out. If this initial bake-out has removed the surface gases from a vacuum envelope, the pressure

rise in the envelope is the result of only the diffusing water vapor.

Consider the two isotherms in Fig. 9 for temperatures q_1 and q_2 where $q_1 > q_2$. If the glass is baked-out at q_1 for time t_1, the resulting concentration gradient is the same as if it had been baked-out at q_2 for time t_0. If the glass is then heated at q_2 for some time t_2, the diffusion proceeds along the q_2 isotherm with the initial time on this isotherm being t_0. The volume V_2 evolved in time t_2 at q_2 is given by the equation,

$$V_2 = (m_1^2 t_1 + m_2^2 t_2)^{\frac{1}{2}} - m_1 t_1^{\frac{1}{2}}. \quad (9)$$

In view of the times required for departure of the V *vs* $\sqrt{t}$ plots from linearity as shown in the preceding section, extrapolation for long times at practical operating temperatures appears valid.

Tables III and IV give the results of some experiments carried out to check on the validity of this type of calculation. The deviation between observed and calculated results falls within the range of experimental error.

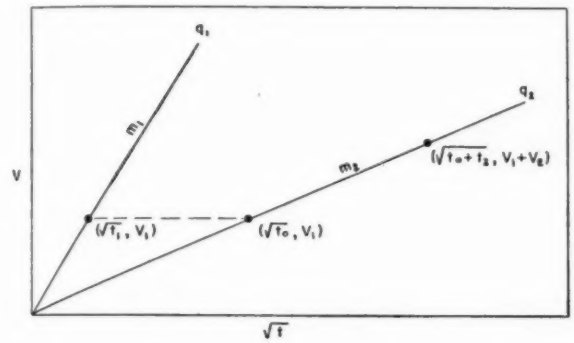

FIG. 9. Hypothetical plot illustrating calculation of water volume diffusing from glass after an arbitrary bake-out. (V *vs* square root of bake-out time.)

The order of increasing effectiveness of bake-out as shown in Table IV is C, B, A. Langmuir's work with a sodium-magnesium-borosilicate glass[8,9] predicts the order would be A, C, B. This anomaly has not been resolved.

Extrapolation of the curves of Fig. 6 shows that for temperatures of 100° or less the m's for the various glasses become extremely small. The diffusion of water from any of these glasses is insignificant in this temperature range, and a bake-out which completely removes the surface gases should be adequate. With increasing temperature and, consequently, higher m, the diffusion of water becomes increasingly important in the deterioration of the vacuum. The data of Table I and Eq. (9) provide a means of evaluating these different glasses at the higher operating temperatures.

[8] I. Langmuir, U. S. Patent No. 1,273,629 (July 23, 1918).
[9] S. Dushman, *Scientific Foundations of Vacuum Technique* (John Wiley and Sons, Inc., New York, 1949), first edition, p. 511.

TABLE III. Calculated and observed values of water evolution from No. 0080 glass in successive time intervals at 450° after a preliminary bake-out at 480° for 0.5 hour.

Time at 450°	Micron (Hg)-liters at 25° per sq dm Calc.	Obs.
First hour	1.7	1.5
Next hour	1.4	1.2
Next hour	1.2	1.2

TABLE IV. Calculated and observed values of water evolution from No. 9014 glass in successive time intervals at 400° after preliminary bake-outs A, B, and C. A. 530°, 1 hour. B. 530°, 0.5 hour; 400°, 0.5 hour. C. 465°, 1 hour.

	Micron (Hg)-liters at 25° per sq dm					
	After A		After B		After C	
Time at 400°	Calc.	Obs.	Calc.	Obs.	Calc.	Obs.
First 0.5 hour	0.07	0.06	0.10	0.05	0.25	0.12
Next 2 hours	0.27	0.20	0.38	0.35	0.98	0.71
Next 2 hours	0.27	0.20	0.37	0.39	0.93	0.71
Next 2 hours	0.27	0.19	0.37	0.39	0.92	0.71

VII. SUMMARY

A more detailed mechanism of the evolution of water from glass than has existed before has been developed. The development depends upon measurement of the outgassing rate; it was found that the water diffusing from glass per unit surface is proportional to the square root of the bake-out time. The temperature dependence of the diffusion process for eight glasses has been determined. The value of the diffusion constant for water and the concentration gradients after bake-out in a soda-lime glass have been calculated from the data and Fick's law for diffusion from a semi-infinite body. Since the concentration gradient depends only on the volume of water removed, and the linearity of the $\sqrt{t}$ relationship persists for so long, it is possible to calculate the amount of water diffusing from glass after an arbitrary bake-out.

ACKNOWLEDGMENTS

The author wishes to thank Dr. C. H. Cartwright, Dr. R. H. Dalton, and Dr. R. B. Randels for helpful advice and discussion.

Prebreakdown Current and Noise in Insulators*

D. A. POWERS AND T. SUITA†
Laboratory for Insulation Research, Massachusetts, Institute of Technology, Cambridge, Massachusetts
(Received May 11, 1955)

The frequency spectrum of the noise associated with prebreakdown currents in insulators has been investigated in the audio-frequency range. Most of the noise is due to surface discharges which can be eliminated by special types of electrodes and careful experimentation. The remaining noise has a frequency spectrum with the highest amplitudes at very low frequencies; it falls rapidly to the Johnson noise level in the measuring resistor at about 10^4 cps. This noise apparently originates from fluctuations in the field-emission current.

INTRODUCTION

THE direct current flowing through an insulator under the influence of high electric fields exhibits characteristic fluctuations or noise, first observed by Haworth and Bozorth[1] and von Hippel.[2] Haworth and Bozorth measured the noise current in Pyrex as a function of applied field strength and analyzed their data in terms of prebreakdown avalanches. This interpretation, taken up recently by Yamanaka and Suita[3] and Kawamura and Onuki,[4] that the prebreakdown noise is evidence of avalanche formation without breakdown, seems dubious.[5] Positive holes left behind in insulators by electron avalanches should have very low mobilities. In consequence, once electron impact ionization sets in, the field strength at the cathode is bound to increase because of the field distortion by the positive space charge, and breakdown should occur.

Breakdown by impact ionization in solids develops in less than 10^{-7} second. Hence the transit time for an avalanche must be approximately of this order and the frequency spectrum of the noise, if caused by avalanches, should be flat to at least one megacycle. To clarify the situation, the authors have investigated the amplitude of the noise as a function of voltage, and the frequency spectrum of the noise in the audio range.

MEASUREMENT TECHNIQUE

The noise current was measured by passing the sample current through the wire-wound input resistor (2.5-megohm) of an audio amplifier with a pass band from 40 cycles to 11 kilocycles (Fig. 1). The amplifier output, measured by a thermocouple milliammeter as in the work of Haworth and Bozorth,[1] or by a General Radio Type 736-A wave analyzer, could be observed visually on an oscilloscope. With no current in the input resistor the output noise spectrum was flat down to 100 cps; its magnitude corresponded to the Johnson noise in the input resistor. Below 100 cycles the flicker noise in the first stage of the amplifier became appreciable; hence no measurements were made below 80 cps. Direct current measurements were made by substituting for the 2.5 megohm resistor a D'Arsonval type microammeter for currents above one microampere or an electronic micro-microammeter for smaller currents. The entire system was carefully shielded against stray pickup; an RC filter (100-sec time constant) isolated the sample from the noise of the high voltage power supply.

The wave analyzer (effective band width of 5 cps)[6] is well suited to a comparative noise analysis in the audio range. Absolute values of the input noise voltage may be calculated on a one-cycle band width basis by subtracting 7 db from the indicated value,[7] provided the noise amplitude has a Gaussian distribution. Even at low frequencies, the cutoff of the crystal filter in the wave analyzer is so sharp that a negligible error is introduced by the (inverse) frequency dependence of the noise current actually found.

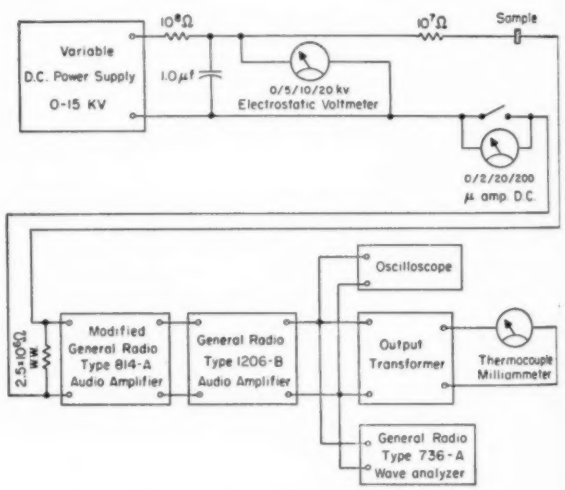

FIG. 1. Block diagram of measuring circuit.

* Sponsored by the Office of Naval Research, the U. S. Army Signal Corps, and the U. S. Air Force.

† Present address: Osaka University, Osaka, Japan.

[1] F. E. Haworth and R. M. Bozorth, Physics **5**, 15 (1934).

[2] A. R. von Hippel, Phys. Rev. **54**, 1096 (1938); *Dielectrics and Waves* (John Wiley and Sons, Inc., New York, 1954), pp. 241.

[3] C. Yamanaka and T. Suita, J. Phys. Soc. Japan **6**, 194 (1951); **7**, 225 (1952).

[4] H. Kawamura and M. Onuki, J. Phys. Soc. Japan **6**, 283 (1951); **7**, 121 (1952).

[5] A. von Hippel and R. S. Alger, Phys. Rev. **76**, 133 (1949).

[6] A. P. G. Peterson, Gen. Radio Experimenter **26**, 1 (1951).

[7] J. E. Hawkins, Jr., and S. S. Stevens, J. Acoust. Soc. Am. **22**, 6 (1950).

INFLUENCE OF ELECTRODE PREPARATION ON NOISE CURRENTS

In their work on space-charge-controlled field emission into crystals, von Hippel and co-workers[8] found large noise components in prebreakdown currents under experimental conditions which would not permit avalanche formation. They concluded that field emission took place from sensitive spots on the cathode, with the emissivity of the spots changing rather slowly with time. Consequently, we searched for an electrode material and configuration which gave minimum noise.

Mica was chosen as the dielectric for these experiments because of the relative ease with which thin samples of suitable size (1.5 cm square by *ca* 0.01 mm thick) can be prepared. Data for samples showing a dielectric strength lower than 6×10^6 volts per cm were discarded on the assumption that low dielectric strength may indicate mechanical damage which could cause abnormally high noise levels. All tests were carried out in a cell which could be pressurized to 100 atmos. In practice, it was found that 450 psi of N_2 completely suppressed corona noise within the test cell at 10 kv, the maximum voltage used; hence pressures of 500 to 600 psi were used.

In Fig. 2 noise current and direct current are plotted *versus* voltage for three typical electrode systems. The noise current represents comparative readings of the thermocouple meter; absolute values were not calculated because the noise current spectrum has an inverse frequency dependence (see below). The reference level is that of the Johnson noise in the 2.5-megohm resistor. The values of direct current did not differ markedly among the three electrode systems, hence are approximated by a single straight line. Figure 3 shows the detailed measurements of the direct current for one mica sample; it corresponds, within the limits of error, to a straight line in a log I *vs* V plot.

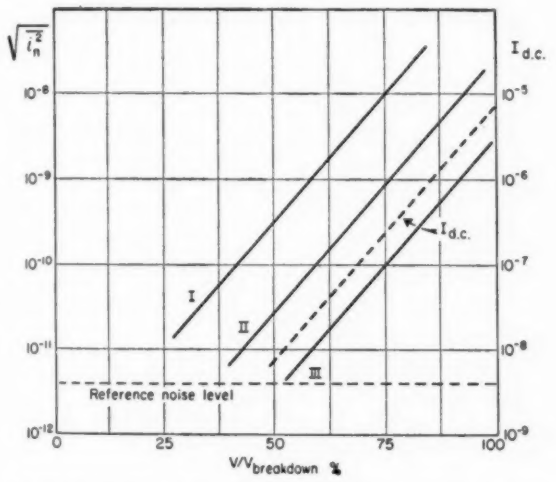

FIG. 2. Current *vs* voltage characteristics for various electrode systems: Curve I, $\frac{1}{4}$ in. diam. Aquadag electrodes, baked at 150°C for 24 hr; Curve II, $\frac{1}{4}$ in. diam evaporated gold electrodes to produce a sharp transition in radial surface conductivity at the electrode edge; Curve III, $\frac{1}{4}$ in. diam gold electrodes, prepared with diffuse edges according to the technique of M. E. Caspari (Tech. Rep. 90, Lab. Ins. Res., Mass. Inst. Tech., November, 1954, p. 11) and Y. Saito [J. Inst. Elec. Engrs. (Japan) **56**, 211 (1936)].

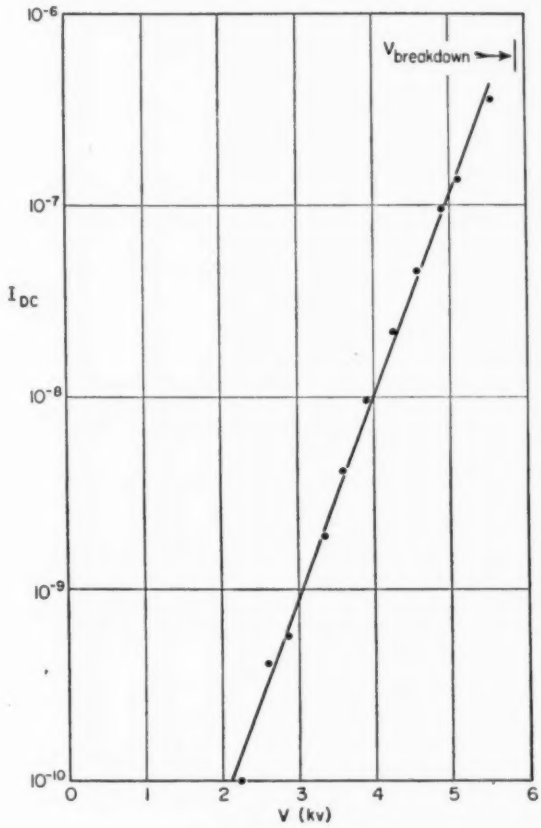

FIG. 3. I_{dc} *vs* V in mica.

The noise level with Aquadag electrodes was high, becoming measurable at about 25% of the breakdown field strength. This noise appears to stem from three sources; surface discharges at the edge of the electrodes, an effect due to the structure and contact of the Aquadag, and a third source which we term field emission noise after von Hippel.[8] The noise reduction in changing from the carbon electrodes of Curve I to the gold electrodes of Curve II amounts to approximately 20 db. This probably represents a decrease in the surface discharge noise due to better contact. By the use of gold electrodes with diffuse edges, a further reduction of the noise by 20 db was achieved due to the suppression of surface discharges. Changing the width of the diffuse zone of the gold from $\frac{1}{16}$ to $\frac{1}{8}$ in. did not change the remaining noise, nor did reduction of the surface leakage distance; hence it can be assumed that the remaining noise was associated directly with the current flow through the volume of the dielectric. Brophy,[9] in his work on thermistor bolometer flakes,

[8] von Hippel, Gross, Jelatis, and Geller, Phys. Rev. **91**, 568 (1953).

[9] J. J. Brophy, J. Appl. Phys. **25**, 222 (1954).

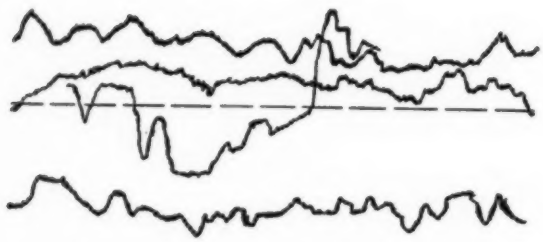

FIG. 4. Typical oscillograms of current noise.

found similarly that the method of applying electrodes proves a major factor in determining the magnitude of the noise.

FREQUENCY SPECTRA OF THE NOISE CURRENT

Observation of the amplified noise on an oscilloscope indicated the presence of large noise components at low frequencies. Figure 4 reproduces four 1/60-sec sweep traces taken at one minute intervals; the prominence of the low-frequency components is apparent. With the help of the wave analyzer, the frequency spectrum of the noise was recorded for mica and KBr with diffuse-edged gold electrodes at various voltage levels (Figs. 5 and 6). While the exact shape of the spectral curves is not readily explained, two general features are apparent: the decrease in noise energy with increasing frequency and the increase at lower frequencies with increasing voltage. Neither of these trends is explainable in terms of the hypothesis that the noise is caused by avalanches.

A single avalanche may be represented as a current pulse of the form $i=i_0e^{\alpha t}(0<t<t_1)$, where t_1 is the transit time and α the ionization probability. The auto-

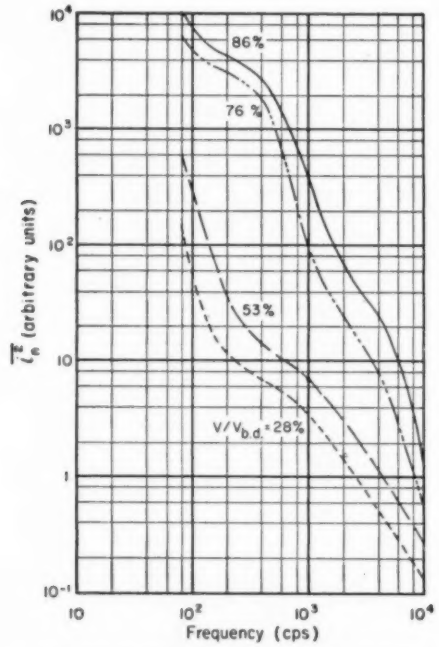

FIG. 5. Frequency distribution of noise current in mica.

correlation function

$$\phi_{11}(\tau)=\int_{-\infty}^{\infty}f(t)f(t+\tau)dt$$

for this current pulse is

$$\phi_{11}(\tau)=\frac{(i_0e^{\alpha t_1})^2}{2\alpha}e^{-\alpha|\tau|}(1-e^{2\alpha(|\tau|-t_1)}),$$

for $0<\tau<t_1$ and zero elsewhere. The corresponding energy density spectrum

$$\Phi_{11}(\omega)=\frac{1}{2\pi}\int_{-\infty}^{\infty}\phi_{11}(\tau)e^{-j\omega\tau}d\tau$$

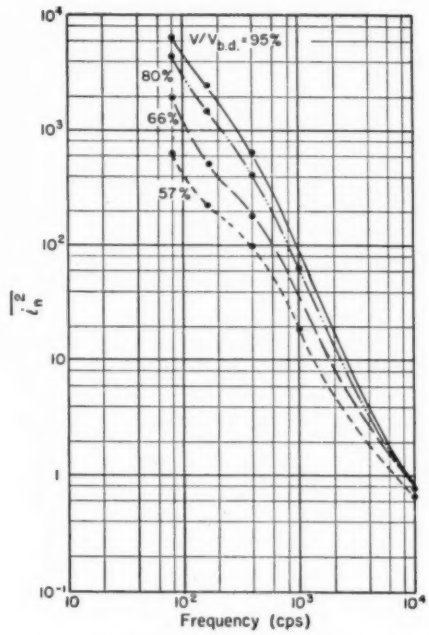

FIG. 6. Frequency distribution of noise current in KBr.

is

$$\Phi(\omega)=\frac{(i_0e^{\alpha t_1})^2}{2\pi}\frac{1}{\alpha^2+\omega^2}(1+e^{-2\alpha t_1}-2e^{\alpha t_1}\cos\omega t_i).$$

With $e^{\alpha t_1}\gg 1$, as it would be for appreciable multiplication, the energy density spectrum reduces to that of an exponentially damped pulse of initial magnitude $i_0e^{\alpha t_1}$ as

$$\Phi_{11}(\omega)=\frac{(i_0e^{\alpha t_1})^2}{2\pi}\frac{1}{\alpha^2+\omega^2}.$$

The power density spectrum of an average number of such events per second has the same frequency distribution as the energy density spectrum of a single event, provided they are independent and occur at random. A decrease in transit time, caused by an increase in the electric field intensity, must shift the spectrum toward

higher frequencies. For a value of $\alpha t_1 = 2$, corresponding to a multiplication process of approximately 7 final electrons for one starting electron, the power density falls to one half of its low-frequency value at the frequency $f = 1/\pi t_1$. The transit time may be estimated from mobility, sample thickness, and electric field strength. For KBr with $b = 100$ cm^2 volt^{-1} sec^{-1}, $d = 10^{-1}$ cm, $E = 10^5$ volts per cm, the transit time is 10^{-8} second and the half-power frequency lies at 3×10^7 cps. In our experiment, while we were unable to establish a half-power frequency, it certainly lies below 100 cps.

TIME DEPENDENCE OF THE NOISE CURRENT

While it was impossible in the limited time available to make a complete study of the noise variation as a function of time, one series of measurements at 400 cps was made on KBr using the wave analyzer (Fig. 1). With a high-voltage switch inserted after the filter, the voltage was applied as a step function and the noise current read at one minute intervals until it became constant. Two curves of noise energy *versus* time at 56 and 83% of the breakdown voltage (Fig. 7) show initial noise-energy levels which are 20 to 30 db higher than the steady-state values.

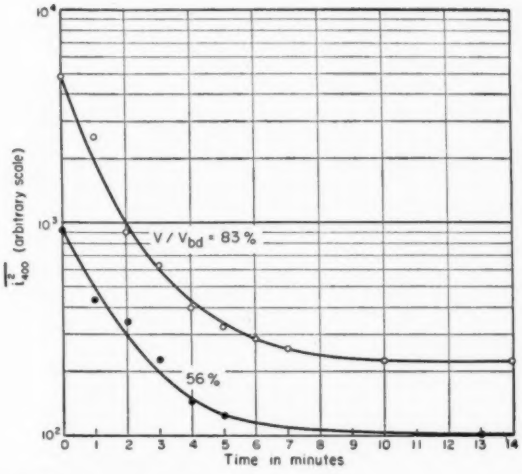

FIG. 7. Time dependence of 400-cycle noise component in KBr.

CONCLUSION

Two experimental facts point to the conclusion that prebreakdown avalanches, if they exist at all, occur with very low probability even at fields quite close to breakdown: The audio-noise spectrum corresponds to a correlation time several orders of magnitude greater than that calculated for avalanches and the noise level at 10 kc is too low for avalanche processes involving an appreciable fraction of the starting electrons. From observations of the oscilloscope display it appears that the correlation time is greater than 0.1 sec perhaps by several orders of magnitude, as was observed by Baker,[12] in germanium rectifiers. Without an adequate measurement of the correlation time, which would require instrumentation and techniques similar to those used by Baker, the authors cannot give a more accurate description of the noise mechanism than the phenomenological outline of von Hippel,[8] who suggested that the audio noise results from the activation and decay of sensitive spots on the cathode which produce electrons by field emission.

[12] D. K. Baker, J. Appl. Phys. **25**, 922 (1954).

Surface Friction in Ballistic Penetration

JOSEPH M. KRAFFT
Naval Research Laboratory, Washington, D. C.
(Received March 9, 1955)

The frictional adhesion between projectile and target during a ballistic penetration has been measured with a torsion-type Hopkinson bar. The apparatus allows measurement of the torsional adhesion of a spinning projectile during target penetration. By assuming the friction resisting rotation to be equal to that resisting axial penetration, the energy loss due to friction was computed. The results show that the torque-time pattern during penetration of a "mechanically" clean projectile can be predicted with the assumption of a frictional energy loss just sufficient to keep the sliding surfaces at the melting temperature of the metal. Metallographic analysis of the target metal at the projectile interface gives a further indication of a molten interface. In these tests, sliding friction accounts for about 3% of the striking energy of the projectile; common surface contaminants, not necessarily special lubricants, reduce this loss to less than 1%.

INTRODUCTION

THE effect of surface friction in retarding penetration of a projectile into a deformable target has long been of interest in the study of terminal ballistics. The need for quantitative estimates of frictional forces has been felt particularly in the development of the theory of armor penetration. In general such theories include consideration only of cohesive strength and inertial characteristics of materials while neglecting the contribution of surface friction to total penetration resistance. That theories so founded[1,2] successfully describe actual penetration experiments may be taken to indicate that whatever the effect of surface friction on high-speed penetration, it is quite likely a small one. But this result, though perhaps sufficient for practical purposes, does nothing to determine the physical processes which make the frictional resistance at high surface velocity (and pressure) so much smaller than that at low velocity. Further question arises as to the effect of adsorbed surface contaminants in high-velocity sliding as compared to their pronounced effect at low velocity. In the hope of clarifying some of these questions this paper describes a measurement and analysis of surface forces for a hard steel cone-tipped projectile during entry into a softer steel target.

BACKGROUND

Unanswered questions pervade the subject of high velocity friction; indeed, even at slow sliding speeds that permit detailed observation, there is still much uncertainty concerning the mechanism of friction. The question arises here of the nature of the adhering bonds between solid surfaces. Early in his extensive friction studies, Bowden[3] proposed a mechanism whereby microscopic metallic asperites projecting from each surface are plastically mashed to an area sufficient to carry the normal pressure and adhere (or cold weld) to the opposite surface so that friction results from their average shear strength. A number of experimental results find plausible interpretation in this framework: such phenomena, for example, as surface temperature increasing to the melting point with increasing velocity,[4] high-temperature bursts coincident with stick-slip transition,[5] true area of contact from resistivity measurements,[3] and correlation of shear strength to hardness ratio with the friction coefficient over a wide range of temperature.[6]

Despite such successes, a dissatisfaction with the simple welded-asperite picture has grown from experiments demonstrating the tremendous effect of adsorbed gases on adhesion and surface friction, particularly the effect of oxides which exist even on carefully cleaned and degreased surfaces. Indeed with the evidence available in 1942, Shumermann asserted that all phenomena interpreted in terms of metal-to-metal shearing could equally convincingly be attributed to shearing of oxide-to-oxide bonds, which could be weaker and thus account for the fact that friction between metal surfaces is less than the shear strength of true metal-to-metal welds.[7,8] In recent years, workers in the field have become increasingly cognizant of the effect of surface impurities.[9]

At high surface speeds, processes leading to friction are dominated by a requirement of thermodynamics.[10] Friction, no matter what the mechanism, involves heat dissipation. At ballistic velocities the duration of the event is so short that ordinary heat conduction could not dispel all the heat generated if ordinary slow-speed friction coefficients were maintained and the surface temperature limited to its melting point. Therefore, surface friction must necessarily be reduced to that just sufficient to maintain the interface at the melting point.

[1] G. R. Irwin, Six. Internl. Cong. Appl. Mech. September, 1946.
[2] J. M. Krafft, Ph.D. thesis, Catholic University Press., Washington, D. C., 1951.
[3] F. P. Bowden and D. Tabor, Proc. Roy. Soc. (London) **169**, 391 (1939).
[4] F. P. Bowden and K. E. W. Ridler, Proc. Roy. Soc. (London) **154A**, 640 (1936).
[5] F. P. Bowden and L. Leban, Proc. Roy. Soc. (London) **169**, 371 (1939).
[6] Simon, McMahon, and Bowen, J. Appl. Phys. **22**, 177 (1951).
[7] R. Shumermann, J. Appl. Phys. **13**, 235 (1942).
[8] A. Gement, J. Appl. Phys. **14**, 456 (1943).
[9] Conference on Mechanism of Friction, Proc. Roy. Soc. (London) **212**, 440 (1952).
[10] C. Zener and R. Peterson, *Mechanism of Armor Penetration*. Watertown Arsenal Report 714/492, 1943.

A mechanism for friction reduction is inherent in the molten interface which becomes, in fact, a liquid film separating the solid components. The role of surface oxides under such conditions should become unimportant as the melting point and thermal conductivity which determine the friction are little affected by small amounts of oxide with a comparable melting point. Thus one would expect that, at ballistic speeds, friction of chemically clean surfaces would not appreciably differ from friction of mechanically degreased but oxide-bearing surfaces.

EVIDENCE OF FRICTION FROM SURFACE APPEARANCE

The striking characteristic of the nose surfaces of recovered projectiles is a snow cap (Fig. 1) suggestive of a molten surface condition during penetration. The area of the snow cap becomes almost the total area of contact when projectile and target surface are "mechanically" clean [Fig. 1(A)]. It can be reduced by lubrication until only a small area at the tip [Fig. 1(B)] shows the snow cap appearance while the remaining imbedded surface appears unchanged. The "snow cap" at the tip on a lubricated projectile is taken as indicating surface melting after the abrasion of contaminants from this region during penetration.

EVIDENCE FROM MICROSTRUCTURE

More quantitative evidence of high surface temperature than the foregoing can be seen from micrographs of target cross section in the region adjacent to the projectile-target interface (Fig. 2). In the case of the "clean" projectile penetration a layer of transformed material is evident [Fig. 2(A)], presumably martensite formed by a heating of the steel from the surface to above the austenitizing temperature (800°C) and then a rapid cooling by normal heat conduction into the body of the target. The thickness of the layer shown is about 1.3×10^{-3} cm. This section, taken midway between the cone tip and target surface, is typical of the appearance and depth all along this length.

The depth to which a temperature of 800°C should have occurred was estimated from calculated curves showing temperature distribution in the metal after holding the surface at 1500°C for various time intervals.[11] From these curves (Fig. 3) it can be seen that 800°C is reached at a depth of 1.3×10^{-3} cm after the melting temperature is applied for about 24 microseconds. This time is in good agreement with the duration of contact derived from force history measurements. The lubricated projectile showed evidence of transformation only near the tip [Fig. (2C)] corresponding to the snow cap region [Fig. 1(B)] where it extends to 0.6×10^{-3} cm—about half the depth observed for a "clean" projectile.

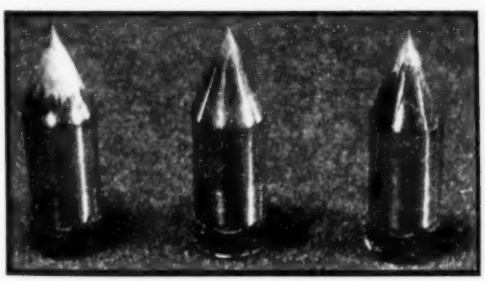

(A) (B) (C)

FIG. 1. Typical "snow cap" appearance of recovered projectiles. (A) Mechanically cleaned. (B) Lubricated. (C) Provided with rotation-arresting flats.

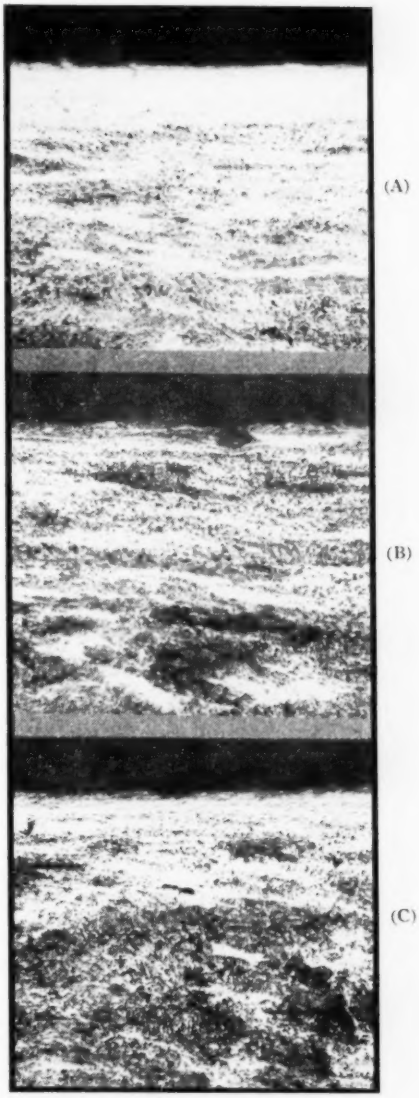

(A)

(B)

(C)

FIG. 2. Micrographs (1000×) of target cross section adjacent to cone penetration surface. (A) Mid-depth for mechanically cleaned penetrator. (B) Mid-depth for lubricated penetrator. (C) Near tip for lubricated penetrator.

[11] Carslaw and Jaeger, *Conduction of Heat in Solids* (Oxford University Press, New York, 1949), p. 45.

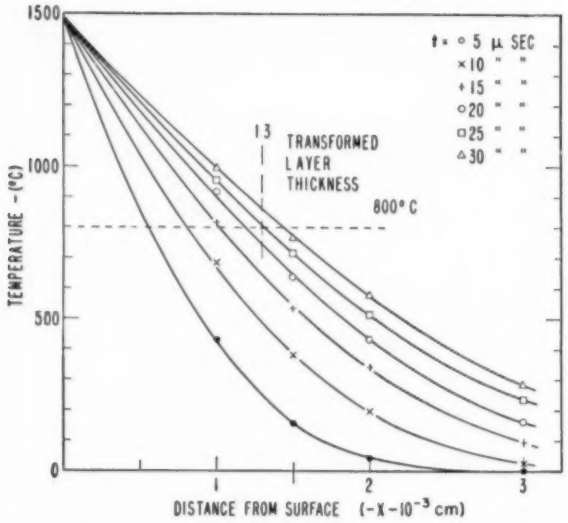

FIG. 3. Temperature distribution adjacent to steel surface held at melting point 1500°C for: ● 5μ sec, × 10μ sec, + 15μ sec, ○ 20μ sec, □ 25μ sec, Δ 30μ sec. From Carslaw and Jaeger (reference 11) using $K=0.11$, $\rho=7.85$, $c=0.16$, cgs units.

THEORETICAL CONSIDERATIONS

In addition to evidence from appearance after the penetration, the validity of the "molten interface" hypothesis is supported by a significant degree of agreement between the friction force one can compute based on this concept, and the experimentally measured friction force curves given later in this paper. For this computation, the magnitude of friction is taken as the amount just sufficient to supply the energy required to maintain melting at the projectile-target interface against energy dissipation by normal conduction into the target and projectile. The solution gives heat quantities proportional to the area under the curves of temperature distribution (Fig. 3). Identical conductivity values have been used in both calculations. The temperature rise incident to gross plastic deformation of target metal is neglected as small with respect to the melting temperature localized at the rubbing surface.

As a basis for the comparison, one can compute the energy flux passing from the surface of a semi-infinite solid with initial temperature uniform after suddenly raising the surface temperature a fixed amount ΔT. This energy is supplied by the frictional force F times the velocity of sliding V, i.e.,

$$FV=-K\left(\frac{\partial T}{\partial x}\right)_{x=0}=\left(\frac{K\rho c}{t}\right)^{\frac{1}{2}}\Delta T, \tag{1}$$

where K is the thermal conductivity, T is the temperature, ρ is the density, c is the specific heat, and t is the time after application of temperature rise ΔT.

To take into account the flow of heat into both the projectile and the target, the required energy as given in Eq. (1) must be doubled. For two sliding surfaces, one may approximate t by S/V, where S is the surface displacement and V is the relative velocity between the surfaces. The friction force F becomes then

$$F\cong 2\left(\frac{K\rho c}{VS}\right)^{\frac{1}{2}}\Delta T. \tag{2}$$

In assigning numerical values to the parameters it was appreciated that over the temperature range to 1500°C the specific heat c (as well as the thermal capacity) varies, being generally greater at high temperatures and particularly so at phase-transition temperatures. Thus, a value of c typical of higher temperatures (0.16 cal g^{-1} $°C^{-1}$) was used while room temperature values were used for the specific gravity (7.85 g cm^{-3}) and thermal conductivity K (0.11 cal cm^{-1} sec^{-1}). After substituting in Eq. (2) and converting to convenient units one has

$$F\cong 2\left(\frac{2500}{SV}\right)^{\frac{1}{2}}\Delta T, \tag{3}$$

where F is in pounds, S in inches, V in inches per second, and ΔT in degrees centigrade. If a temperature rise of 1500°C (to the melting point of steel) is used, Eq. (3) becomes

$$F\cong 15.0\times 10^{4}(SV)^{-\frac{1}{2}}. \tag{4}$$

From Eq. (4), given experimentally measured values of S and V and the geometry relating the surface area to S, one could estimate the frictional force acting to retard the longitudinal motion of penetration. But in the practical experiment, it has been impossible to distinguish friction forces from the longitudinal force necessary to deform the target. It has been possible, however, to measure the torque which the same friction will couple from a spinning projectile into the target. Thus for comparison with experiment, the friction force given by Eq. (4) is converted to values of the torsion which such friction would develop during the penetration of a spinning projectile.

The choice of parameters for this conversion is complicated by the physical complexity of the penetration event. It is clear from geometrical considerations for penetration of a cone that a factor S^2 must be introduced to allow for increase of surface area as a function of depth of penetration, and a factor S to allow for increase in effective moment arm of the friction force at the surface with respect to the axis of spin. After selecting reasonable average values for coefficients to these factors S^2 and S (i.e., giving total imbedded area of 45° cone from S^2 and radius at $\frac{1}{3}$ tip depth from surface from S), the torque may be expressed as

$$T\cong 2.7\times 10^{4}S^{5/2}V_1^{-\frac{1}{2}} \tag{5}$$

where S is the depth of penetration in inches. A median surface velocity V_1 takes into account the increase in ratio of surface velocity due to spin to surface velocity

due to forward motion as the projectile decelerates. It is necessary to estimate V_1 from analysis of the data. The torque from Eq. (5) does not become infinite when the forward motion stops because the projectile is still spinning.

From the experiments described below, a continuous measurement of the friction torque T during entry and arrest of a rotating projectile was compared with values of torque computed from Eq. (5) using simultaneously measured values of displacement S and velocity V.

EXPERIMENTAL PROCEDURE

In this experiment a spinning projectile is fired at the end of a long bar. Localized plastic deformation around the projectile absorbs most of its kinetic energy. Momentum is conserved in elastic waves travelling down the bar—one a compression wave proportional in time to the penetration resistance acting to arrest longitudinal motion, the other a torsion wave proportional to the resistance to spin. Since the normal pressure and surface condition which determine frictional resistance to spin are necessarily identical to those which determine frictional resistance to longitudinal penetration, the two resistances are assumed equal. Thus, independent measurement of the torsional resistance to penetration of a spinning projectile, or the torque applied to the target, is taken as a direct measure of the frictional resistance at the interface.

The torque has been measured with a Hopkinson bar system (Fig. 4) especially adapted to separate the longitudinal force of a penetrating projectile from the torsional force wave resulting from frictional adhesion retarding projectile rotation. The compression wave resulting from longitudinal penetration of the projectile into the bar end was measured as in previous work at the Naval Research Laboratory[12] with wire resistance strain gauges (SR4, C-14, 2000Ω, G. F. 3.3) attached along the bar in diametrically opposite positions. A cathode-ray oscillograph (Dumont 294-A) arranged for single-sweep operation was used to record the compression-wave pattern.

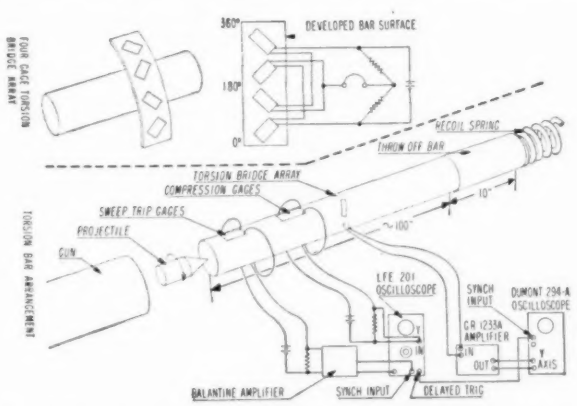

FIG. 4. Bar apparatus for measuring torsion from spinning projectile and arrangement of gauges for torsion measurement.

Measurement of the torsion wave is difficult because of its relatively low magnitude. Again a strain gauge bridge was employed using four gauges (SR4, C-10, 500Ω, G. F. 3.3) positioned at 45° to the longitudinal axis and wired (Fig. 4) to be sensitive to torsional shear but insensitive to compression and bending. Further advantage was taken of the difference in the propagation velocity between the two waves, as the slower torsion wave lags and completely separates from the longitudinal wave after traveling several feet in the bar. Thus by using a long bar and measuring torsion near its center, the torsion wave was measured separate from the dominant influence of the compression wave.

The compression-measuring gauges are located close to the impact end of the bar; the torsion bridge, near the center about four feet from either end. The projectile, fired from the spirally rifled Cal. 30 gun (pitch 1 revolution in 5.92 inches), enters and deforms the end of the bar. The bar (0.803 in. in diameter, 8 ft long) is of homogeneous SAE 4340 steel; it has a measured hardness of Rockwell C-40.

Projectiles were 0.30 in. in diameter with the conical nose of 45° vertex angle. They are sufficiently harder (Rockwell C-58) than the target to remain elastic during penetration. The core was removed with the result that the projectile weighed only 3.3 grams while its moment of inertia about the longitudinal axis was 16×10^{-8} in.-lb-sec. Driving-band material was obtained by electrodeposition of copper.

Projectiles for these tests which are designated as "dry" are washed in a volatile solvent (acetone) and are what is usually described in friction literature as "mechanically" clean. There was no attempt made to remove the adsorbed oxide layer. Results indicate that this precaution would have made little difference at high surface speeds. Lubricated projectiles were coated with a special grease for which these experiments were originally devised, but again, as the results will show, the exact specification of the lubricant is unimportant. The surface on the conical end of the projectile was ground to a fine finish.

CALIBRATION

In addition to the usual methods of strain-gauge calibration, i.e., introducing known increments of resistance in the gauge circuit and direct voltage calibration of the oscilloscope, two methods specialized to ballistic techniques were employed. For the compression wave, a throw-off bar adjoins the measuring bar (Fig. 4) and thus traps the momentum in the compression wave. The momentum of the bar is absorbed by the linear spring through a deflection directly proportional to the initial bar-velocity and correspondingly proportional to the area under the force-time curve or initial momentum of the projectile.

[12] J. M. Krafft, Rev. Sci. Instr. **26**, 539 (1955).

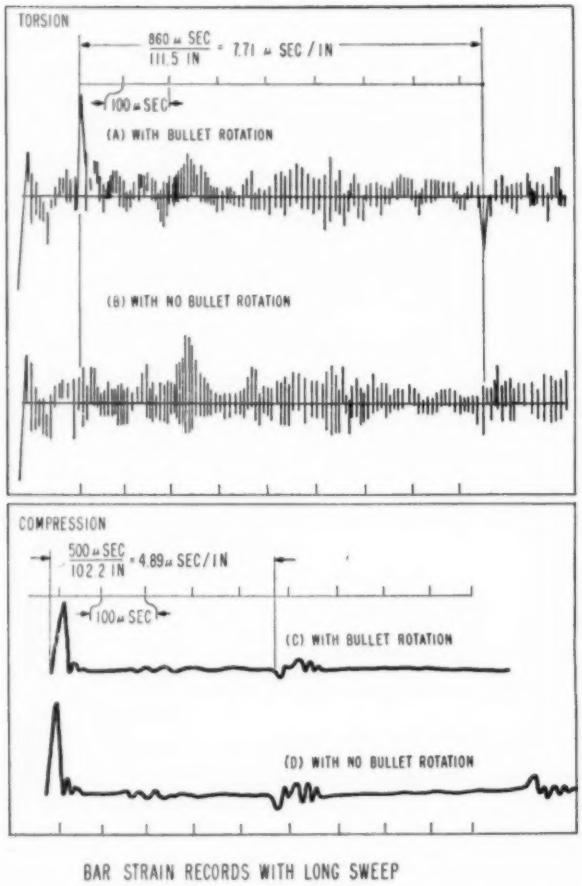
TORSION
860 μ SEC / 111.5 IN = 7.71 μ SEC / IN
100 μ SEC
(A) WITH BULLET ROTATION
(B) WITH NO BULLET ROTATION
COMPRESSION
500 μ SEC / 102.2 IN = 4.89 μ SEC/IN
100 μ SEC
(C) WITH BULLET ROTATION
(D) WITH NO BULLET ROTATION
BAR STRAIN RECORDS WITH LONG SWEEP

FIG. 5. Tracings of oscillograph records using slow sweep speed. (A) Torsion record with projectile spin. (B) Torsion with no spin. (C) Compression with spin. (D) Compression with no spin.

A second ballistic method providing calibration for the torsion wave employs a projectile prepared with flats on the cone surface [Fig. 1(C)]. The flats completely arrest the projectile rotation during penetration, a fact discerned by the lack of audible spinning as the projectile is caught after rebound. Equating the total angular momentum of this projectile to the area under the torque-time curve calibrates the torsional sensitivity of the recording system. Calibrations by the various methods were in agreement within 6%.

RESULTS OF TORSION MEASUREMENTS

The torsional and longitudinal waves as measured at the two gage sites are shown in Fig. 5, a tracing of oscillograph photographic records taken with relatively long sweep-time. The patterns show the difference between the strain waves resulting from penetration with a spinning projectile and those from a nonrotating projectile. While the compression wave records are esentially unaffected by the rotation, the torsion record for the spinning projectile (A) is markedly distinguished by the appearance of signals readily identified as incident and reflected torsion signals. The reflected torsion signal is reversed in sign as a result of reflection from a free end. It appears somewhat reduced in amplitude, presumably a result of attenuation rather than dispersion during its long traverse in the bar.[13–15] The rates of propagation for the torsion and compression waves as indicated in Fig. 5 are in good agreement with accepted values for steel.

It is apparent from Fig. 5(A) that substantial background signal tends to obscure the torsion wave. Fortunately, the background signal is not random but appears quite repeatable if the lateral position of impact on the bar end and striking velocity remain unchanged. The background signal can thus be considerably reduced by taking as the torsion signal the difference between the observed signal for penetrations with torsional friction and without. Two examples of corrected torsion signals obtained by this procedure are shown in Figs. 6(B) and 6(C). The net torsion signal is the dashed curve in each case.

To obtain the records [Fig. (6C)] without torsion, it would be desirable to penetrate with a nonrotating projectile. In actual fact, however, it is very difficult to reproduce striking velocity and crosswise position of impact upon changing guns. Both of these factors profoundly effect the background signal. As a compromise, the background nontorsion record was made by using a well-lubricated projectile fired from the rifled gun. It gave practically no evidence of torsional adhesion, yet corresponded closely to the background signal for the clean-projectile torsion record. The small pip in the lubricated projectile records corresponding to the peak of the clean projectile record has been excepted as the probable result of slight seizure even for this case. This pip is shown by-passed by the dashed line in Fig. 6(C).

A theoretical torque curve resulting from the "molten interface" hypothesis [Eq. (5)] has been plotted [Fig.

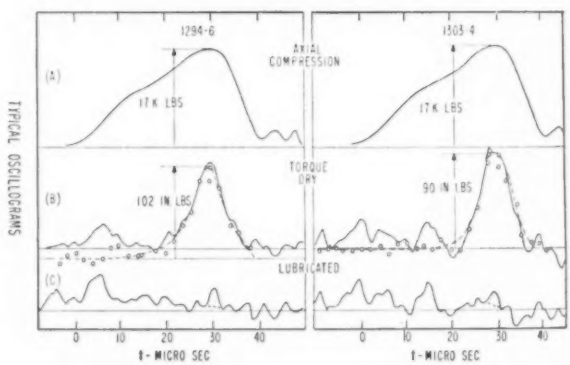

FIG. 6. Tracings of two sets of oscillograph records using fast sweep speed. (A) Torsion or axial force. (B) Torsion. (C) Torsion record using lubricated projectile. Dashed curve shows net difference between (B) and (C).

[13] R. M. Davies, Phil. Trans. Roy. Soc. **240**, 375 (1948).
[14] J. D. Owen and R. M. Davies, Nature **164**, 752 (1949).
[15] R. M. Davies and J. D. Owen, Proc. Roy. Soc. (London) **204A**, 17 (1950).

7(B)] using values of velocity and displacement obtained from the longitudinal force record [Figs. 6(A) and 7(A)]. The plot is shown in Fig. 7(B) superimposed upon the experimental curves for both tests shown in Fig. 6(B). The measured torque curve appears about equal in area to the experimental curve and is qualitatively similar in shape. The agreement lends support to the "molten interface" hypothesis as the dominating factor influencing the physical process of surface friction between "mechanically" clean surfaces at high velocity.

Deviations between the theoretical and experimental curves [Fig. (7B)] appear reasonable. It is observed that the friction is extremely sensitive to surface contaminants which would reduce the melting temperature of material at the interface. The lower than theoretical friction values early in penetration could result from contaminants on the projectile and target even after careful degreasing procedures. The high experimental final peak, on the other hand, could be due to a freezing and adhesion near the tip where, near the end of penetration, rotational velocity becomes very low. That only the tip freezes appears likely, as the maximum torque is only about one-tenth that which should result had the whole imbedded surface seized.

The high-friction records are typical of the maximum friction obtained. They are achieved by careful mechanical cleaning of the target and projectile as described earlier. When this amount of friction is considered to retard longitudinal motion, rather than rotation, it represents only about three percent of the energy loss of the projectile. A lubricant reduces the friction to an unmeasurably small value, although it is found that nearly any surface contaminant, such as that obtained by handling, will almost do this. These results agree with earlier measurements at NRL (unpublished) which showed a change of three to four percent in total penetration energy loss resulting from the same extremes of lubrication. It is clear now that this three to four percent represented all of the frictional-energy loss, not merely an increment of an unknown total loss. The earlier tests also showed only slight changes due to projectile-surface finish, which was not investigated with the present torsion-bar technique.

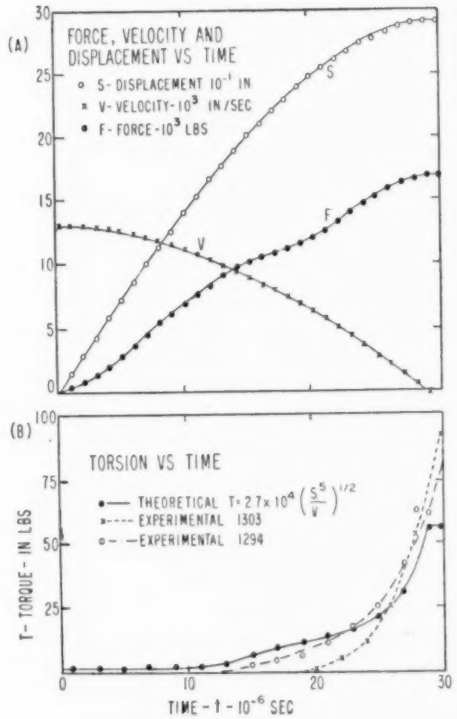

FIG. 7. (A) Measured longitudinal force *vs* time record (from test of Fig. 8). ×—computed velocity *V*. o—computed displacement *S*. (B) Torsion *vs* time records. ●—theoretical using Eq. (5). ×,o—experimental from Fig. 6.

ACKNOWLEDGMENTS

The author is indebted to G. R. Irwin, Superintendent, Mechanics Division, Naval Research Laboratory, for continued interest and encouragement in this problem and to his associate, A. M. Sullivan, for micrographs of the target sections.

Preferred Orientation of Platelets in X-Ray Diffractometer Powder Samples

JAMES E. MANSON
Geophysics Research Directorate, Air Force Cambridge Research Center, Air Research and Development Command, Cambridge, Massachusetts

(Received March 12, 1955)

A method is described for elimination of the effects of preferred orientation of platelets in a compressed powder sample having a plane surface exposed to the x-ray beam. The powder is diluted with a low absorption amorphous resin and the results extrapolated to zero concentration. The extrapolation is justified by analysis of an idealized model of the sample. A comparison between the analytical results and the results of an experimental study using silver iodide indicates the validity of the process.

INTRODUCTION

THE many advantages of x-ray diffraction techniques employing focusing goniometers and Geiger counter detection are sometimes offset in a specific application by preferred orientation in the sample. The form of the sample, a flat plate of powder, is conducive to such orientation. Methods of packing the sample which minimize this effect have been devised,[1] as have moving sample holders which eliminate certain types of orientation. In a recent application in this laboratory, a case was encountered which was not suited to either of these methods of elimination. The substance under study was AgI, which powder was largely made up of hexagonal and trigonal platelets, the plate plane being the hexagonal (0002) or the cubic (111). These planes were preferentially oriented parallel to the sample surface. In this case, the high absorption and scattering factors made it possible to dilute the sample with a neutral powder and eliminate the orientation by an extrapolation to zero density.

THEORY

In order to apply an extrapolation to the experimental data, it was necessary to develop a reasonable model for the oriented sample and to determine an analytic expression of the dependence of the intensity of the oriented reflection on the density of the sample.

The orientation was assumed to be caused by the compression of the powder against the glass slide used in preparing the samples. In this case, orientation at the surface would be nearly complete, and would be transmitted into the powder by particle interactions in the packing process. Thus the sample would be made up of a layer of more or less oriented powder on top of a bulk of randomly oriented powder. The model chosen was a simplified version of this. A thin homogeneous layer of imperfectly oriented particles was assumed at the surface. The thickness of this layer was assumed proportional to the partial density of AgI in the mixture. The remainder of the sample was assumed to be randomly oriented, and to extend indefinitely in thickness. The orientation of the surface layer was assumed perfect enough to eliminate contribution from this layer to any strong reflection other than that from the plate planes, but imperfect in that only a fraction (ϵ) of the particles would contribute energy through the receiving slit during traversal of the reflection region. Absorption by the gum tragacanth was ignored.

On the basis of this model an expression was derived for the ratio of the integrated intensity of the oriented line to the intensity of any other line as a function of the usual variables[2] plus ϵ and the proportionality factor k, relating oriented layer thickness (δ) and AgI partial density (ρ) by $\delta = k\rho$. Since AgI existed as a mixture of hexagonal (H) and face-centered cubic (C) structures at room temperature in all preparations tested, the proportion by volume of each must appear in the expression for this ratio.

This expression is (see Appendix):

$$R(\rho) = (P_{o1} + P_{r1})/P_{r2} \tag{1}$$

where:

$$P_{o1} = \epsilon(aQ_1^H + bQ_1^C)[1 - \exp(-2k\rho^2\mu_m \csc\theta_1)]$$

$$P_{r1} = (ap_1^H Q_1^H + bp_1^C Q_1^C)[\beta/(8\pi \sin\theta_1)] \times \exp(-2k\rho^2\mu_m \csc\theta_1)$$

$$P_{r2} = (ap_2^H Q_2^H + bp_2^C Q_2^C)[\beta/(8\pi \sin\theta_2)] \times \exp(-2k\rho^2\mu_m \csc\theta_2)$$

where:

a = volume of H/(volume of H + volume of C)
$b = 1 - a$
ρ = mass of AgI/unit volume of mixture
β = minimum angular aperture of receiving parallel slit assembly.

Subscripts:

1—oriented line
2—other line
o—oriented region
r—random region.

The other symbols are in common usage.[2]

[1] G. L. McCreery, J. Am. Ceram. Soc. **32**, 141 (1949).

[2] R. W. James, *The Optical Principles of the Diffraction of X-Rays* (G. Bell and Sons, London, 1950), pp. 34–50.

For the purposes of the present work the most important result from this expression is the value

$$\lim_{\rho\to 0} R(\rho)=\frac{(ap_1{}^H Q_1{}^H+bp_1{}^C Q_1{}^C)\sin\theta_2}{(ap_2{}^H Q_2{}^H+bp_2{}^C Q_2{}^C)\sin\theta_1}. \quad (2)$$

If the sample were ideal, no oriented layer would exist. In this case, we may derive the following expression:

$$R_{\text{ideal}}=\frac{P_{r1}}{P_{r2}}=\frac{(ap_1{}^H Q_1{}^H+bp_1{}^C Q_1{}^C)\sin\theta_2}{(ap_2{}^H Q_2{}^H+bp_2{}^C Q_2{}^C)\sin\theta_1}, \quad (3)$$

$$R_{\text{ideal}}\equiv\lim_{\rho\to 0} R(\rho). \quad (4)$$

This demonstrates the validity of the extrapolation process under the assumption of the validity of the theoretical model.

It will be noted that the limit (2) is not dependent on the power of ρ in the exponent of (1). This means that the propriety of the extrapolation is independent of the assumed relationship between oriented layer thickness and partial density.

EXPERIMENT

A. Sample Preparation

Two types of AgI powder were used in this work. Powder I was precipitated by slow dilution of AgI dissolved in concentrated $AgNO_3$ solution[3] and subsequently ground to pass 325 mesh. Powder II was precipitated in the same way, but not ground, since slightly lower temperature during precipitation caused smaller average crystal size, and the powder easily passed 325 mesh without grinding. Powder I was 88% face-centered cubic and Powder II was 94% face-centered cubic, the remainder in each case being hexagonal. These values were determined from the ratio of intensities of the $10\bar{1}3$ and 220–$11\bar{2}0$ lines.

By dilution of these powders with powdered gum tragacanth, a series of mixtures was prepared. The proportion by weight (d) of AgI was determined for each mixture. Samples for x-ray analysis were prepared, using standard Norelco specimen holders. These holders were used as powder pycknometers, thus determining a value of the mass of the packed powder (m). The volume (v) of the hole was known from measurement, and thus a value of the partial density of AgI in the actual packed powder sample was determined by

$$\rho=dm/v. \quad (5)$$

B. X-Ray Measurements

Integrated intensities were measured by totalling counts for a one degree (2θ) diffractometer scan over the region of a diffraction line. Background measurements were interpolated to the center of each line scan. These measurements were made for the 111–0002, 220–$11\bar{2}0$, $10\bar{1}3$ and 311–$11\bar{2}2$ reflections. The tube voltage was kept at 45 kilovolts peak, and filtered copper radiation was used. The receiving slit and tube current were chosen to make the peak of the 111–0002 reflection close to 600 counts per second for each sample. For facility and to avoid readout errors an atomic scale of 1000 scaler was used on the output. The rest of the equipment was the standard Norelco high and low angle Diffractometer and Basic Diffraction Unit with stabilized tube current.

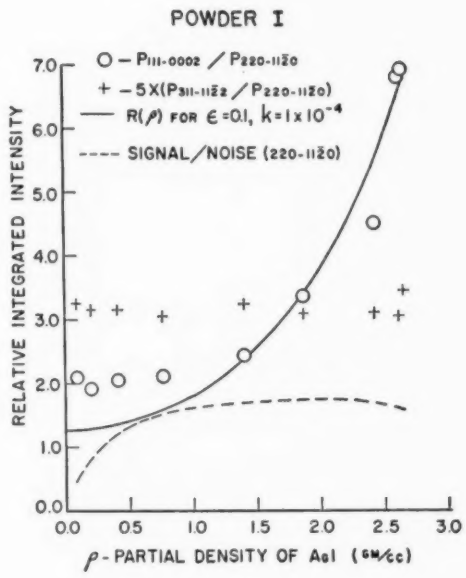
POWDER I
O – P111-0002 / P220-11$\bar{2}$0
+ – 5X(P311-11$\bar{2}$2 / P220-11$\bar{2}$0)
R(ρ) FOR ε=0.1, k=1x10⁻⁴
SIGNAL/NOISE (220-11$\bar{2}$0)
RELATIVE INTEGRATED INTENSITY
ρ - PARTIAL DENSITY OF AgI (GM/cc)

(a)

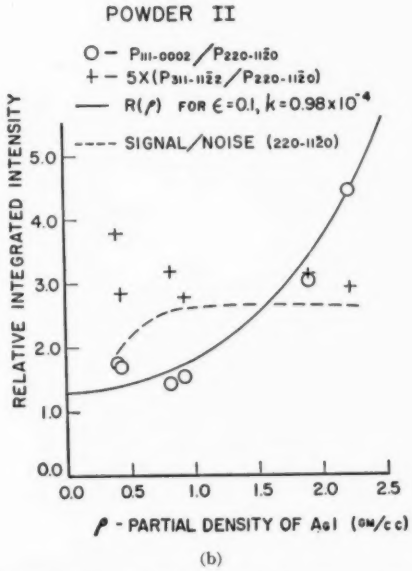
POWDER II
O – P111-0002 / P220-11$\bar{2}$0
+ – 5X(P311-11$\bar{2}$2 / P220-11$\bar{2}$0)
R(ρ) FOR ε=0.1, k=0.98x10⁻⁴
SIGNAL/NOISE (220-11$\bar{2}$0)
RELATIVE INTEGRATED INTENSITY
ρ - PARTIAL DENSITY OF AgI (GM/cc)

(b)

FIG. 1. Comparison of the ratio of the integrated intensities, P, with $R(\rho)$ for (a): Powder I; $a=0.12$, $b=0.88$, and (b): Powder II; $a=0.06$, $b=0.94$. Subscripts of P are indices of cubic and hexagonal planes. The units of k are cm^4/g.

[3] N. H. Kolkmeijer and J. W. A. van Hengel, Z. Krist. 88, 317 (1934).

RESULTS

The integrated intensities are expressed relative to the 220–11$\bar{2}$0 line, and are presented in Figs. 1(a) and 1(b). The solid line curves are calculated from (1). Several values of ϵ were chosen, and values of k found which forced a fit at the point corresponding to highest density. The value of ϵ which gave the best apparent fit was used for the curves shown. The artificial simplicity of the theoretical model is indicated by the fact that at the point of highest density for Powder I, the oriented layer model yielding the solid curve has a calculated layer thickness of about 3 microns. However, the general behavior of (1) indicates that the theoretical model, though an idealization, must correspond to the physical situation rather closely.

The fact that Powder I data extrapolated to a value of R not in agreement with (4) is ascribed to a decrease in the intensity of 220–11$\bar{2}$0 caused by the grinding operation with slip in (111–0002) plane. Disordering in this plane would decrease the intensity of reflections from all nonparallel planes.

The points indicated by crosses in Fig. 1 are values of the intensity ratio of 311–11$\bar{2}$2 to 220–11$\bar{2}$0, multiplied by 5. These values provide a check on the specificity of the effect of the dilution on the 111–0002 line. The value of this ratio calculated for $a=0.10$, $b=0.90$ with no temperature correction is 0.60. The grouping of the crosses around $R=3.0$ thus provides a check on the assumed structures, which have been substantiated in previous work,[4] as well as proving the common basis for the other measurements.

CONCLUSIONS

The method described may be used for the elimination of orientation effects from samples of a platy powder of a substance with high absorption and high atomic number constituents. Once the general behavior of the oriented line intensity has been determined by about 4 samples, a value of d can be chosen for measurement of all other reflection intensities with fair assurance of eliminating all effects of preferred orientation, since the virtual elimination of the orientation of the plate plane assures the smallness of any other orientation effects. Thus, in the work of this laboratory the determination of the proportions of cubic and hexagonal AgI are made by measurement of the ratio of the 10$\bar{1}$3 line to the 220–11$\bar{2}$0 line, from samples made up from a mixture of $\frac{1}{3}$ AgI to $\frac{2}{3}$ gum tragacanth by weight. This corresponds to $\rho \doteq 0.4$ g/cc.

[4] J. E. Manson, J. Appl. Phys. **26**, 423 (1955).

APPENDIX. DERIVATION OF EQ. (1)

The average contribution to the 111–0002 reflection from a crystallite of volume v in the oriented layer is:

$$\Delta P_{o1}' = I\epsilon Q_1 v. \tag{6}$$

Introducing simple absorption and integrating over the volume intercepted by a plane parallel beam of cross section S and intensity I_o we find:

$$P_{o1}' = I_o \epsilon Q_1 N\bar{v} \int_0^{S \csc\theta_1 \delta} \exp(-2\mu z \csc\theta_1) dV. \tag{7}$$

In this expression N is the number of crystallites per unit volume, thus $N\bar{v}=\rho/\rho'$ where ρ' is the density of pure AgI. Also $dV = S \csc\theta_1 dz$, $\mu = \mu_m \rho$ and $\delta = k\rho$. Using these relations we find:

$$P_{o1}' = \frac{I_o S \epsilon Q_1}{2\mu_m \rho'} [1 - \exp(-2k\mu_m \rho^2 \csc\theta_1)]. \tag{8}$$

In the random region below the oriented layer, ϵ is replaced by $p_1\beta/(8\pi \sin\theta_1)$. Here β replaces the factor l/r in Eq. (2.48) of James.[2] The multiplicity factor, p_1, also has been explicitly introduced. Analogous to (8) we find:

$$P_{r1}' = \frac{I_o Q_1 p_1 \beta S \rho \csc\theta_1}{8\pi\rho' \sin\theta_1} \int_\delta^\infty \exp(-2\mu z \csc\theta_1) dz$$

$$= \frac{I_o S Q_1 p_1 \beta}{(2\mu_m \rho') 8\pi \sin\theta_1} \exp(-2k u_m \rho^2 \csc\theta_1). \tag{9}$$

Replacing subscript "1" with "2" yields P_{r2}'. Removal of common factors and introduction of the linear combination of Q and pQ proper for the mixture of structures of equal density leads directly to P_{o1}, P_{r1}, and P_{r2}. The (H) and (C) which appear are superscripts denoting the structure on which p and Q are based.

JOURNAL OF APPLIED PHYSICS VOLUME 26, NUMBER 10 OCTOBER, 1955

Conduction and Breakdown in Hexane*

W. B. GREEN
Laboratory for Insulation Research, Massachusetts Institute of Technology, Cambridge, Massachusetts
(Received April 7, 1955)

Conduction currents in hexane, studied as a function of spacing, metal, and heat treatment of the electrodes over the field-strength range from 0 to 250 kv/cm, obey neither a field-enhanced thermionic emission nor the customary field emission relation. The most important factor determining the currents appears to be a surface layer on the cathode. Exposing the liquid to gamma rays increases the current in a fashion that indicates a decrease of the effective work function rather than merely a collection of ionization products. Heat treatment of the cathode, by changing the nature of the surface layer, changes the emission. It appears that positive ions collect on the more or less insulating surface layer and build up intense local fields that cause electron emission. The size of the local field depends on the number of the ions arriving per second and on the thickness, homogeneity, and conductivity of the surface layer.

For some electrodes the current increases with gap width for constant field; previous investigators have interpreted this fact as evidence of impact ionization in the liquid. However, change of current with gap width proves to be an electrode property; some electrodes do not show it.

In one case the current was measured up to breakdown (1060 kv/cm). There is an indication that impact ionization may exist above 800 kv/cm; if so, the ionization factor is very small.

A variety of purification systems was tried but no influence of the purification treatment on the conduction currents was found.

INTRODUCTION

ONE of the long-range projects of the Laboratory for Insulation Research is to gain an understanding of electrical conduction and breakdown in dielectric materials. Most extensively investigated thus far are the alkali halide crystals since their simple structure allows an easier theoretical interpretation of the experimental results.[1,2] In the course of this work, the importance of electron emission from the electrodes and of field distortion by space charge became increasingly apparent and special techniques were developed for studying these phenomena at field strengths well below breakdown.[3] A recent investigation has clarified the question of the origin of noise accompanying the prebreakdown current in crystals.[4]

Conduction and the sequence of events leading to breakdown in gases at low pressures are today well understood and can serve as a foundation for studies in the condensed phases. In the work of D. R. Young,[5] the electric breakdown of CO_2 was investigated as a function of pressure into the liquid phase; this work showed the importance of electron emission from the cathode in breakdown at high gas pressures. To complete this picture of conduction and breakdown in all phases, a study of the fundamental effects encountered in liquids was undertaken. Since the breakdown itself changes the properties of the liquid, the main emphasis was placed on the study of the prebreakdown currents.

PREVIOUS STUDIES ON LIQUID DIELECTRICS

The earliest detailed investigation of conduction currents in dielectric liquids seems to have been that of Quincke.[6] Using a static generator up to 30 kv and employing interelectrode gap widths of 1 to 3 mm, he reached a maximum field strength of 300 kv/cm and showed that the current depends on voltage, gap width, and the nature of the liquid. Quincke concluded that the currents are nonohmic and probably electrolytic in origin. Schröder,[7] using field strengths up to 8 kv/cm, demonstrated in addition that the magnitude of the current depends on the nature of the gas to which the electrodes are exposed. Jaffé[8] established that, for fields of less than 100 v/cm, a large part of the current is caused by external ionizing radiation.

Nikuradse[9] studied currents in dielectric liquids over a wide range of field strengths and gap widths. He found that the current depends on the purity of the liquid, on temperature, electrode geometry, and electrode material, but is independent of pressure over a wide range. His results were summarized in an ionization equation, $J=J_0e^{\alpha d}$, where J_0 is the current for $d=0$, α an impact ionization coefficient, and d the gap width. This work was attacked by Inge and Walther,[10] who found no gap-width dependence of dc breakdown field down to gaps of 2μ and suggested that field emission is the source of all the prebreakdown current.

* Sponsored by the Office of Naval Research, the Army Signal Corps, and the Air Force under Office of Naval Research Contract N5ori-07801.

[1] See A. von Hippel, J. Appl. Phys. **8**, 815 (1937); Trans. Faraday Soc. **42A**, 78 (1946); A. von Hippel and R. S. Alger, Phys. Rev. **76**, 127 (1949).

[2] A. von Hippel, Z. Physik **68**, 309 (1931); J. W. Davisson, Phys. Rev. **70**, 685 (1946); **73**, 1194 (1948); M. E. Caspari, Tech. Rep. 90, Office of Naval Research Contract N5ori-07801, Lab. Ins. Res., Mass. Inst. Tech., November, 1954.

[3] von Hippel, Gross, Jelatis, and Geller, Phys. Rev. **91**, 568 (1953).

[4] D. A. Powers and T. Suita, Tech. Rep. 91, Office of Naval Research Contract N5ori-07801, Lab. Ins. Res., Mass. Inst. Tech., January, 1955.

[5] D. R. Young, J. Appl. Phys. **21**, 22 (1950).

[6] G. Quincke, Wied. Ann. **54**, 385 (1895).

[7] J. Schröder, Ann. Physik **29**, 125 (1909).

[8] G. Jaffé, Ann. Physik **42**, 303 (1913).

[9] A. Nikuradse, Z. Physik **77**, 216 (1932).

[10] L. D. Inge and A. Walther, Tech. Phys. U.S.S.R. **1**, 539 (1934).

Three subsequent papers attempted to identify the mechanism which creates charge at the cathode. Dornte[11] and Baker and Boltz[12] showed that the cathode is a source of considerable current, since the exposing of electrodes to hydrogen rather than oxygen results in an increase of current by a factor as large as 10^5. These investigations and that of LePage and DuBridge[13] agreed that log I is a linear function of $\sqrt{E}$. The latter conclude that the current is due to field-enhanced thermionic emission and derive the following relation for this case

$$J=AT^2\exp\left[-\frac{\phi e}{kT}+\frac{1}{2.3kT}\left(\frac{e^3E}{\kappa'}\right)^{\frac{1}{2}}\right], \qquad (1)$$

where κ' is the dielectric constant of the liquid. None of these three studies include gap width as a variable; hence a volume effect such as impact ionization could not be observed.

A distinct advance was made in more recent papers by Ruhle[14] and Goodwin and Macfadyen,[15] who measured the currents as a function of electrode gap width and of field strength. Extrapolation to zero gap width showed the existence of a zero gap-width current that obeys a field emission relation of the form

$$J=AE^2\exp\left(-\frac{b}{E}\right). \qquad (2)$$

Jaffé and LeMay[16] studied time-dependent currents in hexane for wide gaps and low voltages and concluded that these currents are ionic and in their magnitude largely determined by polarization effects at the electrodes.

Evidence was presented by Plumley[17] and by Pao[18] in support of a dissociation theory, but objections on theoretical grounds, as well as those concerning the experimental evidence, make this conclusion doubtful.

Additional information concerning the conduction currents in liquids is derived from breakdown data. Salvage[19] obtained a rough correlation between the vacuum work function of electrodes and the breakdown-field strength for hexane. Goodwin and Macfadyen[15] demonstrated that the time lag to breakdown is determined by positive ion mobility. Crowe, Bragg, and Sharbaugh[20] found that the breakdown strength of the aliphatic hydrocarbons is related to their density.

[11] R. W. Dornte, Ind. Eng. Chem. **32**, 1529 (1940).
[12] E. H. Baker and H. A. Boltz, Rev. **51**, 275 (1937).
[13] W. R. LePage and L. A. DuBridge, Phys. Rev. **58**, 61 (1940).
[14] F. Ruhle, Physik. Z. **44**, 89 (1943).
[15] D. W. Goodwin and K. A. Macfadyen, Proc. Phys. Soc. (London) **B66**, 85 (1953).
[16] G. Jaffé and C. Z. LeMay, J. Chem. Phys. **21**, 920 (1953).
[17] H. J. Plumley, Phys. Rev. **59**, 200 (1941).
[18] C. S. Pao, Phys. Rev. **64**, 60 (1943).
[19] B. S. Salvage, Proc. Inst. Elec. Engrs. (London) **98**, Pt. 4, 15 (1951).
[20] Crowe, Bragg, and Sharbaugh, J. Appl. Phys. **25**, 392 (1954).

APPARATUS AND PROCEDURES

The sample holder (Fig. 1) of Pyrex is an integral part of the purification system. The electrodes (Fig. 1), supported by monel rods, consist of a polished monel sphere for anode and a plane cathode. Optical polish of the cathode produced a surface scratch-free and flat within one wavelength. The sphere and plane electrode system was chosen to make gap-width measurements simpler and more accurate. This measurement was made with a 150X microscope which allowed gaps from 75 to 1000μ to be measured to an accuracy of about $\pm 2\mu$. The field distortion caused by the sphere-plane system is so small (*ca* 2%) that $E=V/d$ with sufficient accuracy. A Wilson seal[21] allowed free vertical movement of the anode.

The liquid used throughout this work is hexane. According to the supplier, the liquid contains not less than 99 mole % normal hexane, and, as the most probable impurity, methylcyclopentane. Hexane was chosen because an extensive literature exists on the breakdown of this material.

It has always been assumed that the purity of the liquid plays an important role in the final experimental results. To test this point, two purification systems were developed. The first of these systems (Fig. 2) was similar to that of Plumley.[17] A purification cycle in this system consisted of distillation under reduced pressure with a small temperature difference, filtration, drying with silica gel and metallic sodium, and an electrolytic removal of ions with a strong dc field. Flask 3 and the

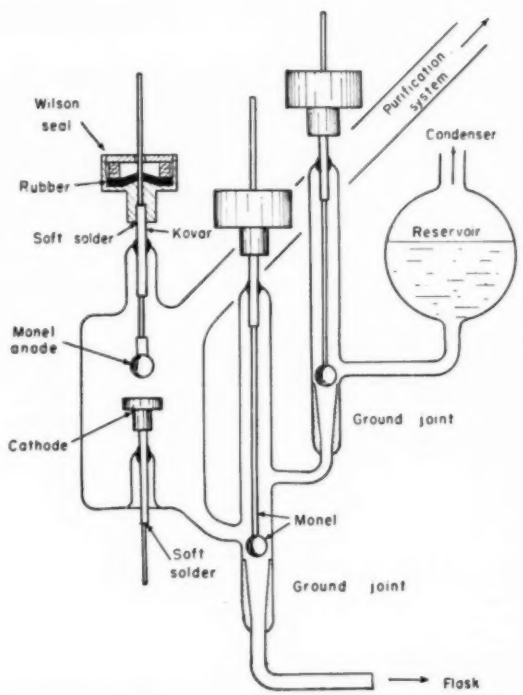

FIG. 1. Sample holder, electrodes, and valve assembly.

[21] R. R. Wilson, Rev. Sci. Instr. **12**, 91 (1941).

associated reservoir and condenser were used for introduction of the hexane sample and for flushing the sample holder. The design of the valves connecting this part of the system to the sample holder is shown in Fig. 1. A monel ball bearing, attached to a monel lift rod, seats in the outer half of a conical ground joint. The ball, lapped to fit the ground joint, had a tendency to bind, which, combined with the friction between the lift rod and Wilson seal, served to keep the valve closed.

After studies were completed on this system, a second system was set up utilizing only distillation and electrolytic cleaning, This change was made to ascertain whether the chemicals used in the first systems were a source of contaminant.

To achieve the desired voltage stability, batteries were employed throughout this work. Several sizes of batteries were used so that almost any voltage in the range 0–8000 v could be obtained. Voltage was measured with an electrostatic voltmeter. Current measurements were made with a vibrating reed electrometer which allowed continuous coverage of the range of currents from 10^{-15} to 10^{-7} amp. The sample holder, electrometer connection, and voltage supply were completely shielded.

To obtain meaningful data, currents must be steady for all the voltages in the operating range and reproducible for the same electrode and gap width. Only after extensive and careful conditioning can this requirement be met. On a new set of electrodes a stable current was usually obtained for low voltages; at higher voltages the current may increase rapidly and with great variability. To achieve a stable current at any particular voltage, it was usually necessary first to increase the voltage for a short period beyond the desired value. The achievement of a steady current does not necessarily indicate reproducibility. For some electrodes each new current-voltage curve for the same gap spacing will show a different current level while the shape of the curve remains constant. Conditioning must continue until this effect is eliminated or, at least, minimized.

To be comparable, all current-voltage data must be obtained in precisely the same manner. As previous investigators have shown, the value of the current measured one minute after an increase of voltage is only negligibly different from that measured after several hours, hence a one-minute interval between voltage increases and current reading was maintained throughout this work. At the conclusion of a run the voltage was reduced to a small value (usually 18 v) until the current reached equilibrium. This process of reaching equilibrium usually takes from several to 45 minutes depending on the nature of the electrode. If equilibrium is not awaited between runs, the current values for the lower voltages are usually not reproducible.

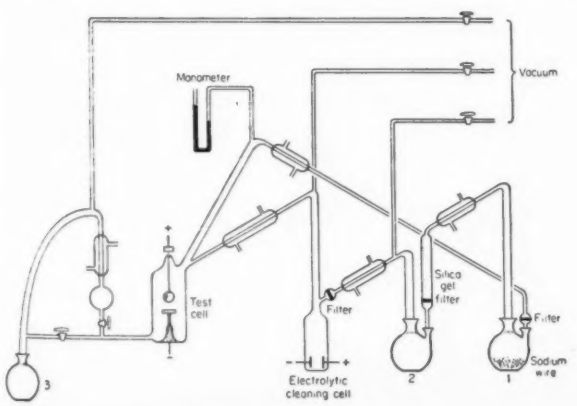

FIG. 2. Hexane purification system.

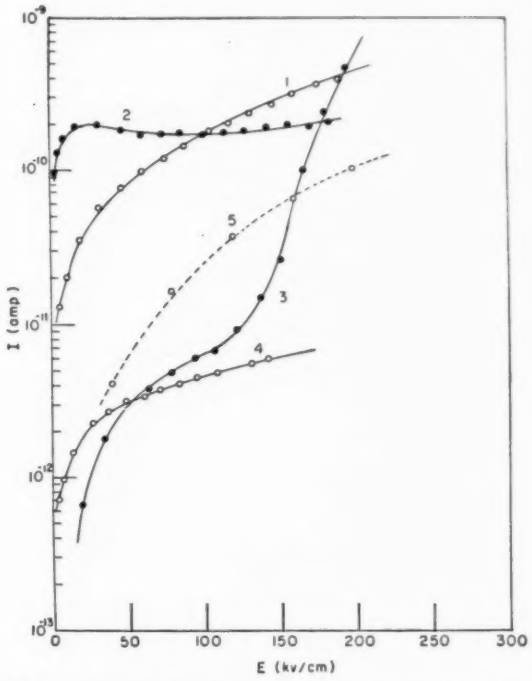

FIG. 3. Curves 1 to 4 are emission characteristics of various cathodes selected to show variations of slope and magnitude of current for a fixed electrode geometry. Curve 5 is a plot of Eq. (3).

RESULTS AND DISCUSSION

Figure 3 shows a series of current-voltage curves chosen to show the possible variations in magnitude and slope caused solely by changes of the cathode. Curves 1 to 4 are taken from measurements discussed in detail below; their differences are due to changes in cathode material and heat treatment. They represent data taken for the same sample, a gap width of about 420μ, and identical electrode geometry.

The first conclusion to be drawn from this figure is that the magnitude of the current depends strongly on the nature of the cathode. Figure 7 below, where gap width is a variable, indicates that a significant current would remain for zero gap width. It is apparent that the cathode is a source of at least part of the current.

From Fig. 3 it is reasonable to conclude also that negative space charge has only a small effect, if any, on the shape of these curves. If the shape of curve 4 were determined by negative space charge, curve 1, where

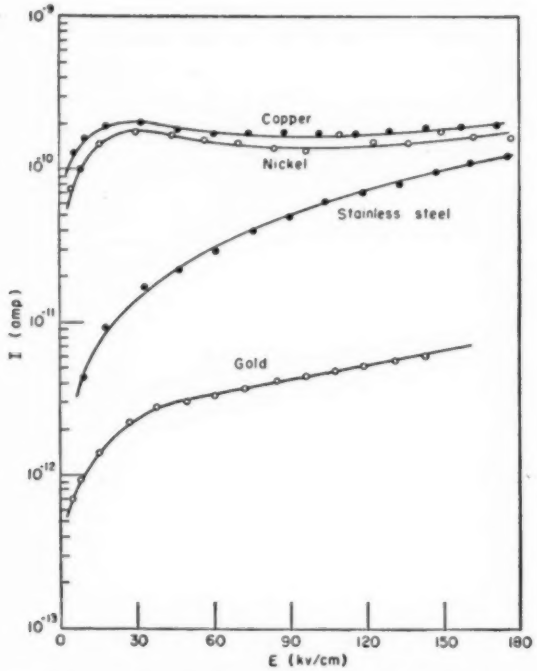

FIG. 4. Emission characteristics for cathodes of various materials with a fixed electrode gap width.

the current is higher by a factor of about 500, should increase more slowly, if at all, with increasing field strength. Curve 3, with its even steeper slope supports this argument.

There exists a considerable variation in the slope of the curves 1 to 4 at a given field strength. Since the liquid is the same for all four curves, the simple field-enhanced thermionic emission theory represented by Eq. (1) is obviously not valid.

If ϕ in the field emission Eq. (2) becomes smaller than 0.01, the exponential current dependence on field strength disappears, and approximately

$$J = AE^2. \tag{3}$$

A simple field-emission relation such as Eq. (2) cannot account for currents which increase more slowly with increasing field strength than prescribed by Eq. (3). Curve 5 of Fig. 3 is a plot of Eq. (3) with the constant A assigned appropriately. Only in the upper portion of curve 3 does the current increase faster with field then curve 5. Hence the usual picture of field emission is also not able to explain these results.

As a working hypothesis, let us assume the following situation. Positive ions are always present in the liquid because of external radiation or dissociation of impurity molecules. When an external field is applied, these ions drift toward the cathode, but a cathode surface layer impedes their immediate neutralization. The ions then set up a local field across the surface layer that tends to produce electron emission. The size of this local field depends on the magnitude of the ionic current and the probability of neutralization of the ions. For a given applied field some equilibrium results; the details of the local field then depend on the nature of the surface film.

The number of electrons which pass through the surface potential barrier under the influence of this local field will be determined by the thickness, homogeneity, and electrical properties of the surface layer. Since such detailed knowledge on surface films on metals is not now available, it is likely that only the major features of this theory can be verified.

Figure 4 shows the result for four different metals as cathode under otherwise constant conditions. The work functions for these metals increase in the order Fe<Ni<Au<Cu. The slopes should similarly increase and the magnitude of the current decrease with increasing ϕ, but apparently no such simple dependence exists on the electrode work function. If the crucial factor is not the electrode metal but its surface layer, this result is not surprising.

The form of the curves for gold and stainless steel are similar and seem to indicate that an increasing field leads to an increased number of positive ions on the surface, hence to higher emission. This is borne out by a study of the current as a function of gap width. Figures 5 and 6 show the results for the gold and the stainless steel cathodes, respectively. In both cases a volume dependence of the current suggests that a larger liquid volume increases the ion supply, and hence the emission. In both cases the surface layer seems to be a fairly good insulator.

A detailed study of the surface of 18-8 stainless steel by Vernon and associates[22] shows that surfaces obtained by polishing, as in the present work, are affected by the heat of polishing and the resulting material is largely

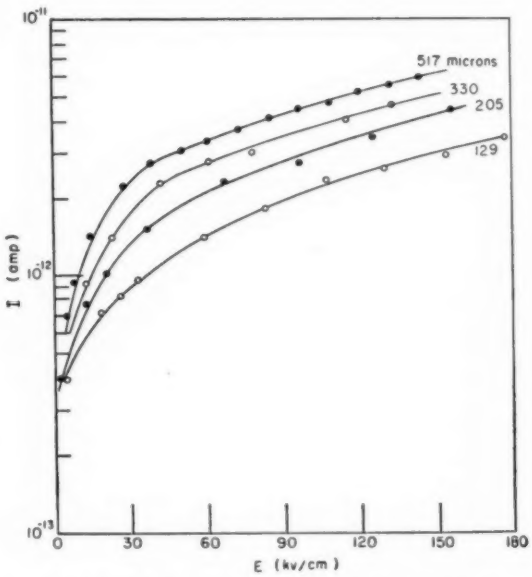

FIG. 5. Emission characteristics of a gold cathode for various gap widths.

[22] Vernon, Wormwell, and Nurse, J. Iron and Steel Inst. (London) **150** (2), 81P (1944).

Cr_2O_3. For a "high grade" polish the composition of the surface material was 90% Cr_2O_3 and 10% Fe_2O_3 by weight; the percentage of Cr_2O_3 increased by further polishing. Our material is 440*C* stainless steel which contains the same amount of chromium as 18-8 stainless steel. Considering the exceptional polish applied to the cathode in this work it seems likely that the surface layer is nearly all Cr_2O_3, which apparently is a good insulator.

The surface layer on gold presents a much different problem since the gold was evaporated on a polished monel surface. Gold is supposed to form no oxide, and the work of Trapnell[23] shows that at room temperature gold will not chemisorb O_2, N_2, or H_2, but will chemisorb CO, C_2H_2, and C_2H_4. The affinity for these latter two hydrocarbons suggests that if no other layer is present a layer of hexane molecules may be bound to the surface of the gold and act as an insulator.

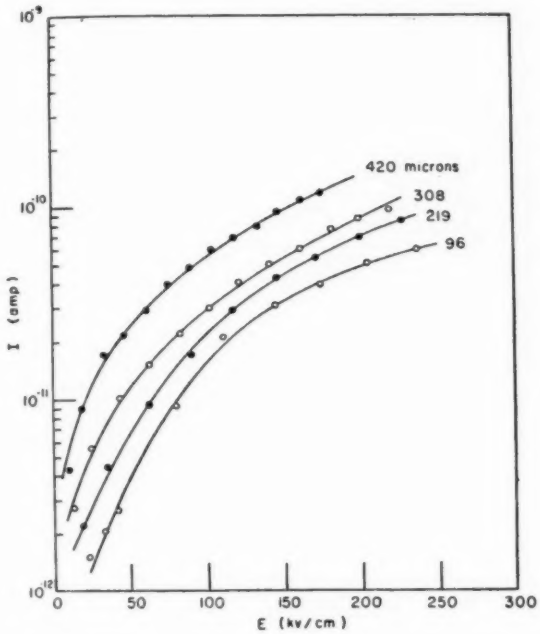

FIG. 6. Emission characteristics of a stainless steel cathode for various gap widths.

The form of the curves for copper and nickel (Fig. 4) are almost identical and suggest that after the attainment of an initial equilibrium at low field strengths, adequate electrons are available to neutralize incoming ions and prevent increase in the local field at the cathode. A detailed study of copper (Fig. 7) supports this contention; the results for nickel are not shown here, since they are nearly identical. No change of current with gap width occurs except for very small fields, showing that an increased volume of liquid, that is, an increased ion supply, does not influence the emission.

No detailed studies of the surface of polished nickel seem to have been made, although it appears that the surface layer is NiO. Studies on copper[24] show that the material on a polished surface is entirely Cu_2O to a depth of 100 to 200 A. It is well known that Cu_2O is a semiconductor, especially when containing some excess Cu.

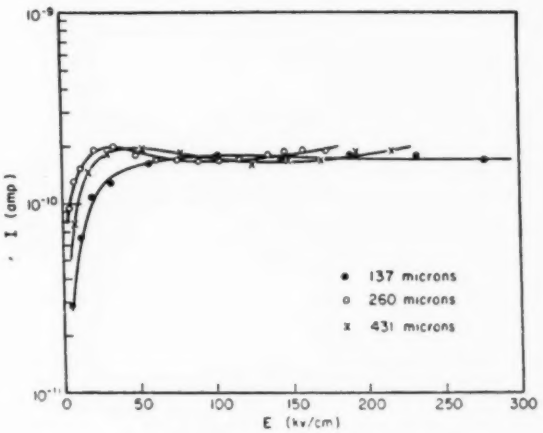

FIG. 7. Emission characteristics of a copper cathode for various gap widths.

Since the surface material apparently is the critical factor for the current voltage relation, heat treatment in controlled atmospheres should change the surface and with it the current values. Figure 8 gives the results for three different treatments of 440*C* stainless steel. Curve

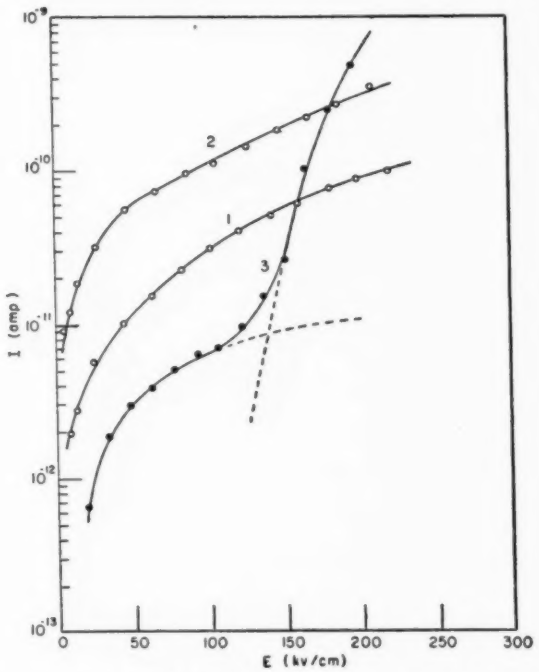

FIG. 8. Emission characteristics of a stainless steel cathode showing variations of current by heat treatment for constant gap width: (1) no treatment; (2) 1 hour at 600°C in air; (3) 1 hour at 400°C in H_2.

[23] B. M. W. Trapnell, Proc. Roy. Soc. (London) **A218**, 566 (1953).

[24] G. D. Preston and L. L. Bircumshaw, Phil. Mag. [7] **20**, 706 (1935).

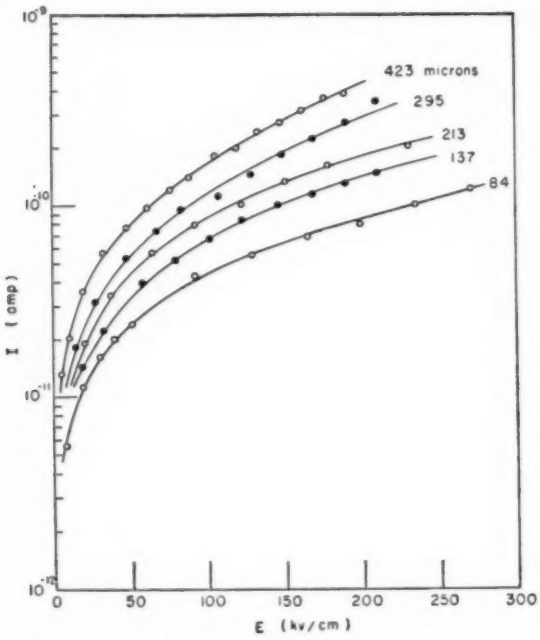

FIG. 9. Emission characteristics of a stainless steel cathode heated 1 hour at 600°C in air, for various gap widths.

1 from Fig. 6 for an untreated polished electrode, has been discussed above. For curve 2, taken from Fig. 9, the electrode was heated for 1 hr in air at 600°C. The study by Vernon[22] indicates that this treatment should favor the growth of a small amount of Fe_2O_3, a relatively good insulator. The current has increased, as would be expected for an increase in surface field.

Curve 3 of Fig. 8, taken from Fig. 10, is the result of heating a stainless steel electrode at 400°C for 1 hr in hydrogen. The portion of the curve below 100 kv/cm seems to indicate, by its decrease, that the insulating layer at the surface, and with it the surface field, has been weakened, but above 150 kv/cm the current increases much more rapidly than for any other case studied in this investigation. Apparently a part of the surface begins to emit with a work function different from that of a normal oxidized area. The dashed portion of curve 3 is added to suggest the possibility that the measured current is the sum of current from two different sources. Further treatment with higher temperatures and longer times did not produce any further changes in these curves.

Similar heat treatment both in oxidizing and reducing atmospheres failed to produce any change in the emission from nickel.

Since it seems that ions from the liquid produce the surface charge responsible for field emission, an increase of the ion concentration in the liquid should increase emission. The hexane was therefore irradiated by a (9.64 mg) Ra source. The 1.1-Mev gamma rays from radium are strongly absorbed and very effective ionizers. Because of the geometry of the electrodes, it is possible that the number of ions collected increases with increasing voltage because we collect from a larger volume. Hence, the additional current caused by radiation should increase in any case with increasing voltage. However, the increase of current appears to be constant on a logarithmic scale (Fig. 11), hence represents not merely an increase of collected ionization current, but a change in the effective work function caused by an increased number of ions at the cathode layer. This is confirmed by a comparison of the situation for steel *vs* copper (Figs. 11(a) and 11(b)). The collected ionization current should be identical; actually the separation of the curves is only half as large in (b) as in (a). In addition to indicating that the increase of current is due to a change of ϕ, these results appear to verify that the difference in the shape of the curves found for copper and stainless steel lies in the efficiency of neutralization of ions at the surface layer. The copper surface layer allows freer neutralization of the incoming ions, hence shows no volume dependence of the current and no increase of current with field strength over a wide range.

The intensity of the radiation from the source used here is approximately 3×10^4 times greater than the background radiation; still the increase of current due to this radiation is relatively small, It seems, therefore, reasonable to conclude that the source of the ions for most of the measured current must be dissociation in the liquid.

In the same manner as the layer forms on the cathode, a layer may form on the anode surface. Furthermore, in the liquid equal numbers of positive and negative ions must be created; hence a charged surface layer might

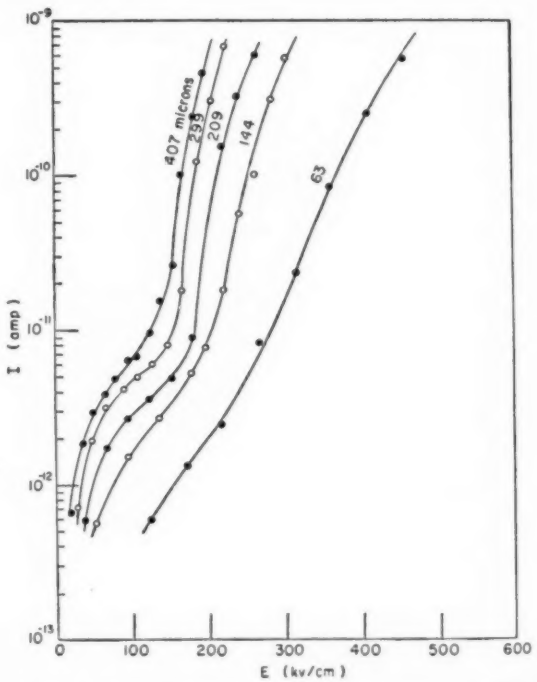

FIG. 10. Emission characteristics of a stainless steel cathode heated 1 hour at 400°C in H_2, for various gap widths.

exist at the anode as well. The influence of such an anode field, however, should be negligible as long as the electrons can pass.

To test this experimentally, the polarity of the sample holder was reversed and a stainless steel and a monel anode compared, since these two materials behave very differently as cathodes. No effect was observed.

It has been suggested by many previous investigators that the separation of the current-voltage curves produced by changing gap width (see Fig. 9) indicates impact ionization. The results in Fig. 12 refute this contention. Without space-charge effect, α is a function of field strength alone. For two gap widths, d_1 and d_2, and corresponding currents I_1 and I_2 for a constant field

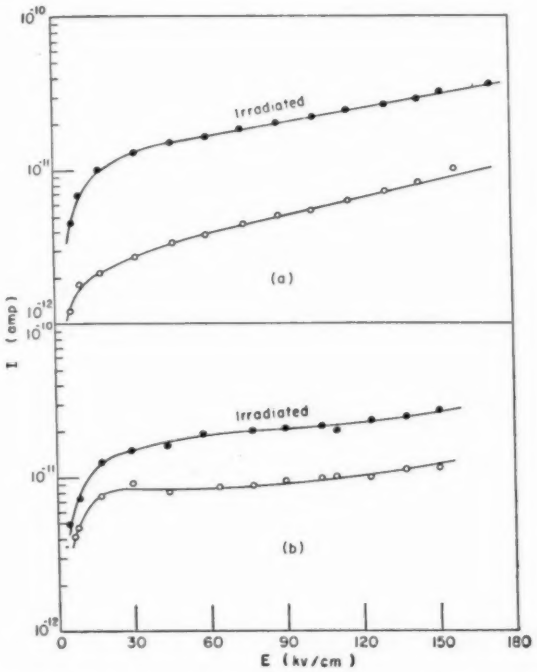

FIG. 11. The influence of gamma radiation on emission characteristics for a constant gap width: (a) stainless steel cathode, (b) copper cathode.

strength $I_1/I_2 = e^{\alpha(d_1-d_2)} = \text{constant}$. In Fig. 12 is plotted the current from 3 different electrodes for 2 values of gap width, the same d_1 and d_2 in all three cases. The stainless steel curves show a wide separation, gold a smaller one, and copper no separation at all. These results definitely establish that the curve separation is determined, not by the liquid, but by a property of the cathode.

A further evidence for the absence of impact ionization at these field strengths is the curve shown for copper. If α is large enough to contribute to the current, the current-voltage curves should rise rapidly with increasing field strength. The rise in the copper curves is negligible.

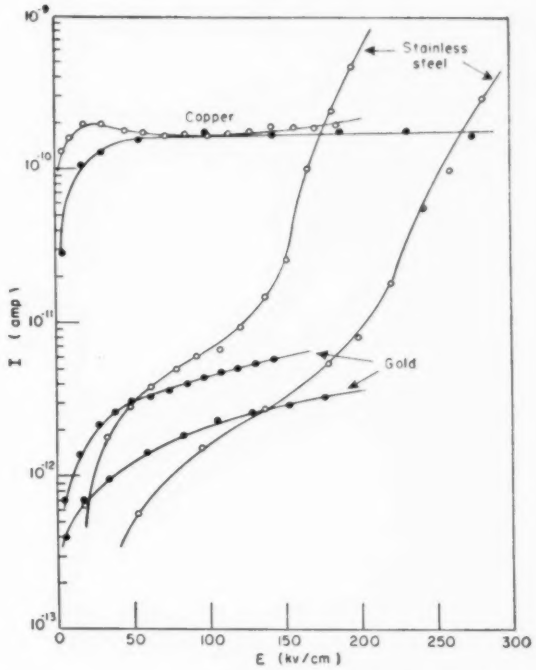

FIG. 12. Emission characteristics of 3 cathodes showing curve spacing: gap widths about 100 and 420μ for each cathode.

BREAKDOWN IN HEXANE

Figure 13 gives a current characteristic up to breakdown for a well-conditioned electrode; the field strength was increased to 1045 kv/cm several times before a further increase of voltage resulted in breakdown at 1060 kv/cm. A stable current was observed at all fields up to 1045 kv/cm; however, the increase to 1060 kv/cm resulted in a widely fluctuating current followed immediately by a spark.

The small increase in current slope above 800 kv/cm

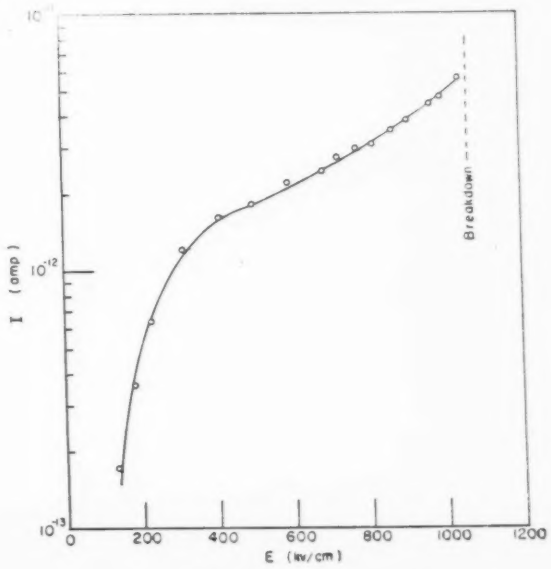

FIG. 13. Prebreakdown current.

may indicate that a new source of current is present. If this is impact ionization, e^{ad} has a value immediately below breakdown of not more than 2.

The value of breakdown field strength, 1060 kv/cm, agrees well with the work of Salvage[19] for dc breakdown of hexane.

STUDIES ON THE EFFECT OF PURIFICATION

The purification system of Fig. 2, allows one to investigate the effects of drying by Na and by silica gel. The modification of this system previously described eliminates all chemical treatment and depends entirely on distillation and electrolytic cleaning. With these systems, a wide variety of purifying operations are possible. Many of these were repeated numerous times and electrolytic cleaning cycles up to one week in length were tried. In addition, the liquid was pretreated before introduction into the system with mercury, water, concentrated H_2SO_4, and concentrated NaOH. None of these treatments vary in any measurable way the current-voltage curves.

Since it appears that positive ions, probably produced by dissociation of impurities, provide the charges needed for field emission, the conclusion is that the level of this impurity is not materially reduced by these attempts at purification. It should be noted that no low-field ionic saturation current, observed by other investigators, was was seen in this work either before or after purification efforts.

CONCLUSIONS

The experimental evidence collected here gives a clear qualitative picture of the behavior of hexane under field strengths from small values up to breakdown. As the voltage increases from zero, positive ions accumulate in front of the cathode and set up an intense local field across a surface layer. This field induces field emission. For any applied field strength, the local field thus established is determined by a balance between the supply of ions from the liquid and the neutralization of these ions by electrons emitted from the metal. The efficiency of the neutralization depends on the conductivity, homogeneity, and thickness of the surface layer. As the applied field strength increases, the number of ions reaching the cathode, and with it the emission, increases.

The electrons emitted from the cathode gain energy from the field in the liquid but lose it by exciting vibrations in the molecules by inelastic collisions as postulated by von Hippel.[25] They do not acquire ionizing velocities until about the breakdown field strength is reached. When the current of ions becomes sufficiently large to distort the applied fields (here apparently for e^{ad} of the order of 2), breakdown must occur.[26]

If, instead of a dc voltage, a pulse voltage of adjustable length and amplitude is applied, the breakdown strength should be affected. In shorter times, fewer ions in the liquid are able to reach the cathode; the surface charge is reduced and the emission impaired. A larger field strength is needed in order to produce the electron emission required for breakdown. Hence an increase in breakdown field strength might be expected, when the pulse length becomes smaller than a few microseconds.

ACKNOWLEDGMENT

The author wishes to acknowledge his gratitude to Professor A. R. von Hippel for suggesting this problem and for many helpful discussions which have contributed much to the interpretation of the results.

[25] A. R. von Hippel, J. Appl. Phys. **8**, 815 (1937).
[26] A. R. von Hippel, *Dielectrics and Waves* (John Wiley and Sons, Inc., New York, 1954), pp. 234 ff.

JOURNAL OF APPLIED PHYSICS VOLUME 26, NUMBER 10 OCTOBER, 1955

Effect of Water Vapor on Grown Germanium and Silicon *np* Junction Units

J. T. Law and P. S. Meigs
Bell Telephone Laboratories, Incorporated, Murray Hill, New Jersey
(Received May 4, 1955)

The effect of water vapor on the photoresponse curves and reverse current characteristics of germanium and silicon *np* junction units has been investigated. It is concluded that changes in surface recombination velocity are only important at low relative humidities. Channel conduction accounts for the increased current of a silicon unit but another mechanism must be postulated for the germanium case. The possibility of this being ionic conduction is discussed.

1. INTRODUCTION

IT is well known[1–3] that the presence of water vapor has a marked effect upon the reverse current of germanium and silicon diodes. It has been established that these changes may be caused by any one or more of the following, (i) change in surface recombination velocity(s), (ii) formation of channels, (iii) ionic conduction in the adsorbed water.

(i) When an *np* junction is biased in the reverse direction, the holes and electrons, in the *n* and *p* regions, respectively, reach the junction by diffusion. This takes place down a gradient whose value depends directly on the filament lifetime of the minority carrier, i.e., an increase in the lifetime reduces the gradient and therefore decreases the value of the saturation current (I_s). The filament lifetime is made up from a bulk and a surface contribution so that any change in the surface recombination rate will affect the saturation current. Morrison[4] found that the value of s could be changed by admitting water vapor to a germanium sample so that changes in I_s from this effect would be expected.

(ii) A channel consists of an inversion region at the surface of the semiconductor, e.g., a thin *n*-type layer on the surface of *p*-type bulk material. This effect was first studied by Brown[5] on *n-p-n* germanium transistors. He determined that the *n*-type inversion region (which was induced by water vapor) could be attributed to the presence of excess positive charge on the surface of the germanium. He also showed that once the charge had been established by the applied bias, the specimen could be cooled to −78°C and the charge stabilized. In the case of a diode, the presence of a channel on the *p*-type material will effectively increase the area of the collecting junction and therefore increase the value of the saturation current. The charge carriers will be holes and electrons.

(iii) When the amount of adsorbed water on the germanium surface reaches the multilayer region the water molecules are quite mobile[6] so that the presence of any impurity ions will produce a layer of electrolyte across the surface. Here it is possible to have ionic conduction. It has previously been shown[2] that an etched germanium surface contains a considerable number ($\sim 10^{14}/cm^2$) of impurity ions available for this process.

From the previous remarks we would expect processes (i) and (ii) to be important in the monolayer region of adsorbed water and (iii) in the multilayer region. The present paper describes measurements on both germanium and silicon units over a wide range of water vapor pressures. These include photoresponse curves and conductance measurements, the latter over a temperature range. Methods are described for separating conduction due to channels and to ions and an explanation is offered for the difference in behavior between germanium and silicon units.

2. EXPERIMENTAL

The type of apparatus used for the photoscanning experiments differed slightly from the conventional ones because the sample was placed in a vacuum. This meant that the light spot had to be moved while the sample was held in a fixed position. The *np* junction unit was mounted on a glass stem and attached to a vacuum system by means of a ground glass joint. It could therefore be readily removed for etching. The system was evacuated by means of a three stage oil diffusion pump which produced an ultimate vacuum of 10^{-6} mm. The vapor source consisted of well degassed liquid water from which varying amounts of vapor could be admitted to the system. A 30 cps chopper and light source were mounted in place of the eyepiece of a traveling microscope which was calibrated in divisions of 10^{-3} cm. The light spot, which was 3×10^{-3} inch in diameter passed through a water filter and then through a planar glass window sealed directly to the experimental tube. With the junction biased in the reverse direction the signal produced by the 30 cps chopped light was measured on a wave analyzer as a function of distance as the light spot was moved normal to the bulk junction. An oscilloscope was used to check the wave form, which after suitable precautions

[1] H. Christensen, Proc. Inst. Radio Engrs. **42**, 1371 (1954).
[2] J. T. Law, Proc. Inst. Radio Engrs. **42**, 1367 (1954).
[3] A. L. McWhorter and R. H. Kingston, Proc. Inst. Radio Engrs. **42**, 1376 (1954).
[4] S. R. Morrison, J. Phys. Chem. **57**, 860 (1953).
[5] W. L. Brown, Phys. Rev. **91**, 518 (1953).
[6] J. T. Law, J. Phys. Chem. **59**, 67 (1955).

TABLE I.

Material	Resistivity of n-type ohm-cm	Resistivity of p-type ohm-cm
1. Germanium	2.0	0.2
2. Germanium	8.5	1.1
3. Silicon	0.05	3.0
4. Silicon	9.0	0.2

remained square at all times for germanium. In the case of silicon the signal had the shape expected when traps are present.[7] If a steady light was shone on the bar to keep the traps filled a normal square wave was observed but the steady light affected the channel length (see below) so that a non-square wave signal had to be used. Provision was made for shining a variable amount of steady light on the junction during these measurements.

In addition to the photoscanning experiments which gave the photoresponse curves, the reverse current-voltage characteristics were measured at various humidities. These were obtained both in the dark (I_D) and with the junction bar flooded with light (I_L).

The data to be discussed were taken on bars cut from several np germanium and silicon grown crystals. The resistivities are listed in Table I.

The units used were prepared by cutting the crystals into bars 0.25×0.25×2.5 cm, wet lapping with 600 mesh carborundum, and etching with CP-8.* The germanium units were then immediately placed in the tube. At first, soldered and masked leads were used but these gave so much contamination that later measurements were made using spring molybdenum clips in which the unit was placed after etching. In the case of silicon units the ends were copper plated before being placed in the holder. This gave a practically ohmic contact. Eliminating the masking step in the etching procedure led to much more reproducible results.

3. EXPERIMENTAL RESULTS

The type of curve obtained when photoresponse is plotted as a function of distance is shown in Fig. 1. The various curves correspond to different partial pressures of water vapor over the sample at 300°K. In vacuum the curve is approximately linear up to the junction. Goucher[8] has shown that the slopes of the curve on either side of the junction are proportional to the lifetime of minority carriers. The carriers produced by the light spot diffuse a distance x to the junction with decay factors of exp $(-x/L)$ where $L=(D\tau)^{\frac{1}{2}}$ is the diffusion length and τ is the filament lifetime. As the addition of water vapor only affects the surface it is reasonable to ascribe any change in the slope of the curve to changes in surface recombination velocity so that the effect of this quantity on the reverse current of a junction can be determined.

Brown[5] first suggested scanning a pn junction with a light spot as a means of detecting channels and this method has been used by various workers.[1,3] If an inversion region exists at the surface then there must be a collecting junction between it and the body of the semiconductor. Any carriers produced along the length of the channel will be collected at this junction before they have time to recombine so that the photoresponse curve will have a flat top instead of a sharp peak. This effect is shown at the higher humidities in Fig. 1. The length of the plateau is taken to be the length of the channel so that the area of the induced junction can be calculated if we assume that the channel extends an equal distance from the bulk junction at all points.

Unlike the results reported by McWhorter and Kingston,[3] it was not found necessary to leave the etched unit in contact with oxygen before a channel could be detected. All the data reported in the present paper were obtained on freshly etched samples so that the presence of a relatively thick oxide film is not a prerequisite for channel formation.

4. DISCUSSION

4.1 Effect of Ambient on Surface Recombination Velocity

It has been found that the slopes of the photoresponse curves change with ambient. If a freshly etched junction bar is placed in a vacuum the change is in the direction

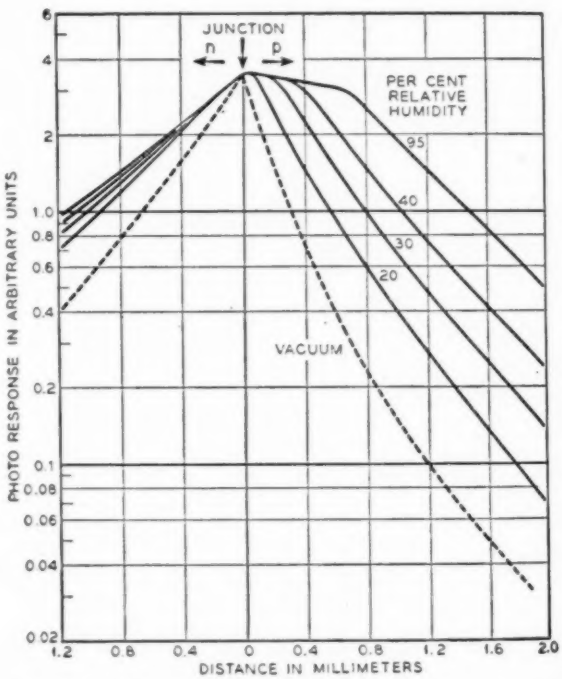

FIG. 1. The effect of water vapor at various relative humidities on the photoresponse curve of a grown germanium np junction unit at 300°K, with 3 volts applied reverse bias.

[7] J. R. Haynes and J. A. Hornbeck, Phys. Rev. **90**, 152 (1953).

* This etch has the following composition: 50 cc nitric acid and 25 cc hydroflouric acid.

[8] F. S. Goucher, Phys. Rev. **81**, 475 (1951); **78**, 816 (1950).

of increased surface recombination. This change does not occur immediately, but may proceed steadily for about one hour. It is reversible, in that addition of water vapor decreases the surface recombination rate (s), which returns to its previous high value on evacuation. If the bar is warmed slightly during the pumping process ($\sim$100°C), s increases more rapidly and reaches a higher value.

From sets of curves similar to those shown in Fig. 1 for the effect of water vapor on a germanium junction, values were calculated for the effective lifetimes of the minority carriers in the n and p regions, before and after addition of water vapor. The variation of s with relative humidity for the n-type material is shown in Fig. 2. The conductance of the junction at low voltages, eI_s/kT, is due to hole flow in the n-region and electron flow in the p-region. It can be calculated in terms of intrinsic conductivity σ_i, the conductivities of the two sides σ_p and σ_n, the lifetimes of the injected carriers τ_p for holes and τ_n for electrons and the diffusion constants D_p and D_n. It is therefore possible to calculate values of the saturation current I_s, and compare them with the measured values to determine whether the decrease which occurs at low humidities is in fact due to a change in minority carrier lifetime.

The saturation current is given by[9]

$$I_s = A\frac{kTb\sigma_i^2}{q(1+b)^2}\left(\frac{1}{\sigma_n L_p}+\frac{1}{\sigma_p L_n}\right)$$

where A is the area of the junction, $b=\mu_p/\mu_n$ and $L=(D\tau)^{\frac{1}{2}}$.

For germanium at 293°K it has the numerical value in amperes,

$$I_s = 2.4\times10^{-7}\,A\left(\frac{1}{\sigma_n(\tau_p)^{\frac{1}{2}}}+\frac{1}{\sigma_p(\tau_n)^{\frac{1}{2}}}\right).$$

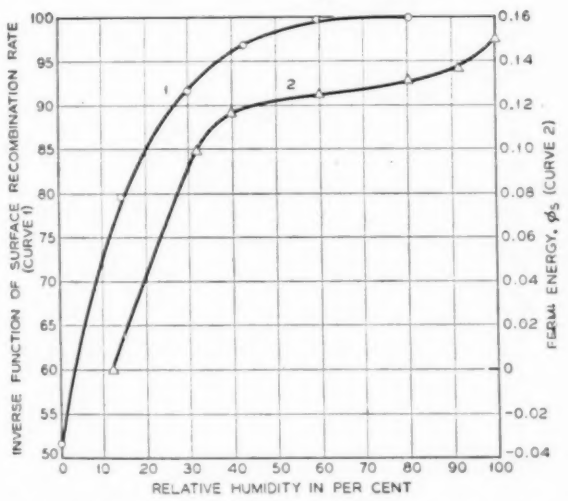

FIG. 2. The change in surface recombination rate and quasi-Fermi level as a function of relative humidity. The function of the surface recombination rate shown is inversely proportional to the slopes of the curves in Fig. 1 in the n-type region.

[9] W. Shockley, Proc. Inst. Radio Engrs. **40**, 1289 (1952).

TABLE II.

	Vacuum	10% relative humidity
Crystal 1		
I_s(exp)	9 μamp	7 μamp
I_s(calc)	7 μamp	5.5 μamp
Crystal 2		
I_s(exp)	25 μamp	23 μamp
I_s(calc)	23 μamp	21 μamp

The results of these calculations are given in Table II. Therefore, the decrease in surface recombination rate during the adsorption of the first 1–2 layers of water is sufficient to account for the decrease in dark current and the corresponding increase in photocurrent. In the case of silicon practically no change in recombination rate was observed.

The slopes of the photoresponse curves and presumably therefore the surface recombination rates on germanium could be changed by sparking in the vacuum space containing the junction bar. This caused a marked *increase* in surface recombination rate and at the same time the reverse dark current of the junction increased. A series of curves were taken after sparking for varying lengths of time, all of the order of a few seconds. The changes found after this treatment were much greater than those produced by varying the ambient from wet to dry. The lifetimes of holes in the n-side obtained from these curves, together with experimental and calculated reverse saturation currents were as follows.

Vacuum	1st sparking	2nd sparking	3rd sparking
τ_p 32.8	5.1	3.3	0.6 μsec
I_s(exp) 8	18	20	63 μamp
I_s(calc) 7	20	25	59 μamp

4.2 Mechanism of High Reverse Dark Current

As was mentioned in the introduction, there are two possible mechanisms which may lead to increased reverse dark current (neglecting changes in surface recombination rate), namely, channel conduction and ionic or surface leakage.

Either one or both of these must explain the observed effect of water vapor on the reverse dark current (I_D) and photocurrent (I_L). The results for germanium are shown in Fig. 3 and will be discussed first. The decrease in dark current and increase in photocurrent at low humidities has already been explained in terms of surface recombination velocity so we will confine our attention to the region above 20% relative humidity.

McWhorter and Kingston[3] have correlated channel length with reverse dark current and obtained good agreement with a simple theory. The channel length is taken as the region between the two points when the slope of the photoresponse curve changes abruptly. In the present work the channel length was only

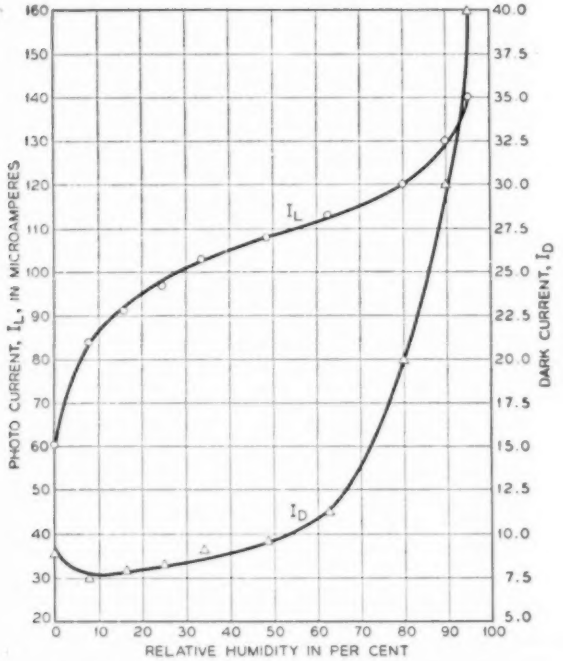

FIG. 3. The effect of water vapor on the reverse dark current (I_D) and photocurrent (I_L) of a germanium unit.

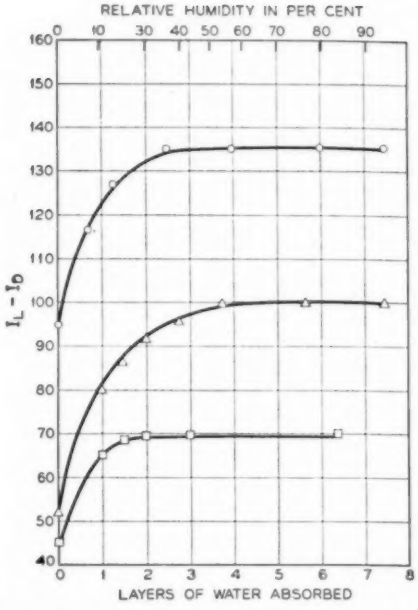

FIG. 4. The corrected photocurrent (I_L-I_D) of a germanium unit as a function of relative humidity and the number of layers of adsorbed water.

roughly proportional to the excess dark current (this being the increase in dark current over its minimum value), it being frequently possible to detect channels of up to 0.2 mm in length without any measurable increase in reverse dark current. In the region above 20% relative humidity both I_D and I_L are increasing so that changes in surface recombination rate cannot account for the observed effects. A change in s changes the dark and photocurrents in opposite directions. We are therefore left with either channels or ionic conduction as possible mechanisms. If the latter of these is operative, the amount of excess current should be independent of light intensity, i.e., the change in dark current with humidity should equal the change in photocurrent. This would not be true if the current limiting barrier was at the electrolyte-semiconductor interface, for as Brattain and Garrett[10] have shown, the current is increased in the presence of light but the current also saturates with increasing voltage. In the measurements on an *np* junction in a high humidity ambient the reverse current did not saturate but increased linearly with voltage. This would indicate that the flow of electrons from the semiconductor into the electrolyte on the surface is not the current limiting step. This is not too surprising as there is only a limited number of water molecules and foreign ions on the surface. If this concentration factor limits the current then changing the light intensity will not affect it. Increasing the voltage however will increase the current as the velocities of the ions are increased. The quantity I_L-I_D, plotted against the number of layers of water adsorbed and the relative humidity is shown in Fig. 4 for several units. In each case the curves increase up to about the second layer of absorbed water and then flatten out.

If one compares the curves in Fig. 4 with those shown for channel formation in Fig. 1 it is immediately obvious that the corrected photocurrent (I_L-I_D) is not increasing in the high humidity range where the channel is forming. This is very surprising as the junction formed near the surface at high humidities should be a good collector of injected carriers. For this reason photoresponse curves were taken with varying amounts of steady light on the unit. The results shown in Fig. 5 indicate that as the amount of steady light is increased, the channel decreases in length and finally disappears. This could possibly be explained by the observation

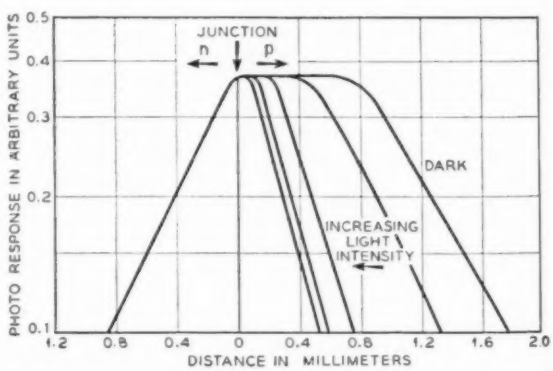

FIG. 5. The effect on the photoresponse curve caused by changing the intensity of the steady light. Note the decrease in channel length (l).

[10] W. H. Brattain and C. G. B. Garrett, Bell System Tech. J. **34**, 129 (1955).

of Brattain and Bardeen[11] that the change in contact potential with light, $(\Delta CP)_L$ for a water vapor exposed unit was opposite in sign to the change in contact potential ΔCP between a dry and wet condition. (See following section on channels.) By illumination it may therefore be possible to eliminate or at least drastically reduce the inversion region at the surface. This gives us a means of separating channel and ionic conduction. If one measures reverse current as a function of steady light intensity at a series of humidities one of two things should happen.

(i) If we are only dealing with channel conduction, the current at high light intensities in the wet condition (when the channel no longer exists) should approach the corresponding current observed for the dry state.

(ii) If ionic conduction is the controlling mechanism the increase in current between the dry and wet states should be the same irrespective of the light intensity.

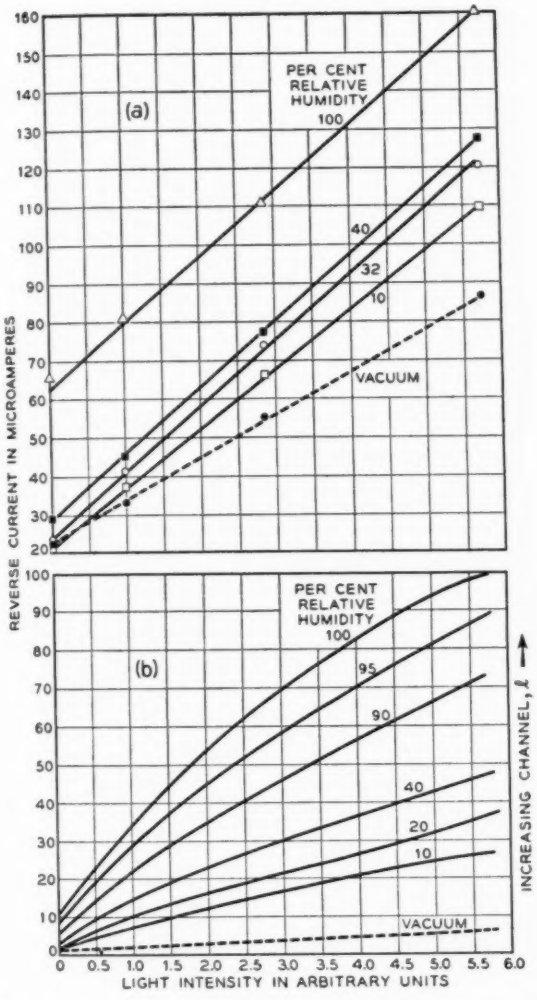

FIG. 6. (a) The reverse current of a germanium np junction at 300°K plotted as a function of steady light intensity at various relative humidities. (b) The reverse current of a silicon np junction plotted as a function of light intensity at various relative humidities.

[11] W. H. Brattain and J. Bardeen, Bell System Tech. J. **32**, 1 (1953).

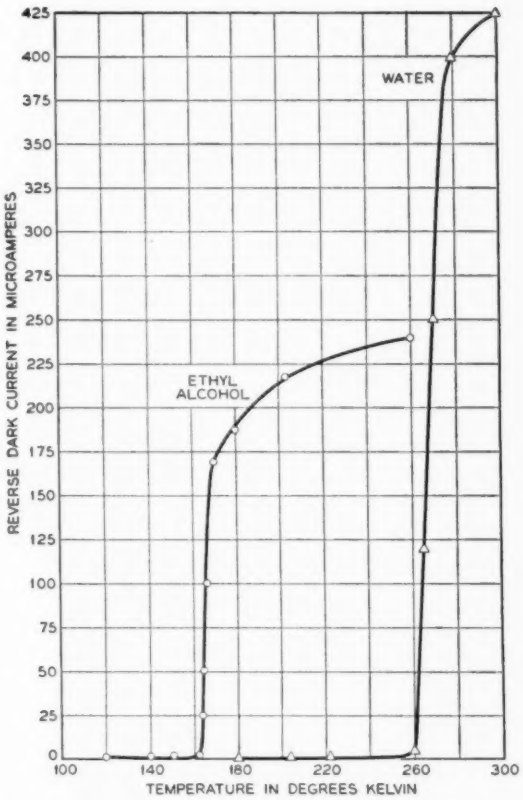

FIG. 7. The reverse dark current of a germanium np junction in the presence of saturated water and ethyl alcohol vapor as a function of temperature.

These measurements were carried out and the results are shown in Figs. 6(a) and 6(b). Figure 6(a) represents data on germanium and Fig. 6(b) data on silicon. The results shown were taken at 20 volts but similar curves were obtained between 5 and 60 volts. At low humidities the surface recombination rate on germanium changes and this accounts for the change in slope between curves 1 and 2 of Fig. 6(a). From 30% humidity to saturation, however, the curves of Fig. 6(a) are effectively parallel so that the majority of the excess current must be carried by a mechanism that is not affected by the amount of steady light, such as ionic conduction.

Unlike germanium, the curves obtained on silicon samples [6(b)] were not parallel straight lines but had an initial slope that increased as the channel length increased. As the value of the channel length l was decreased by increasing the steady light intensity in just the same way as for germanium, the curves departed from linearity as would be expected if mechanism (i) was operative. Attempts were now made to suppress ionic conduction on germanium by cooling below the freezing point of the adsorbed water (where the ionic mobilities must be very low) and to measure channel

conduction. A *p-n* junction bar was placed in a high humidity ambient and cooled to 180°K with the bias applied and then warmed slowly to room temperature, measuring the temperature of the bar (with a thermocouple) and the reverse current. The results are shown in Fig. 7 where it can be seen that the current is practically zero until temperatures close to 273°K are reached. Below 220°K no current could be measured. This rapid increase of current near the melting point of ice confirms the previous observation that an ionic conduction mechanism is an important one in increasing reverse currents of *n-p* junction units in high humidity ambients. A similar curve is shown for the effect of ethyl alcohol. In this case the current increases at 165°K. The melting point of pure ethyl alcohol is 156°K but the material used could easily have been contaminated with water. No normal junction could be expected to show an appreciable current at these low temperatures so that the mechanism must be one involving ions. It would be interesting to investigate the effect of temperature on current at humidities other than saturation but there seems to be no obvious way of doing this as increased adsorption occurs when the junction bar is cooled.

If the excess current found at relative humidities above 40% is ionic in nature, one would expect to find some gas evolution at the electrodes as a result of electrolysis of the water. One of the authors has previously reported[2] an unsuccessful attempt to observe this gas evolution. More recently gas evolution has been observed using a differential pressure system of small volume, incorporating an oil manometer. The various humidities were obtained from salt solutions and a nitrogen ambient. When the pressure differential was observed as a function of time after reverse biasing the junction two effects were observed. The pressure always increased rapidly at first and then became linear

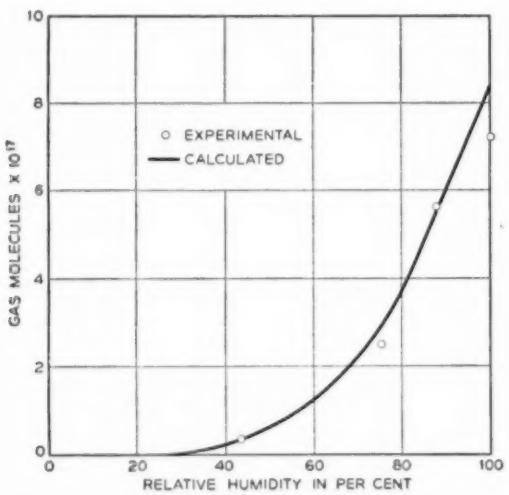

FIG. 8. The number of molecules of gas evolved from a germanium junction plotted as a function of relative humidity. The curve is calculated from the number of coulombs of excess current passed at constant time.

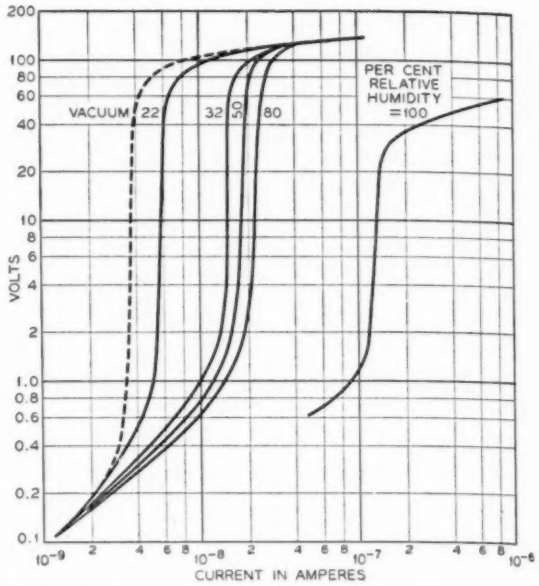

FIG. 9. The reverse dark current of a grown silicon *np* junction unit as a function of applied voltage for various relative humidities.

with time. After switching off the current the pressure decreased for 2–3 minutes and then remained constant. It is probable that the rapid initial increase in pressure and the decrease after switching off are due to heating and cooling respectively. If one takes the difference in pressure before passing current and after temperature equilibrium this should give a measure of the ionic current passed. In Fig. 8 the number of gas molecules evolved is plotted as a function of relative humidity. The curve is calculated on the basis that all the excess current is ionic in nature and leads to the evolution of hydrogen and oxygen. The agreement between the calculated and observed values is strong evidence for the existence of ionic conduction on freshly etched junction units in high humidity ambients.

On the basis of a simple picture one would expect the first layer or two of adsorbed water to produce the inversion region at the surface of the semiconductor. In the photoscanning experiments this is not found to be the case but in a study of the effect of water vapor on *n-p-n* transistors Kingston[12] has found that the conductivity from emitter to collector changes most rapidly in the low humidity (<40%) region, where only one or two layers are adsorbed. From values of the conductivity he calculated figures for the quasi-Fermi level (φ_s) for electrons at the surface. In Fig. 2 these are plotted as a function of humidity where values are also given for the surface recombination rate variation as found in the present work. The most striking thing is that both quantities φ_s and s change most in the low humidity range during the adsorption of the first two layers of water and are almost constant above 40%. This implies that any excess current produced at

[12] R. H. Kingston, Phys. Rev. **98**, 1766 (1955).

humidities above 40% is not an electron current in the semiconductor but more probably an ionic current in the water film.

In the case of the silicon samples little or no evidence has been found for ionic conduction. Water vapor did not appreciably change the reverse current-voltage characteristic of crystal No. 4 and all the measurements reported below were taken on samples from No. 3 with a higher resistivity *p*-side. In Fig. 9 the reverse dark current of a unit from crystal No. 3 is plotted as a function of voltage at several humidities.

The primary effect of water vapor is to increase the saturation current without markedly affecting the breakdown voltage—except at 100% relative humidity. These changes are what one would expect for the formation of a channel or surface inversion region. The effective area of the junction is increasing so that the current increases but no marked change is made in the breakdown voltage. As the channel increases in size the current would be expected to saturate at steadily higher voltages and this is what is actually found. In vacuum, it saturates at less than 0.5 volt while at 80% relative humidity it does not saturate until a bias of 2 volts is applied. One might expect to observe the growth of the channel in the photoresponse curve, but no change is apparent until the unit is in 100% water vapor. As we could detect a channel of 0.1 mm length, we must conclude that the one existing at humidities below saturation is shorter than this. This means that its saturation current is $>2\times10^{-6}$ amp/cm^2 compared with the bulk junction saturation current of 7×10^{-8} amp/cm^2. At 100% relative humidity the channel current is 1×10^{-7} amp/cm^2.

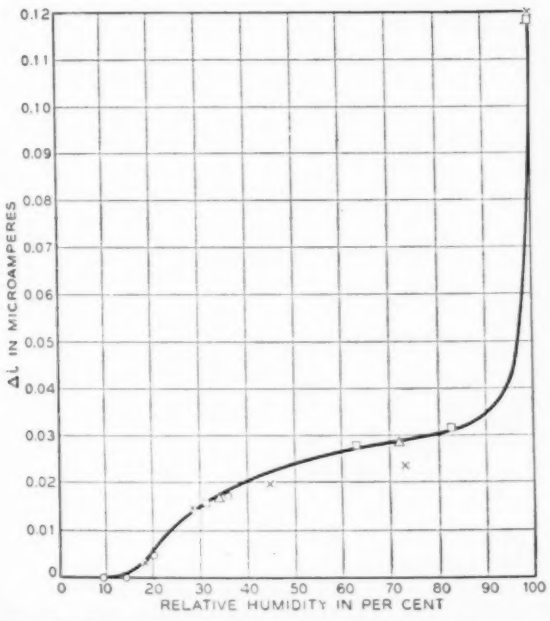

FIG. 10. The increase in reverse dark current above that found in a vacuum (Δ_i) as a function of relative humidity for a silicon *np* junction.

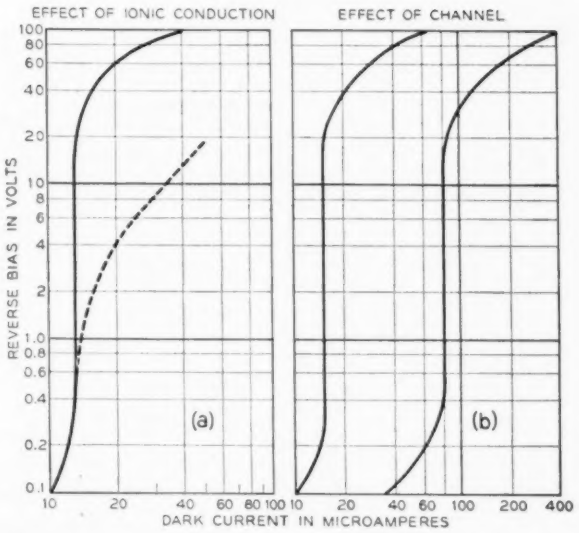

FIG. 11. (a) The effect of ionic leakage on the reverse dark current-voltage characteristic. The curves shown were obtained on germanium. (b) The effect of channel conductance on the reverse dark current-voltage characteristic. The curves shown were obtained on silicon.

This formation of channels without the complication of ionic conduction is just what one would expect in the presence of a stable oxide film. The difference between these results and those obtained on germanium[3] is further evidence that in the latter case another conduction mechanism is operative.

As a first approximation, we can treat the silicon surface as a silicon dioxide surface. The adsorption isotherm for water on SiO_2 has been measured[13] as well as the extent of its reversibility[6] so that it should be possible to compare these results with the changes in reverse dark current with humidity. In Fig. 10 the excess dark current is plotted as a function of humidity. No change is observed below 15%, but as the first layer of adsorbed water on SiO_2 is formed at a humidity of 10% and cannot be removed by pumping this is in fair agreement. The steady increase in current between 20 and 80% can only be due to channels as mobile water, which is a prerequisite for ionic conduction, is not adsorbed at humidities belwo 40%. The current increases very rapidly near 100% humidity but we know from the photoresponse curve that the channel has increased enormously in this region so that it could be due to electronic conduction in the channel. The rapid increase in channel size near saturation would lead one to believe that actual ion movement is contributing to its formation. When the water film is very thick ions may be able to move even though an oxide film is present on the silicon surface. It is reasonable to say therefore, that all the excess current found when a silicon *np* junction is exposed to water vapor is due to channel conduction.

The difference between germanium and silicon is

[13] H. K. Livingston, Ph. D. thesis, University of Chicago, 1941.

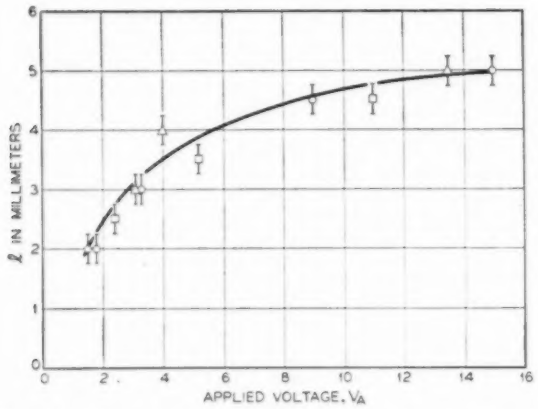

FIG. 12. Channel length (l) plotted as a function of applied voltage for a germanium np junction at constant relative humidity. The curve is calculated from the theory of McWhorter and Kingston.

shown in Fig. 11 where the reverse current is plotted as a function of voltage for the wet and dry conditions. Figure 11(a) is typical of the germanium results while 11(b) is typical for silicon. The first shows a complete change in the shape of the characteristic while the latter only indicates an increase in the saturation current. Whenever the excess current is completely due to a channel one should obtain curve 11(b).

4.3 Channels

We will now describe some of the properties of the channels that are formed after the adsorption of appreciable quantities of water vapor. To separate the channel phenomenon from other possible current carrying mechanisms it is necessary to deal only with channel length l and not the values of reverse current.

4.31 Change of l with Applied Voltage

McWhorter and Kingston[3] have treated a channel as a rectifier and resistance in series and obtained an expression relating channel length, or current to the applied voltage.

$$l^2=\frac{2}{AI_s}\ln\frac{V_A}{V_0}.$$

From this equation where A, I_s, and V_0 are constants we would expect l^2 to be proportional to $\ln V_A$ the applied voltage.

In Fig. 12 the channel length for several runs on germanium is plotted as a function of applied voltage and the curve represents the theoretical relation $l^2=k\ln V_A$. The agreement is quite good. If current is used in place of l no such agreement is found. A similar agreement was found for silicon except that the current was used in place of l.

The only difference between these results and those obtained by McWhorter and Kingston is the size of the channel obtained, which was about four times larger in the latter work. We may therefore conclude that the simple theory adequately describes the effect of applied voltage on the channel length.

4.32 Effect of Steady Light on Channel Length

We have already mentioned that the length of the channel (l) on both silicon and germanium decreased as the intensity of steady light illumination was increased. If the light was turned off, the channel returned to its previous value over a period of several minutes. The decrease in channel length with increasing light intensity could possibly be ascribed to any one or more of three causes. (i) Brattain and Bardeen[11] showed that the effect of shining a bright light on a germanium surface was to change the contact potential to a value which was independent of whether the ambient was wet or oxidizing and which for a p-type sample was fairly low. However this only applies to a chopped light source as Garrett and Brattain[14] have shown that $(\Delta C.P.)_L$ for a steady light is zero. In the present work therefore this cannot explain the observed effects. (ii) The relationship obtained by McWhorter and Kingston[3] relating channel length to the saturation current of channel-bulk semiconductor junction (I_s)

$$l^2=\frac{2}{AI_s}\ln\frac{V_A}{V_0}$$

would imply that as I_s was increased (for example by shining light on the surface), l would decrease. This however will only be true if A is independent of light intensity. The value of A depends upon the relationship

$$R=AV_A$$

where R is the resistance of the channel and V_A is the applied voltage. If the number of electrons in the surface region is increased R will decrease and therefore A will also decrease. The product AI_s may therefore be practically unaffected by light intensity. (iii) The most obvious explanation and probably the correct one is that as the light intensity is increased the current through the channel is increased and therefore the voltage drop along the channel is increased. This causes the channel to pinch off at a shorter distance from the bulk junction.

Even (iii) however cannot be the complete explanation of the changes produced by the light as the channel does not return to its original length immediately upon turning off the light. This suggests that some process with a high activation energy is involved such as the ionization of impurities in the presence of the applied field or the movement of ions across the surface. Either of these changes would be due to the fact that the surface ionic charge should change in such a way as to restore the surface potential to its equilibrium value.

[14] C. G. B. Garrett and W. H. Brattain, Phys. Rev. **99**, 376 (1955).

In many cases the effect of the light was to make the channel vanish completely so that any excess current produced by the water in this case could hardly be ascribed to channel conduction. This makes the flooded light measurement useful as a means of separating channel and other effects. Unfortunately, it has not been possible to obtain an equation relating photocurrent to light intensity for channels of fixed length. By analogy with normal *pn* junction theory one would expect a linear relationship but an extension of the theory of McWhorter and Kingston[3] indicates that the current should be proportional to the square root of the light intensity. This may be the result of treating the case as a one-dimensional instead of two-dimensional problem.

5. SUMMARY

A series of measurements have been made on grown germanium and silicon *np* junction units in various ambients. In the case of water vapor the following conclusions are possible.

(i) Low relative humidities decrease the surface recombination rate of germanium relative to the vacuum condition but do not affect silicon.

(ii) Humidities above 30% produce channels on both germanium and silicon units.

(iii) High humidities produce excess current on germanium even at temperatures close to 273°K but not below.

(iv) Channel length as a function of voltage obeys McWhorter and Kingston's equation.

(v) Shining steady light on the unit decreases the channel length on both germanium and silicon samples but as Figs. 6(a) and 6(b) show, the excess reverse current is only changed from the value which is found in the dark condition for silicon. Hence some other mechanism than channel conduction is operative at germanium surfaces. It is probable that this is ionic in nature and the low temperature and gas evolution data confirm this.

It is concluded that the effects found when water vapor is adsorbed are due to impurities over which little or no control is at present possible and that at least two current carrying mechanisms are operative. The existence of two mechanisms, is in agreement with the results obtained by Christensen.[1]

Permanent-Magnet Properties of Elongated Single-Domain Iron Particles

L. I. MENDELSOHN, F. E. LUBORSKY, AND T. O. PAINE
Measurements Laboratory, General Electric Company, Lynn, Massachusetts

(Received May 13, 1955)

Previously described fine-particle magnets have been based upon crystal anisotropy; this paper reports permanent-magnet properties derived from the shape anisotropy of substantially elongated single-domain iron particles. The shape anisotropy of these particles overcomes the limitation imposed on the energy of previous fine-particle iron magnets by the low crystal anisotropy of iron.

The predicted and observed properties of crystal anisotropy fine-particle magnets are reviewed and compared with an ideal fine-particle iron magnet based upon the shape-anisotropy model of Stoner and Wohlfarth. Experimental results are reported for magnets made by aligning and compacting single-domain iron particles 150 angstrom units in diameter, with a median length-to-diameter ratio of three to one, and an intrinsic coercive force before packing of 1600 oersteds. The effect of particle alignment and packing fraction on magnetic properties is described, and energy products above three million gauss-oersteds are reported. These results are compared with properties predicted from theoretical considerations, and with existing permanent-magnet materials.

I. INTRODUCTION

RECENT advances in the domain theory of ferromagnetism suggest the possibility of developing powerful new permanent-magnet materials by taking advantage of the anisotropy forces which oppose the rotation of the magnetization of single-domain particles. Domain theory accounts for the easy demagnetization of low coercive force materials in terms of the movement of domain boundaries; one way to achieve the high resistance to demagnetization required of permanent-magnet materials is to completely eliminate domain boundaries from the material. Since domain boundaries have a finite width extending over hundreds of atomic distances, very fine particles may be too small to contain a boundary. These "single-domain particles" must then respond to a demagnetizing field by the difficult process of rotating their magnetization vectors, which will be opposed by magnetic anisotropy forces. This can lead to very high values of coercive force, if the magnetic anisotropy is high. This, briefly stated, is the basic idea of the fine-particle magnet; for a more rigorous discussion the reader is referred to the excellent review by Kittel.[1]

The concept of the single-domain particle has opened up an entirely new field of permanent-magnet development. It is now possible to predict the magnetic properties which can be achieved from measurements of the fundamental physical constants of the material. Magnetic anisotropy forces play a basic part in determining the coercive force of single-domain particles, so an understanding of these forces is essential to fine-particle magnet development. Four effects have been proposed: crystal anisotropy,[2] strain anisotropy,[3,4] shape anisotropy,[4–6] and surface anisotropy.[7] Of these, only crystal anisotropy has been thoroughly investigated, leading to the discovery of three fine-particle magnets. Strain and surface anisotropy effects have not been experimentally observed, but recent work at this laboratory has demonstrated the effect of shape anisotropy on the properties of single-domain particles.[8] Shape anisotropy offers many advantages for magnet development, and it is the purpose of this paper to report the permanent-magnet properties which have been achieved from the shape anisotropy of substantially elongated single-domain iron particles.

II. FINE-PARTICLE MAGNETS BASED UPON CRYSTAL ANISOTROPY

In 1943 Guillaud[9] demonstrated the relationship between crystal anisotropy and the coercive force of fine particles of manganese-bismuth. He prepared three-micron-diameter particles with an intrinsic coercive force of 12 000 oersteds, and observed that upon lowering the temperature the coercive force decreased in direct proportion to the crystal anisotropy, both becoming zero at 84°K. By hot-pressing magnetically-aligned particles of manganese-bismuth, Adams[10] has produced fine-particle magnets with energies as high as 4.3 million gauss-oersteds. Practical applications of this interesting material have been hampered by its cost and temperature coefficient.

The first commercially-produced fine-particle magnet was introduced in France in 1945 as a result of work by Néel[11] and others[12] on the properties of single-domain iron particles. Honda[13] had prepared low-energy fine-particle iron magnets in 1937 from reduced iron salts, and a year later Dean and Davis[14] reported fine-particle iron magnets made from iron electrodeposited

[1] C. Kittel, Revs. Modern Phys. **21**, 541 (1949).
[2] L. Néel, Compt. rend. **224**, 1488 (1947).
[3] C. Kittel, Phys. Rev. **70**, 965 (1946).
[4] E. Stoner and E. Wohlfarth, Phil. Trans. Roy. Soc. **A240**, 599 (1948).
[5] L. Néel, Compt. rend. **224**, 1550 (1947).
[6] C. Guillaud, J. phys. radium **8**, 347 (1947).
[7] L. Néel, Compt. rend. **237**, 23 (1953).
[8] Paine, Mendelsohn, and Luborsky (to be published).
[9] C. Guillaud, thesis, Strausbourg, 1943.
[10] Adams, Hubbard, and Syeles, J. Appl. Phys. **23**, 1207 (1952).
[11] L. Néel, J. phys. radium **5**, 241 (1944).
[12] L. Weil and S. Marfoure, Compt. rend. **225**, 229 (1947).
[13] K. Honda, Nippon Kinzoku Gakkai-Shi **1**, 3, 19 (1937).
[14] R. Dean and C. Davis, U. S. Patent 2,239,144; 4/22/41.

into a mercury cathode. The French process for preparing single-domain iron particles from the low-temperature reduction of iron formate was the first commercial success, and produces magnets with an energy of 1.1 million gauss-oersteds. This can be increased to 1.7 million gauss-oersteds by adding 30% cobalt.[15] Electron micrographs of these particles published by Franklin[16] show that they are approximately spherical in shape, with the possibility of slight elongation arising from random variations in particle dimensions. The low crystal anisotropy of iron combined with the essentially spherical shape of the particles limits the coercive force and energy product of these magnets.

Much higher crystal anisotropy constants were reported by Went *et al.*[17] in 1952 for hexagonal iron oxides of the formula $MO \cdot 6Fe_2O_3$, where M is barium, strontium, or lead. Fine particles of this material have the expected high coercive force. Rathenau[18] describes an oriented barium-iron oxide magnet with an intrinsic coercive force of 4500 oersteds, and an energy product of 3.0 million gauss-oersteds. The maximum energy that can be attained with this material is limited by its low intrinsic saturation induction; B_{is} is only 4200 gauss. Directionalized barium-iron oxide magnets with an energy product of 2.5 million gauss-oersteds are now commercially produced in Europe.[19]

The results achieved with these magnets illustrate the value of a high crystal anisotropy constant. The predicted relationship between crystal anisotropy and the coercive force of a favorably oriented spherical single-domain particle is:

$$H_{ci}=2K/I_s \qquad (1)$$

where K is the crystal anisotropy constant, and I_s the saturation magnetization of the material.[1] Table I compares the predicted and observed coercive force for various materials. The differences can be accounted for in terms of variations in the size, shape, alignment, agglomeration, and crystal structure of the particles. In addition, there may be contributions from other anisotropy effects, and domain boundaries may form at high demagnetizing fields.[18]

TABLE I. Coercive force from crystal anisotropy.

Material	Crystal anisotropy constant, K, ergs/cc $\times 10^{-4}$	Saturation magnetization, I_s, gauss	Maximum coercive force: Predicted $2K/I_s$, oersteds	Maximum coercive force: Reported H_{ci}, oersteds
Manganese-bismuth[a]	1160	620	37 000	12 000
Barium-iron oxide[b]	300	335	17 000	4500
Cobalt[c,d]	400	1400	5500	1500
Iron[c,d]	40	1700	500	1000
Nickel[c]	4	485	140	200

[a] See reference 9.
[b] See reference 18.
[c] L. Weil, International Powder Metallurgy Day, Graz, July, 1948, No. 17.
[d] See reference 26.

TABLE II. Predicted coercive force due to shape anisotropy of elongated single-domain iron prolate ellipsoids.[4]

Length-to-diameter ratio	Predicted coercive force: Parallel alignment	Predicted coercive force: Random alignment
1.0	0	0
1.3	2150	1030
1.5	3200	1530
2.0	5100	2450
3.0	7200	3450
5.0	8900	4250
10.0	10 000	4800

Although a quantitative confirmation of Eq. (1) has not been obtained, the correlation observed between crystal anisotropy and fine-particle coercive force is noteworthy. The three crystal-anisotropy magnets which have been described represent a major advance in permanent-magnet development, even though none possesses an ideal combination of properties. The success of this approach to magnet development has stimulated an intensive search for new materials combining high saturation induction with large crystal anisotropy constant, and further advances can be expected in the future.

Some of the limitations of crystal-anisotropy magnets might be overcome with a different type of anisotropy. The shape-anisotropy effect proposed in 1947 by Stoner and Wohlfarth,[4] Néel,[5] and Guillaud,[6] and recently verified in this laboratory,[8] represents a particularly attractive possibility.

III. THE SHAPE-ANISOTROPY APPROACH TO MAGNET DEVELOPMENT

Shape anisotropy arises from differences in demagnetizing energies along the major and minor axes of an elongated particle. Detailed calculations predicting the effect of shape anisotropy on the coercive force of single-domain prolate ellipsoids have been made by Stoner and Wohlfarth.[4] These calculations are based upon certain assumptions: (1) the particles remain single-domain, (2) no other anisotropy forces contribute, (3) the magnetization vectors rotate uniformly, and (4) there is no interaction between particles. Under these ideal conditions, Stoner and Wohlfarth predicted that the coercive force of a prolate ellipsoid measured parallel to its length should be:

$$H_{ci}=(N_d-N_l)I_s \qquad (2)$$

where N_d and N_l are the demagnetizing factors along the diameter and length, respectively, and I_s is the saturation magnetization of the material. This coercive force is reduced by the factor 0.479 in the case of randomly oriented ellipsoids. These calculations place an upper limit on the coercive force of highly elongated

[15] R. Steinitz, Powder Met. Bull. **3**, 124 (1948).
[16] Franklin, Campbell, and Weinman, J. Appl. Phys. **24**, 1040 (1953).
[17] Went, Rathenau, Gorter, and van Oosterhout, Philips Tech. Rev. **13**, 194 (1952).
[18] Rathenau, Smit, and Stuyts, Z. Physik **133**, 250 (1952).
[19] "Permanent magnets," Mullard Ltd., Shaftesbury Avenue London, W.C.2 (1953).

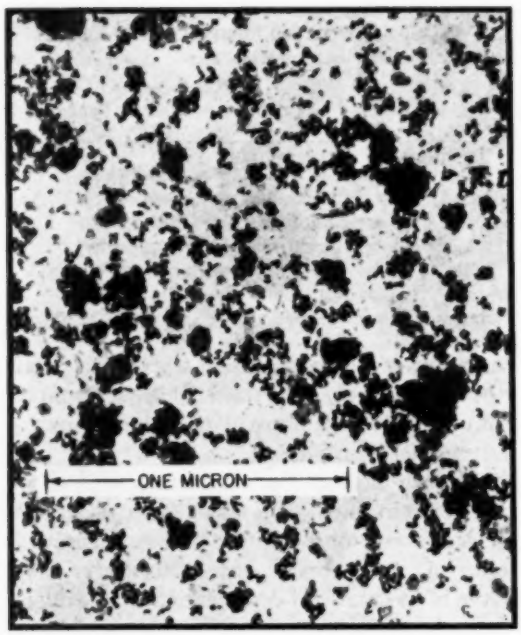

FIG. 1. Electron micrograph of single-domain iron particles. Median elongation 1.3. Intrinsic coercive force 1090 oersteds.

particles of $2\pi I_s$, or half the intrinsic saturation induction: $B_{is}/2$. Table II summarizes the coercive-force predictions for ideal single-domain iron prolate ellipsoids with various ratios of length to diameter.

The values listed in Table II represent an upper limit; the actual coercive forces attainable in a practical magnet are much less. One problem is the reduction of coercive force resulting from the magnetic interaction between particles as they are compacted together to form a magnet. Kittel[1] points out that this interaction should reduce the intrinsic coercive force of individual particles by the factor $(1-p)$:

$$H_{ci}\ \text{magnet} = (1-p)H_{ci}\ \text{particles} \qquad (3)$$

where p is the packing fraction of the magnetic particles. This has been confirmed for fine-particle iron-cobalt by Weil.[12]

Since the residual induction of a fine-particle magnet will be directly proportional to the packing fraction of the magnetic particles, the maximum energy product will lie at some intermediate packing fraction representing a compromise between coercive force and residual induction. An ideal magnet made by uniformly packing perfectly aligned single-domain particles of high elongation will achieve its maximum energy product at a packing fraction of $\frac{2}{3}$. The maximum energy will occur at a lower packing fraction if the coercive force of the elongated particles is less than the maximum predicted. The limiting energy product of an ideal elongated single-domain particle iron magnet should be 39 million gauss-oersteds; this hypothetical magnet would have a residual induction of 14 300 gauss and a coercive force of 3600 oersteds. The addition of 30% cobalt raises the energy limit to 50 million gauss-oersteds, with a residual induction of 16 300 gauss and a coercive force of 4100 oersteds.

Although these intriguing possibilities have been well known for eight years, the crystal-anisotropy approach to magnet development has received the greater experimental attention for several reasons. The shape-anisotropy calculations are based on rather sweeping

FIG. 2. Electron micrograph of single-domain iron particles. Median elongation 2.7. Intrinsic coercive force 1600 oersteds.

FIG. 3. Electron micrograph of single-domain iron particles. Median elongation 4.5. Intrinsic coercive force 2050 oersteds.

assumptions, and the lack of experimental observation of particles with the predicted high coercive force has caused the shape-anisotropy effect to remain somewhat speculative. It has been suggested that elongated single-domain particles might reverse their magnetization by an easier process: for example, Bean and Jacobs[20] have proposed a nonuniform magnetization rotation which leads to substantially lower predicted coercive forces. Another obstacle which has prevented the development of a shape-anisotropy magnet is the difficulty of preparing the elongated single-domain particles. Recent work at this laboratory has led to the discovery of a method for producing substantially elongated single-domain iron particles. The relationship between shape anisotropy and the coercive force of these particles has been described elsewhere.[8] The excellent permanent magnets made from these particles confirm the validity of the shape-anisotropy approach to permanent-magnet development.

IV. PROPERTIES OF SHAPE-ANISOTROPY MAGNETS

The magnets to be described were all prepared by compacting fine iron particles produced by the electrodeposition of iron into a molten metal cathode. This process was used by Herschel[21] over a century ago, and has since been used to produce single-domain iron particles by Nagaoka,[22] Antik and Kubyschkina,[23] Dean and Davis,[14] Pawlek,[24] Mayer and Vogt,[25] and Meiklejohn.[26] By changing this process in certain essential details, it was discovered that particles with a substantial degree of elongation could be prepared.

TABLE III. Properties of single-domain iron particles.

Figure	Mean diameter angstrom units	Median ratio length-to-diameter	Intrinsic coercive force: Parallel alignment	Intrinsic coercive force: Perpendicular alignment
1	145	1.3	1090	1090
2	150	2.7	1600	1080
3	175	4.5	2050	1800

A. Properties of the Particles

Figures 1 and 2 are electron micrographs of particles dispersed in a collodion film using a special technique developed by Fullam.[27] The particles in Fig. 3 were dispersed on a film for shadowing and stereoscopic electron micrography. High-resolution electron micrographs* were made at a magnification of 100 000 diameters, with resolutions down to 20 angstrom units. Accurate measurements of particle diameter and length were made from these micrographs to the nearest quarter millimeter (25 angstrom units). Figure 1 shows essentially round particles similar to those previously prepared by others. Substantially elongated particles are shown in Fig. 2, while Fig. 3 contains particles with an even greater elongation, but with a branching, dendritic structure. Some of these have length-to-diameter ratios as high as 40 to 1. Distribu-

FIG. 4. Electron micrograph of aligned and compacted single-domain iron particles.

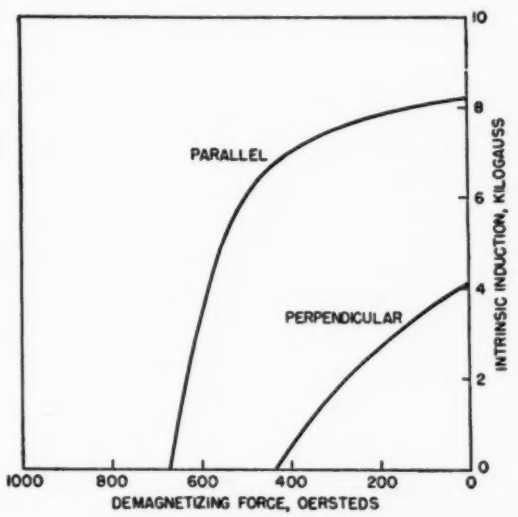

FIG. 5. Effect of directionalization.

[20] C. Bean and I. Jacobs, American Institute of Electrical Engineering Magnetics Conference Proceedings, 1955.
[21] J. Herschel, Phil. Trans. **114**, 183 (1824).
[22] H. Nagaoka, Ann. Physik 3, **59**, 66 (1896).
[23] I. Antik and T. Kubyschkina, Wiss. Ber. Mosk. Univ. **11**, 143 (1934).
[24] F. Pawlek, Metall. **58**, (1950).
[25] A. Mayer and E. Vogt, Z. Naturforsch. **7a**, 334 (1952).
[26] W. Meiklejohn, Revs. Modern Phys. **25**, 302 (1953).
[27] M. Schuster and E. Fullam, Ind. Eng. Chem., Anal. Ed. **18**, 653 (1946).

* The authors are greatly indebted to E. F. Fullam, of E. F. Fullam, Inc., for his beautifully detailed electron micrographs.

TABLE IV. Effect of particle alignment.

	B_{is} Gauss	B_r Gauss	H_{ci} Oersteds	H_c Oersteds	BH_{max} Gauss-oersteds	B_r/B_{is} Ratio
Parallel	9600	8250	675	660	$2.78\ 10^6$	0.86
Perpendicular	9250	4150	435	405	$0.51\ 10^6$	0.45

tion curves of particle diameter and elongation were prepared from data obtained by measuring each of the 100–200 particles which could be resolved in these pictures.[8] The characteristics of the particles are listed in Table III, which shows the correlation observed between particle shape and coercive force.

The intrinsic coercive force measurements reported in Table III were made at liquid-air temperature after the particles had been dispersed in a liquid to a packing below 5%, aligned by a magnetic field, and frozen in place. The sample was then magnetized and its intrinsic coercive force determined both parallel and perpendicular to the direction of the field applied during freezing. These coercive-force values are accurate to better than 5%, and reproducible to within 2%. The essentially spherical particles of Fig. 1 have a low coercive force and cannot be aligned by a magnetic field. Their temperature coefficient of coercive force is close to that of the crystal anisotropy of iron. The highly elongated particles of Fig. 3 have a high coercive force derived from shape anisotropy,[8] and a temperature coefficient of coercive force approaching that of the saturation magnetization of iron, but do not exhibit as great a difference of coercive force due to alignment as the particles of Fig. 2. This effect is probably associated with the branching dendritic structure of the particles. Figure 2 provides the clearest example of elongated single-domain iron particles, and all of the magnets reported in this paper were prepared from similar particles.

B. Alignment of the Particles

The difference between the parallel and perpendicular coercive force of the particles in Fig. 2 indicates that a substantial degree of particle alignment has been achieved. This is confirmed by Fig. 4, which is an electron micrograph made by stripping some of the particles from the surface of a magnetically-aligned sample with a collodion film, for viewing in the electron microscope. This pseudo-replica technique preserves the orientation of the particles, and shows that the magnetic alignment is associated with a high degree of particle orientation. Another measure of the directionality achieved is given by the ratio of residual induction to intrinsic saturation induction: B_r/B_{is} ratios as high as 0.88 have been observed.

The influence of particle alignment on the demagnetization curves of magnets prepared from these particles is shown in Fig. 5, which compares the results obtained on bars directionalized parallel and perpendicular to the direction of measurement. These results are summarized in Table IV. All measurements on magnets were made at room temperature with a magnetic permeameter accurate within 2%.

The excellent directionality achieved by magnetically aligning these particles is an important advantage derived from the use of elongated particles. The essentially round iron particles previously used for fine-particle magnets cannot be directionalized to any significant degree. This effect alone results in a considerable increase in the energy product achieved in these magnets. The alignment of the particles is not lost with increasing packing fraction, in fact, somewhat improved directionality is observed at high packing.

TABLE V. Effect of packing.

Volume percent iron	B_{is} Gauss	B_r Gauss	H_{ci} Oersteds	H_c Oersteds	BH_{max} Gauss-oersteds $\times 10^{-6}$
7	1460	1130	1480	890	0.26
28	5950	4950	1125	1070	2.20
46	9600	8250	675	660	2.78
56	11 800	10 200	345	340	1.67
61	12 850	11 100	205	200	1.04

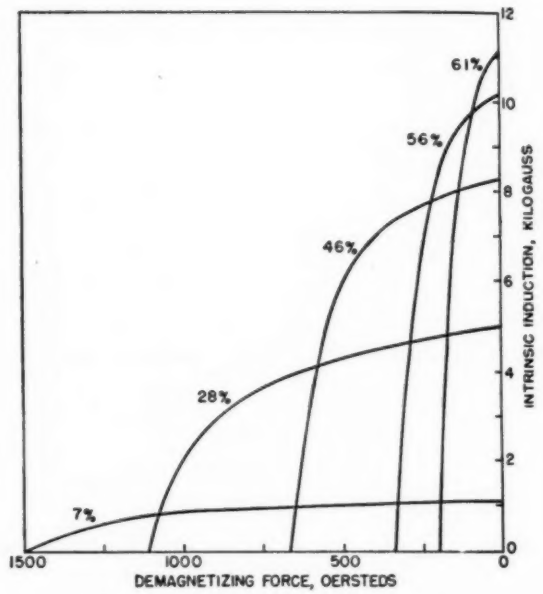

FIG. 6. Effect of packing iron particles.

C. Permanent-Magnet Properties of Compacted Particles

The predicted increase in residual induction and decrease in coercive force with greater packing fraction of iron particles is observed in the actual magnets. Table V and Fig. 6 show the properties of magnets as a function of the volume percent of iron. The general

relationships between magnet properties and packing are summarized in Fig. 7.

The residual induction is directly proportional to the packing fraction of the particles as expected, but the coercive force deviates from the relationship predicted by Eq. (3) at higher packing fractions. This is probably due to inhomogeneity of packing, some of the particles physically contacting others with consequent loss of coercivity, even though the average packing density is less than the 78% value at which cubically-packed cylinders are in contact. If we assume that the outermost five-angstrom shell of each particle is nonferromagnetic, as suggested by König,[28] but becomes ferromagnetic upon contact with an adjacent particle, perfect cylinders 150 angstrom units in diameter can only be packed cubically to 68% before contact, which agrees with the observed very low coercive force at this packing. The maximum energy product is observed to occur at a packing fraction of $\frac{1}{2}$, since the coercive force

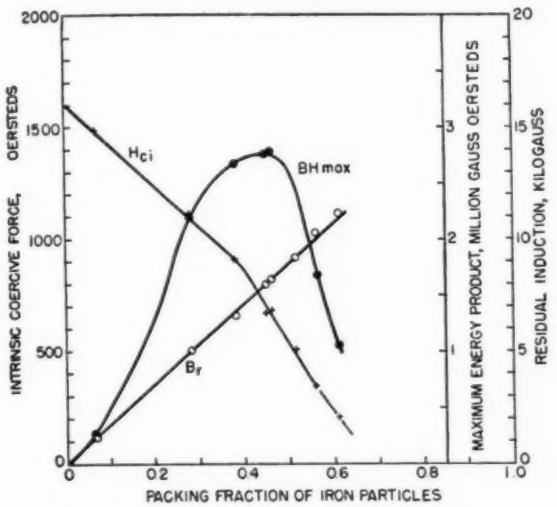

FIG. 7. Effect of packing on H_{ci}, B_r, and BH_{max}.

of the particles used is much less than the 10 000 oersteds which would optimize energy at a packing fraction of $\frac{2}{3}$. Within these limitations, the general features of the predictions are borne out by the experimental results. By carefully controlling packing and alignment, magnets have been produced with energy products as high as 3.32 million gauss-oersteds.

D. Comparison with Other Permanent Magnets

The permanent-magnet properties which have been achieved with elongated single-domain iron particles compare very favorably with the properties of presently used commercial materials. Only Alnico V and VI have greater energy products, as shown in Table VI. The demagnetization curves of two shape-anisotropy iron magnets are compared with the Alnico alloys in Fig. 8, and with other permanent-magnet materials in Fig. 9.

[28] H. König, Naturwiss. **33**, 71 (1946).

TABLE VI. Comparison of permanent-magnet materials.

Material	B_r Gauss	H_c Oersteds	BH_{max} Gauss-oersteds $\times 10^{-6}$
Alnico V[a]	12 000	575	4.5
Alnico VI[a]	10 000	750	3.5
Elongated single-domain iron 50%	8800	715	3.3
Elongated single-domain iron 30%	5700	1105	2.9
Alnico VII	7200	1000	2.5
Directional barium-iron oxide[b]	3600	1400	2.5
Formate process iron 30% cobalt[c]	8600	410	1.7
Alnico II[a]	7200	540	1.6
Cunife[a]	5400	550	1.5
Formate process iron[c]	6000	480	1.1
Cunico[a]	3400	660	0.8
Vectolite[a]	1600	1000	0.6

[a] Alnico Design Manual, Carboloy Department, General Electric Company, Detroit, Michigan (1951).
[b] See reference 19.
[c] See reference 15.

The two elongated single-domain iron-particle magnets reported (ESD 30 and ESD 50) illustrate the range of properties which can be obtained by controlling the packing fraction of iron particles. Other combinations of residual induction and coercive force have also been measured, as shown in Fig. 6.

V. DISCUSSION

There are three reasons why the energy products of the magnets reported in this paper are less than the maximum predicted from theoretical considerations: (1) the coercive force of the particles used was substantially less than the predicted limit, (2) the packing of the particles was not completely uniform, and (3) the alignment of the particles was imperfect.

The principal reason why the observed energy product of 3.3 million gauss-oersteds fell so far short of the predicted limit of 39 million is the low coercive force of the particles; this has been discussed in another paper.[8] Although the coercive-force limit of 10 500 oersteds may not be attainable, there is no question

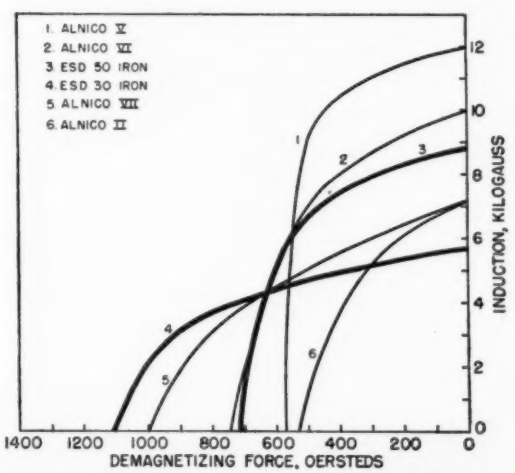

FIG. 8. Demagnetization curves of Alnico alloys.

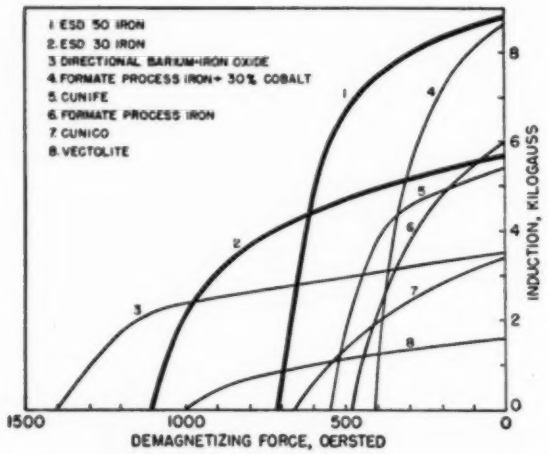

FIG. 9. Demagnetization curves of permanent-magnet materials.

that substantial improvements over the present 1600 oersteds can be made: values greater than 2000 oersteds have already been observed. Lesser improvements in magnet energy can be realized by improving the techniques to obtain a more uniform packing and a higher degree of particle alignment. The addition of cobalt to increase the intrinsic saturation induction of the particles would also result in a higher energy product.

The shape-anisotropy fine-particle iron magnets reported in this paper compare favorably with the best alloy magnets, and there appear to be excellent prospects for improving this new material. Only Alnico V has significantly better energy, and even this does not seem to be beyond the reach of shape-anisotropy magnets. Indeed, Nesbitt, Williams, and Bozorth[29] have conducted a detailed investigation of single crystals of Fe_2NiAl and concluded from torque curves and electron micrographs that the shape anisotropy of an elongated precipitate is a major factor contributing to the permanent-magnet properties of Alnico V. Kronenberg[30] has obtained electron micrographs which show an elongated precipitate in Alnico V heat treated to maximum coercive force. The properties of the elongated single-domain iron particles reported in this paper demonstrate that the shape anisotropy effect is of the right order of magnitude to account for the permanent magnet properties of Alnico V, and provide additional direct experimental evidence for the explanation of Alnico V in terms of shape anisotropy advanced by Nesbitt, Williams, and Bozorth.

VI. CONCLUSIONS

The utilization of the shape anisotropy of elongated single-domain particles represents a promising new approach to the development of fine-particle magnets, and removes the limitation on the coercive force of fine-particle iron magnets previously imposed by the low crystal anisotropy of iron. Elongated particles can be readily aligned to achieve directional magnetic properties. By controlling the packing density of the particles, a wide range of permanent magnet properties duplicating previous materials can be achieved. Elongated single-domain iron particles have been compacted into magnets with energy products as high as 3.32 million gauss-oersteds, and the possibility of achieving higher energies appears to be excellent. These results provide direct experimental evidence for the existence of a shape anisotropy effect of sufficient magnitude to account for the permanent-magnet properties of Alnico V.

ACKNOWLEDGMENTS

The authors are deeply indebted to I. F. Kinnard whose encouragement and support made this work possible. The contributions of J. H. Hollomon, J. C. Fisher, W. H. Meiklejohn, C. P. Bean, and I. Jacobs of the General Electric Research Laboratory, and P. G. Gormley and D. S. Jones of this laboratory are gratefully acknowledged.

[29] Nesbitt, Williams, and Bozorth, J. Appl. Phys. **25**, 1014 (1954).

[30] K. Kronenberg, Z. Metallkunde **45**, 440 (1954).

Letters to the Editor

Magnetically Controlled Microwave Directional Coupler

R. W. DAMON
General Electric Research Laboratory, The Knolls, Schenectady, New York
(Received June 27, 1955)

THE use of magnetic materials in microwave circuit elements has become increasingly important in recent years. Most applications are based on the ferromagnetic resonance effect, which causes a selective absorption or phase shift of electromagnetic waves dependent on the direction of circular polarization of these waves. The magnitude of the phase shift or attenuation can be controlled by changes in magnitude and direction of an applied magnetic field.

The earliest of these devices made use of the Faraday rotation in circular wave guide combined with rectangular wave guide polarizers and analyzers.[1] More recently, it has been recognized that the circularly polarized H-vector which is present at some points in a TE_{10} mode rectangular wave guide can be utilized also to construct nonreciprocal microwave components.[2,3] This same principle has been extended to the construction of a directional coupler, in which a magnetic material couples power directionally between two wave guides. The coupling can be controlled by changes in the sense and the magnitude of the applied magnetic field, which is parallel to the electric vector in the wave guide.

The construction of this directional coupler is shown in Fig. 1. The magnetic material, for which a cylinder of nickel-zinc ferrite has been used, is placed a distance x_0 from one wall of the wave guide, near the location of complete circular H-polarization. With the configuration shown, power will be coupled from the main guide to the auxiliary guide and will travel in the same direction. The strength of the coupling is determined by the magnitude of the applied magnetic field. If either the direction of propagation or the magnetic field is reversed, there will be no coupling, while if both are reversed power will again be coupled into the auxiliary guide and will travel in the same direction as in the main guide. It is thus possible to measure incident power out of one arm of the auxiliary guide for one field direction and, by reversing the field, to measure reflected power out of the other arm of the auxiliary guide. The direction of propagation in the auxiliary guide can also be made opposite to that in the main guide by laterally displacing the guides a distance $a-2x_0$.

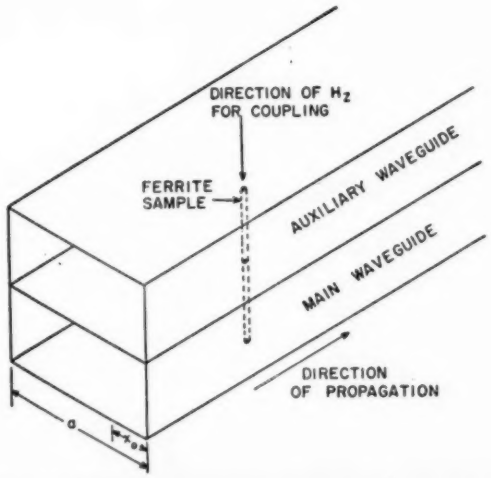

FIG. 1. Schematic construction of the magnetically controlled directional coupler.

The operation can be explained by observing that the magnetization vector of the sample, near resonance with the H-vector in the main guide, also precesses in that portion of the sample which is in the auxiliary guide, since the material is magnetized to saturation. This excites a wave in the auxiliary guide which is circularly polarized in the same sense as the original wave and leads to propagation in the same direction if the sample is at the corresponding position of circularly polarized H-vector in this guide. The general dependence of the coupling and directivity on the sample properties and field strength can be calculated from the theory of the ferromagnetic resonance.[4]

In the usual theory of coupling through holes,[5] the radiated field is expressed in terms of the magnetic and electric dipole moments of the hole. For coupling holes between wave guides, these moments can be related to an equivalent circuit of the junction[6] and the coupling calculated in terms of this equivalent circuit. With the hole filled with a magnetic material, the usual expressions for the magnetic moment should be replaced by $M^{\pm}V$, the magnetic moment of the sample. Here M^{+} is the component of magnetization with the direction of precession the same as the direction of polarization of the exciting field, while M^{-} is the reverse component and V is the sample volume. We neglect elements in the equivalent circuit arising from the electric polarizability, although these can be included in a straightforward manner. The sample then acts essentially as a magnetic dipole of strength $M^{\pm}$ radiating into the coupled guide. The power radiated in the forward direction is proportional to $(M^{+}V)^2$, where the constant of proportionality depends on the coupling to the normal modes of the guide. In the reverse direction, M^{+} is replaced by M^{-}, leading to a directivity $(M^{+}/M^{-})^2$. The neglect of electric polarization is more serious in this case, since M^{-} is much smaller than M^{+}, and may be of the order of magnitude of the electric moment. Consequently, we may overestimate the directivity.

Assuming that the polarization of the exciting field remains constant over the volume of the sample, we can calculate the magnetization vectors from the theory of the ferromagnetic resonance.[4] We obtain

$$M^{\pm}=M_x\pm iM_y=\frac{\pm iM_0H_1{}^{+}\gamma T_2}{1+i(H_0\pm H)\gamma T_2^2},$$

where $H_1{}^{+}$ is the right circularly polarized component of the microwave field of angular frequency ω. The external field required for resonance, H_0, is determined from the internal field for resonance, ω/γ, and the demagnetizing factors of the sample. For an ellipsoidal sample with demagnetizing factors N_x, N_y, N_z, the relation is

$$[H_0+(N_x-N_z)M_0][H_0+(N_y-N_z)M_0]=(\omega/\gamma)^2.$$

In these expressions, γ is the gyromagnetic ratio of the material and γT_2 is a measure of the width of the resonance. Using these

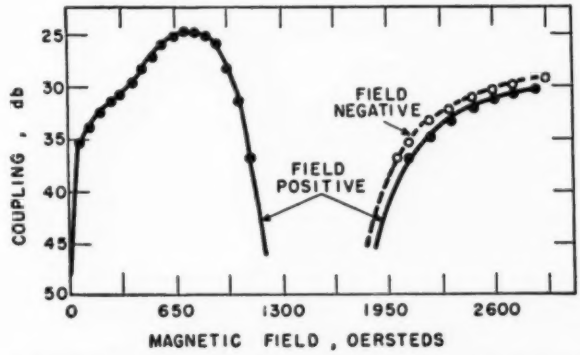

FIG. 2. Coupling *vs* magnetic field strength for a sample ¼ in. in diameter by 1 in. long; frequency 8400 Mc/sec. No signal was observed with the field negative and less than 1500 oe, corresponding to a directivity at resonance greater than 30 db. At 700 oe, the main guide attenuation was 2.3 db and the voltage standing wave ratio was 1.7.

expressions for $M^{\pm}$ and the coupling and directivity relations obtained above, we can calculate the expected behavior of this device.

$$\text{Coupling}=C\left(\frac{M^{+}V}{H_1^{+}}\right)^2=C\frac{(M_0V\gamma T_2)^2}{1+(H_0-H)^2(\gamma T_2)^2}$$

$$\text{Directivity}=\left(\frac{M^{+}}{M^{-}}\right)^2=\frac{1+(H_0+H)^2(\gamma T_2)^2}{1+(H_0-H)^2(\gamma T_2)^2}.$$

Typical results for a device of this type are shown in Fig. 2. The sample was located halfway from one wall to the center of the guide, and no attempt was made to determine the optimum position. The coupling is measured relative to the main guide power at $H=0$. Since there is some attenuation of the main guide power when the magnetic field is positive (2.3 db at resonance, in this case), the true coupling is somewhat higher than that shown. The directivity could not be measured with this sample but was greater than 30 db at the position of maximum coupling. The increased coupling for both field directions at high field strength is attributed to a dimensional resonance in the sample; it is not observed in samples of smaller diameter which were also used. The coupling can be increased by using samples of larger diameter although the directivity is lower because of ellipticity in the H_1-polarization. The coupling can also be increased with no loss of directivity by increasing the longitudinal extent of the sample, or by using an array of samples.

[1] C. L. Hogan, Revs. Modern Phys. **25**, 253 (1953).
[2] Kales, Chait, and Sakiotis, J. Appl. Phys. **24**, 816 (1953).
[3] E. H. Turner, Proc. Inst. Radio Engrs. **41**, 937 (1953).
[4] C. Kittel, Phys. Rev. **73**, 155 (1948).
[5] H. A. Bethe, Phys. Rev. **66**, 163 (1944).
[6] N. Marcuvitz, *Waveguide Handbook*, MIT Radiation Laboratory Series (McGraw-Hill Book Company, Inc., New York, 1951), Vol. 10.

New Type Ferrite Microwave Switch

R. F. Sullivan and R. C. LeCraw
Diamond Ordnance Fuze Laboratories, Washington 25, D. C.
(Received May 7, 1955)

An x-band ferrite cavity-type switch has been developed in this laboratory utilizing a ferrite rod placed axially in a cylindrical cavity fed and terminated by rectangular wave guide. When a longitudinal magnetic field is applied, the cavity is detuned for each circular wave component of the TE_{11} mode.[1] Rotation of the plane of polarization also occurs. At the output the rectangular wave guide acts as a polarization filter.

Because rotation in a cavity is cumulative, it may be shown by summing the electric field vectors at the output iris that the net rotation tends to 90° for all values of magnetic field. The broad isolation *vs* applied steady magnetic field characteristic shown in Fig. 1(A) is caused by this effect and by cavity detuning. The isolation is limited by mode ellipticity at the output. The two peaks in the characteristic are not as yet fully understood.

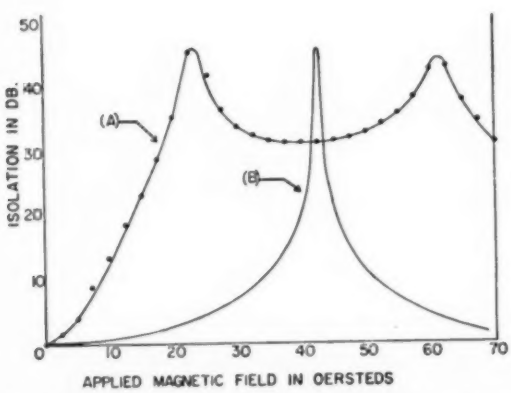

Fig. 1. Isolation *vs* applied steady magnetic field. (A) Cavity-type switch. (B) Rotation-type switch.

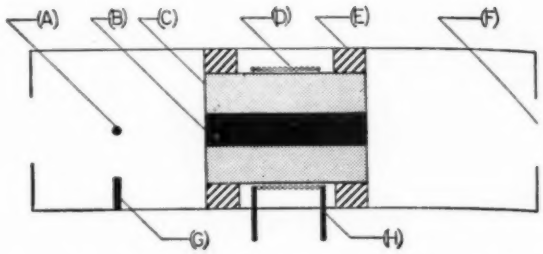

Fig. 2. Cross-sectional view of switch. (A) Tuning stub. (B) Ferrite rod. (C) Teflon cylinder. (D) Coil. (E) Polyfoam washer. (F) Iris. (G) Phasing stub. (H) Coil lead.

Figure 1(B) shows the magnetic field *vs* isolation characteristic of the usual rotation-type switch.[2,3] This switch has a very narrow characteristic for isolations of the order of 30 db and at half the corresponding field value has only 3 db isolation.

The cavity switch (Fig. 2) consists of a cylindrical wave guide 3.375 in. long and 0.875 in. internal diam, in the center of which is an axial ferrite rod[4] 1.19 in. long and 0.230 in. diam. The diameter of the irises is 0.45 in. A 20-turn coil, wound on a Teflon cylinder 0.625 in. diam, surrounds the ferrite and is supported in the cavity by polyfoam washers. The Teflon cylinder places the coil in a region of low microwave field, reducing mode ellipticity and losses caused by the coil. The coil leads are brought out perpendicular to the unrotated plane of polarization of the TE_{11} mode. Winding the coil inside, rather than outside of a slotted cavity, eliminates ellipticity at the output caused by slot radiation as the plane of polarization is rotated. This also reduces the current per unit inductance required for a given rotation.

Tuning is accomplished by a diametral stub parallel to the unrotated electric field. A diametral phasing stub is inserted in the same cross-sectional plane perpendicular to the tuning stub. The phasing stub reduces ellipticity caused by the tuning stub as the plane of polarization is rotated, thus preserving the initial steep isolation characteristic of the switch.

At 9160 mc, the loaded Q is 200, the $VSWR$ 1.2, and the insertion loss 0.8 db, including residual magnetic detuning. The coil inductance is 5 μh.

Figure 3(A) shows a 0.25 μsec current pulse supplied to the switch coil by a thyratron pulser, and Fig. 3(B) shows the output microwave pulse. The peak coil current of 19 amp corresponds approx to the 42.5 oersted point in Fig. 1(A). The voltage reflection coefficient at this operating point is approx 0.97.

For pulse operation, a switch of this type overcomes two major disadvantages of the usual rotation-type switch: the slow rise

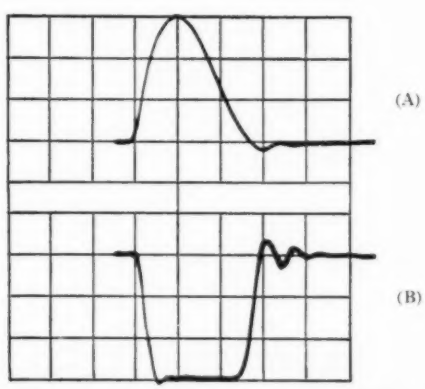

Fig. 3. (A) Current pulse (I_{max} =19 amp). (B) Microwave output pulse. (Time scale =0.1 μsec/div. Same external sweep trigger used for both oscillograms.)

time characteristic and the high sensitivity of the isolation to variations in peak current.

[1] A. A. Th. M. Van Trier, Appl. Sci. Research, **B3**, 305–371 (1953).
[2] R. C. LeCraw, J. Appl. Phys. **15**, 678 (1954).
[3] A ferrite switch designed by C. H. Luhrs has been referred to as a cavity-type switch [Fox, Miller, and Weiss, Bell System Tech. J. **34**, 5 (1955)]. The characteristics of this switch, however, are essentially identical to a simple rotation-type switch (H. W. Herman, Naval Research Laboratory Report 3883).
[4] A MgMn ferrite, Type R-1, manufactured by General Ceramics Corporation, Keasbey, New Jersey.

Failure of the Ionic Centrifuge Prior to the Ionic Expander

JOSEPH SLEPIAN
Westinghouse Research Laboratories, East Pittsburgh, Pennsylvania
(Received June 15, 1955)

A CENTRAL discharge, in a circular cylindrical vacuum vessel, set in an aligned uniform magnetic field between conducting planes, could apparently serve as an isotope separator. The ions of the discharge apparently reach the cylindrical bounding wall according to whether inherent mass of the ion is greater or less than a certain function of the radius and magnetic field. The space charge of the positive ions in transit would be effectively neutralized by an emission of electrons from the end plane electrodes.[1]

We had such an idea in the early forties and used for the central discharge a short arc, about 0.25 in. in length, between a cathode and an anode of the metal desired at that time, namely, uranium. For the cathode which was only slightly consumed in an experiment of a few hours, we used a cored carbon manufactured by the National Carbon Company. Our arc current was usually about 10 amp, and arc voltage 20 to 100 v. At 10 amp, the ion current drawn into the vacuum space was about 500 ma. At 100 amp in the arc, the ion current was about 10 amp to the space. There was no limitation of the vacuum. The deposit of neutral atoms from the arc was very small.

The electrodes of this arc were brought in by long arms through central holes in the top and bottom plates of our vacuum vessel. We used a variety of dimensions of vacuum vessels, ranging from a cylinder a foot in diameter and a few inches in height, to four feet in diameter and three feet in height. These vessels were operated between the pole pieces of a magnet producing fields up to 10 000 gauss.

We had originally planned to use this device, the ionic centrifuge, in World War II for large scale separation of the isotopic ions of the metal used as the anode of the arc, but the results obtained were exceedingly disappointing. The vacuum discharge obtained differed from that expected in an important respect, which made the enrichment obtained only equal to about $e-1=\frac{1}{2}(\delta m/m)$, where e is the enrichment, m the mass of one istope, and $m+\delta m$ the mass of the other isotope. This was obtained with ion accelerating effects as high as 2000 v or as low as 30 v, and currents as low as 10 ma.

I will take one type of experiment which we tried in various voltages and geometrical dimensions with invariably disappointing results.

The accelerating electric field of V volts was applied to the top and bottom flat plates around the electrodes, and the anode of the arc was grounded at 0 volts. The vacuum space was closed by the cylinder set at a distance r cm from the arc. This cylinder was made up of a large number of approximately radial slats which could be insulated from the top and bottom plates. In the experiments describe here the slats were left floating.

The potential applied to the top and bottom plate was varied from -20 v to a large negative value. The voltage at which the cylinder floated was found to be nearly equal to that impressed upon the top and bottom plates, so long as the voltage was numerically less than about the Larmor voltage, $V_L=-(e/8mc^2)H^2r^2$ absolute volts, but it did not increase much with further numerical increase in impressed voltage as shown in Fig. 1.

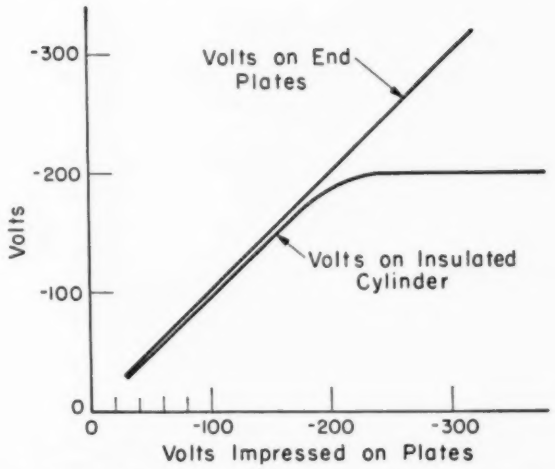

FIG. 1. Voltage on insulated cylinder *vs* voltage on excited end plates.

When the top and bottom plates were at a potential more negative than the Larmor voltage, they took approximately half the positive ion current, and the insulated cylinder took the other half of the positive ion current as determined, for example, by the amount of deposit on one side of the slats. An equal amount of negative electron current accompained the positive ions there. This result was obtained when r was varied from one to twenty inches, and the magnetic field varied from a few hundred up to over ten thousand gauss. The electric potential varied from minus twenty volts to more than minus two thousand volts, although the Larmor formula above did not hold for obvious reasons for the higher voltages. Figure 1 gives the curve for $V_L=-200$ v.

This result is completely at variance with that expected by the usual theory believed in at that time, about 1940. We had expected that the voltage on the insulated cylinder in the ionic centrifuge would stay at nearly zero potential, while the voltage on the end plates was varied, and that the voltage on the end plates would have to reach values high enough to release electrons before the extremely tiny space-charge-limited positive ion current would be exceeded. Instead, at low potential, less than -50 v, currents of the order of hundreds of milliamperes were received by the end plates, and a like current of positive ions, accompanied by a like current of electrons, was flowing to the outer part of the end plates and/or to the insulated cylinder.

The analyses of the enrichment of the isotopes of the uranium found in the deposits showed that the material on the excited end plates was about one-half percent richer in the lighter isotope than the material on the insulated cylinder and independent of the voltage used.

The circular symmetry of the electrodes used in the ionic centrifuge insured that the component of the electric field perpendicular to the radius was zero. The field was actually a radial one. The current was, therefore, a spiral one, and deposits on the slats were on one side of the slats only. A spiral current of electrons equal to one-half the initial total ion current also was drawn out from the arc by the electric field, with the cooperation of the positive ions, even though the field apparently opposes the motion of the electrons.

The use of two radial electrodes with front edges close to the arc, and rear edges far from the arc and from each other, was then suggested, and the ionic expander was born.[2]

The project was ably led from inception of the work until October 1, 1952 by Dr. Wilson M. Brubaker now at the Consolidated Engineering Company, Pasadena, California. He was ably assisted by Edward F. Federmann, Westinghouse Electric Corporation.

[1] Smith, Parkins, and Forrester, Phys. Rev. **72**, 989–1002 (1947).
[2] Joseph Slepian, Proc. Natl. Acad. Sci. (July 15, 1955).

Erratum: Rocket Measurements of Upper Atmosphere Ambient Temperature and Pressure in the 30- to 75-Kilometer Region

[J. Appl. Phys. 25, 161–168 (1954)]
H. S. Sicinski, N. W. Spencer, and W. G. Dow
Department of Electrical Engineering, University of Michigan, Ann Arbor, Michigan.

FIGURE 8 is in error in the position of the first four values in the curve of P_0'. These values actually continue the trend of the other values and should be replaced by the following: 214 mb, 31.2 km; 201 mb, 31.7 km; 179 mb, 32.1 km; and 168 mb, 32.5 km. These four values did not enter into the computations presented in the other figures.

Erratum: Nucleation of Lead with Preferred Orientation

[J. Appl. Phys. 26, 918–919 (1955)]
H. A. Atwater and B. Chalmers
Gordon McKay Laboratory, Harvard University, Cambridge, Massachusetts

IN the third paragraph, on impure lead, instead of "free surface of the solid," read: "free surface normal axis of the solid."

Research Reports

Propagation in Semi-Infinite Wave Guides. J. Shmoys, Report No. EM-63. Write to New York University, Institute of Mathematical Sciences, Division of Electromagnetic Research, 25 Waverly Place, New York 3, N. Y. (No charge.)

This report contains translations of six papers by L. A. Vajnshtejn dealing with problems of radiation of acoustic and electromagnetic waves from parallel-plane and cylindrical wave guides. The following papers have been included:

(1) Rigorous solution of the problem of an open ended parallel-plane wave guide, Izvest. Akad. Nauk Kazakh S.S.R., Ser. Fiziol. **12**, 144–65 (1948);

(2) On the theory of diffraction by two parallel half planes, *ibid.*, **12**, 166–180 (1948);

(3) Theory of symmetric waves in a cylindrical wave guide with an open end, Zhur. Tekh. Fiz. **18**, 1543–64 (1948);

(4) The theory of sound waves in open tubes, *ibid.*, **19**, 911–30 (1949);

(5) Radiation of asymmetric electromagnetic waves from the open end of a circular wave guide, Doklady Akad. Nauk **74**, 485–8 (1950);

(6) Diffraction at the open end of a circularly cylindrical wave guide whose diameter is much greater than the wavelength, *ibid.*, **74**, 909–12 (1950).

In the first two of these papers, which deal with the parallel-plane wave guide, both even and odd symmetry and both boundary conditions ($u=0$ and $\partial u/\partial n=0$) are considered simultaneously. The first paper presents the solution of the problem, and the second gives the asymptotic form of the solution and the physical interpretation of this asymptotic form. The remaining four papers deal with the case of a cylindrical wave guide. Of these the first deals with symmetric electromagnetic waves presenting the solution and a discussion of asymptotic behavior; the second one deals with sound waves, both symmetric and asymmetric, and includes a discussion of resonance phenomena in organ pipes; the third presents a generalization of the previous treatment of electromagnetic waves to asymmetric modes; and the fourth and last paper gives a physical interpretation of the asymptotic form of the solution for electromagnetic waves.

In this country, as is well known, these problems have also been solved by the Wiener-Hopf method.[1] However, the published presentations of these solutions usually contain some restrictions and the generalizations have nowhere been explicitly carried out. The papers of Vajnshtejn presented here should prove to be of value because of the thoroughness with which the problems are treated and because Vajnshtejn has introduced some interesting concepts and methods not included in the aforementioned works.

[1] A. E. Heins, Quart. Appl. Math. **6**, 157–66 (1948); *ibid.* **6**, 215–20 (1948); *ibid.* **8**, 281–91 (1950). H. Levine and J. Schwinger, Phys. Rev **73**, 383–406 (1948).

Units of Weight and Measure—Definitions and Tables of Equivalents. Dr. L. V. Judson, National Bureau of Standards Miscellaneous Publication 214, pp. 64. Order from the Government Printing Office, Washington 25, D. C. Price 40 cents (55 cents outside the U. S.).

This publication, superseding Miscellaneous Publication 121 issued in 1936, defines the units of length, mass, area, volume, and capacity in use in the United States. It also gives tables of interrelation and tables of equivalents for these units in the metric system and in the U. S. customary system. The volume also contains sections of the fundamental equivalents, the approved spelling and abbreviation of each of the most common units of weight and measure, and the status of the metric system in the United States. All of the tables and other material have been revised to conform to current definitions, equivalents, and usages.

Books Reviewed

Basic Processes of Gaseous Electronics. Leonard B. Loeb. Pp. 1012+xvii, University of California Press, Berkeley, 1955. Price $13.50.

The whole field of fundamental processes in gases is discussed in this book. The subjects considered in detail are: ionic mobilities, diffusion of charge carriers in gases, distribution of electron energies in an electric field, formation of negative ions, recombination, electrical conduction in gases, ionization by electron impact, and the second Townsend coefficient. The emphasis is on the analysis of recent experimental and theoretical research.

Proceedings of the International Conference of Theoretical Physics. Pp. 942+xxviii, Japan Society for the Promotion of Science, Tokyo, 1954. Price $10.00, postage $1.00 (order from Kinokuniya Book-Store Company, Ltd., 826 Tsunohazu 1-chome, Shinjuku-ku, Tokyo, Japan).

In September, 1953 a conference on theoretical physics was held at Kyoto and Tokyo. Fifty-five foreign physicists and many Japanese physicists participated. Readers of the *Journal of Applied Physics* will probably be particularly interested in the following sections of the *Proceedings*: Polymers, dislocations, molecules, metals, electron theory of intrinsic magnetization, antiferro- and ferri-magnetism, magnetic resonance, dielectrics, color centers, liquid helium, and superconductivity. About one-half of the book is devoted to the topics cited; the other half is devoted to field theory, elementary particles, nuclear physics, and statistical mechanics.

Defects in Crystalline Solids. Pp. 457, The Physical Society, 1 Lowther Gardens, Prince Consort Road, London S.W. 7, 1955. Price 40s. Postage 1s.

The papers presented in this volume were presented at an international conference held at the University of Bristol in July, 1954. The forty-seven papers in this volume are for the most part concerned with point imperfections and dislocations. There are ten papers on the application of magnetic resonance to the study of imperfections in solids. There are many papers on the effects of radiation upon solids, on diffusion, and on the theory and effects of dislocations.

The Physics of the Ionosphere. Pp. 406, The Physical Society, 1 Lowther Gardens, Prince Consort Road, London S.W. 7, 1955. Price 40s. Postage 1s.

This volume contains the papers presented at the international conference on the physics of the ionosphere held under the auspices of the Physical Society at the Cavendish Laboratory, Cambridge, September 6–9, 1954. The fifty papers are divided into four groups: The lowest ionosphere, irregularities and movements in the ionosphere, the ionospheric F2 layer, and the mathematics of wave propagation through the ionosphere.

Radio Astronomy. J. L. Pawsey and R. N. Bracewell. Pp. 361+x, Figs. 150, Plates 23, Oxford University Press, New York, 1955. Price $8.80.

The heart of this book is the description and analysis of observations of radio waves from the sun, the moon, the galaxy, and external galaxies. In order to provide the basis for the analysis, about one-half of the book is devoted to the study of the technique of radio wave observations, the theory of radio waves in ionized gases, and the aspects of solar physics and astrophysics which are relevant to radio astronomy. Radio observations of meteors, the possibilities of echo measurements on extraterrestrial objects, and the effects of terrestrial atmosphere on extraterrestrial radio waves are discussed.

Quantum Mechanics. Leonard I. Schiff. Pp. 417+xii, Figs. 30, McGraw-Hill Book Company, Inc., New York, 1955, second edition. Price $6.50.

The new edition of Schiff's textbook of quantum mechanics differs from the first edition principally in the following ways: modifications have been made in eight of the fifty sections; seventeen new problems have been added; the length has been increased by thirteen pages. The book is a textbook for a graduate level course for physicists.

Microwave Spectroscopy. C. H. Townes and A. L. Schawlow. Pp. 698+xviii, Figs., McGraw-Hill Book Company, Inc., New York, 1955. Price $12.50.

The object of this book is to provide a thorough and comprehensive discussion of the microwave spectroscopy of gases. It presents a systematic account of the theory, experimental data, and experimental apparatus and techniques in the relatively new field of microwave spectroscopy. High resolution and high-temperature spectroscopy, the theory of hyperfinestructure and magnetic interactions, free radicals, hindered internal molecular motions, and the technique of millimeter wave measurements are among the recent topics discussed. Appendices totaling 150 pages provide tables and information needed for research and interpretation of data. A bibliography lists over 1000 references.

Practical Physics. M. W. White, K. V. Manning, and R. L. Weber. Pp. 484+xii, Figs., McGraw-Hill Book Company, Inc., New York, 1955, second edition. Price $5.50.

Chapters on color, modern physics, and nuclear physics, and a section describing laboratory experiments have been added in this second edition. The book is designed as a textbook for an introductory college course in physics. Calculus is not used, and the part of trigonometry that is employed is explained in an appendix.

Books Received

Everything and the Kitchen Sink. Pp. 160. Farrar, Straus, and Cudahy, New York, 1955. Price $4.00.

Electro-Technology. M. G. Say. Pp. 167, Figs. Philosophical Library, Inc., New York, 1955. Price $6.00.

Cover Photograph

Argonne National Laboratory constructed the "Borax I" reactor in the summer of 1953 at the Arco AEC reactor test station. The reactor was used in a series of experiments in 1953 and 1954 in order to determine the characteristics of a water-cooled, water-moderated reactor under boiling conditions. A cutaway drawing of the reactor is shown below. The reactor tank, four feet in diameter and about thirteen feet high, contained the reactor core which consisted of a number of enriched uranium-aluminum fuel elements and five neutron-absorbing control rods. The reactor tank was contained in a larger shield tank ten feet in diameter which was sunk into the ground and had earth piled around it for additional shielding. The reactor tank was filled with water to a height of three to four and one-half feet above the top of the core.

At the conclusion of these tests, the reactor was subjected to a final test in which the power was increased to more than 10^{10} watts in 0.1 sec. The photographs on the cover are frames from a motion picture of the experiment. The light streaks in the third and fourth frames are believed to be fragments of the uranium-aluminum fuel plates which burned in the air. The fourth frame was taken at the height of the explosion and shows portions of the reactor tank, control rod mechanism, and reactor core which have been hurled 80 feet into the air. Most of the fuel elements fell to earth within a radius of 200 feet from the reactor. There was no dangerous fall-out at distances greater than a few hundred feet.
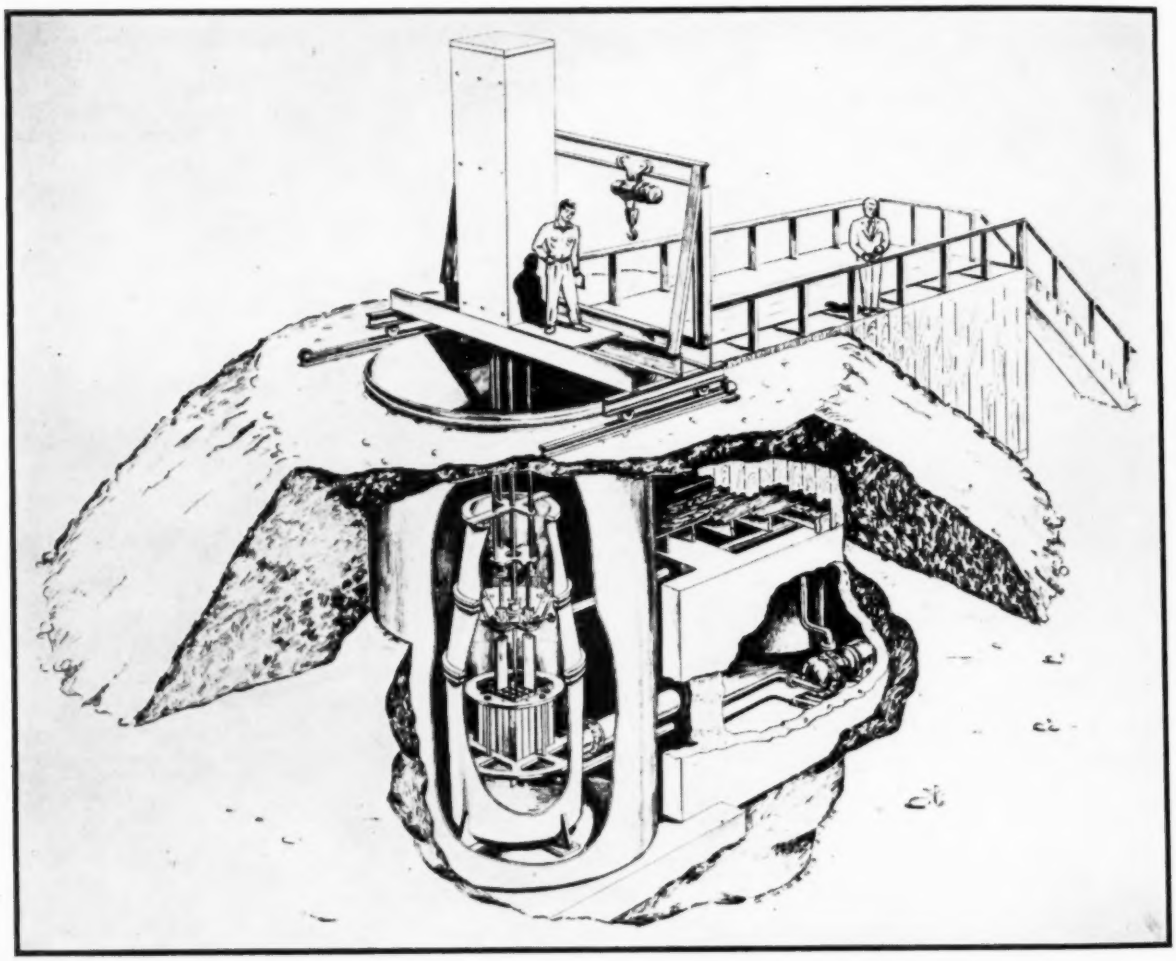
These photographs were supplied by W. H. Zinn and L. C. Furney of the Argonne National Laboratory.